GEO-3900

MASTER'S THESIS IN GEOLOGY

Fluid flow features along the Bjørnøyrenna Fault Complex west of West Loppa High, SW Barents Sea

David Selvåg Larsen

November, 2011

Faculty of Science and Technology

Department of Geology

University of Tromsø

GEO-3900

MASTER'S THESIS IN GEOLOGY

Fluid flow features along the Bjørnøyrenna Fault Complex west of West Loppa High, SW Barents Sea

David Selvåg Larsen

November, 2011

Fluid flow features along the Bjørnøyrenna Fault Complex west of West Loppa High, SW Barents Sea

David Selvåg Larsen[1]

Institute of Geology, Dramsveien 201, 9037 Tromsø

Abstract

This master thesis contributes to better understand the occurrence and development of giant to medium scale vertical fluid flow structures in the area west of the Loppa High at the Bear Island Fault Complex (BIFC). The study area lies in the SW-Barents Sea and the study was based on the interpretation of a 3D seismic cube "West Loppa 2008".

Fluid emissions features and accumulation area visualized using seismic attributes, which mark characteristic areas of seismic anomalies with acoustic masking, bright spots, dimmed zones and flat spots. The lateral extent of the observed features varies from Giant Gas Chimneys (GGC) encompassing areas of < 100km^2 and vertical heights of ~3 km to Medium Gas Chimneys (MGC). Amplitude Anomalies (AA), Potential fault related Leakage Zones (PLZ) and Flat spot Amplitude Anomalies (FAA) are smaller scale features but may be as well very important in the whole fluid flow system including the storage and leakage potential within the study area.

The recent oil and gas discovery of Skrugard located within one of the major fault blocks represented in the study area underlines the importance for understanding fluid flow systems in complex sedimentary basins. An older wildcat (7219/9-1) that lies ~12km southwest of Skrugard showed only residual hydrocarbons.

[1] david.larsen@bakerhughes.com

”Why do you want to climb Mt. Everst? Because it’s there!”

- George Leigh Malloroy

Acknowledgements

Jeg har i de siste årene brukt mye tid og krefter på å skrive denne oppgaven som skal presentere meg på en best og mest profesjonell måte. Det har vært en travel tid, med både spennende oppdagelser i datamaterialet jeg har hatt tilgjengelig, og en ny jobb med et hav av uutforskede og interessante geologiske målemetoder å lære. Siden jeg nå er så nærme en avslutning av denne masterepoken vil jeg takke en rekke personer som har hjulpet og støttet meg gjennom hele denne perioden.

Mine veiledere Professor Jürgen Mienert og førsteamanuensis Stefan Bünz har vært veldig behjelpelige underveis. Til tross for sine travle dager har døren til kontoret deres alltid vært åpen for meg. Tusen takk!

Western Geco fortjener en takk for å være behjelpelige med å gjøre datagrunnlaget for oppgaven tilgjengelig.

Takk til Kenneth, Torgeir, Arne og alle de andre flinke og fantastiske menneskene på brakka, både de som har noe tid igjen og de som er ferdig.

Kristine, Malin og Morten fortjener en ekstra takk for gjennomlesning.

Takk til Tromsø for de fantastiske ski mulighetene område rundt har å tilby, med godt folk.

Takk til ”guttaboys” hjemme i Stavanger og spesielt Thomas Ole, Erlend og Anders som har fått meg til å holde motet oppe!

Familien min som alltid stiller opp.

Takk til kollegaene på Baker Hughes som har gitt meg spillerom.

En meget spesiell takk til Ane som har holdt liv i meg gjennom denne perioden.

Contents

1 Introduction

1.1 Objectives

This master thesis in marine geology and geophysics has as main topic fluid migration in sedimentary basins. The study is based on a 3D seismic cube provided by Western Geco. Well profiles are included in the study for rock physical property and depth correlations. 2D seismic lines are used for a regional geological understanding of the area.

The study area lies in the south-western Barents Sea at the southern flank of a major cross-shelf trough called Bjørnøyrenna (Bear Island trough) (Fig. 1.1.1). The specific working area is west of the Mesozoic structural high West Loppa High in the Bear Island Fault complex. The geological setting of the West Loppa High makes this a favourable study area for hydrocarbons due to several reasons including the potential source rocks (Ohm et al., 2008).

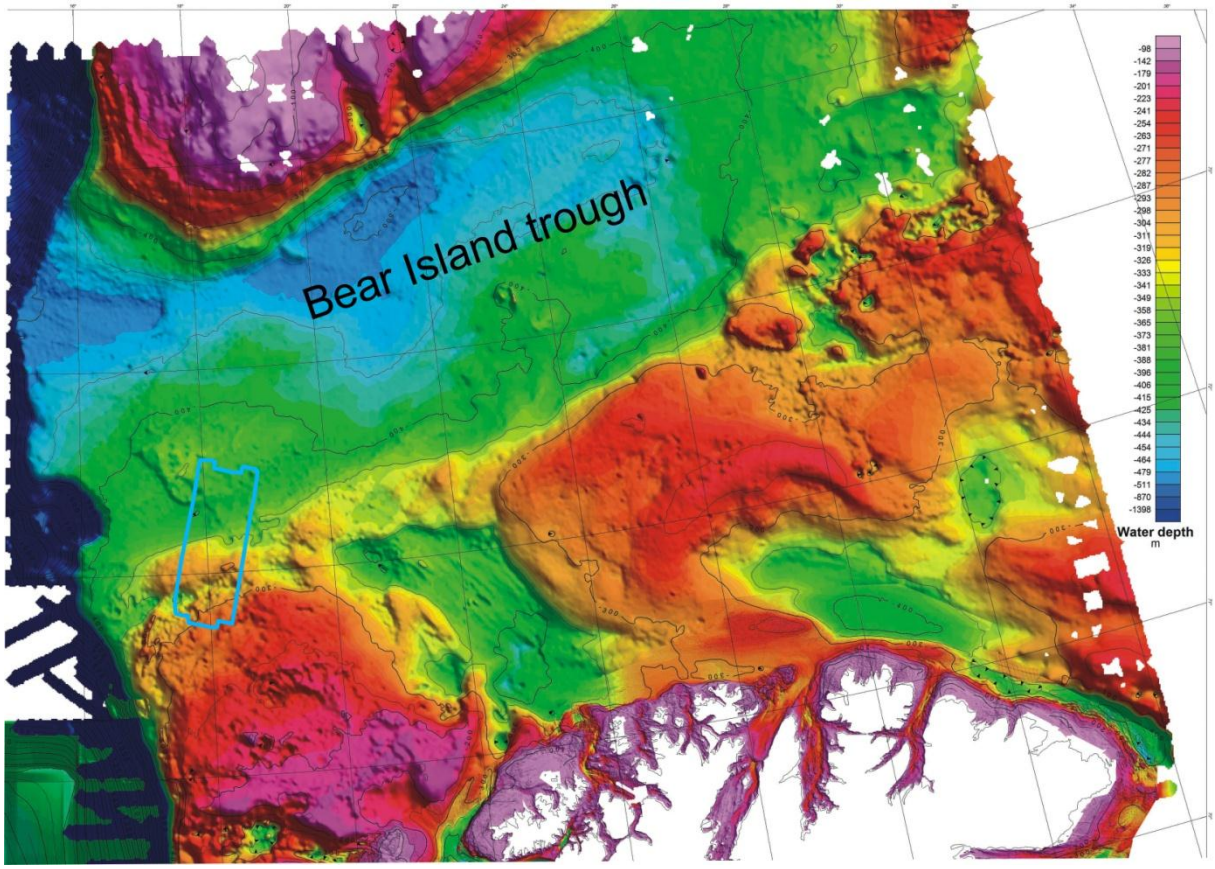

Figure 1.5.1 Bathymetric map of south-western Barents Sea with location of the seismic cube used in this thesis indicated with blue line. Figure is modified from (Smelror et al., 2009).

The Pliocene uplift and erosion may have impacted by reducing the overburden pressure, which in turn caused a mobilization of fluids due to a change in the equilibrium. Chand et al., (2008) calculated that gas expanded by about twice its size since the late Cenozoic uplift and glacial erosion periods.

Based on these findings fluid flow features along the Bjørnøyrenna Fault complex, west of Loppa High will be studied to improve the knowledge of geological processes that govern basin-scale fluid flow. Particularly, we may anticipate from the results a contribution to better understand the occurrence and development of giant vertical fluid flow structures in the area west of Loppa High.

3D seismic is according to Cartwright (2005) one of the greatest inventions regarding Earth Science over the last century. It allows 3D mapping of stratigraphic features and imaging of fluid pathways within the rock formation.
Cartwright (2007) and Løseth (2009) among others interpreted various fluid flow features. I have attempted through my thesis to use their terminology.

The University of Tromsø has produced a considerable number of master theses concerning the topic fluid migration: Hustoft (2005), Thingnes (2007), Martens (2009), Pless (2009), Kristensen (2010) and Dahl (2011). I shall try to build on their gained knowledge though none of the previous studies were pursued west of Loppa High in the Bear Island Fault Complex.

The main goal is to map fluid flow pathways and accumulation areas at the Polheim Sub-Platform and the Bjørnøyrenna Fault Complex to better understand the underlying controlling mechanisms for the occurrence and development of giant vertical fluid flow features (chimneys) and their relationship to the structural development and the regional denudation history. Secondary goals include the analysis of shallow gas accumulations.

The thesis includes the sedimentary environment and tectonic development to understand how it affects fluid flow. Visualizing fluid flow in relation to the geological setting with the use of 3D seismic data will be the main task. The analysis will also use and correlate the physical properties of rocks to the seismic data to elaborate on the causes of acoustic anomalies.

1.2 The Petroleum System:

A petroleum system is “a natural system that encompasses an active source rock and all related oil and gas accumulations in which all the geologic elements and processes that are essential if a hydrocarbon accumulation is to exist” (Magoon, 2003).

The geologic elements are: petroleum source rock, reservoir rock, seal rock and overburden rock. The basic processes are trap formation and the generation-migration-accumulation period of hydrocarbon which includes temperature and pressure.

There is a critical point in time where all factors have to be present for generating hydrocarbon accumulation. After a successful accumulation of oil and gas the preservation of the hydrocarbon reservoir over time is critical which of course is determined by the geological evolution.

Source Rock:

A source rock is rich in organic material and can produce hydrocarbons (oil and gas) if buried at high enough temperatures and pressure. High concentrations of organic matter tend to accumulate in environments where water is stagnant and the organic productivity-is high. Typical environments would be: nutrient rich coastal upwelling, swamps, shallow seas and lakes (Gluyas and Swarbrick, 2004). However, to preserve the organic matter in sediments the water column above needs to be anoxic.

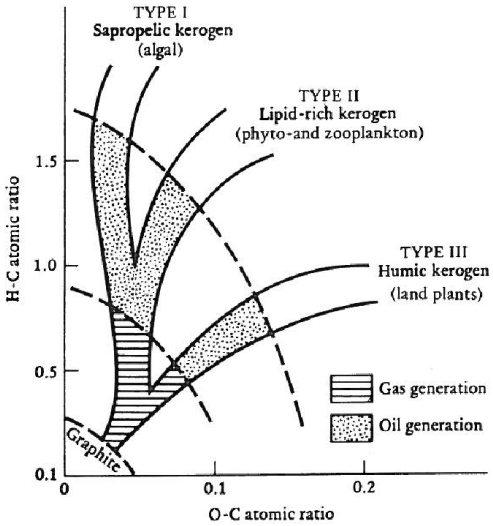

Figure 1.2.1.2.1 Maturation paths of the three different types of kerogen with their origin (Selley, 1998).

The end product (hydrocarbon) of the source rock is dependent on various elements, were temperature is the main contributor. Generally speaking oil is generated on lower temperatures (60-120°C) than gas (120-225°C). Temperatures above 225°C transform the remaining carbons into Graphite through a metamorphosis (Fig.1.2.1) (Selley, 1998). The hydrocarbon generated is also dependent of the origin of organic material and can be classified into different types of kerogen determined on organic source and HI[2] (Hunt, 1996) (Fig.1.2.1).

[2] Hydrogen index is the number of hydrogen atoms per unit volume divided by the number of hydrogen atoms per unit volume of pure water at surface conditions.

Reservoir Rock:

The reservoir rock contains moveable fluids in the interconnected pore space of rocks, often characterized by permeability. A reservoir rock can also be called an aquifer (Fig.1.3.1).

Traps (Seal rock):

Traps allow hydrocarbon to accumulate due to sealing conditions. Fluids cannot migrate through traps. However, traps are limited in extent and may have a spill point. There are several types of traps; stratigraphic traps, structural traps and a combination of the two. A seal rock is in basic a rock that is impermeable.

1.3 Fluid migration:

Fluid migration in the subsurface may include both liquid and gas phase. Fluid migration is often separated into three different classes: primary migration, secondary migration and tertiary migration (Gluyas and Swarbrick, 2004; Tissot and Welte, 1984) figure 1.3.1.

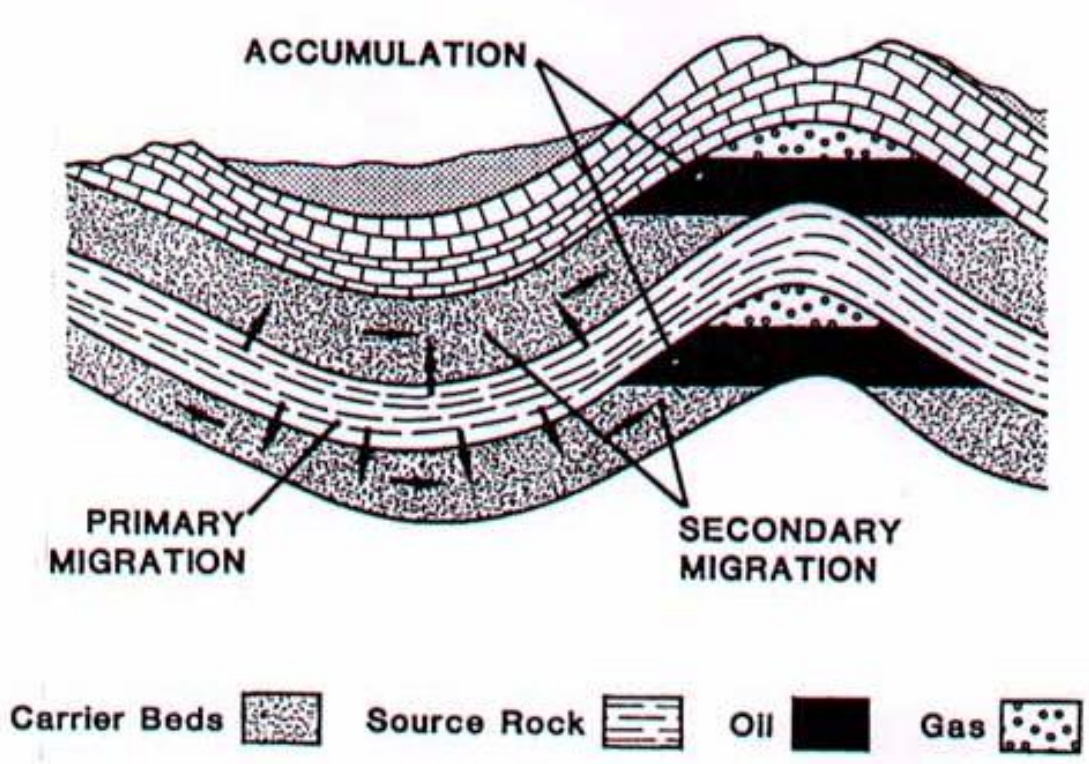

Figure 1.3.1 Shows the classical figure from Tissot and Welt 1984. Descriptive sketch of the basics between source-reservoir- cap rock and primary- and secondary migration.

Primary migration also called expulsion is- defined as "the release of petroleum compounds from kerogen, and their transport within and through the capillaries and narrow pores of a fine-grained

source rock" (Tissot and Welte, 1984) (Fig.1.3.1). Because of the complexity of primary migration and the problems related to laboratory research, primary migration is still a topic of widely discussion. Nevertheless the basic idea introduced by Snarsky (1962), suggests that a large increase in pore space is sufficient to overcome the capillary pressure or exceed the mechanical strength of rock and induce micro cracking. The main two causes for the pressure build up are thermal expansion of water, volume increase by generation of hydrocarbons from kerogen and partial transfer of the geostatic stress field in an overall increase into pore pressure (Tissot and Welte, 1984).

The rate of expulsion is estimated to be about 0.005-0.75 m/Myr. It is several magnitudes slower than secondary migration (J.E.Skeie, 2006).

Secondary migration is the movement of petroleum compounds through rocks with high enough permeability that allows free migration of hydrocarbons into a trap. The important parameters for secondary migration control are high buoyancy of oil and gas in water-saturated porous rocks, low capillary pressure which is forced downwards since the pressure is higher in the porethroats than in porespace and hydrodynamic fluid flow (Tissot and Welte, 1984). The rate and efficiency of secondary migration will be covered in physics (Chap.1.4).

Tertiary migration is defined as leakage and alteration of petroleum as it reaches the Earth's surfaces escaping an already accumulated reservoir. Typical features of tertiary migration are gas chimneys, gas hydrate layers, pockmarks, mud volcanoes and live "tar oil" and gas seepages at the sediment surface. If leakage from an already accumulated reservoir occurs, it shows higher magnitudes than secondary migration (Gluyas and Swarbrick, 2004).

1.4 Basic fluid migration physics

In general terms buoyancy of liquid has to exceed capillary pressure for migration to occur in water saturated rock (Fig.1.4.1). It is important to note that the following description uses only single phase because migration will be much more complex with several phases, which is beyond the scope of the thesis.

Buoyancy (Pz) = z*g(ρw – ρo) Equation 1

z = Height of oil column (cm)

g = Gravitational factor (cm/s^2)

ρw= Weight of water (g/cm^3)

ρo = Weight of oil (g/cm^3)

The height of the oil string is important since there is more resistance to flow in small oil or gas columns, which is due to higher surface energies per unit volume (Tissot and Welte, 1984).

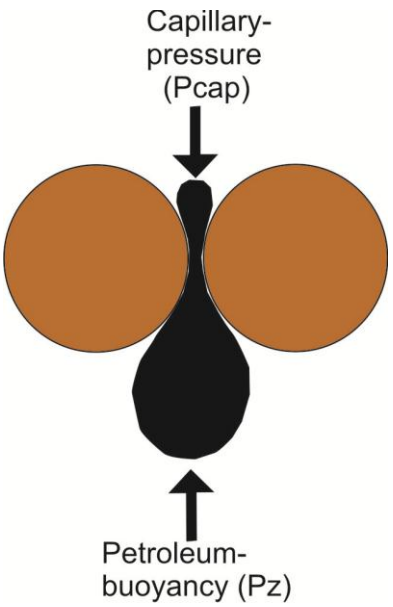

Figure 1.4.1 Relation between buoyancy and capillary pressure.

Capillary pressure *(Pcap) = 2γ (1/rs – 1/rp)* Equation 2

γ = Friction forces between oil and water (10^{-5} N/cm)

rs = Radius of porethroat in sealing barrier (cm)

rp = Radius of porespace in reservoir rock (cm)

Equilibrium of capillary forces and buoyancy (Fig.1.4.1):

2γ (1/rs – 1/rp) = (Pz) = z*g(ρw – ρo) Equation 3

According to Equation 1, buoyancy is determined on weight differences of fluid. This means that gas will have higher buoyancy than oil and could migrate through tighter pore throats than oil.

Hydrodynamics surfaces are also an important factor which inflicts on the regional migration pattern (Weibull, 2010). If the hydrodynamic gradient is upwards it would aid the buoyancy forces and

increase it. While if the gradient is downwards it would decrease the buoyancy force and oil could be hold in place.

Different flow regimes:

It is common to separate between focused (confined) and defocused (unconfined) flow where fracture- and darcy flow represent focused flow and diffusion- and matrix flow represents defocused flow (Sylta, 2004).

Darcy flow:

Darcy flow is the most described and known type of flow (Hubbert and Willis, 1957) and is as follows:

$$\mathbf{Q} = -\frac{K}{\mu}\,\rho\, A\,\frac{\delta\phi}{\delta l}\,, \qquad \text{Equation 4}$$

Where: Q = fluid flow (cm^3/s), K = permeability, μ = viscosity, ρ = density of fluid, A= cross section of where migration occurs, $\frac{\delta\phi}{\delta l}$ = hydrodynamic gradient along the flow path according to porosity.

The equation in a simpler version (Nordling and Österman, 2006) refers to:

$$\mathbf{Q} = \frac{KA\Delta P}{\mu L}, \qquad \text{Equation 5}$$

ΔP is the pressure difference over the migrated Length (L).

The effects from capillary restrictions and wettability, plus the overall height of the hydrocarbon column and carrier architecture (porosity and permeability variation) will also influence both direction and overall mass transfer during secondary migration. (J.E.Skeie, 2006) states that it is practical impossible to study migration with a mathematic approach.

Darcy flow rates (Løseth et al., 2009) vary from 100 – 1000 m^3/km^2/year.

Fracture flow causes additional complications. Darcy flow assumes a homogenous formation while with fracture flow we have to calculate fluid flow with even more empirical assumptions. Fracture flow rates may be very variable.

Matrix and diffusion flow are defocused leakage mechanisms. Usually occurs above a hydrocarbon-filled trap, laboratory measurements results that these leakage processes have very low flow rates varying between 0.16-89 m^3/km^2/year

1.5 Fluid identification in reflection seismic data

My main data set in this master thesis will be a processed 3D seismic cube. There are different seismic techniques as for example refraction seismic, borehole seismic (VSP) and reflection seismic. This thesis will only concern and discuss reflection seismic data.

1.5.1 Basic theory of reflection seismic

Seismic waves are travelling through fluids (P-wave), solids (P- and S wave) and porous solids. By knowing the mechanical and acoustic properties of rocks we can create a reflection seismic image of the subsurface.

The seismic source, for an example an air gun, produces a pressure wave which can be detected and recorded by hydrophones. When a wave field explained by a seismic ray travels through a sedimentary formation it is bent, reflected, refracted, diffracted, scattered and attenuated which will decrease the signal amplitude. Geometric spreading due to an expanding wavefront will cause the amplitude to decrease proportionally with the radius of the propagating wave front sphere eg. (Andreassen, 2009). The resolution between layers and the penetration into the sub-surface when performing a seismic survey is related to frequency. The higher the frequency the higher the resolution but lower the penetration and vice versa (Andreassen, 2009). Seismic resolution is reviewed in detail in chapter 1.5.2.

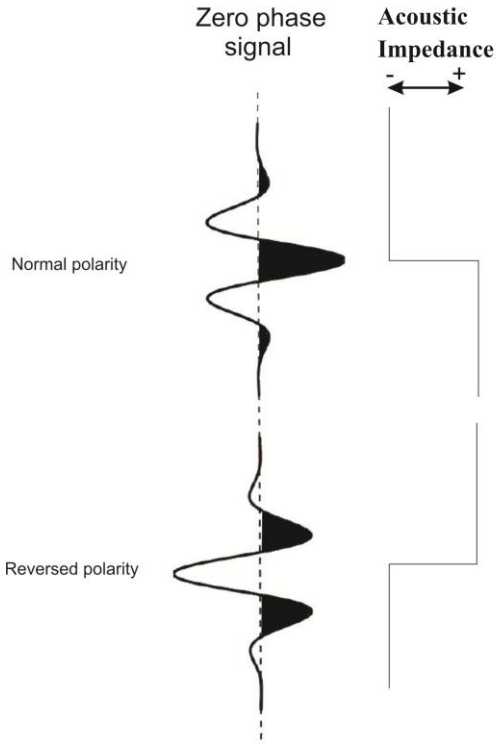

Figure 1.5.1 Schematic view of polarity convention (Sheriff and Robert, 1995)

Important basic terms in reflection seismic:

Acoustic impedance (Z) = density x velocity Equation 6

Reflection coefficient (R) = $(Z_2-Z_1) / (Z_2+Z_1)$ Equation 7

Where the density is defined and calculated by formula:

$$\rho = (\rho f)\phi + \rho m(1-\phi)$$ Equation 8

When the seismic wave propagates downwards through sediments it will only be reflected when it encounter a substance with higher or lower acoustic impedance (Eq.6). Such impedance contrast is the response of lithological differences, faults, fluid densities and artefacts and the reflection coefficient (Eq.7). The reflection coefficient (R) can be positive or negative dependent on the velocity and density (Fig.1.5.1). The energy reflected back and the energy transmitted into next substance is determined by Snell's law (Fig.1.5.2):

$Sin_{\psi}inc /V1 = sin_{\psi}trans/V2 = sin_{\psi}ref/V1$ Equation 9

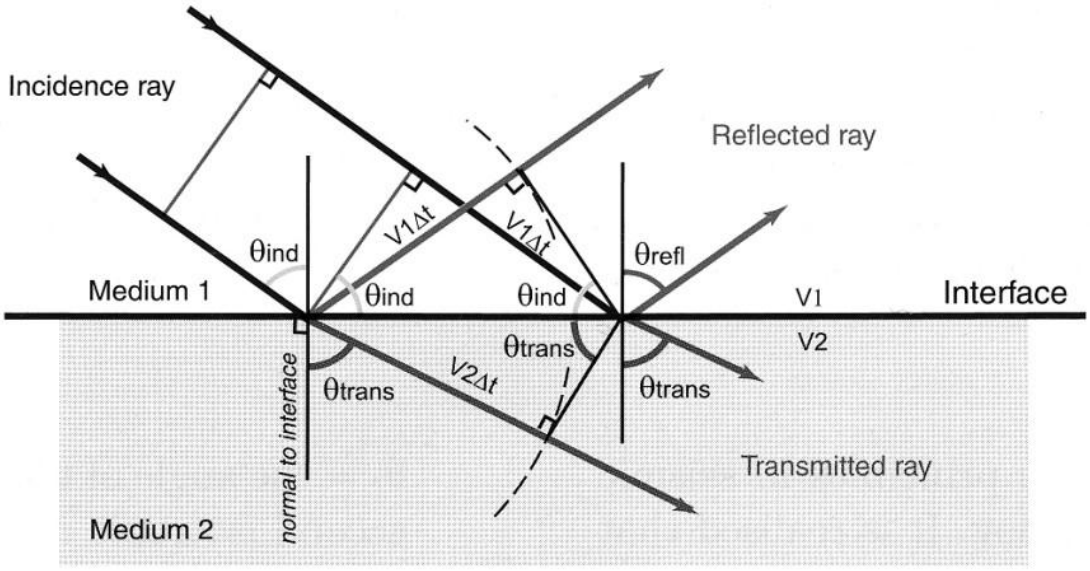

Figure 1.5.2 Acoustic sound waves are affected by velocity and density of medium (acoustic impedance which results in the reflection coefficient). P and S-wave generation is ignored for this figure. Figure generated from (Andreassen, 2009).

Compressional (P) wave and shear (S) wave propagates differently in the subsurface and have different velocity which can be calculated based on the empirical formulas from Gassman (Gassman, 1951):

$$V_p = \left(\frac{\rho}{0.32}\right)^4$$ Equation 10

$$\frac{V_p}{V_s} = 1.8$$ Equation 11

1.5.2 Seismic Resolution

Resolution is defined as the ability to separate to separate features that are close together or in other words the minimum separation of two boundaries before their individual identities are lost in a cross-section (Sheriff, 2006).

It is of major importance to understand the principles and effects of seismic resolution when working with seismic. You need to understand the relation with being in time domain and what limits your resolution based on a combination between velocity and frequency. It is also important to determine structures and understand your limitations to what is visible.

Generally we can say that resolution decreases with depth, which is due to the wavelength increase with depth (Fig.1.5.3). There are several reasons for the wavelength decreases while penetrating down into the subsurface. Reasons for the decrease in amplitude, energy and frequency are:

Spherical divergence which is an effect of seismic energy is spread over an expanding wavefront while travelling in the subsurface. Energy decreases proportionally with the increasing radius of the travelling wavefront sphere (Andreassen, 2009).

Absorption of energy into heat related to neo-elastic behavior. Absorption difference with substance and there is a relative increase of absorption with increasing frequency.

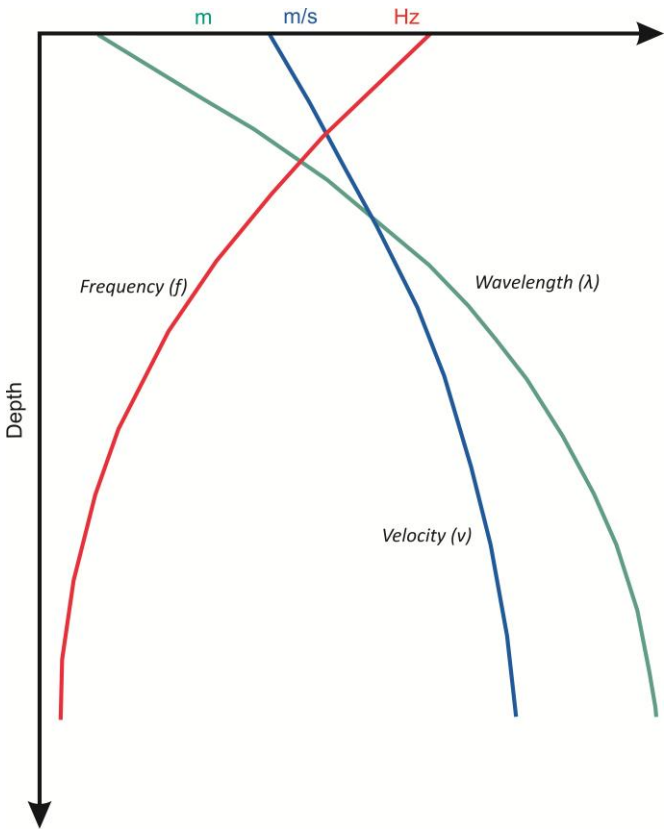

Figure 1.5.3 Sketch of the general relation between frequency, velocity and wavelength. Velocity and wavelength increases with depth and frequency decreases. Figure is modified from (Brown, 1999).

Amplitude decrease caused by reflection-, refractions conversions and scattering of energy (diffractions[3]).

[3] Change in the directions and intensities of a group of waves after passing by an obstacle or through an aperture whose size is approximately the same as the wavelength of the waves (www.answers.com).

These three factors will cause the wavelength to increase while going deeper into the subsurface. Also the velocities of rocks are in general naturally increasing with depth due to the compaction and increase density.

Vertical resolution:

Defined as the minimum vertical distance two objects can have and still be visible on a seismic profile. i.e top and base of the objects have to be distinguished. Vertical resolution is determined by ¼ of a wavelength (Fig.1.5.4) (Badley, 1985; Brown, 1999).

$$\lambda = \frac{v}{f} \qquad \text{Equation 12}$$

This means that it is possible to distinguish the top and base layers that are thicker than ¼ of the wavelength.

Tuning thickness is another term defined as the limit of visibility, and is determined as the lowest possible thickness of a layer to have an effect of the seismic signal. Tuning thickness is generally defined as 1/30 λ (Badley, 1985). Still tuning thickness or limit of visibility is for most cases not 1/30 λ because of background noise, so it should be determined of s/n ratio of dataset (Bulat, 2005).

Horizontal resolution:

Horizontal resolution is defined as the minimum lateral distance two objects where they still are distinguished. Consider the seismic signal as a spherical expanding wavefront which is called the Fresnel zone at given depth/time (Figure 1.5.4) From vertical resolution we determined the vertical limit of separation to be ¼ λ meaning all data reflected from the flat reflector within next wave will be indistinguishable from one another (Yilmaz, 2001). The fresnel zone (Eq.13) is a function of depth, velocity and dominant frequency.

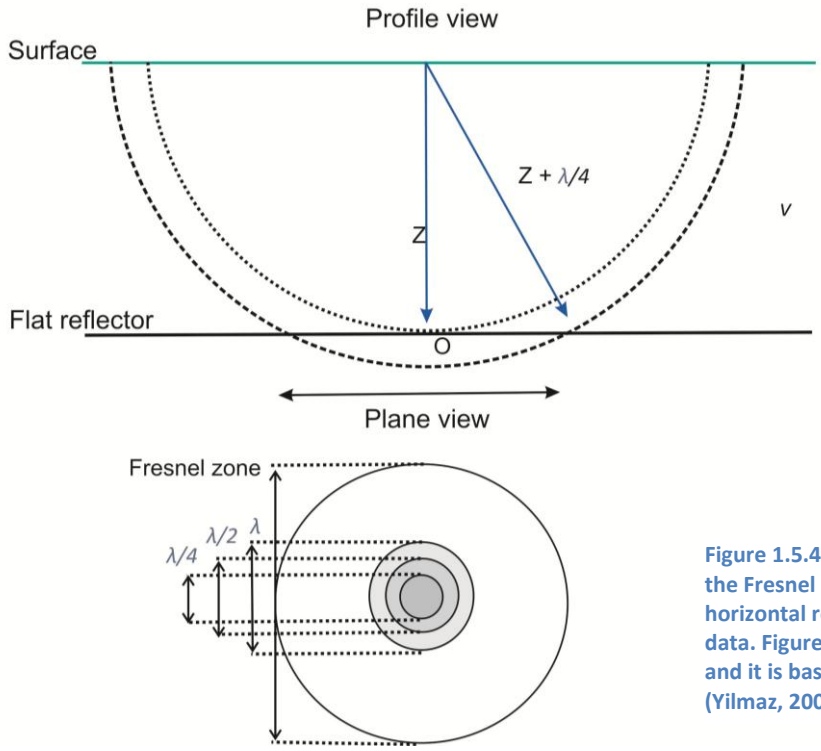

Equation 13

$$rf = \frac{v}{2} \times \sqrt{\frac{t}{f}}$$

rf = Fresnel zone

v = velocity

t = TWT of Z (time to reflector)

f = dominant frequency

Figure 1.5.4 Demonstrating the principle of the Fresnel zone which determines the horizontal resolution of unmigrated seismic data. Figure is modified from (Bulat, 2005) and it is based on the principles from (Yilmaz, 2001).

Different migration techniques[4] are used to increase the horizontal resolution. This is done by reducing the Fresnel zone. The workflow counts for both 2D and 3D seismic data, while the effect is greatest on 3D data because of crossing lines. Horizontal resolution can be as good as ¼ λ in all directions on 3D seismic data (Brown, 1999; Bulat, 2005).

[4] Processing technique where reflections are out of order, focusing energy and distribute diffraction patterns is parts of the process (Brown, 1999).

1.6 Fluid identification

There are several methods to determine fluid flow pathways and fluid accumulation areas. This thesis uses seismic methods to categorize and map different types of fluid flow features.

Fluid flow features are commonly separated into two categories (Løseth et al., 2009);

1. Fluid flow processes that have permanently changed sediment and caused permanent deformations and / or created a new permanent “syn leakage” feature.
2. Changes in pore fluid densities that do not deform the sediment bedding but show changes in the seismic response.

1.6.1 Permanent deformation

Fluid migration can cause different post-depositional changes of the primary layering; mud mobilization and sand injection, permanent alteration of rocks and faults.

These features form because of moveable fluids due to pressure gradient increases. Fluids could also contain nutrient fluid which will contribute to formation of different abnormal biogenic organisms. These biogenic organisms can create or build up local algal mats, shell banks and carbonate (Løseth et al., 2009).

Pockmarks are sediment surface expressions of fluid expulsions and can occur in different hydrocarbon prone sedimentary basins around the world (Hovland and Judd, 1988a). Pockmarks are shallow seabed depressions from a few meters to tens of meters deep. Laterally the pockmarks diameter varies from less than 5 meter to several hundreds of meters. They generally form in soft, fine-grained sediments by the escape of fluid from subsurface. The process is not completely understood, but it is believed to be related to low permeability and to be eruptive cycles (Hovland et al., 2002). Pockmarks are also often characterized by a vertical zone of degraded seismic signal beneath and is often connected with a shallow accumulation of gas (Løseth et al., 2009).

1.6.2 Reflections associated with changes in pore fluid density

Not all reflections are related to lithological changes. If hydrocarbon substitutes water in a porous rock, it will cause a change in p-wave velocity due to change in pore fluid density.

When hydrocarbon substituting water of a highly permeable rock the acoustic wave will be reduced, the effect can be calculated by the Gassman equation (Gassman, 1951) which is simplified in equation 10.

The Gassman equation is based several empirical approximations. Based on sandstones the bulk modulus and shear modulus are used and one can calculate expected synthetic velocities of both shear (Vs)- and compressional (Vp) wave velocity (Eq.10-11).

Gas will show the most distinct decrease in seismic velocities (Andreassen, 2009).

Common indicators of gas are (Andreassen, 2009):

1. Amplitude anomalies (Fig. 1.6.2, 1.6.3)
    i. Bright Spot
    ii. Dim Spot
2. Flat spot (Fig 1.6.2, 1.6.3)
3. Polarity Reversal (Fig. 1.6.3)
4. Velocity effects (Fig.1.6.1)
5. Loss of high frequencies
6. Diffractions
7. Masking and piping

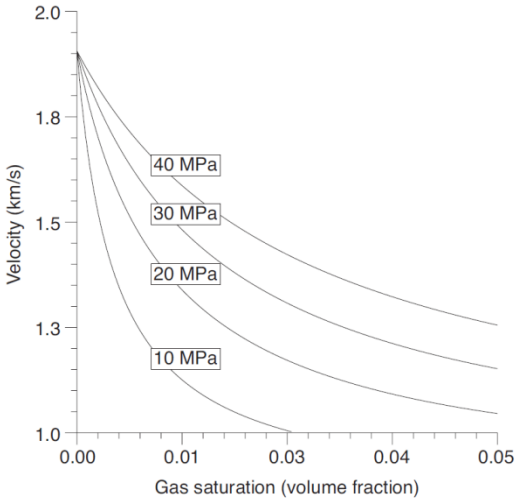

Figure 1.6.2 Compressional seismic velocity as a function of gas saturation and pore pressure where temperature is constant at 48°C. Figure from (Arntsen et al., 2007).

1. Amplitude anomalies show a difference in amplitude along a continuous reflector. An amplitude anomaly can be strong and positive-, strong and negative- or weak (figure 1.6.2 and 1.6.3). When describing a reflector as positive or negative it will always be relative to the seafloor reflector.

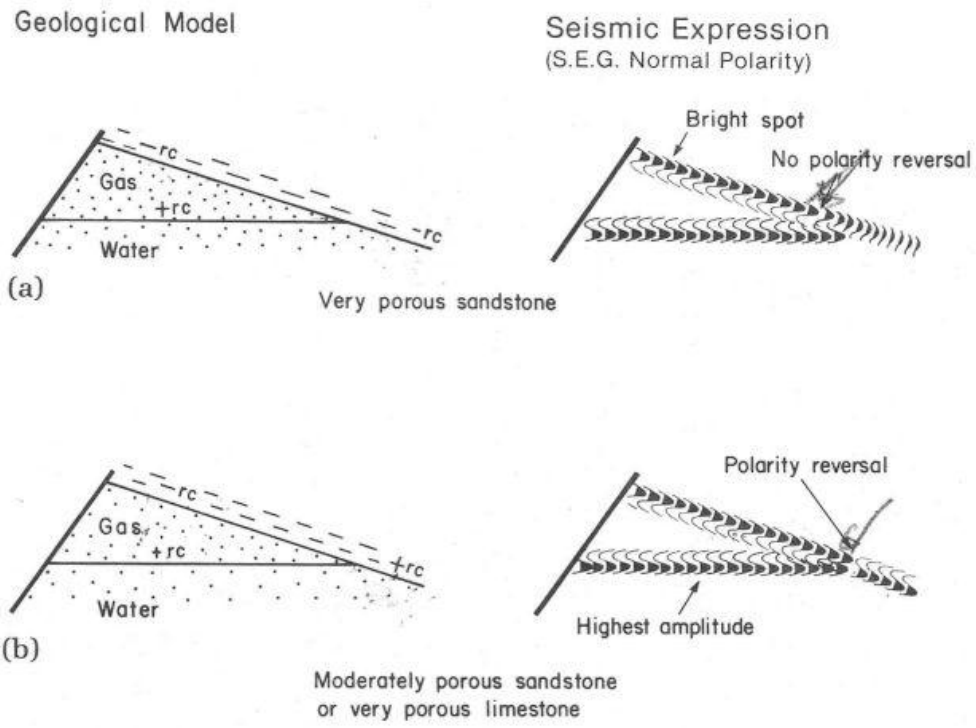

Figure 1.6.2 a,b) Illustrating the basic theory behind flat spot, bright spot and dim spot. Notice the polarity convention. Figure from (Andreassen, 2009).

2. Flat spot (Fig 1.6.2 and 1.6.3) can be observed in both the gas and oil contact. The difference in pore fluid density is the basic theory behind the occurrence of a flat spot. A flat spot will often break the original sedimentary structure and it will always be positive reflection. Different velocity effects can cause the reflection to not appear horizontal. Flat spots are usually not found below 2.5 km due to pressure decrease the impedance contrast

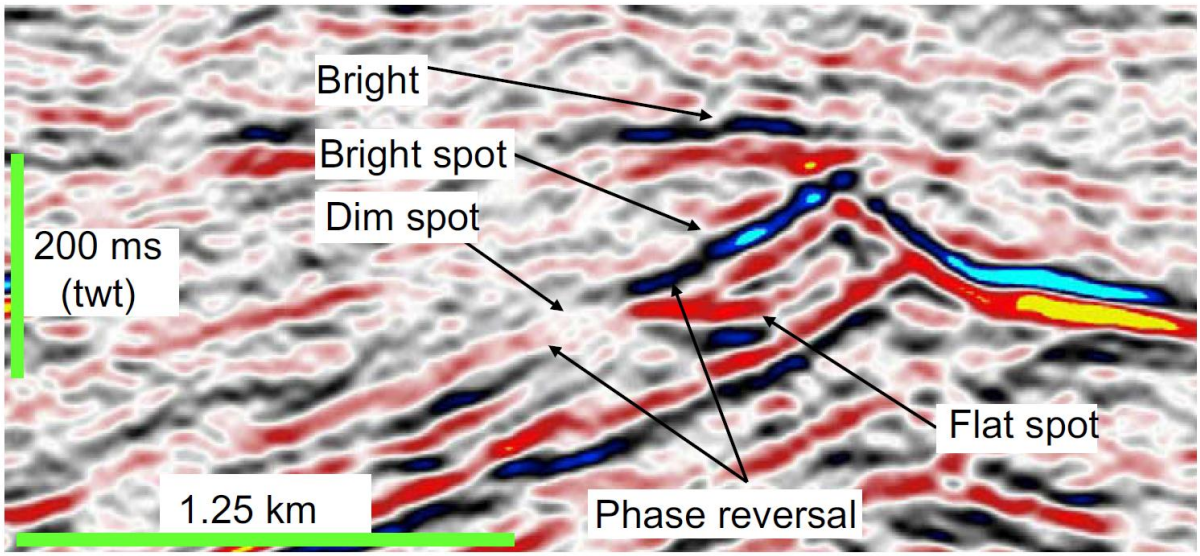

Figure 1.6.3 Classical example of bright, dim and flat spots. Phase reversal is also indicated. Figure from (Løseth et al., 2009).

(Andreassen, 2009).

3. Polarity (phase) reversal is due to changes in the reflection coefficient. This occurs when the polarity convention is changing 180° along a continuous reflector. Figure 1.6.2 b) illustrates this effect. Figure 1.6.3 shows a seismic example.

4. When a gas / fluid zone is thick enough it may create a push-down effect on underlying horizons. The effect can be removed by applying depth conversion on data.

5. Loss of high frequencies can be observed beneath bright spots. Reasons for the loss of high frequencies are the natural increase of absorption of seismic energy with depth as well as absorption within gas / fluid bearing layers.

6. Diffractions can be seen on flanks of gas/fluid pockets, which is due to the difference in impedance contrast.

7. Acoustic masking can occur along fault zones and pipes.

1.6.3 Seal by system (SBS)

Cartwright et al., 2007 defined SBS as “where fluids are allowed to migrate across sealing sequences in pathways vertically or subvertically”. It is relevant for this thesis and sequences as “SBS” are defined where possible cross-strata fluid migration features occur within a sealing sequence. One reason for classifying SBS is to make it easier to explain what process is leading fluid to migrate through impermeable layers. All seals may be permeable if one considers a long time period (Cartwright et al., 2007), meaning that within one period of time the seal can be breached and migration can occur.

SBS is classified in three main groups mainly based on seismic interpretation criteria’s (Cartwright et al., 2007):

Intrusion related SBS are intrusive structures breaching the integrity of a sealing sequence and create a higher permeable sequence which will work as the SBS.

i. Sandstone Intrusions, in which the flow is not restricted to the period of the intrusion event (could be only a few days). After the formation of intrusion it could stay as a high permeable conduit for millions of years allowing fluid flow through SBS until the vertical continuity is broken by deformation or the pore space is cemented. Typical flow rate is 1-2 cm/year (Cartwright et al., 2007).

ii. Igneous Intrusions where permeability is much lower than in sandstone intrusions. Intrusion of hot magma greater than 1000°C Into cold and wet sediments results in a major change in host rock properties for tens of meters around the intrusion (Gerhardt Einsele, 1980). Hydrothermal flow is highly mineralizing and the fractures would be cemented rapidly, destroying the permeable pathway created.

iii. Mud Diapirs and Diatremes are a very Important and widespread subgroup of SBS. Main flux of fluid is linked to the mud events itself and is highly episodic.

iv. Salt diapirs often occur in hydrocarbon provinces and involve forced folding and concentric faulting.

Fault related, when a fault is the origin for allowing fluid migration:

i. Trap, where a fault defines and delimits trap within a lateral sealing succession (figure 1.6.4).

ii. Supratrap, where a fault is embedded within the sealing sequence. It causes a constrained flow through the sealing, but does not necessarily imply an empty reservoir. A polygonal fault[5] system is classified as a supratrap.

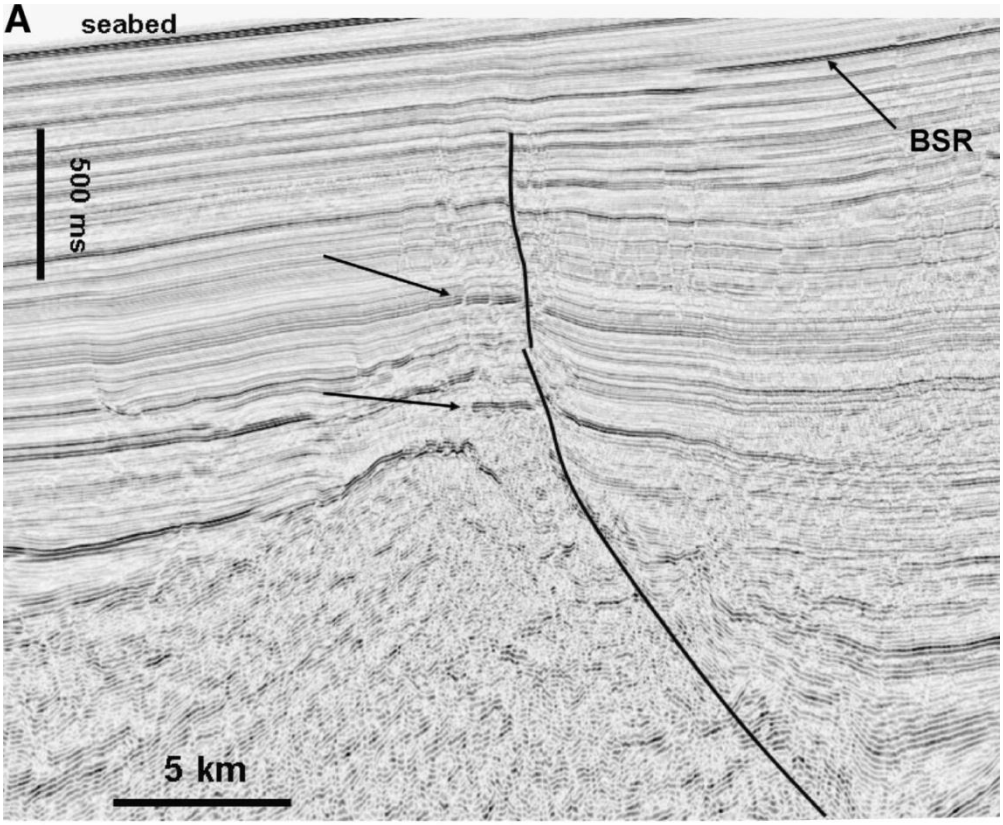

Figure 1.6.4 Seismic section of a large tilted fault block where arrow indicates different vertically distributed amplitude anomalies. Defined as hydrocarbon leakage zone and trap to be a major trap-defining fault. There is also indicated a bottom simulation reflector (BSR) which is relevant to hydrocarbon leakage. Figure modified from (Cartwright et al., 2007)

Pipe related features are defined on reflection seismics as columnar zones of disturbed reflections that could be associated with sub vertically stacked amplitude anomalies. Often related to surface features, such as pockmarks (Cartwright et al., 2007).

i. Dissolution of rocks at depth causes the overburden to collapse and is likely to occur in areas where evaporites and karst[6] exist.

[5] Polygonal faults occur in fine grain sediments, relative small scale faults with its origin related to overpressure (Cartwright et. al 2003).

ii. Hydrothermal, fluid related to igneous intrusions are characterized as columnar or steep-sided, downward-tapering conical zones of distributed or collapsed stratigraphic reflections. They may be formed in direct connection with an igneous sill layer.

iii. Blowout, is easiest to classify beacuse of their association with surface or paleopockmarks (Løseth et al., 2001). They have their origin often at natural leakoff points for overpressured pore fluids, typically an overpressured gas reservoir. It is suggested that blowout pipes are the first stage in the evolution of a mudvolcanoes (Cartwright et al., 2007).

iv. Seepage may form under the same conditions as blowout pipes, but lack blowout craters (pockmarks) and high flow rates.

[6] Karst is dissolved carbonates forming at both surface and subsurface resulting in an empty space (Wikipedia, 2011, www.wikipedia.org.

1.7 Gas Hydrates

Figure 1.7.1 Gas hydrate recovered from an embedded hydrate structure of a sediment ridge offshore Oregon, USA. Gas Hydrates are not stable under atmospheric pressure and will release gas and water if not kept under high pressure and low temperature (picture from: http://feww.wordpress.com/category/east-siberian-arctic-shelf/).

1.7.1 Gas hydrates Basics

Gas hydrates occurs in large parts of the world's continental margins and high latitude permafrost regions onshore and offshore (Henriet and Mienert, 1998). The existence of gas hydrates is most common in deep marine basins, where the temperature- and pressure conditions are favorable for the formation of hydrates. Gas hydrates are also abundant in permafrost regions (Maslin, 2010). Naturally occurrence of gas hydrates was first discovered in high pressure gas pipelines (Shipley et al., 1979).

Gas hydrates are ice-like crystalline solids (figure 1.7.1) which are formed when water molecules freezes and gas is trapped within the structure. The trapped gas consist of mainly methane, but other molecules such as ethane, propane, CO_2, H_2S or H_2 may substitute it (Sloan, 1998a). Typical condition for the creation of gas hydrates are when temperatures are less than 300K and pressure

are higher than 0.6 MPa (Chand and Minshull, 2003) (figure 1.7.2). Controlling factors for the possible existence of gas hydrates are: temperature, pressure, amount of gas and water present.

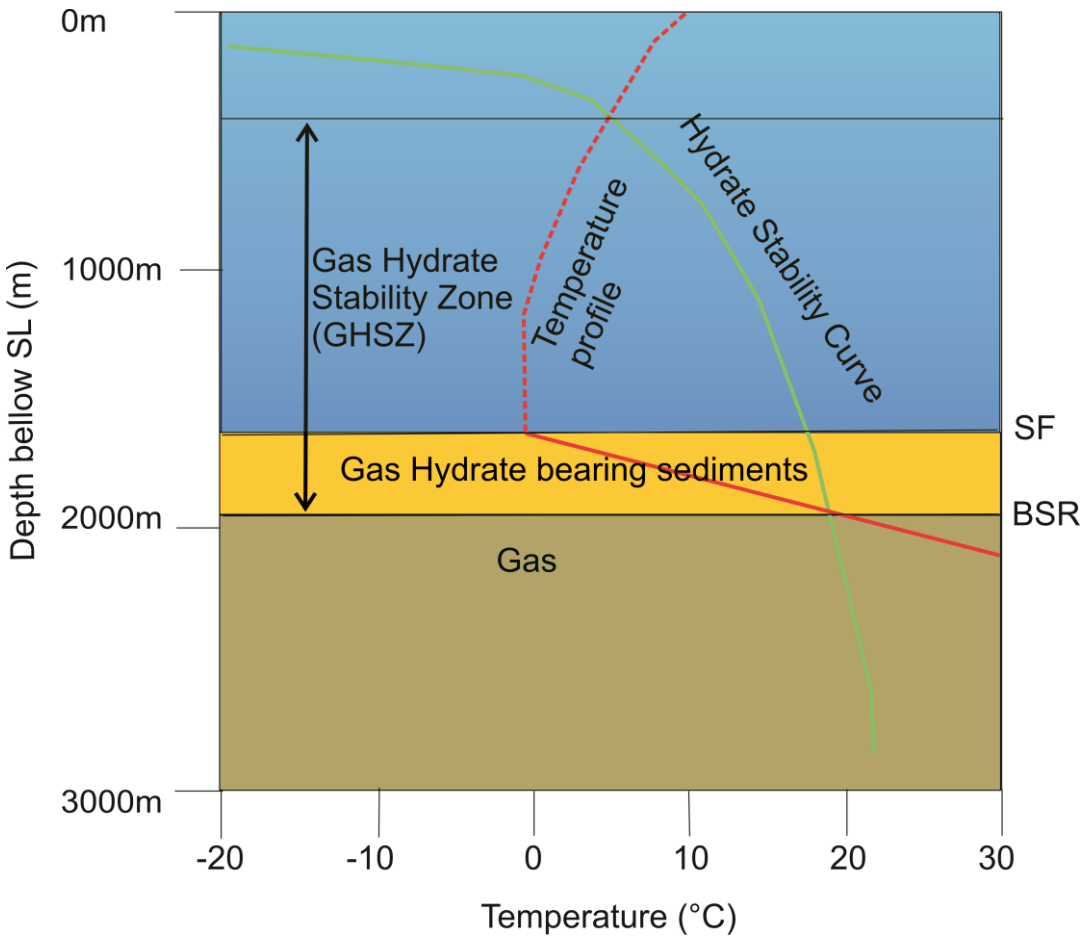

Figure 1.7.12 Basic phasediagram indicating the transition state from gas hydrates to free gas. Gas hydrates released to the water column will due to positive buoyancy rise and dissociate before reaching sea level. Gas hydrates created below seafloor will be trapped and can make up a constant layer. Temperature is mainly affected by the geothermal gradient below seafloor. Figure is modified from (Chand and Minshull, 2003) and is based on polar conditions.

1.7.2 Gas Hydrate Stability Zone (GHSZ)

Gas hydrates remain stable under certain pressure and temperature conditions (Figure 1.7.2). If they change and exceed the GHSZ gas hydrate will dissolve. This reaction will cause a change in phase from solid to gas and liquid (Sylta, 2004). The zone where gas hydrates are stable is called the gas hydrate stability zone (GHSZ) (figure 1.7.2). GHSZ is referred as a geological section where gas hydrates may exist under in-situ conditions (Ginsburg and Soloviev, 1997). The GHSZ is limited in particular by the geothermal gradient, pressure, gas composition, pore water salinity, bottom water temperature and the physical properties of the host sediment (Bünz et al., 2003). The thickness of the GHSZ varies according to these parameters. The thickness will increase with increasing water depth due to increasing pressure. Higher order gases such as ethane, butane and propane will

increase the GHSZ thickness as well (Sloan, 1998c). A higher geothermal gradient will cause a decrease of the GHSZ thickness.

1.7.3 Gas hydrate structure

Gas hydrates can form three different structures: structure I, II or H (Sloan, 1998b). Lower order gases will create structure I, higher order gases from propane to normal butane will create structure II, and H structure is combining I and II structures.

1.7.3.1 Identification of gas hydrates on seismic sections

Where gas hydrates inhabit the pore space of sediments it will increase the bulk and shear modulus, which in turn will cause an increase in both P- and S-wave velocities (Chand and Minshull, 2003). Vp interval velocities of 1700-2400 m/s are common for hydrate bearing sediments (Andreassen et al., 1990).

The formation of gas hydrates in the pore space of sediments will reduce the porosity and permeability of the host sediments. This makes sediments within the gas hydrate stability zone impermeable and the base of gas hydrate stability zone (BGHZ) may act as a seal for upward moving fluids. As mentioned before, the occurrence of gas in sediments drastically reduce pressure wave velocity. Both the increase in density and velocity within the BHGZ and the low velocity at the BHGZ with the free gas zone creates a distinct change in acoustic impedance and a strong reflection coefficient. The impedance contrast is easily traced on seismic data and is known as a bottom-simulating reflection (BSR) (Bünz and Mienert, 2004). This phenomenon on seismic data was first described and documented in (Shipley et al., 1979).

1.7.3.2 Environmental perspective

Methane is an important greenhouse gas, which is >20 times more potent than CO_2 (Manne and Richels, 2001). It takes about a decade for methane to be oxidized into CO_2 in the atmosphere (Archer et al., 2009).

Gas hydrates are stable under low temperature conditions, which mean that a climate warming can have an effect on the GHSZ in the world's gas hydrated continental margin and permafrost regions. This is one of the reasons why gas hydrates are seen as a critical material in the global climate scenario.

Another environmental impact of gas hydrates may come from the fact that they may influence the stability of continental slopes (Mienert et al., 2005). The dissociation of gas hydrates and the mobilization of gas may cause the development of over-pressurized layers (McIver, 1982). The overpressure and the loss of cementation are the main controlling factors for a slide to occur.

Finally, gas hydrates may provide an enormous energy potential if the technology can be developed to recover the gas form gas hydrates (Ristinen and Kraushaar, 2006).

2 Study Area

2.1 Introduction

The Barents Sea region is located in the Norwegian and Russian Arctic with boundaries to Novaya Zemlya in the east, Franz Josef Land and Svalbard in the north and the continental slope towards the Nordic Seas in the west (Fig.2.1.1). The Barents Sea is at the deepest 500 meters, which characterize it as a shallow continental shelf. The Barents Sea is one of the largest offshore shelf in the world with an area of 1 300 000 km^2 (Dore, 1995) and has an average water depth of only 300 meters.

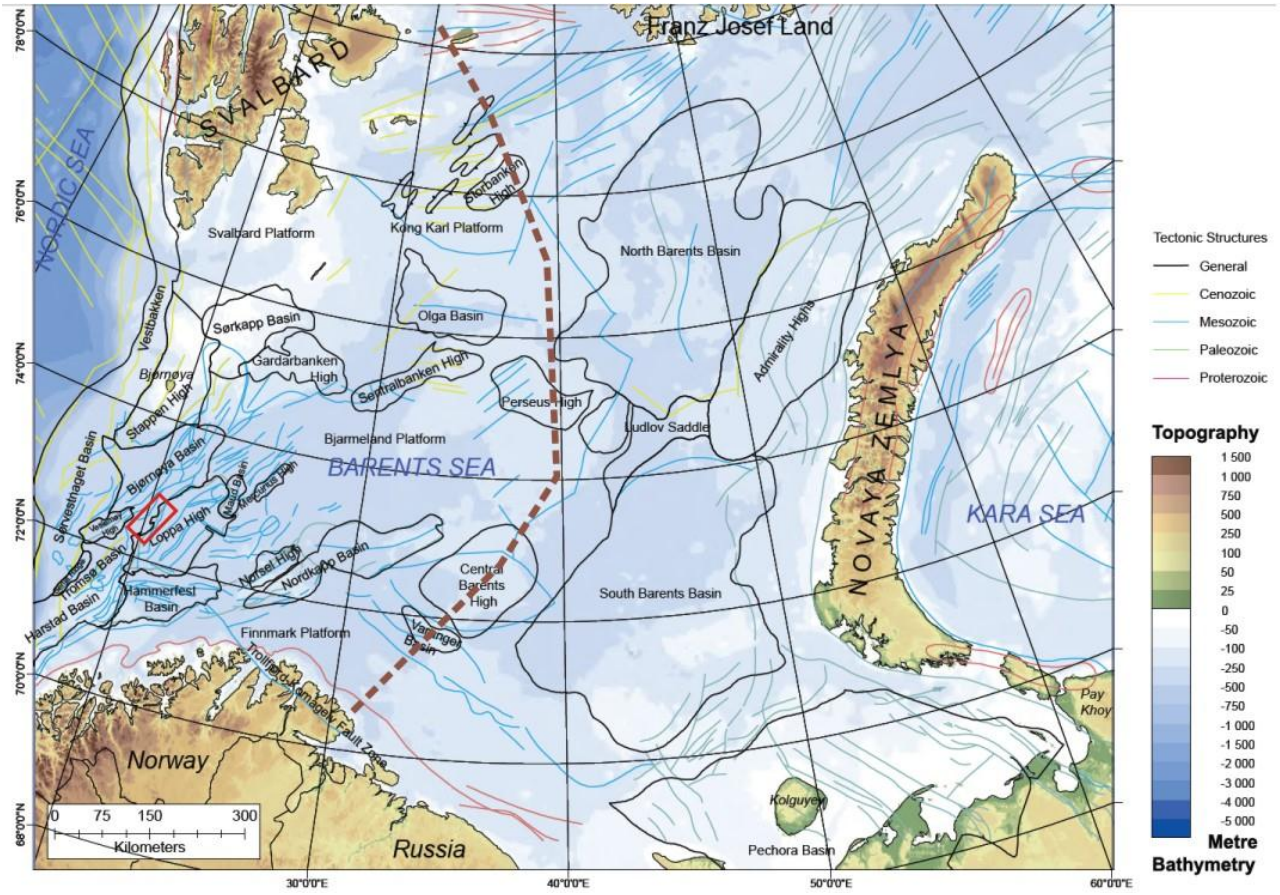

Figure 2.1.1 Structural overview map of the Barents Sea. Regional faults are colour labelled according to stratigraphic time. Dashed-brown line indicates separation of east and west Barents Sea. Red rectangle indicating the study area (WLoppa08, WG) figure modified (Morten Smelror, 2009).

The Barents Sea is an epicontinental shelf build up by complex structural features such as; platform areas, basement highs, graben features and large sag-basins. The Barents Sea has gone through major climatic, depositional and structural changes since Silurian time (440-415 ma) while it has drifted from approximately 50^o S to 70^o N (Torsvik and Cocks, 2005). The base of the Barents Sea geological formations corresponds to deformation of Caledonian

age, which means that sediments laying on top can be as old as 500 Ma (Morten Smelror, 2009).

The largest and deepest sediment basins lies in the eastern part of the Barents Sea and will not be further discussed in this thesis because it is beyond the working region. A structural high crossing from north to south is called Central High (Figure 2.1.1) and separates the west- from the east Barents Sea. This master thesis focuses on the western Barents Sea, the West Loppa (Fig.2.1.1).

The western Barents Sea (Fig.2.1.1 and Fig.2.1.2) is a large Perm-Triassic platform representing several episodes of rifting that cause graben-type basins (Morten Smelror, 2009). At least five phases of basin development can be recognized in the western Barents Sea area before the final crustal break-up and seafloor spreading occurred in Early Eocene. (Ryseth et al., 2003). Sørvestnaget, Bjørnøya, Tromsø and Harstad Basin defines the eastern flank of the last phase of rifting before the successful rifting lead to crustal break-up of Laurentia and Baltica and the formation of oceanic crust (Gudlaugsson et al., 1998).

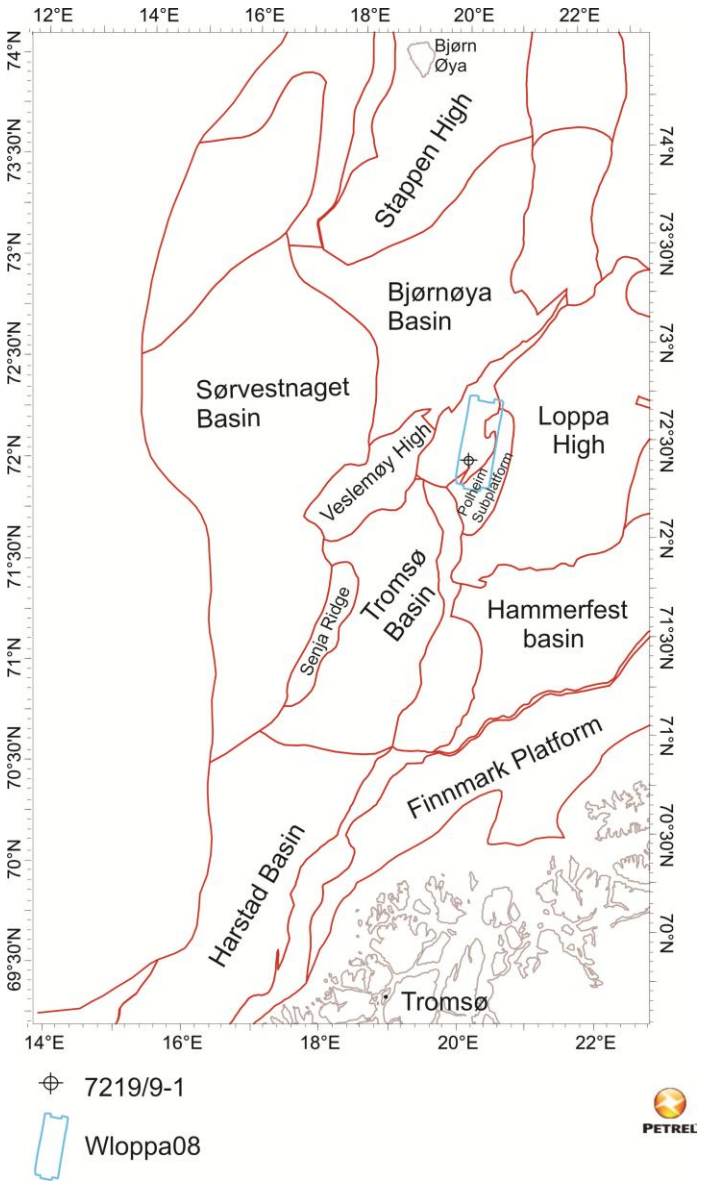

Figure 2.1.2 Structural map of South Western Barents Sea, location of dataset and study area is marked with blue box.

2.2 Tectonic evolution of the south-western Barents Sea.

Important features: Loppa High, Polheim sub-platform, Bjørnøya fault complex and Bjørnøya - Tromsø Basin.

The Caledonian Orogonesis provided the fundamental structure framework for the south-western Barents Sea in Early Devonian. This is directly related to north east Atlantic – Arctic rifting later which will in regional scale determine tectonic development, subsidence and sediment accumulation through whole of Paleozoicum. Through Devonian the tectonic link to the Arctic rifting and collapse of the Innuitian Orogeny grows stronger (Gudlaugsson et al., 1998). From Mid-Carboniferous and Permian was a tectonic quiet period with passive subsidence and sedimentation. In Early Triassic, rifting in a northerly trend was reactivated by the crustal east-west extension between Norway and Greenland (Gudlaugsson et al., 1998).

In the Mesozoic the same north-southwards rifting process was active. The process is mainly controlled by the already existing faults (Faleide et al., 1993). In the Mesozoic the rifting is divided into two main phases; Middle Kimmerian and Late Kimmerian tectonic phase (Faleide et al., 1984). The Middle Kimmerian is characteristic with normal faults and sedimentary basins. While when going into later Kimmerian the faults evolves deeper and reactivates old Caledonian faults.

Before the opening of the Norwegian-Greenland Sea in Cretaceous the western Barents Sea was under tectonic tension, and shearing led to transform faulting. This again led to subsidence in the Western Barents Sea. This caused a massive westward progradation which is equivalent to the Kolmue- and Torsk Fm (Breivik et al., 1998).

In Early Eocene the last stage of rifting occurs, which led to the opening of the North Atlantic rift.

2.3 Geological History of the area of Western Loppa High, Polheim Sub-Platform, Bjørnøyrenna Fault Complex and Bjørnøya- and Tromsø Basin (Smelror et al., 2009)

The depositional history of the western Barents Sea starts in Early Devonian (Lochkovian) which is directly overlaying crystalline basement (Gudlaugsson et al., 1998). Reference well 7220/6-1 on Loppa High (Fig.3.1.1) is not penetrating deeper than Gipsdalen Group which correlates to late Carboniferous. (NPD, 2007).

In Lochkovia (Fig.2.3.1) the area was dominated by the breakdown of the Caledonian orogenesis with an extensive high erosion factor. Sediments are confined deposited in intracratonic – and foreland basins created by the north easterly rifting process Sediments are mainly continental siliciclastic materials.

Late Devon (Fig.2.3.1) (Frasnian): Extensive erosion of the Caledonian Orogen in the western Barents Sea which is supplying the intracratonic basin with siliclastic sediment referred to

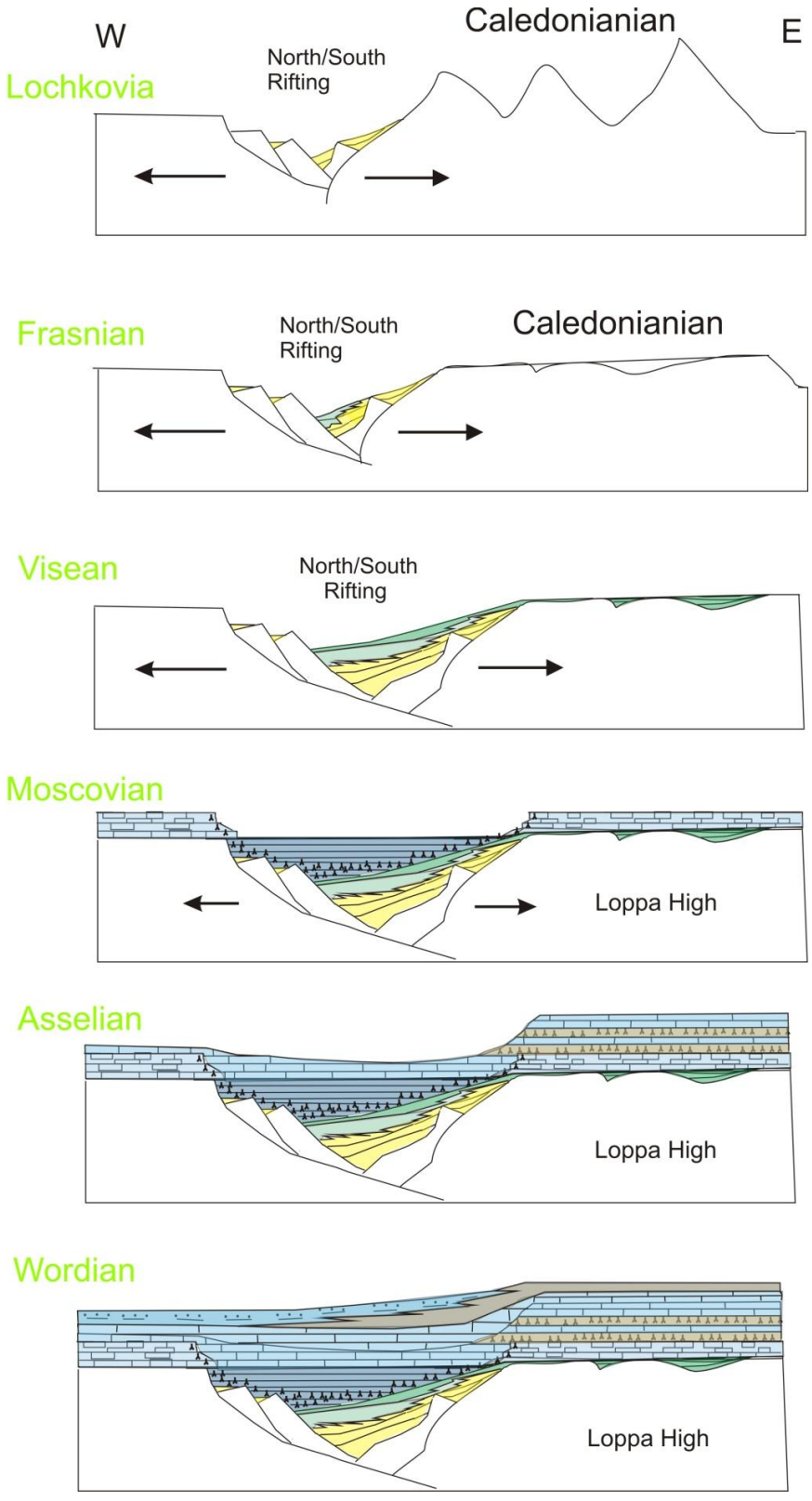

Figure 2.3.1 Geological summary from Lochkovia to Wordian. Specified geological time indicated on figure. See figure 2.3.2 for legend.

as the “old red sandstone”. The development of this structure is continued from the crustal extension. Deposits are preserved in the Basin. Adjacent areas to the rifting are highlands that were eroded.

Middle Carboniferous (Visean) (Fig.2.3.1): After the erosion of Caledonians and a regime governed by mass deposits from continental clastic sediments it changed into fluvial controlled river systems on a massive fluvial plain prograding eastward.

Late Carboniferous (Moscovian) (Fig.2.3.1): Rising sea level from the east caused a flooding of the whole south-western Barents Sea while the continent (Pangaea) is moving northwards from tropical humid to sub-tropically arid environments contributing to evaporate formation and carbonate build ups. The Rift Basin is still subsiding in a north easterly direction contributing to the carbonate build up.

Early Permian (Asselian) (Fig.2.3.1): Continued overall transgression with high frequency and high amplitude of eustatic sea-level changes due to “glacial phases” of the world. Rifting has completely stopped. During sealevel maxima the entire area was flooded and shallow water carbonate build ups were created on Loppa High which is bordering by the paleo rift basin.

Middle Permian (Wordian) (Fig.2.3.1): Continued overall transgression with temperature fall resulting in a gradual change from carbonate to siliciclastic depositional regime. Loppa High is still a positive relief in the area with coastal and shallow water deposits while the area west of Loppa High consist of deeper shelf deposit (Morten Smelror, 2009).

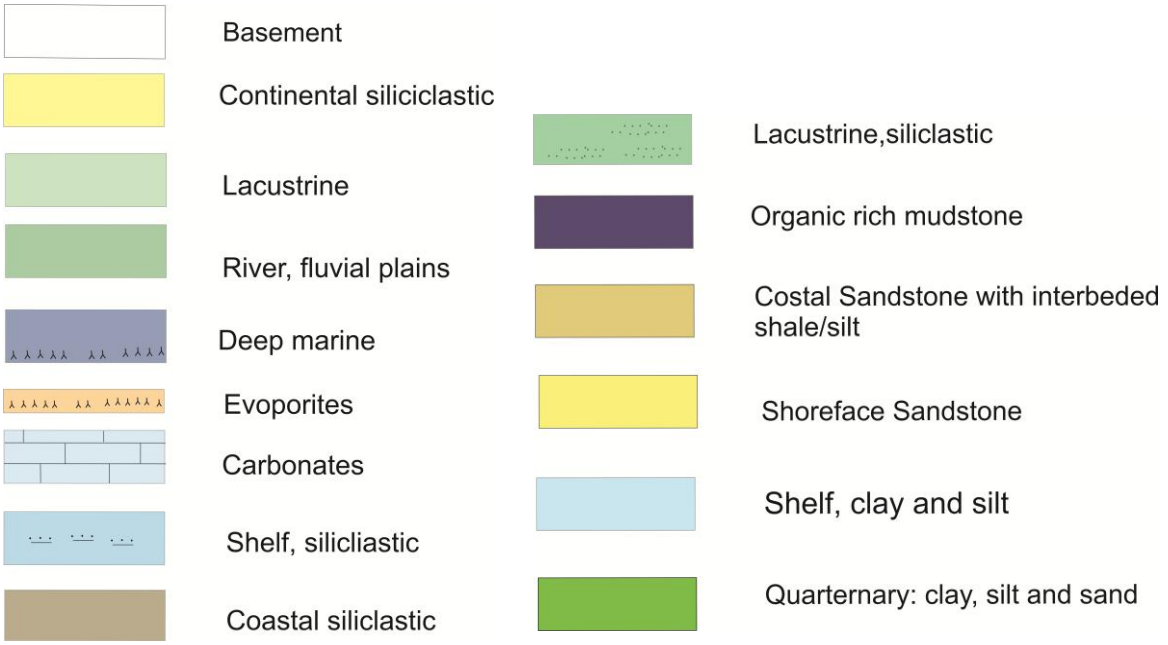

Figure 2.3.2 Legend for figure- 2.3.1- 2.3.3- 2.3.4.

Early Triassic (Induan) (Fig.2.3.3): Loppa High is uplifted and eroded due to rifting in the west of Loppa High, Bjørnøya Fault complex. Siliciclastic shelf sediments continue to be deposited in this area. By the end of the period Loppa High is in a more lacustrine environment with deposition of siliciclastic sediments.

Middle Triassic (Ansian) (Fig.2.3.3): Restricted anoxic environments are present in the deeper rift basin along the western border of Loppa high where coastal sediments are deposited. Organic rich sediments are equivalent with the Kobbe Formation.

Late Triassic (Carnian) (Fig.2.3.3): Period is known for its massive regression due to uplift in the east which lead to the extensive westward costal progradation.

Early Jurassic (Hettangian) (Fig.2.3.3): Loppa High was uplifted and eroded. Along the western boarder of Loppa High occurred the deposition of costal sands prograding northwestwards with interbedded sequences of marine shales indicating flooding periods.

Later Early Jurassic (Toarcian) (Fig.2.3.3): Loppa High continues to be exposed to erosion while transgression is developing a retrogressive costal shoreline west of Loppa High. Fine sand are deposited in stacked shoreface sequences.

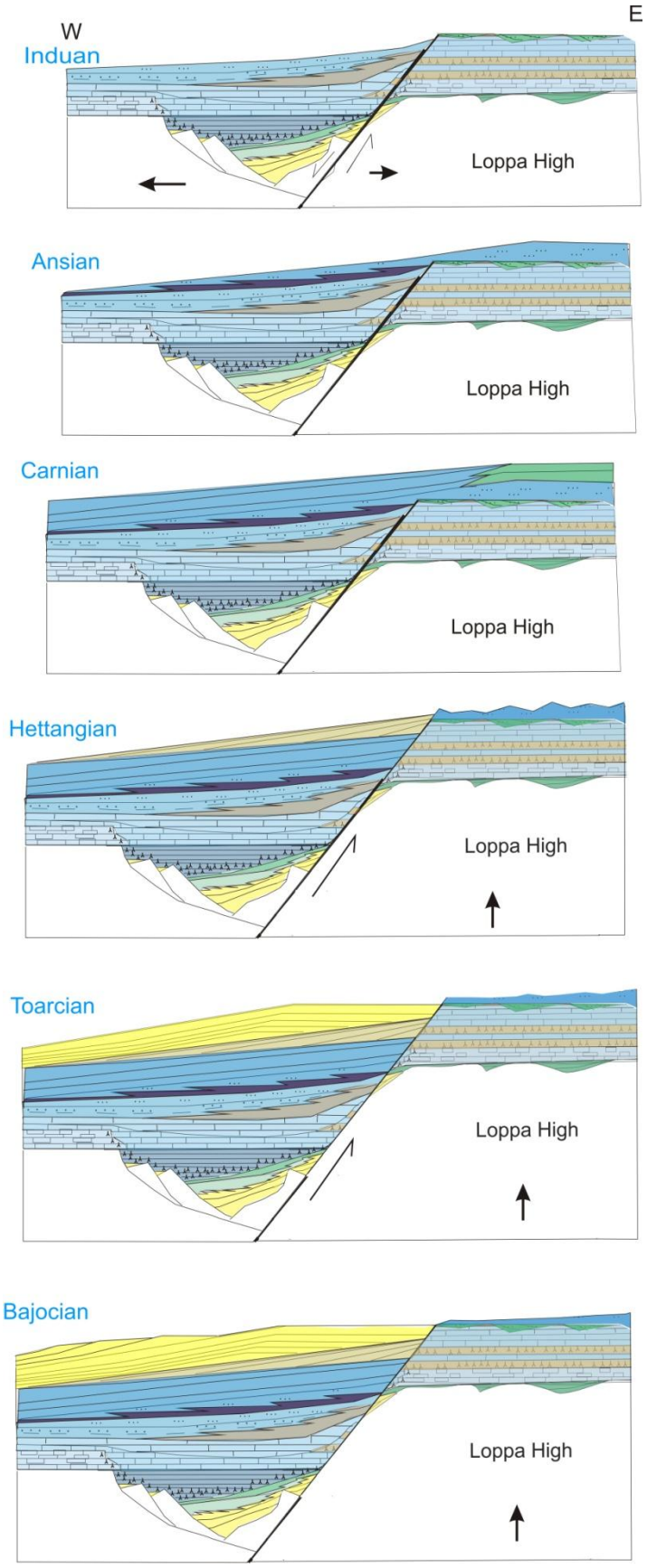

Figure 2.3.3 Geological summary from Induan to Bajocian. Specified geological time indicated on figure. See figure 2.3.2 for legend.

Middle Jurassic (Bajocian) (Fig.2.3.3): Continued overall uplift leading to maximum regression, only the area furthest to the west shows deposition with the same fine quality sands as in Toarcian.

Late Jurassic (Tithonian) (Fig.2.3.4): Maximum transgression led to flooding of the whole area. Gentle local uplift of Loppa High caused an exposure of shallow water shelf deposits on the high while organic material were deposited in anoxic conditions west of Loppa High.

Early Cretaceous (Fig.2.3.4): Uplift of Loppa High continued contributed to the creation of Polheim subplatform. In the late early Cretaceous subsidence in Tromsø Basin started the development of the Bjørnøya fault complex.

Middle Cretaceous (Albian) (Fig.2.3.4): Rapid subsidence in Tromsø – Bjørnøya Basin lead to the formation of the large asymmetrical listric fault blocks one observes in Bjørnøya fault complex. Due to an uplift in the east large amounts of sediments where deposited in syn-rift sedimentary wedges westwards over Bjørnøya fault complex and Bjørnøya - Tromsø Basin. Sediments are

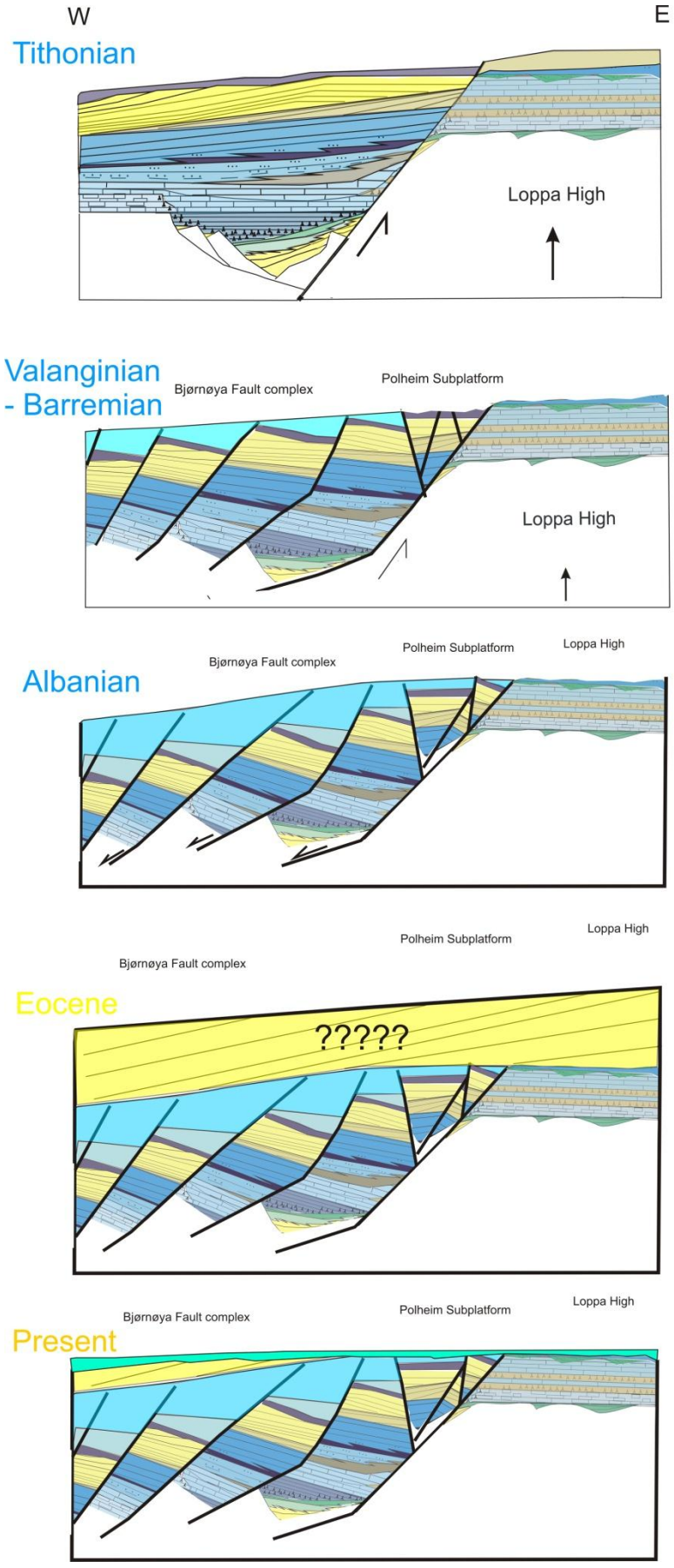

Figure 2.3.4 Geological summary from Tithonian to Present. Specified geological time indicated on figure. See figure 2.3.2 for legend.

dominated by clay and silt with minor sand layers.

Early Tertiary (Eocene) (Fig.2.3.4): Continued sedimentation occurred in the west because of the break-up of the north Atlantic. Deposits were preserved in the Bjørnøya fault complex and Tromsø Basin while on Loppa High sediments are absent due to post Eocene erosion processes.

Late Tertiary (Neogene) and Quaternary (Fig.2.3.4): The whole Barents Sea has been uplifted and several glaciations phases with ice sheet advance and retreats dramatically increased the erosion rates. Approximately 1000 m – 1500 m of sediments has been removed. (Ohm et al., 2008).

2.4 Stratigraphy

The stratigraphy in “Bear Island fault complex” consist of a deep (<5km) sedimentary basin which is prograding towards west (Fig. 2.4.1). The Mesozoic and Cenozoic stratigrapy is described and defined by *Worsley et al.* (1988) (Fig.2.4.2). In the late Cenozoic the area was under the influence of major glacial erosion which formed a significant erosive surface (URU).

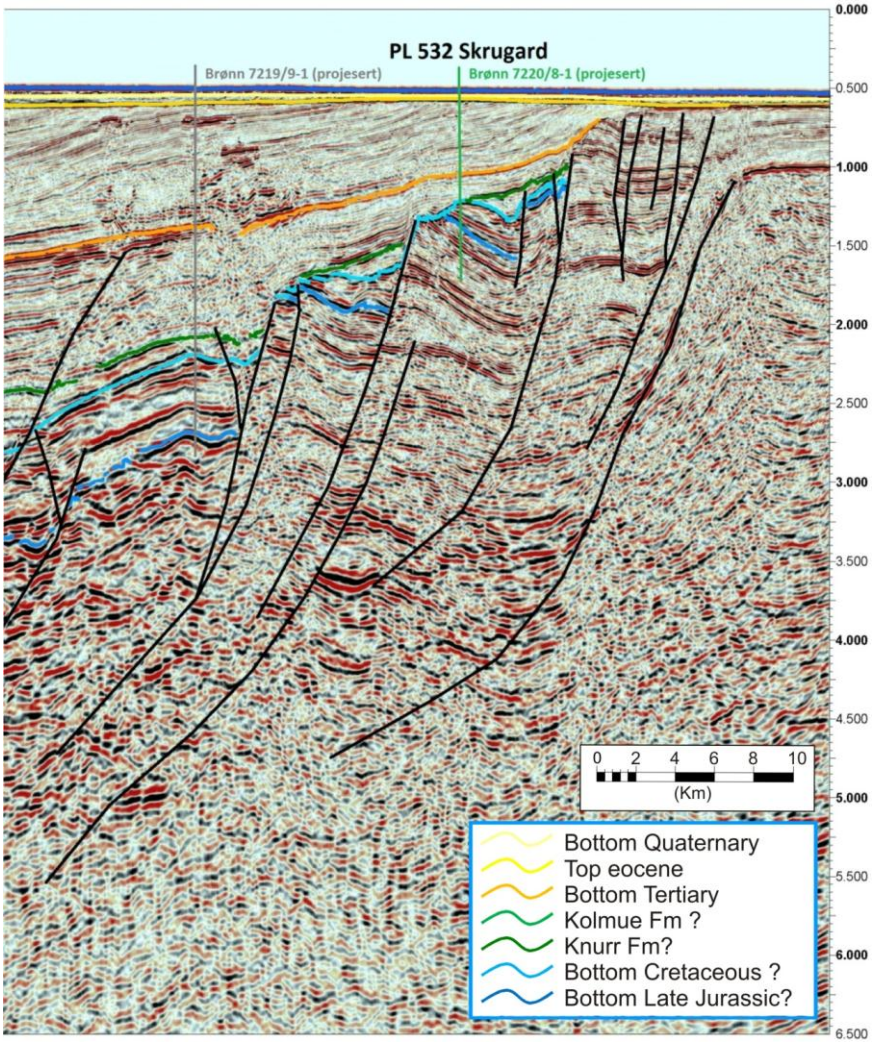

Figure 2.4.1 Suggested stratigraphy from Bent Erlend Kjølhamar in TGS, published in GEO, 3-2011. Formations in area are defined by (Worsley et al., 1988) (Fig. 2.4.2).

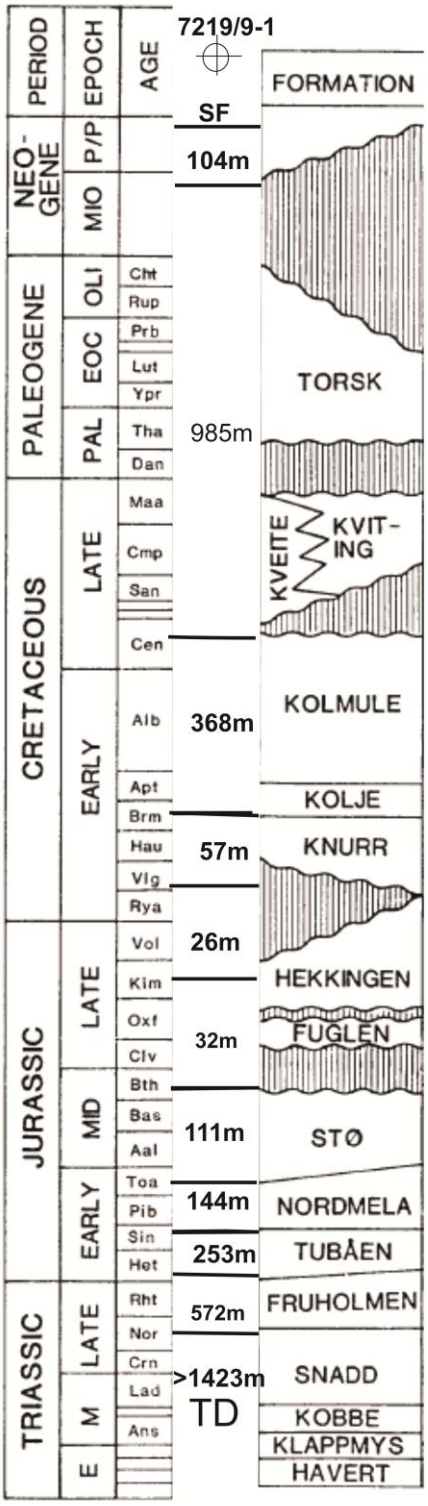

Figure 2.4.2 Stratigraphic units from the southwest Barents Sea defined by (Worsley et al., 1988) with reference well 7219/9-1 vertical extension indicated.

Top Depth m (MD[7])	Lithostratigraphic unit	GR (API)	Sonic (µs/m^{-1})	Density (g/cm^3)	Neutron Porosity (fractions)
379	**NORDLAND GP**	75	125	2.1 - 2.2	0.5-0.4
483	TORSK FM	60 - 80	162-105	2.4 - 2.0	0.5 - 0.35
1468	**ADVENTDALEN GP**				
1468	KOLMULE FM	115-130	100	2.0 - 2.5	0.5 - 0.4
1836	KNURR FM	110	90	2.5	0.3
1893	HEKKINGEN FM	140	100	2.4	0.35
1919	FUGLEN FM	120	90	2.5	0.3
1951	**KAPP TOSCANA GP**				
1951	STØ FM	60	80	2.1	0.2
2062	NORDMELA FM	80	70	2.2	0.25
2206	TUBÅEN FM	40	75	2.05	0.2
2305	FRUHOLMEN FM	120-90	80-70	2.4-2.1	0.35-0.25
2877	SNADD FM	20-100	80-60	2.4-2.1	0.35-0.25

Table 2-1 Detailed geophysical data of the different formations penetrated in reference well 7219/9-1 (NPD, 2007).

The Kapp Toscana GP consists of shales, siltstones and sandstones deposited from late Triassic to Middle Jurassic. Reference well 7219/9-1 do not penetrate deeper than Snadd Fm in Kapp Toscana GP.

Snadd Fm was deposited during the middle Triassic and consists of shale to siltstone - sandstone coarsening upwards sequences. It was deposited in distal marine environments under transgressive periods. The base was not penetrated in the reference well suggesting that the total thickness must exceed 1423 m.

Furuholmen Fm (source rock) - consists of Interbedded sandstones, shales and coals. Sandstone dominates the middle part of the formation. Sediments were deposited in a prograding system from open marine to coastal and fluvial environments during late Triassic. The thickness in the reference well is 572 m.

Tubåen Fm is dominated by sandstone with minor shales and coals deposits. The depositional environment is interpreted to be tidal inlets, estuaries and lagoons. The age of the formation is late Rhaetianto to early Hettangian with a thickness in the reference well of 253 m.

[7] Measured depth bellow RKB (rotary Kelly bushing).

Nordmela Fm consist of interbedded siltstones, sandstones and clay with minor coal depostits. The sediments were deposited in a tidal flat to flood plain environments. The sandstone sequences represent tidal channels. The age of the Nordmela Fm is early Jurassic and the thickness in the reference well is 144 m.

Stø Fm consists of a well to moderately sorted sandstone with minor shale and siltstone layers. It was deposited as a stacked shore facies sedimented in a prograding coastal environment during early to mid Jurassic time. The thickness in the reference well is 111 m

The Adventdalen GP consists of sediments deposited during the Cretaceous and late-mid Jurassic and shows a total thickens of 483 m. The group is divided as follows:

Fuglen Fm consists of shale and silt with interbedded thin limestone layers deposited in marine environments with an ongoing tectonic movement during late Callovian to Oxfordian time. The thickness in the reference well is 32 m.

Hekkingen Fm (source rock!) consists of a dark shale and clay rich in organic material. Occasionally thin beds occur of limestone, dolomite, siltstone or sandstone. It was deposited in deep water with anoxic conditions during Kimmeridgian time. The thickness in the reference well is 26 m.

Knurr Fm is a dark to brown clay deposits with thin layers of dolomite and limestone. It was deposited in a deep shelf environment in Ryzanian/Valanginian to early Barrenmian time and have a thickness in the reference well of 57 m.

Kolmule Fm with claystone and shale and minor thin interbedded siltstone and limestone stringers. Sediments were deposited in open marine environment during Aptian to mid-Cenomanian and have a thickness in the reference well of 368 m.

Bellow the URU is the Torsk Formation, which consists mainly of non-calcareous clay deposited in a open to deep marine shelf in the time period from late Paleocene to Oligocene (NPD, 2007). Rare limestone stringer[8] exists within a 985 m thick formation of the reference well, referred to as IntraH1 in the thesis.

The uppermost section belongs to the Nordland GP, which is resent deposits consistent of muddy marine sediments. It is deposited post the last glacial period (ie. less than 20 kyr). The Nordland GP

[8] Industry term of a thin layer within another rock, usually a harder substance.

lies on top of upper regional unconformity (URU) which has a large lateral extent in the Barents Sea. The URU marks an erosional surface of the last 2 Ma with six major glacial periods (Vorren et al., 1989). The Thickness of the Nordland GP in reference well is 104m. (NPD and OED, 2010).

2.5 Source rocks of the western Barents Sea:

As described in chapter 1.2 source rocks are rich in organic material and can produce hydrocarbon if temperatures exceeds generation limits. The organic material also has to be preserved which means that conditions have to be anoxic and such environments is often found in subsiding areas as lakes, lagoons, deltas and swaps (Bjørlykke, 2001). The Western Barents Sea has been known to include source rock sedimentary facies and there has been in recent years proven that also accumulation of hydrocarbon exist in Skrugard and Goliat (NPD and OED, 2010). (Ohm et al., 2008) described several possible source rocks (Fig. 2.5.1) and the most promising are the lower Hekkingen which has been sampled and measured in 32 different wells.

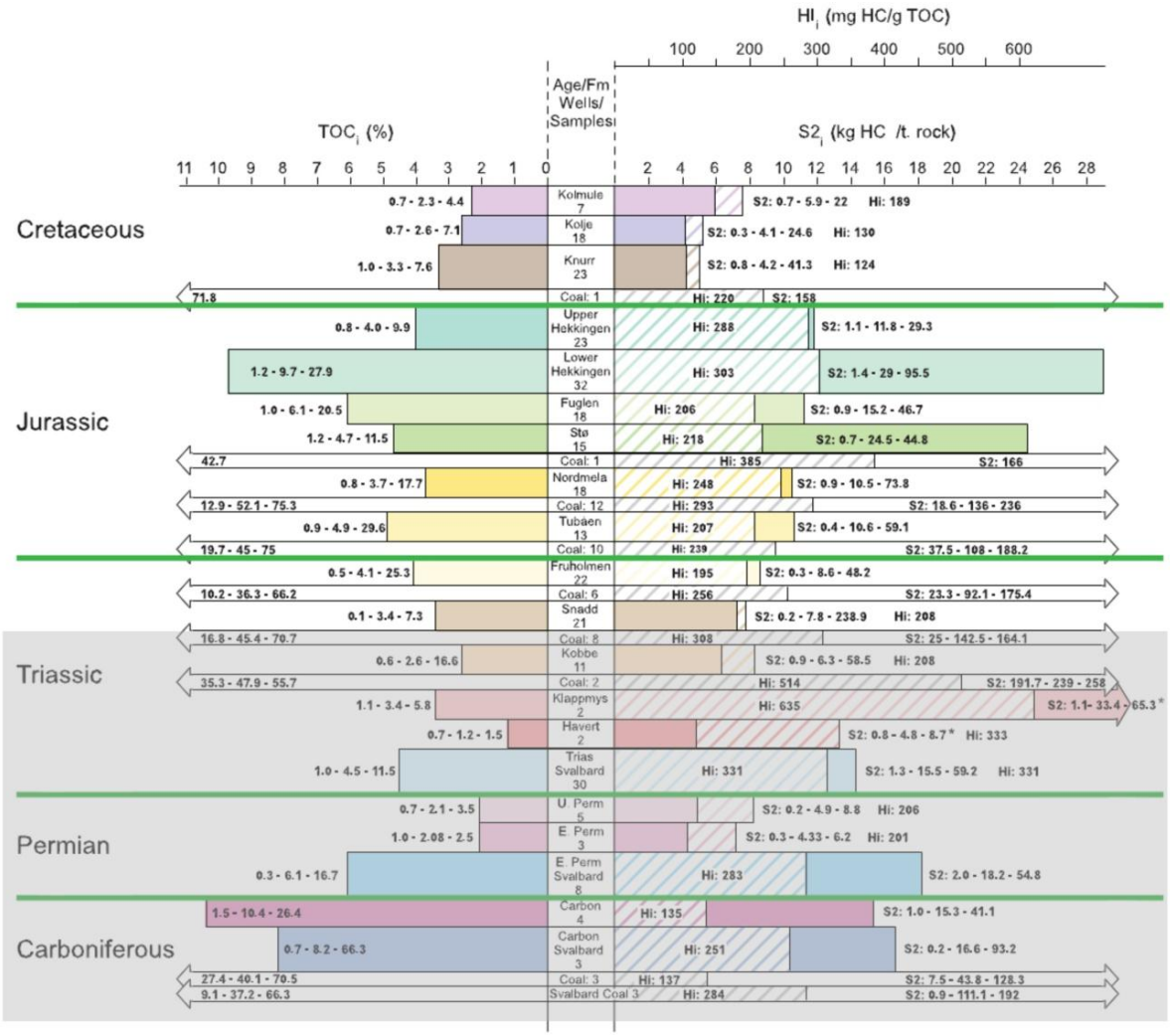

Figure 2.5.1 Source rocks in the Western Barents Sea with characteristics indicating initial total organic carbon (TOC), S2(hydrocarbon generative potential and hydrogen index (HI) All samples are based on different wellcores and start means that the sample has high maturity and the calculated TOC is highly uncertain. Grey area indicates source rocks which is not proven in the study area due to well 7219/9-1 do not penetrate deeper than into Snadd Formation (Figure modified from (Ohm et al., 2008).

3 Data and Methods

3.1 Data

The 3D seismic data set “West Loppa 2008”, is a mulitclient data set supplied by Western Geco (Fig 3.1.1) (table 3.1). In addition I have used 2D lines (Fig.3.1.1) to determine the regional geological setting and the lateral extension of amplitude anomalies.

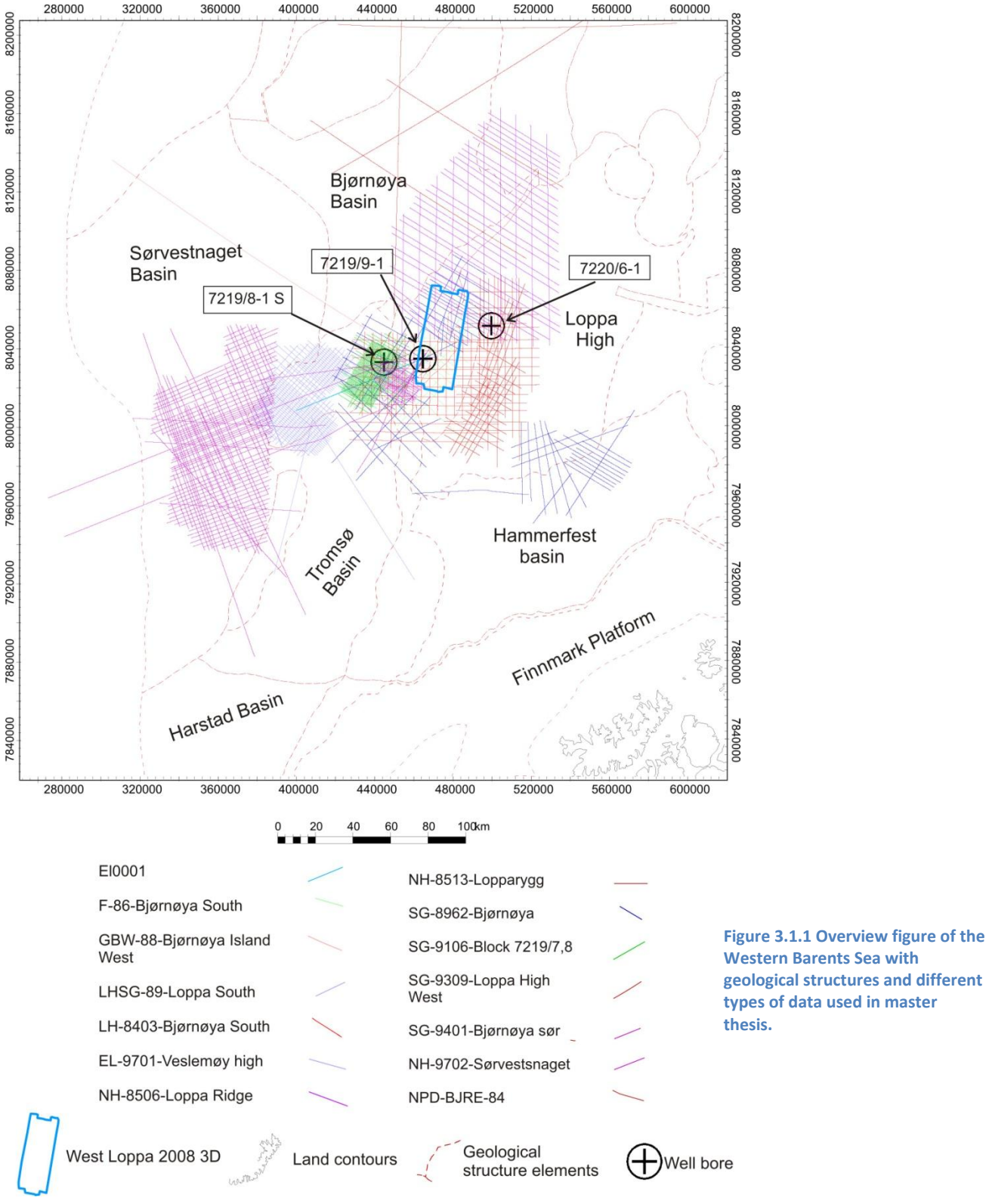

Figure 3.1.1 Overview figure of the Western Barents Sea with geological structures and different types of data used in master thesis.

3.2 Seismic Processing:

"West Loppa 2008" was processed by Western Geco. Western Geco is one of the world's leading seismic Company they include the most advance tools for processing seismic data. Western Geco uses their internal software "Omega" and "West Loppa 2008" was delivered fully processed in zgy[9] format.

The interpretation software "Promax" provided by Landmark was used during the master thesis for analysing the seismic cube.

Inline 1358 was exported as a 2D line and imported into Promax for performing a spectral analysis to determine the dominant frequency, which lies between 9 and 40 Hz (Fig. 3.2.1). A spectral analysis is using the Fourier Transformation to calculate the dominant energy window.

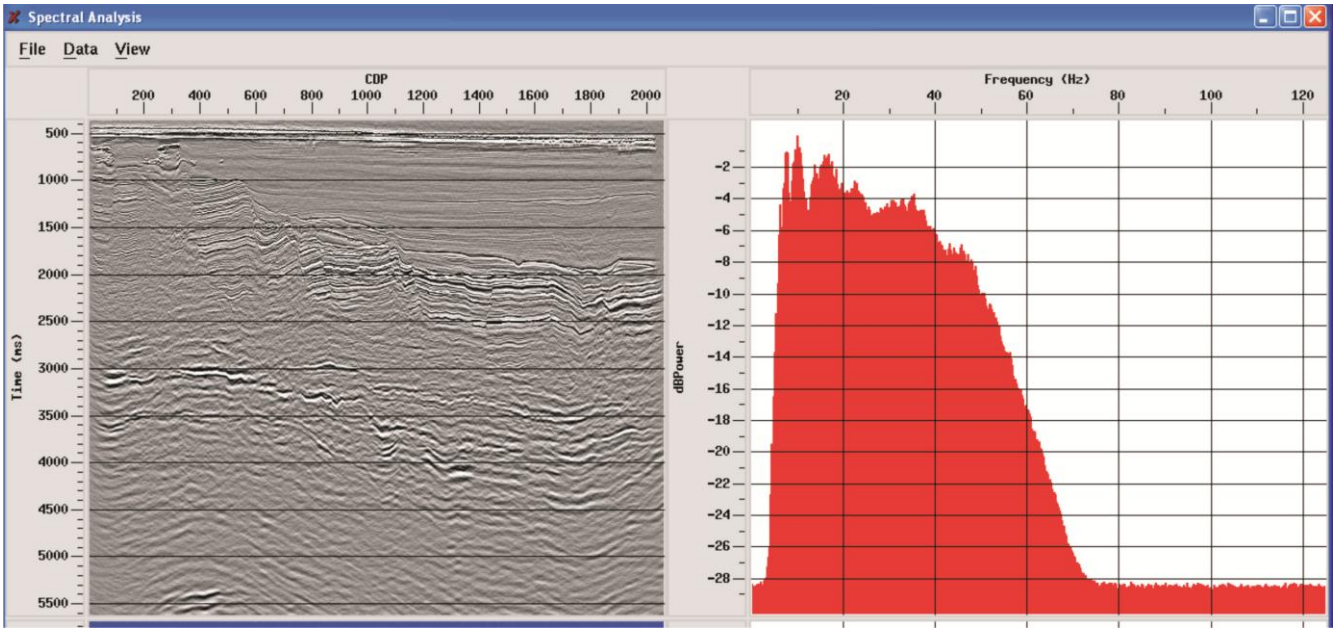

Figure 3.2.1 Spectral analysis of inline 1358. Dominant frequency 9-40hz. Analysis is preformed with the software "Promax".

Yilmaz (Yilmaz, 2001) described in detail all the necessary processing steps for generating a stacked-data line and provide information about velocity of the P-wave.

[9] Is a compressed format from ZEGY and is vendor specific for Western Geco (Schlumberger), ZGY enables faster data management than traditional ZEGY seismic.

The acquisition parameters of "West Loppa 2008" seismic cube are:

Vessel	**Western Patriot**
Streamers:	
Number of streamers	8
Active length (m)	5 000
Cable Separation (m)	100
Streamer depth (m)	8
Group interval (m)	12.5
Group	400
Source:	
Dual source, size (in^3)	3047PSI
Shot point interval (m) (distance between shots)	18.75 Flip-Flop
Recording:	
Sample rate (ms) / Recording Length (s)	2/6
Sample interval	4

Table 3-1 Acquisition parameters for the dataset "WestLoppa2008" Data (http://www.slb.com/services/westerngeco.aspx).

3.3 Petrel software interpretation and visualization tools

In this thesis the main interpretation and visualization tool has been Petrel 2009-2010 (Schlumberger, 2009). Petrel is a software for the G&G industry owned and developed of Schlumberger. Petrel includes all the "classical" and recent attributes which will be described further on. They also provide a large variety of interpretation methods and tools. In the following chapter I shall describe the methods I have used for interpreting seismic data based on (Schlumberger, 2009).

3.3.1 Interpretation of 3D data

Interpretation of horizons, structural elements and anomalies in the time-domain data on seismic uses cross sections, 2D windows and 3D window with several different parameters such as regular seismic traces, attribute maps and volumes.

Autotracking allows one to interpreted continuous reflectors. Before using this tool one needs to determine on which point of the wave trace (peak, trough, etc (Fig. 4.3.1)) autotracking should start. The tool is building on values of amplitudes in a seismic trace and will follow the given reflector determined by the continuity and signal strength. There are several parameters where the interpreter can chose different constrains of the seismic signal to be followed. Autotracking can also be used as guided autotracking for which you determine two points on a seismic cross section.

Paint brush is used in two and three dimensional windows and will trace a pointed volume/area.

The seismic trace is visualized in Petrel as a zero phase single. Troughs and peaks are selected when measuring the depths of reflectors dependent on the polarity of the interpreted layer reflector (Fig.3.3.1).

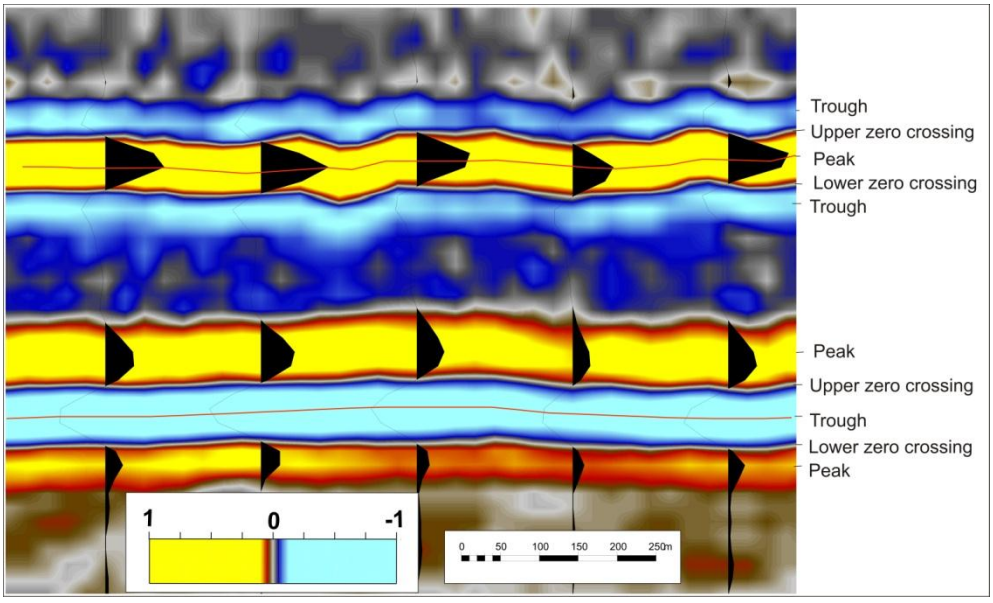

Figure 3.3.1 Visual outcrop of the seismic signal with peak, trough, upper and lower zero crossing used in this thesis. The different polarity of a negative and positive reflector is indicated. Colour scale and polarity is a standard in this thesis and are indicated if different scaling are used.

3.3.2 Seismic attributes

A seismic attribute is defined a “quantitative measure of a seismic characteristic of interest” (Chopra, 2005). Development and analysis of seismic attributes has been going on since the 1930s, and is closely linked to the evolution of computer technology. There are more than 50 distinct seismic attributes to choose from trace displays to complex volume calculations. (Marfurt, 2005) (Taner, 2001).

The attributes used in my master thesis are described here and classified into volume attributes and surface attributes

3.3.2.1 Volume attributes

Volume attributes are extracted data from a seismic volume where different physical properties of the seismic traces are calculated and displayed in a volume window. Volume attributes do not necessary consist of only seismic data, other types of data can also be applied i.e well data. (Schlumberger, 2009).

3.3.2.1.1 Ant Trackng

Ant-tracking is a patent-protected technology from Schlumberger and is used for automatic identification and extraction of faults and faults from a pre-processed seismic volume. Ant tracking is named based on the theory which is explained by having a swarm moving around in the data volume and evaluating based on faults, fractures and other linear anomalies (Schlumberger, 2009) The parameters can be changed based on the requested resolution of interesting faults.

3.3.2.1.2 RMS

RMS (root mean square) can both be calculated of a seismic volume but is mostly used as a surface attribute. RMS amplitude is the square root of the sum of the squared amplitudes divided by the number of live samples in interval. Means RMS amplitudes are only positive and shows the strength of amplitude over a given interval.

3.3.2.1.3 Chaos

The chaos attribute visualize the “chaoticness” of the seismic data within a given volume. Practical this means that chaos attributes measures regions with low consistency of the seismic traces and can be related to geological features corresponding to such a responds such as: faults/discontinuities, reef textures, channel infill and acoustic masking. Important to remember is that chaos attribute produce the same response whether in high or low amplitudes, dipping or non-dipping regions.

3.3.2.1.4 Variance

Variance is similar to Chaos attribute and is also used for imaging discontinuities based on the difference in where fault planes are laterally separating data which can be auto-tracked using voxel-picking algorithms. By displaying variance attributes over a short interval in time or as a timeslice it can be used to confirm depositional features. The outer rim of fluid flow features can be mapped with this method. Filters are applied by default for inline and crossline and for a vertical smoothing.

Both Chaos and Variance attribute cubes are based on the edge detection method.

3.3.2.1.5 Dominant Frequency

The dominant frequency is defined as the square root of the sum of squares of the instantaneous frequency and instantaneous bandwidth, i.e RMS of frequencies. Used for localising low frequency shadows due to velocity effects.

3.3.2.1.6 Structural smoothing

Structural smoothing uses a given volume and locally smoothes the input data by increasing the continuity of seismic reflections (Schlumberger, 2009).

3.3.2.2 Surface attributes

Surface attributes extracted data of a given interval above, below or both of an interpreted surface or another interpreted object within a seismic volume.

RMS surface attribute has been applied, where you can specify a certain depth, time, surface or between two surfaces and perform RMS on the selected volume.

3.3.3 Depth Conversions

"West Loppa 2008" was delivered by Western Geco as a fully processed seismic cube in timedomain. For depth conversion it is needed to convert the z-axis which is in two-way-travel time [ms] to meters [m]. The process was done manually at a given depth in time by applying the formula distance divided on time equals velocity. Equation:

$$v\left(\frac{m}{s}\right) x\ twt\ (s) = z\ (mTVD)$$ *Equation 14*

Petrel was used to do depth conversion on a seismic cube by defining interpreted surfaces and apply a velocity model based on welltops from well 7219/9-1 together with the interpreted surfaces for depth conversion (Fiugre 3.3.2).

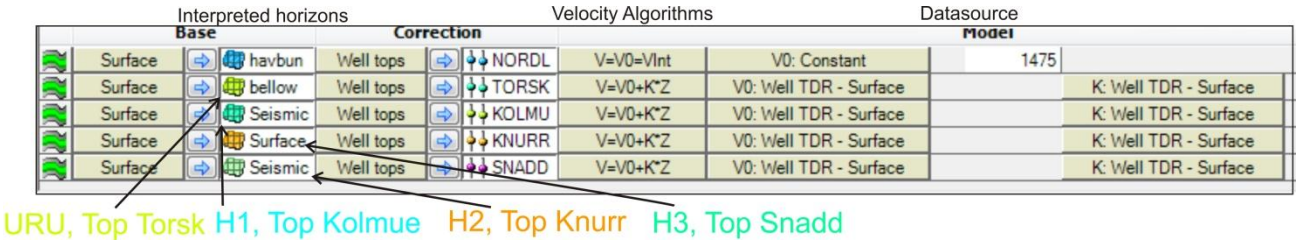

Figure 3.3.2 Snapshot of depth conversion tab in Petrel, where you can see the linear equation used to determine the interval velocities in the velocity model. Also the different welltops and equivalent surfaces are listed. Velocity for seawater is constant set to be 1475. V= Interval velocity, V0= velocity at start interval of layer, K*Z = velocity(K) change with depth (Z).

By applying a correction option the velocity model adjust the seismic surfaces to the welltops correcting for possible errors. The correction was up to 60m for one layer (URU).

3.4 CSMHYD

CSMHYD is a program used for calculating the gas hydrate stability zone (Chap.1.7.2) where the different gas composition and temperature is taking into account.

3.5 Presentation of seismic anomaly analysis

Interpreting seismic amplitude anomalies can be tricky since there are so many different aspects to consider and basically one can find amplitude anomalies on all reflectors. Therefore one needs to be constructive and follow a clear strategy while work your way through a seismic cube. Løseth et al. (2009) presented a workflow for interpreting amplitude anomalies in a hydrocarbon point of view.

Critical points to follow are:

1) Investigate and observe anomalies on interpreted 2D surfaces and in 3D
2) Use various types of attributes maps (Aminzadeh et al. 2002) on fluid features. Correlated anomalies with surfaces.
   Attribute maps at depositional surfaces may reveal palaeo surface anomalies and one needs to distinguish them from fluid flow related anomalies.
3) Separate interpretation of different anomalies.
4) Systematically organize leakage anomalies according to stratigraphy

The descriptive terms are listed in tables bellow:

Term	Definition
High or low amplitude anomalie	Local variance in postitive or negative amplitude along a reflection for any reason
V-shaped bright	High amplitude V-shaped reflection in vertical section which is discordant to reflection from depostitonal surfaces.
Flat spot	Relative flat seismic reflection wich is discordant to reflection from depositional surfaces.
Phase reversal	Phase shift of 180degrees along a continous reflection
Reduced continuity	local reduction of continuity of a seismic event
Increased continuity	Local increase of continuity of a seismic event
Bottom simulating reflectors	High amplitude reflection in vertical section where it is parallel to the seafloor. Distinguished from multiple when analysing reflector in slope
Reduced frequency	Local decrease of frequency

Table 3-2 Descriptive terms of an amplitude anomaly, modified by (Løseth et al., 2009)

Term	Definition
Vertical wipe-out zone	The area of a seismic volume where the reflections from the stratigraphic layers are deteriorated so the primary reflections either are absent or very weak.
Vertical dim zone	The area of a seismic volume where the reflections from the stratigraphic layers are absent, but have lower amplitude than adjecent areas.
Vertical high amplitude or bright zone	The area of a seismic volume where there are several high amplitude reflections which can be grouped together.
Discontinuity zone	The area of a seismic volume where the refelections from stratigraphic layers are more discontinous that in adjecent areas.
Chaotic reflection zone	The area of a seismic volume where the refelections pattern is chaotic compared to adjecent areas.
Local depression features	Negative real down-bending or sag of a seismic reflection. The underlaying reflector can be truncated, be parallel to the described structure or they can have any type of reflection pattern (chaotic).
Mounds	Positive structure of any shape rising above the normal top of a reflection. The reflection pattern below the mound can be of any type
Push down	Apparent down-bending produced by a local, shallower low-velocity area
Pull up	apparent uplift produced by a local, shallower high-velocity area

Table 3-3 Describing anomalous patterns on seismic, figure modified from (Løseth et al., 2009).

Term	Definition
Impedance contrast	Increase or decrease of ampltitude on the seismic reflection (relative).
Base and top	Stratigraphic level of top and base of anomalie
Important shift zone	Important zones within the anomalie where amplitude changes
Shape	Geometric shape of anomalie
Height, width and volume	Meassurments of anomalie
Texture	Texture within the anomalie, changes in texture
Geographic location	spatial distribution and location relative to important geological features such as faults and possible reservoirs
Corona or halo	High amplitude anomalies occuring around the rim of a gas chimney

Table 3-4 Descriptive terms used for an anomaly, figure modified from (Løseth et al., 2009).

3.6 CorelDraw

CorelDraw is a graphic software with more than 100 million users worldwide(CorelDraw, 2007). Base of CorelDraw is the vector based editing functionality which allows the user to work in different layers and simplifies the process of generating advanced models. All figures modified and generated in this master thesis are done by work in CorelDraw.

4 Results

This chapter present observed and analysed seismic anomalies in the Bear Island fault complex including the seismic stratigraphy and faults. Seismic profiles, volume render, time-slices and attribute maps with various parameters are used for presenting the results in the most descriptive manner.

4.1 Seismic Stratigraphy

The Stratigraphy interpretation is based on the well data (7219/9-1 correlated to seismic reflector-continuity, characteristics and strength of seismic traces. The regional stratigraphy which is based on work from (Dore, 1995; Faleide and Gudlaugsson, 1984; Worsley et al., 1988) Interpreted horizons/surfaces are shown in figure 4.1.1.

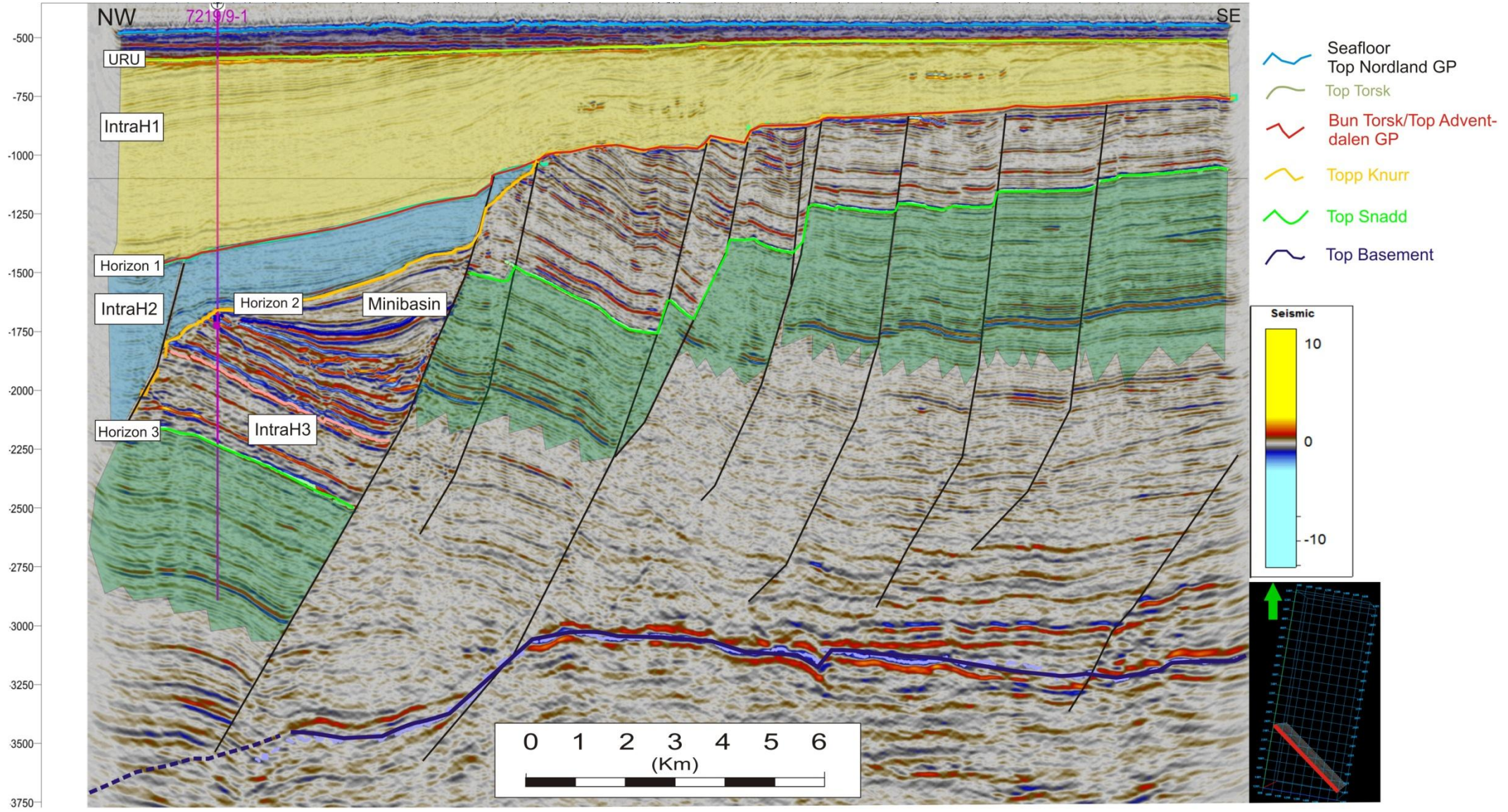

Figure 4.1.1 Seismic cross section with the different stratigraphic sequences labeld. Position of the seismic line is indicated with red on the overview figure.

4.1.1 Seafloor:

The Interpreted seafloor (bathymetric map) is shown in figure 4.1.2. Water depths range from 316 m to 424 m where there is a gradual shallowing towards the south. The present day topography of the Barents Sea was mainly shaped during major glacial events in the Late Cenozoic (Vorren et al., 1998). Major glacial derived seafloor features are observed: Elongated curvilinear furrows with dominantly a southwest-northeast orientation in the northern area and a west-east orientation in the southern area of the 3D seismic dataset "West Loppa 2008" (Fig.4.1.2 A). At ~338 m water depth the dominant orientation is west-east. Based on previous work eg. (Andreassen et al., 2007b) the elongated

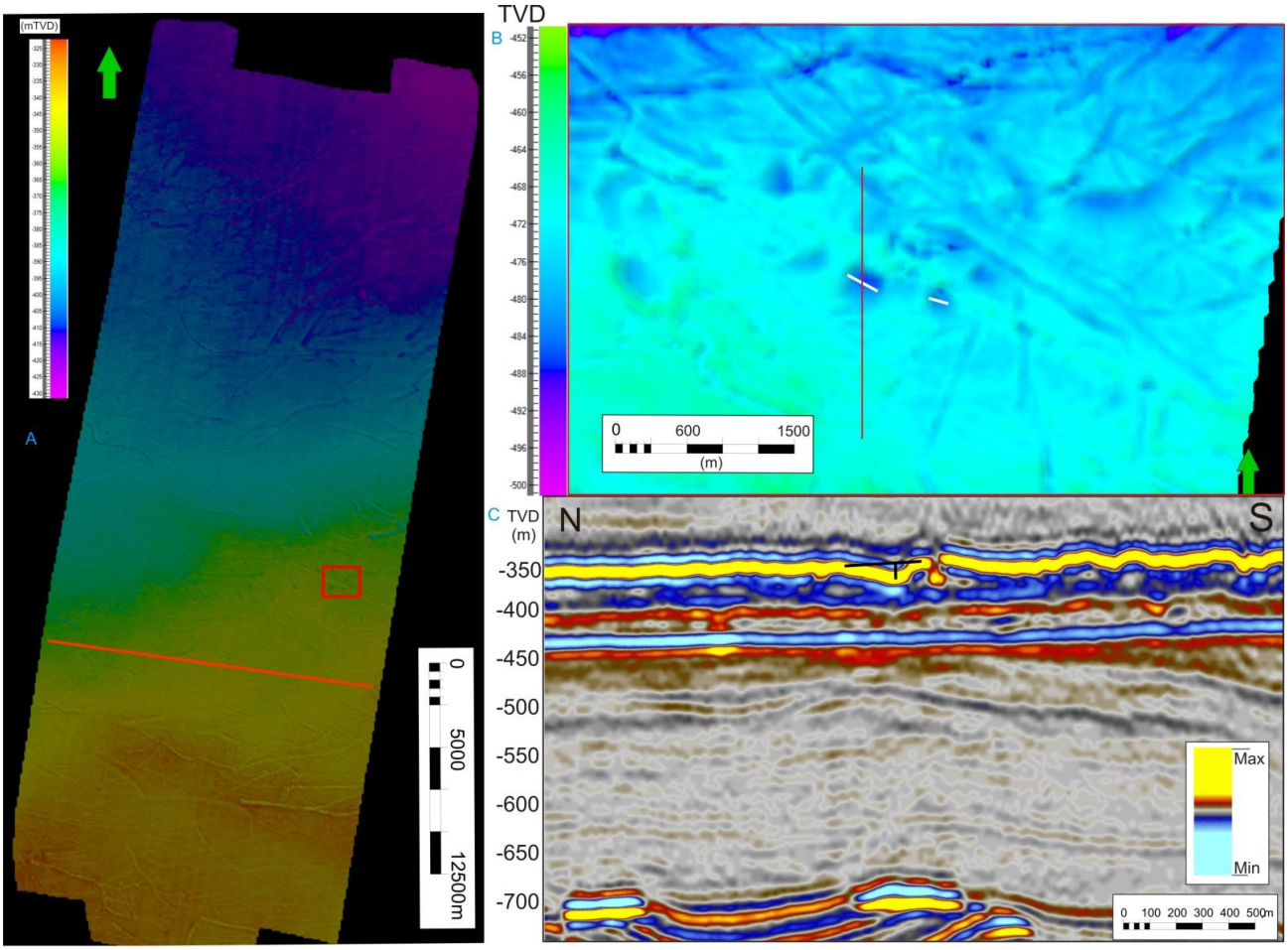

Figure 4.1.2 A) Shaded overview map of the interpreted seabed in the 3D seismic survey "West Loppa 2008". Depths have been converted to TVD. Red line indicates position of seismic cross section in figure 4.1.3 B) Pockmarks C) seismic cross section through possible pockmark.

furrows are interpreted to be iceberg ploughmarks formed by the keel of drifting icebergs.

There are observed circular depressions measured to be ~300 m on the long axis and ~13 m deep (Fig.4.3.2C). Interpreted to be pockmarks which indicate postglacial fluid emissions (Hovland and Judd, 1988b) (Fig.4.1.2 B). There is no visual fluid flow indicators between IntraH1 sediments and seafloor pockmarks observed.

4.1.2 Upper Regional Unconformity (URU):

The URU is a significant erosive surface and presents a widespread unconformity where dipping layers are cut (Fig.4.1.3) (Vorren et al., 1989). Amplitude strength varies and shows as a characteristic negative polarity which is caused by the hard glacial sediments overlaying softer sediment of the top Torsk Fm (NPD, 2007). The amplitudes are extremely high as seen on eastern part of (Fig.4.1.3).

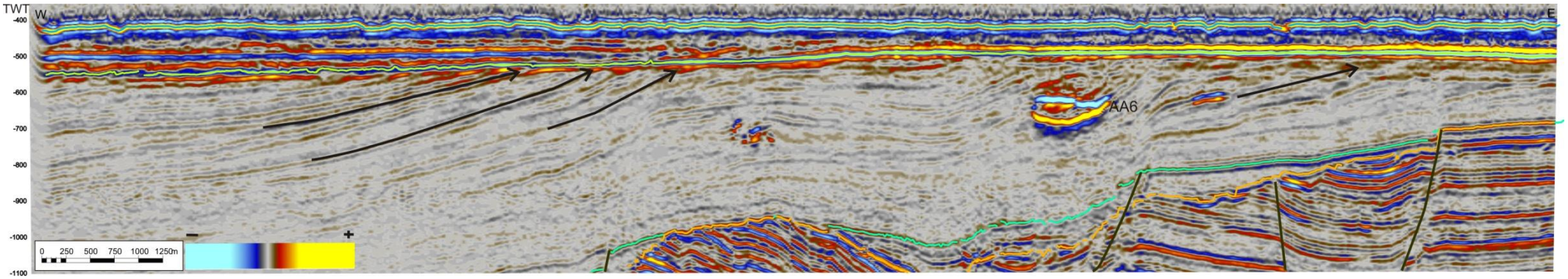

Figure 4.1.3 Seismic cross section of the seismic cube West Loppa 2008, position indicated with red marker on figure 4.1.2. Variation in amplitude is clearly seen on the continuous reflector URU. AA6 can also be seen in this figure and will be further described in chapter 4.3.4

4.1.3 Horizon 1.

The reflector called Horizon 1 (H1) reflector are continuous and exists throughout the whole dataset (Fig.4.1.3). The volume between URU and H1 will be referred to as IntraH1. IntraH1 is equivalent to the Torsk formation (NPD and OED, 2010). The Strata are dipping towards southwest and are represented as clinoforms with sediment supply from Loppa High (Vorren et al., 1991) and are onlaping onto H1. Horizon 1 is equivalent to the top Kolmue formation (NPD, 2007). In addition H1 marks the boundary between Tertiary and Mesozoic deposits. H1 resembles both a depositional and erosive surface with the depositional surface in west where subsidence has occurred. In the east H1 represents both an erosive and an unconformity surface.

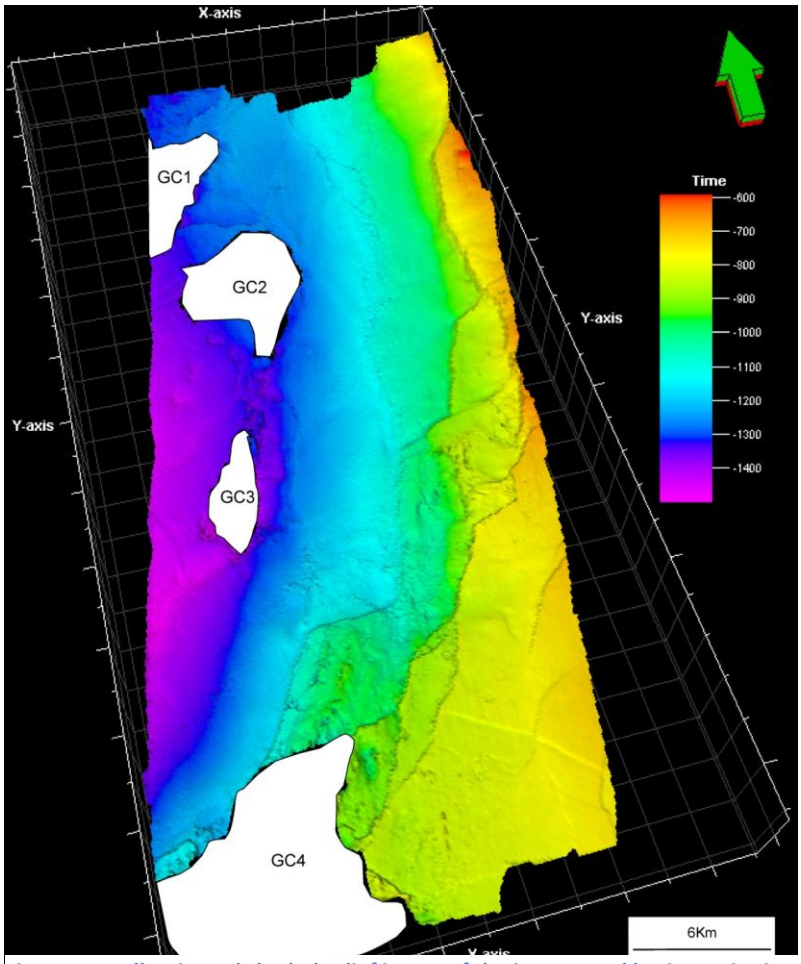

Figure 4.1.4 Illuminated shaded relief image of the interpreted horizon 1 in time domain from 3D seismic cube West Loppa 2008. The vertical exaggeration is 5.

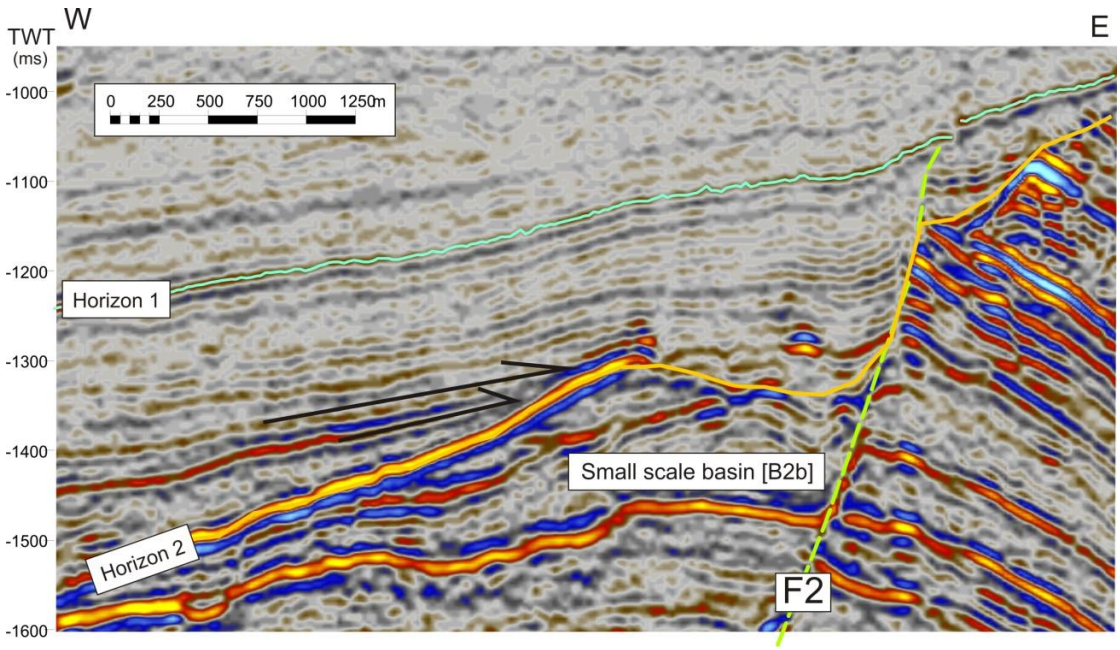

Figure 4.1.5 Seismic cross section indicating onlaping onto H2 in intraH2 sediments.

4.1.4 Horizon 2

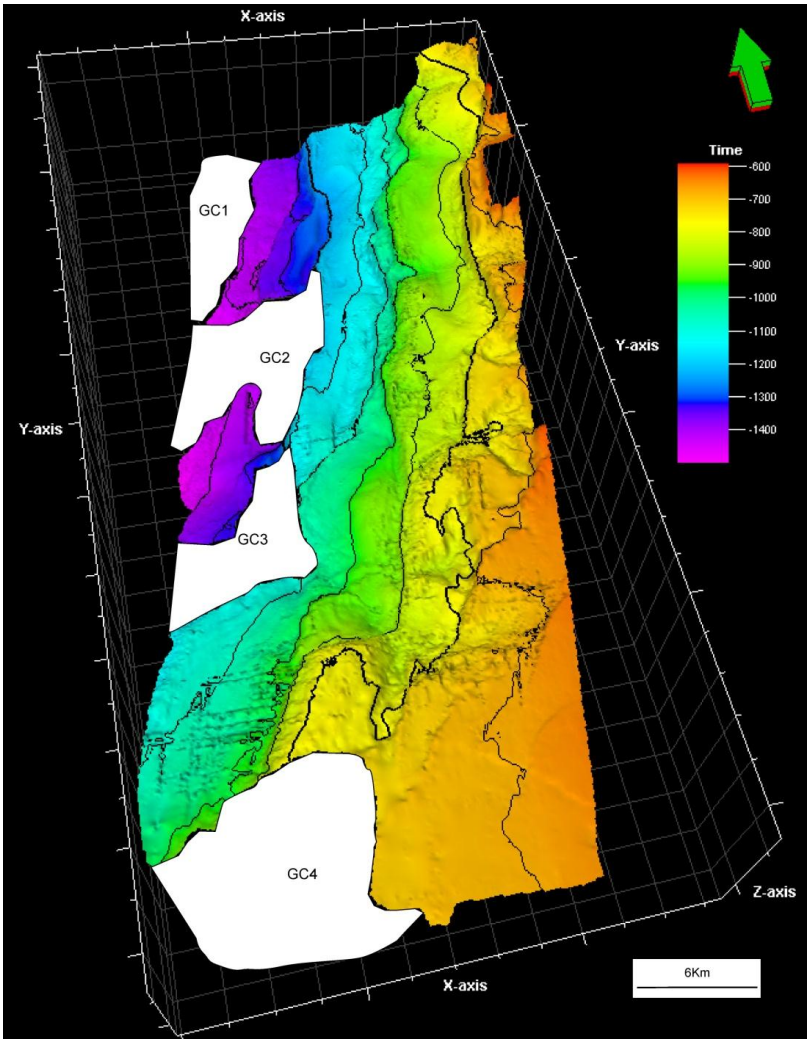

Figure 4.1.6 Illuminated shaded relief image of the interpreted horizon 2 in time domain. The vertical exaggeration is 5,

Horizon 2 (H2) is located beneath H1, its top represents a depositional horizon in the west and an erosive horizon at the top of the listric asymmetrical fault blocks and east of F2. In the eastern part of the seismic cube horizon- 1 and 2 resembles the same stratigraphic level. The Sediments in between H2 and H1 are referred as IntraH2 and are equivalent to the Kolmue formation (Fig.4.1.1). Horizon 2 is equivalent to the top Fuglen formation in reference well 7219/9-1(NPD, 2007).

Horizon 2 is both an erosive and depositional horizon. The erosive horizon is indicated as an unconformity where westward propagating channels cuts down into deeper strata (Fig 4.1.6). The channels may follow fault weakened zones. The tops of the pre-rotated and faulted blocks has been eroded. The upper section of H2 shows a south-westward depositional sequence with onlapping[10] features on H2 (Fig. 4.1.5).

[10] Sequence stratigraphy term of successively younger rock strata extending progressively further across an erosion surface cut in older rocks (Wikipedia).

4.1.5 Horizon 3.

Horizon 3 is equivalent to the top Snadd formation based on the reference well 7219/9-1 and 7220/6-1. The Sequence between H3 and H2 is referred to as IntraH3 sediments. IntraH3 sediments are updipping in the north and have gone through extensive compressional forcing in a north-south direction causing a folded sequence in the IntraH3. The lateral extension of H3 is shown on figure 4.1.7.

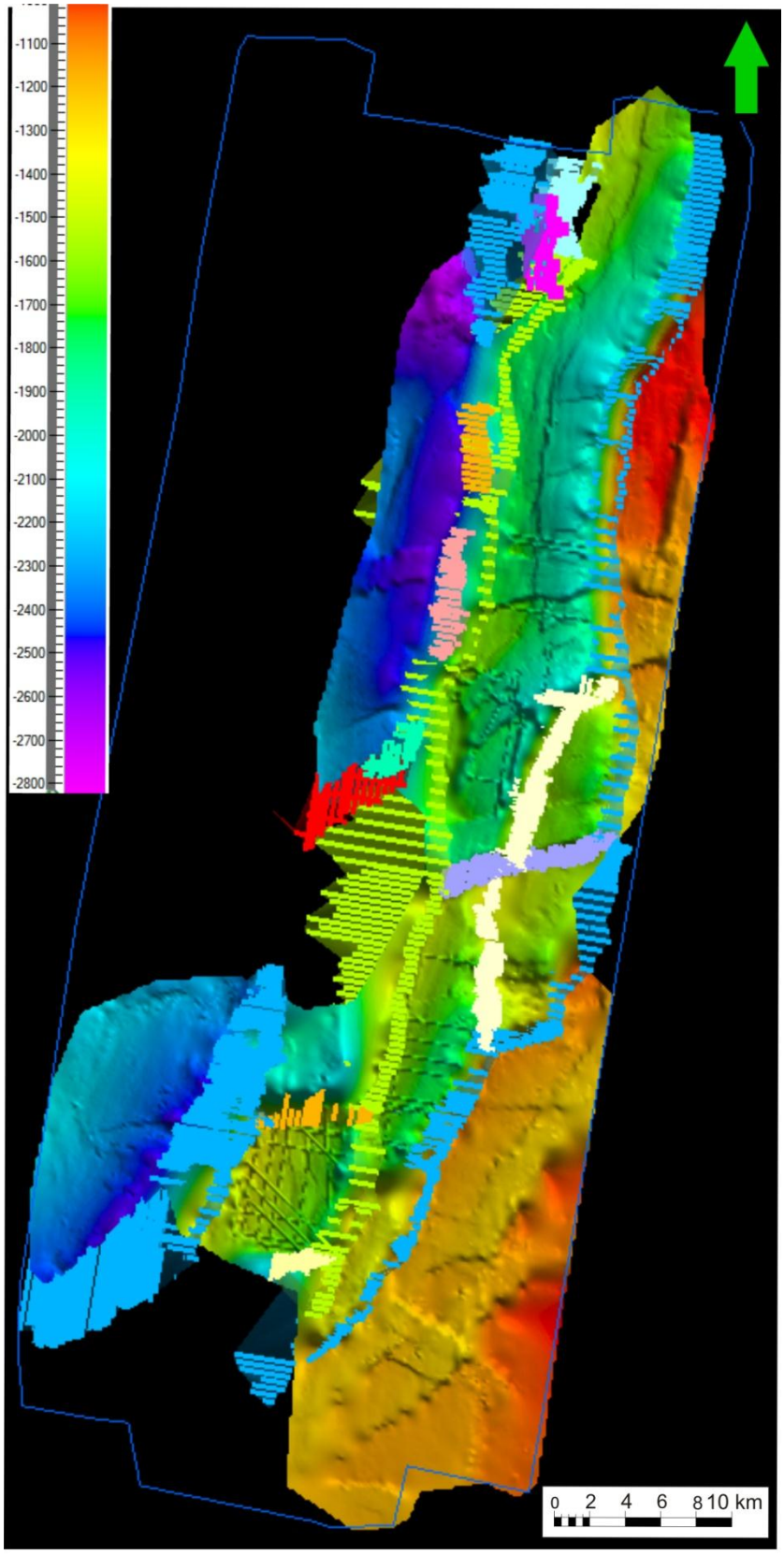

Figure 4.1.7 Birdview of horizon 3 with faults. The faults are reviewed in detail in chapter 4.2. The vertical exaggeration is 4.

4.1.6 Locally small scale basins

On the top eastern side of the listric asymmetrical fault blocks (Fig. 4.2.1) there seems to have been deposited syn-faulting sediments as can be seen in a cross section on figure 4.1.1. These are controlled and limited by the main faults as indicated on figure 4.1.7. There is not possible to determine if the faulted block 4 and 5 also have evolved these kinds of basins due to the poor quality of seismic data. The lateral extension of the minibasins are indicated on figure 4.1.8. The sediments deposited in these locally small scale basins are equivalent to Knurr/kolje Fm.

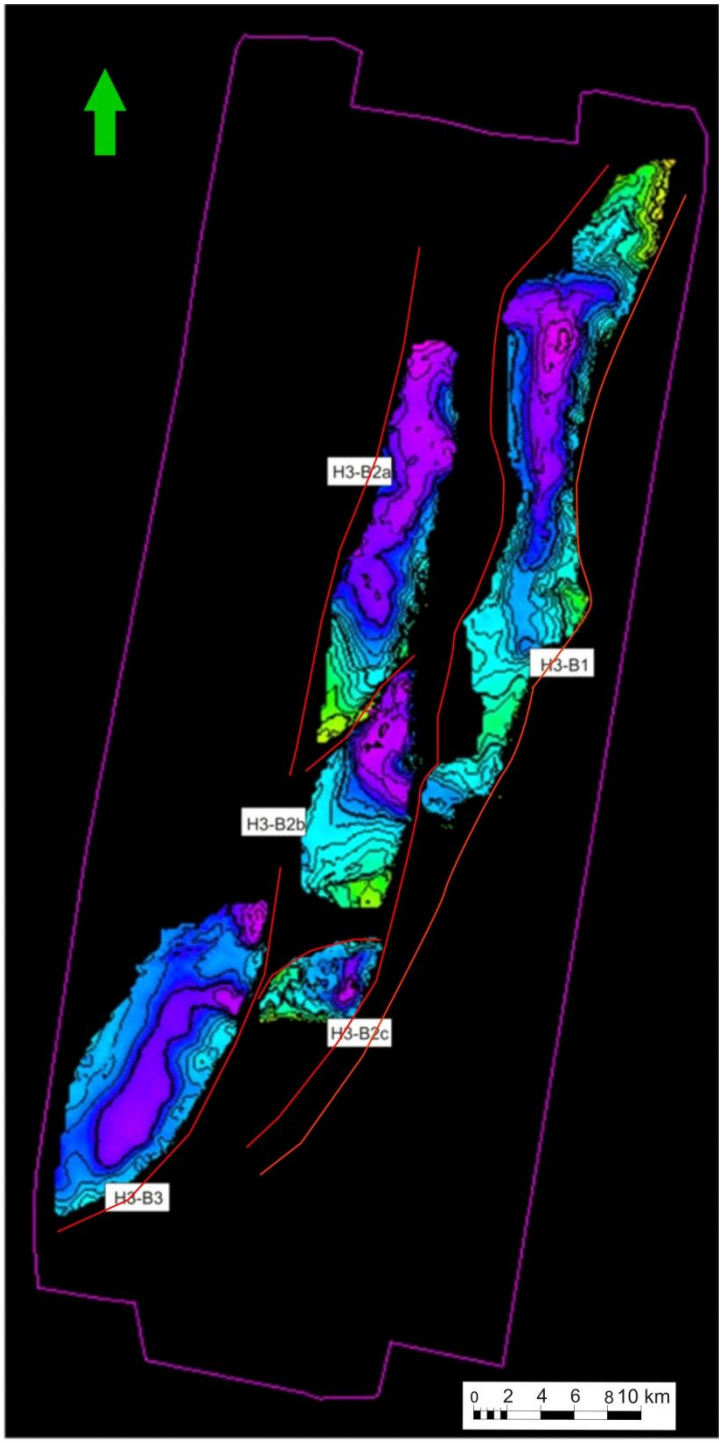

Figure 4.1.6 2D view of the lateral extent of the different minibasins, colour tablets are irrelevant on this figure. Red lines indicate the main faults.

4.2 Structural Interpretation

There is a large variety of faults in the study area. To simplify the process describing and discussing the different features I have classified the study area into several “blocks” determined on the lateral propagation. Figure 4.2.1 visualizes the main faults and the different blocks both in a plane view and cross-section. There after I have sub grouped and classified the smaller faults based on the stratigraphic age the fault truncates.

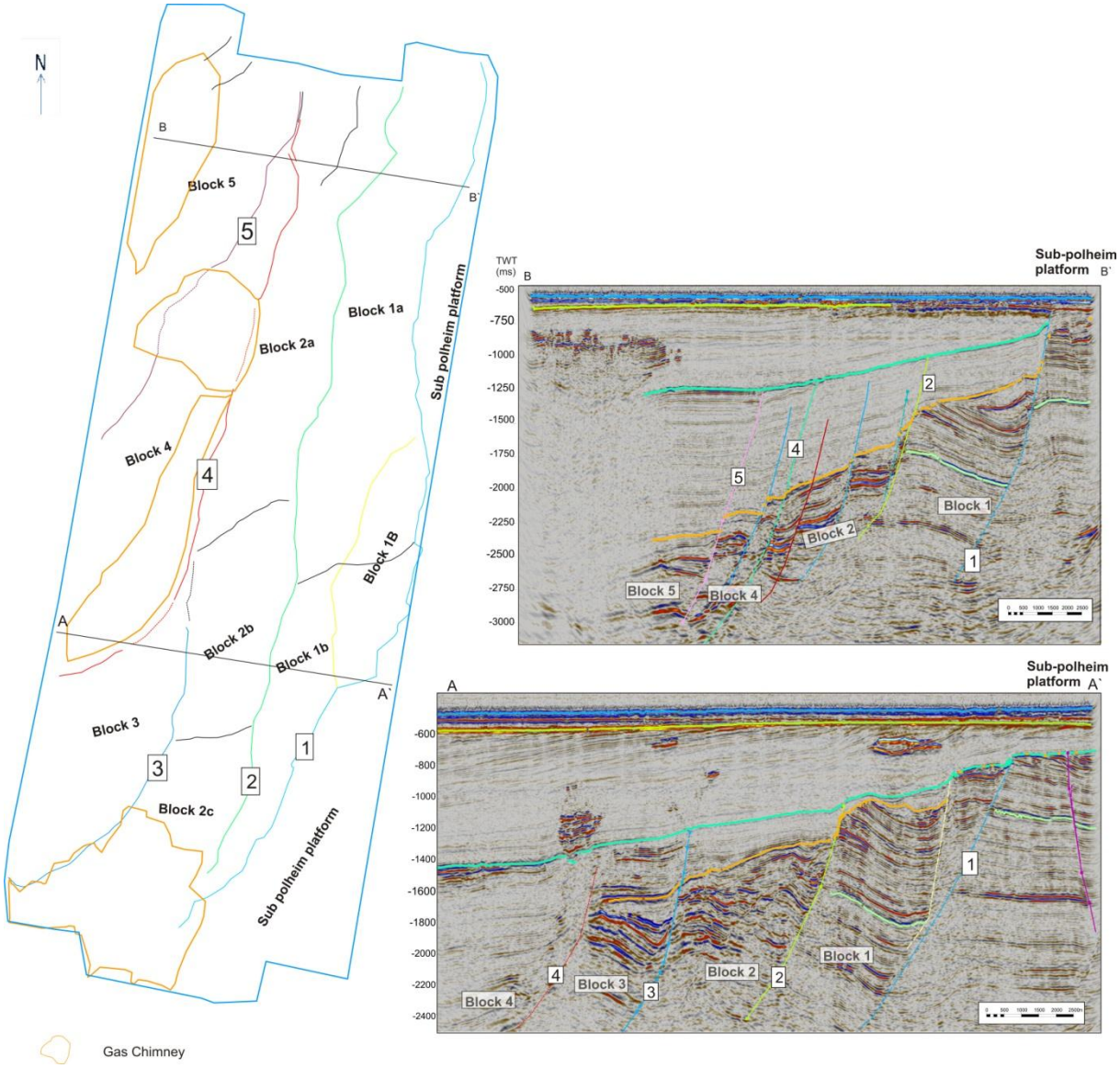

Figure 4.2.1 Structural overview of the main faults with additional seismic crossing the seismic cube indicating the vertical extension of the faults.

4.2.1 Asymmetrical normal faults

There are five dominant asymmetrical faults evident in the whole dataset (Fig.4.2.1). They occur as normal faults with an NE-SW orientation and a dip towards west. In the southern part, the faults curve more into a W-E trend. The top of the faults are truncated mainly by H1 (Fig. 4.1.1). Which leads to faults in the eastern part of the dataset has a shallower vertical extent (Fig.4.1.1). Throws varies from 500 ms (TWT) for the deepest F5 (table 4-1) to 1000 ms (TWT) for the F3 (table 4-1). Detailed information about the faults can be found in table 4.1.

		max	min						
No.	**lateral (km)**	**vertical extent (TWT)**	**vertical extent (TWT)**	**lateral x-axis (km)**	**Throw (ms)**	**Orientation**	**top**	**top (TWT)**	**base**
1	50	2500	1400	2	950	NE-SW	H1	800	Basement
2	40	2700	2000	4,5	840	NE-SW	H1	1060	Basement
3	16	2100	1800	5	1000	NE-SW- W-E	H1	1000	Basement
4	35	2800	2400	3	540	NE-SW- W-E	H1	1200	Basement
5	18	3000	2500	3,5	500	NE-SW	H1	1200	Basement

Table 4-1 Summarized details for the main faults.

4.2.2 Small faults

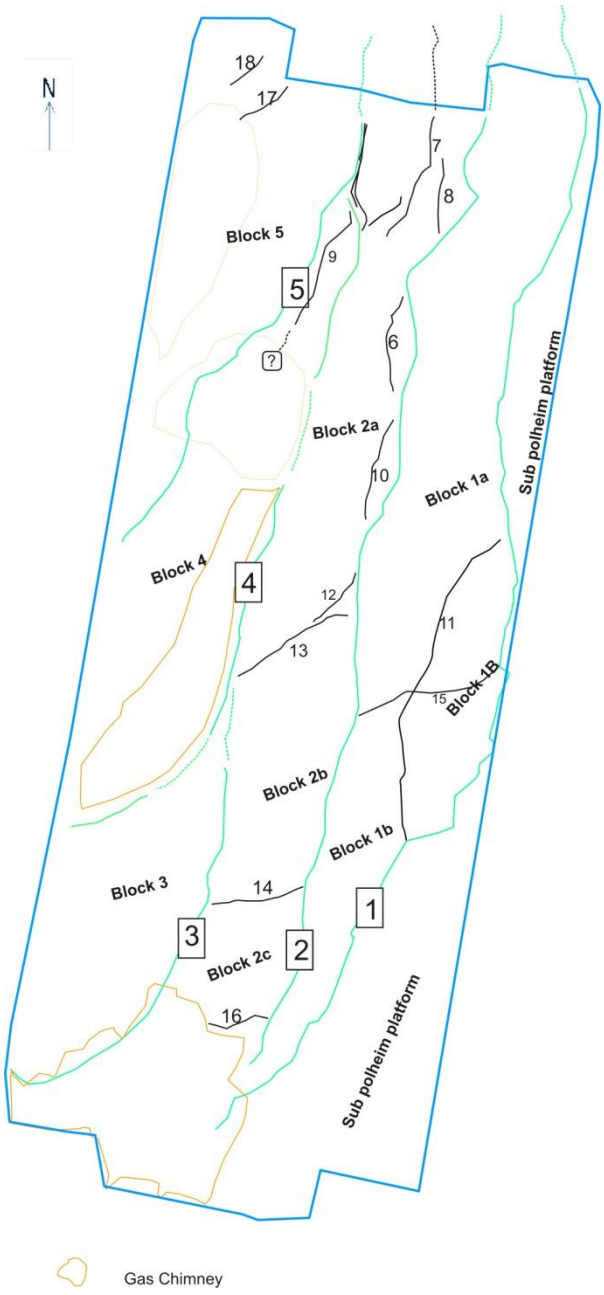

Figure 4.2.2 Overview figure displaying the main faults and the smaller faults. The faults divieds the cube into several blocks which is named respectiv to the faults.

Within the major system of controlling asymmetrical normal faults there are several smaller scale normal-faults. They are characterised by less lateral extent, less throw and typically terminated by the larger “main faults”.

The typical orientation of the small faults is an N-S trend with a dip towards west. The faults are described, visualized and labelled in figure 4.2.2 and table 4.2.

Most of the faults truncates at H2 and some terminates at H1 (table 4-2).

No	lateral (km)	vertical extent (TWT) (max)	vertical extent (TWT) (min)	lateral x-axis(m)	Throw (ms)	Orientation	top (stratigraphic)	top (TWT)	base
6	4,9	1600,0	1300,0	1100,0	200,0	N-S	H1 /truncates on fault 2	1100,0	2700,0
7	6,5	1500,0	900,0	2400,0	60,0	N-S	Intra H2 / diminish in between 2-4 in S	1300,0	2200,0
8	3,8	1200,0	1000,0	500,0	100,0	N-S	Intra H2 /truncates on fault 2 in S.	1200,0	2200,0
9	6,0	1600,0	1200,0	1500,0	100,0	N-S	Intra H2 / diminish in between F4-5 in S.	1300,0	3200,0
10	5,0	1200,0	1100,0	100,0	120,0	N-S	IntraH2	850,0	Basement
11	16,0	1700,0	500,0	2000,0	500,0	N-S	H1	860,0	2200,0
12	2,2	900,0	600,0	1200,0	80,0	Circular, NE-SW to E-W	Intra H2	1400,0	fault 2-12
13	5,0	1400,0	900,0	2000,0	180,0	NE-SW	Intra H2	1400,0	2800,0
14	4,1	1300,0	500,0	1400,0	340,0	E-W	H1	1000,0	fault 2
15	6,9	1250,0	450,0	1200,0		E-W	H1, see fig	900,0	Fault 1
16	2,2	835,0	241,0	925,0	54,0	NE-SW	H1	977,0	Fault 2
17	4,7	1094,0	800,0	3300,0	?	NE-SW	H1	1280,0	?
18	2,5	819,0	600,0	2000,0	?	NE-SW	H1	1313,0	?

Table 4-2 Detailed specifics about all the smaller faults in the dataset "West Loppa 2008".

4.2.3 IntraH3 faults

There are many faults limited by the larger faults inside the IntraH3 sediments. These are labelled and visualized in figure 4.2.3. The general trend for the faults are southwest-northeast. Apparent angle of throw seems to vary from the faults on block 1 and block 1B (~40°-60°). For specifics about the faults see table 4.3. Similar faults are also identified within the intraH3 sediments on the other blocks (Tab. 4-3).

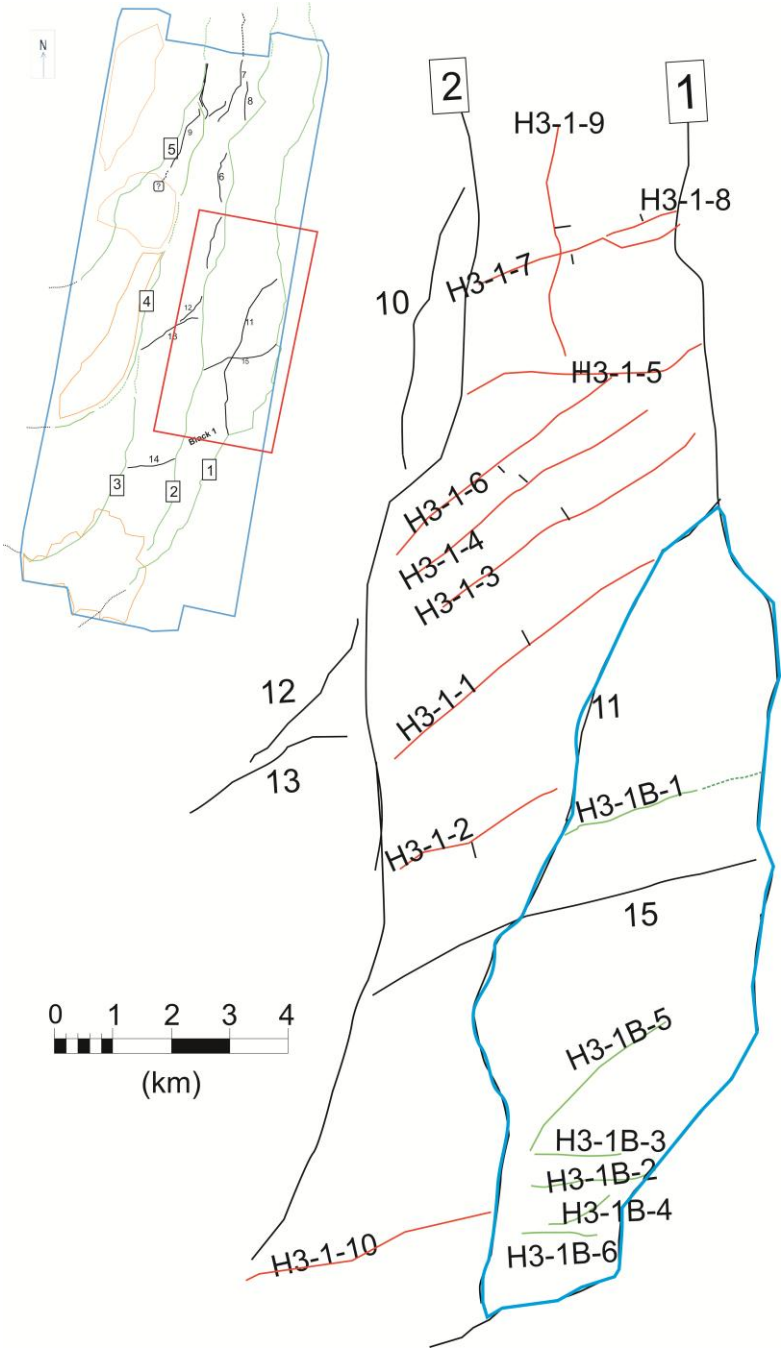

Figure 4.2.3 Overview of faults on block 1. Based on seismic cross sections and attribute maps.

No*	lateral (km)	vertical extent (twt) / (m)	lateral x-axis(m)	Throw (ms) / (m)	Apperent angle of throw (°)	Orientation	Block	Dip	Top
H3-1-1	6,5	1100 / 1925	2200,0	142 / 248	41,0	NW-SE	1	N	IntraH3
H3-1-2	3,2	1050 / 1837	1050,0	85 / 149	60,0	NWW-SEE	1	S	H2
H3-1-3	5,2	750 / 1312	2100,0	100 / 175	31,0	NW-SE	1	N	IntraH3
H3-1-4	5,8	700 / 1225	1800,0	47 / 82	34,0	NW-SE	1	N	H2
H3-1-5	4,4	766 / 1340	1440,0	106 / 185	42,0	NW-SE	1	N	IntraH3
H3-1-6	5,6	1185 / 2073	1395,0	35 / 61	58,0	NNW-SSE	1	S	H2
H3-1-7	3,6	1040 / 1820	1600,0	64 / 112	48,0	NW-SE	1	S	IntraH3
H3-1-8	1,9	510 / 892	890,0	32 / 56	45,0	NNW-SSE	1	N	IntraH3
H3-1-9	4,5	1100 / 1925	770,0	52 / 91	68,0	N-S	1	E	H2
H3-1-10	3,1	940 /	676,0			NE-SW	1	S	H2
H3-1B-1	2,5	1325 / 2319	1070,0	48 / 84	65,0	NE-SW	1B	S	IntraH3
H3-1B-2	1,3	1080 / 1890	960,0	60 / 105	48,0	E-W	1B	S	IntraH3
H3-1B-3	1,7	1395 / 2441	1100,0	43 / 73	65,0	E-W	1B	N	IntraH3
H3-1B-4	1,2	900 / 1575	760,0	18 / 31	64,0	NW-SE	1B	N	IntraH3
H3-1B-5	3,9	1270 / 2222	980,0	68 / 119	66,0	SE-NW	1B	S	H2
H3-1B-6	3,2	1200 / 2100	866,0	60 / 105	67,0	E-W	1B	N	H2
H3-2-1	2,0	600 /	1200,0	130 /		N-S	2	W	IntraH3
H3-2-2	2,7	838 /	1400,0	53 /		NEE-SWW	2	S	IntraH3
H3-2-3	2,7	906 /	1385,0	65 /		NEE-SWW	2	N	IntraH3
H3-2-4	1,7	540 /	930,0	44 /		NEE-SWW	2	N	IntraH3
H3-2-5	1,1	430 /	532,0	25 /		NEE-SWW	2	S	IntraH3
H3-2-6	1,1	290 /	901,0	35 /		N-S	2	W	H2
H3-2-7	0,5	227 /	680,0	10 /		N-S	2	W	IntraH3
H3-2B-1	6,3	970 /	1800,0	63 /		NEE-SWW	2B	N	H2
H3-2B-2	2,0	368 /	570,0	42 /		NEE-SWW	2B	S	IntraH3
H3-2B-3	1,8	580 /	680,0	34 /		NEE-SWW	2B	N	IntraH3
H3-2B-4	6,2	1180 /	1660,0	200 /		NEE-SWW	2B	N	H2
H3-3-1	2,6	512 /	1150,0	55		W-E	3	N	IntraH3

Table 4-3 Detailed overview of all faults truncating H2 and prior west of main fault 1.

4.3 Seismic evidence for fluid migration

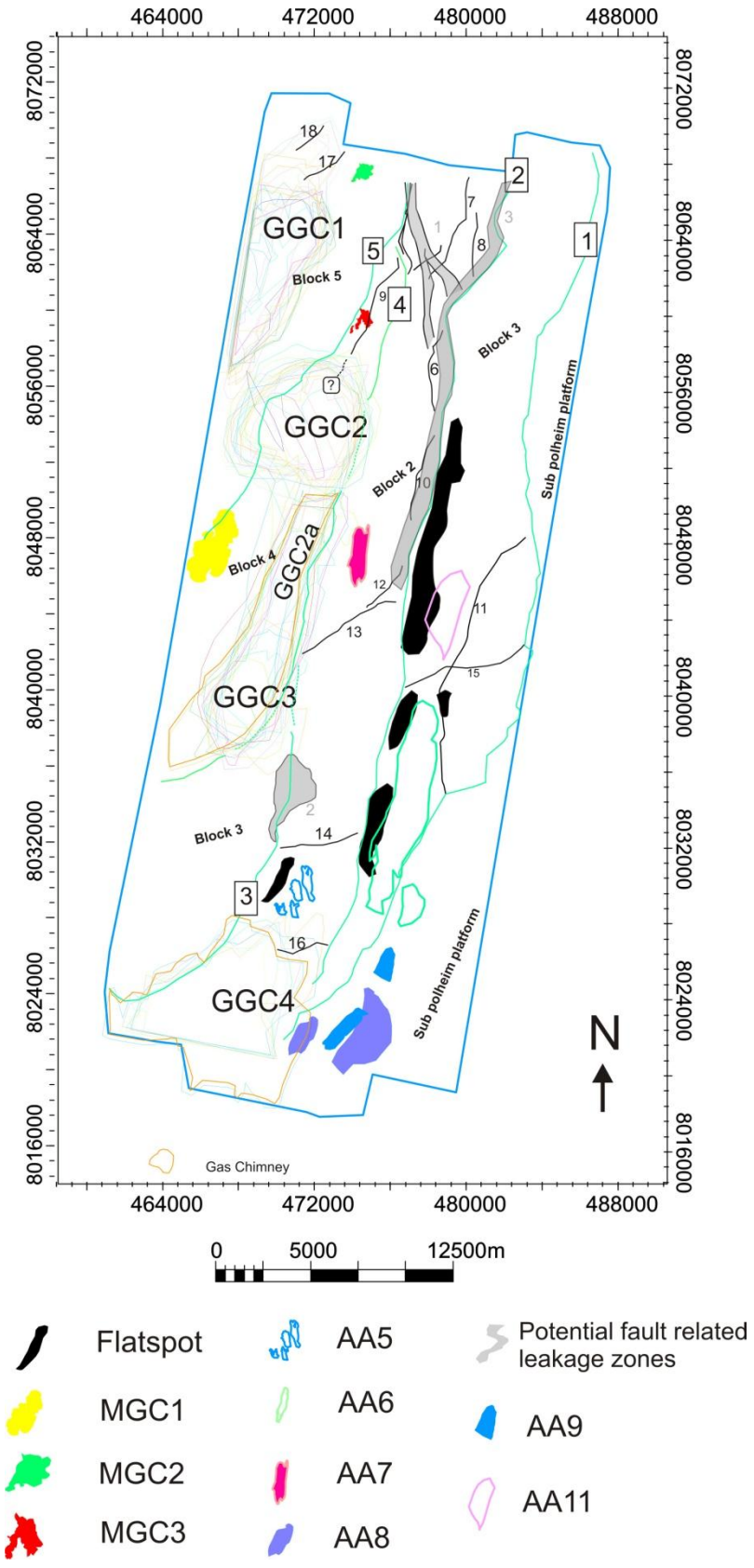

Areas with seismic masking occur with a large variety in shape, lateral and vertical extension and stratigraphic level in the study area as can be seen on figure 4.3.1. Characteristics for these features are among other high amplitude reflectors. Acoustic masking and amplitude anomalies are typical for fluid migration and there are clearly similarities observed which can be compared to what's been published before (Løseth et al 2009). In this chapter I will describe my observations concerning different fluid migration features observed in the dataset "West Loppa 2008" (Fig. 4.3.1).

Figure 4.3.1: Overview of the different fluid flow features I have observed in the area. Features occur at different stratigraphic depths and figure does not take that into consideration. Circles around chimneys represents the outer rim at different stratigraphic levels

4.3.1 Gas Chimneys:

In the thick western Cretaceous / Tertiary sedimentary basin there are observed large local zones of low, dim and chaotic reflectors. Top of the anomalies are characteristic as high amplitudes as a corona. Shapes vary from diffuse shadows, funnels and pipes to distinctive obelixes and cigars in a triangular or circular form (Fig. 4.3.1.1 and 4.3.1.2).

Typical push-down features are observed beneath and on the flanks of the features and detailed frequency analysis reveals lower frequencies within the features. The features are also correlated to be limited to one or more of the main faults.

Comparing these results with published articles there are clearly a close link to what Løseth et al., (2009) and Cartwrigth et al., (2007) interpreted and defines as Gas Chimneys. Based on the lateral extent of the gas chimneys (>15 km^2) I am observing I will refer the chimneys as "Giant Gas Chimney" (GGC) (Fig. 4.3.1.1).

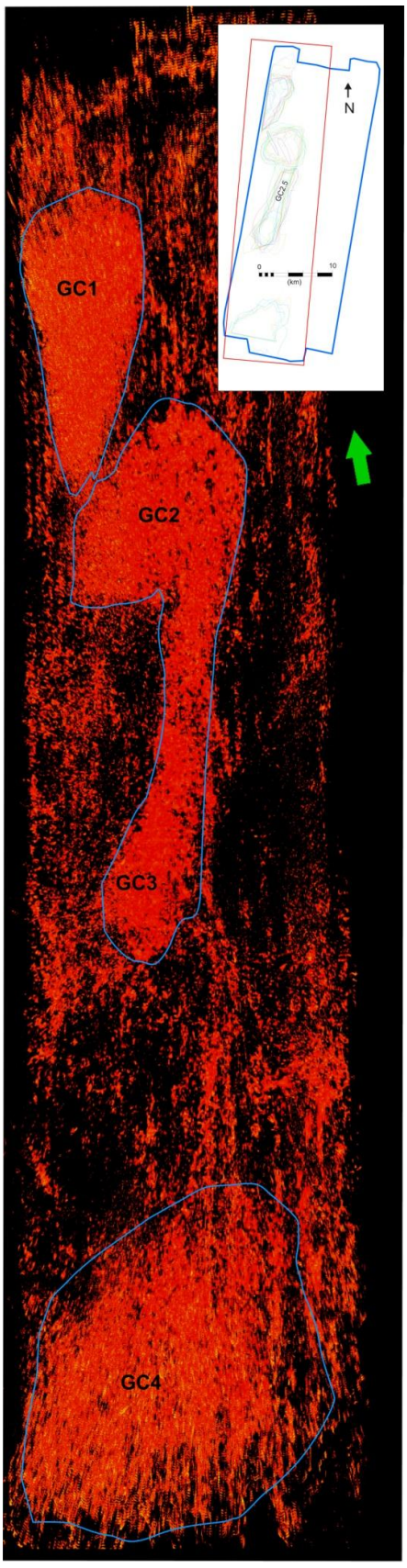

Figure 4.3.1.1: 3D map of a variance cube, displaying only the high values. Orientation is shown with arrow at top of figure. Blue lines mark the different Gas Chimneys

4.3.1.1 Giant Gas Chimney 1:

Giant Gas Chimney 1 (GGC1) is located in the north eastern corner of the dataset in block 5 (Fig. 4.3.1). Roughly 3/4 of GGC1 is covered in the dataset. A study of the 2D lines indicates that the chimney terminates outside the "West Loppa 2008" cube. The estimated extent of GGC 1 is as indicated on figure 4.3.1.2

Gas Chimney 1 has a triangular shape, the top in IntraH1 sediments have a negative polarity which is also the only possible reflector to follow within the gas chimney. Figure 4.3.1.2 displays the outcrop of GC1 in a cross section, where the blue transparent colour represent the whole feature. Red line indicates the area where the reflections are increased (corona), while yellow line determines where reflectors are dimmed. Inside of the chimney the reflection pattern is chaotic (Fig.4.3.1.2). H1 is still possible to be traced at some point indicated with green dashed line on figure 4.3.1.2. A push-down can clearly be identified in the reflections surrounding the gas chimney.

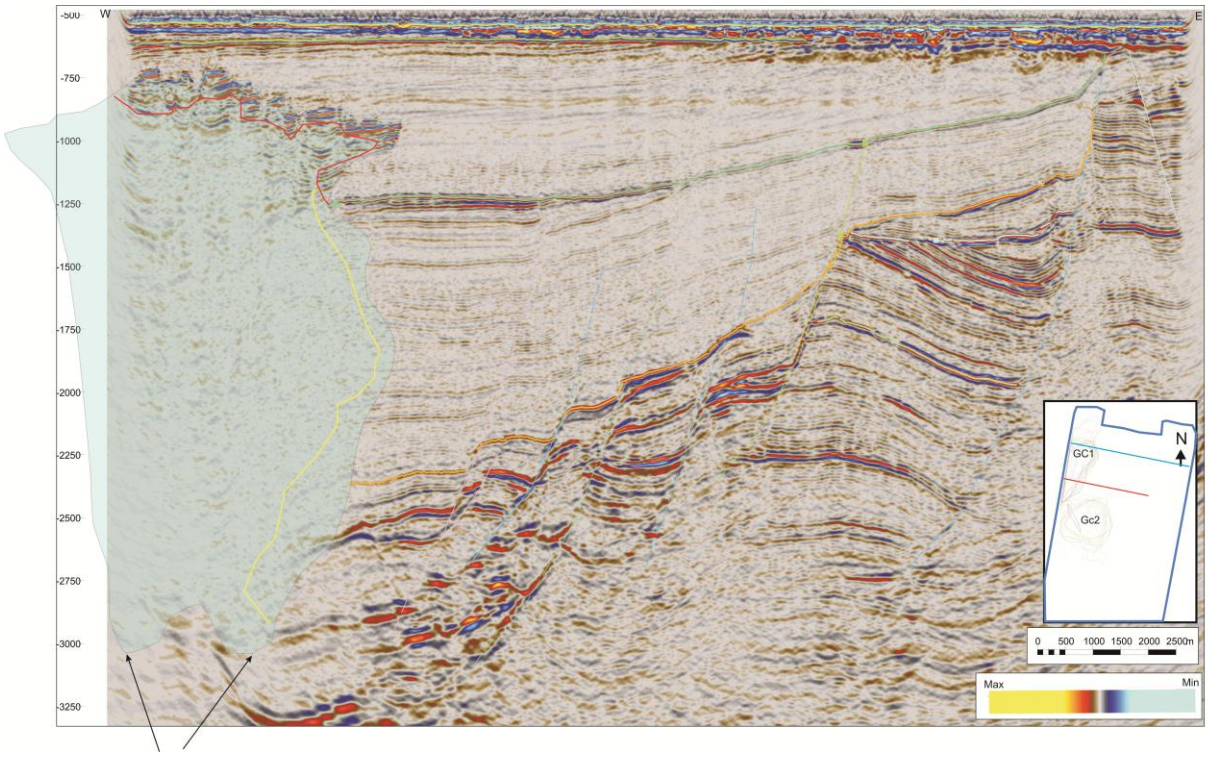

Figure 4.3.1.2: Cross section of GC1 where the structural setting is indicated. Arrows may indicate possible root zones, Blue line on overview figure shows the position of the seismic line. Red line indicates position of cross section in figure 4.3.1.5.

The horizontal extent of the chimney is gigantic! The length in a north south direction is 14.3 km while the x-axis in west north direction is 6.2 km. The volume calculations are based on a constant velocity of 2.2 km/s. From reference well sediments in the current area varies from 1.8 km/s to 3.2 km/s. More details of calculation metrics can be found in table 4.4.

The height of the chimney is measured to be 2625 ms, which is converted to 2887.5 m (Equation 14).

Due to the triangular shape of the chimney, the formula for a triangular object has been used for calculating areal and volume. The calculated areal of gas chimney 1 is 44 km^2 and volume is 128 km^3

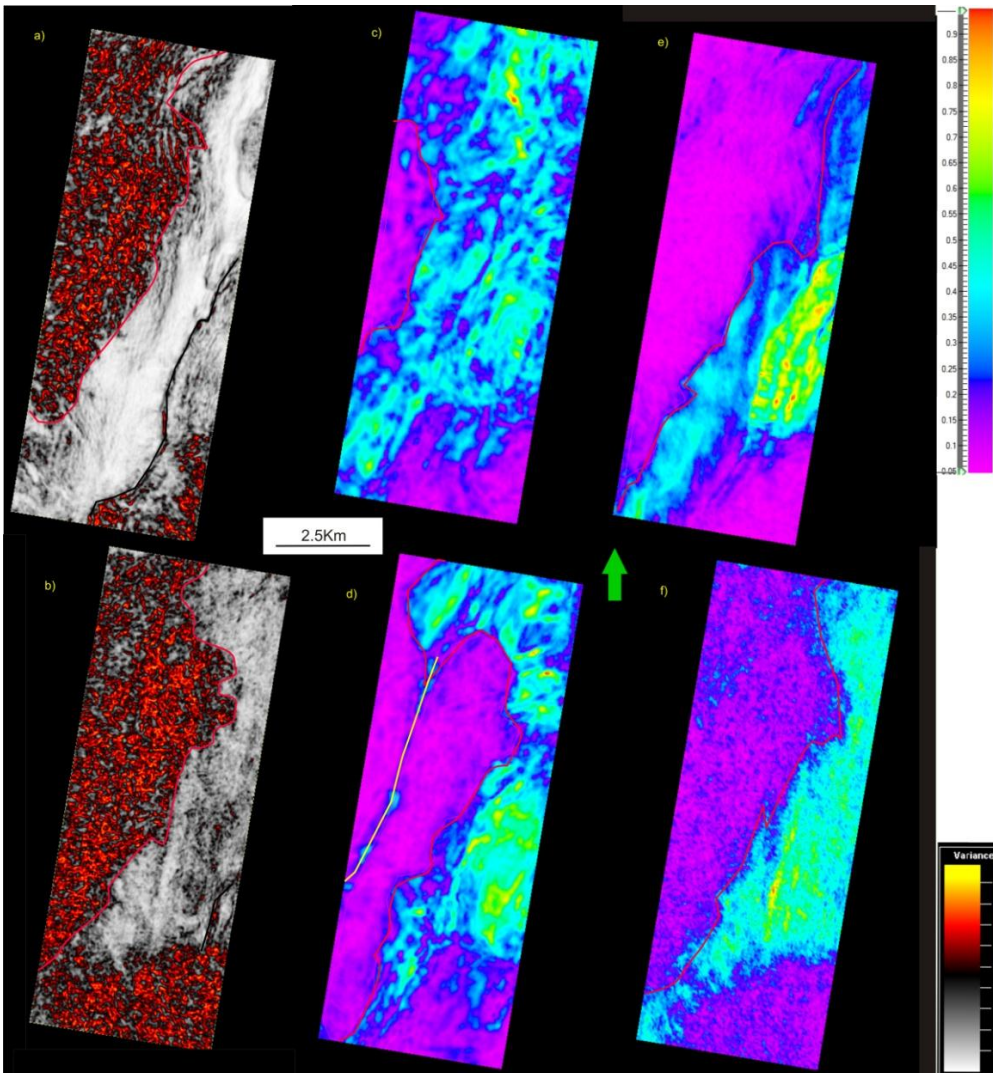

Figure 4.3.1.3: Seismic attribute maps of GC1. a) 2500ms TWT time slice of a variance cube, b) 2000ms TWT time slice of a variance cube. c)-f) are RMS attribute maps. c) Displaying all values of volume between 3600-3400ms TWT. d) 3200-3000ms TWT, e) 2800-2600ms TWT, f) 2200-2000ms TWT. Red line indicates the extent of GC1. Variance map reveals fault **5 which is marked with black line. Also a part of GC2 can be seen in the south-eastern corner. Location of map is seen on figure 4.3.1).**

Base of the chimney is referred to as the leakage zone root (Fig.4.3.1.2). Detailed studies performed applying RMS attributes maps reveals a possible fault plane in the base of gas chimney1, which is visualized on figure 4.3.1.3d of the 3200-3000 ms TWT RMS attribute map. RMS attribute map also reveals that the deepest part of the chimney is in the western part. The stratighraphic unit the base of gas chimney 1 are within are uncertain, but most likely IntraH3.

The highest visual feature observed related to the gas chimney is at 704 ms TWT or 685 m TVD. The top reflector consists of narrow elongated zones with deep depressions in between as seen on figure 4.3.1.4.

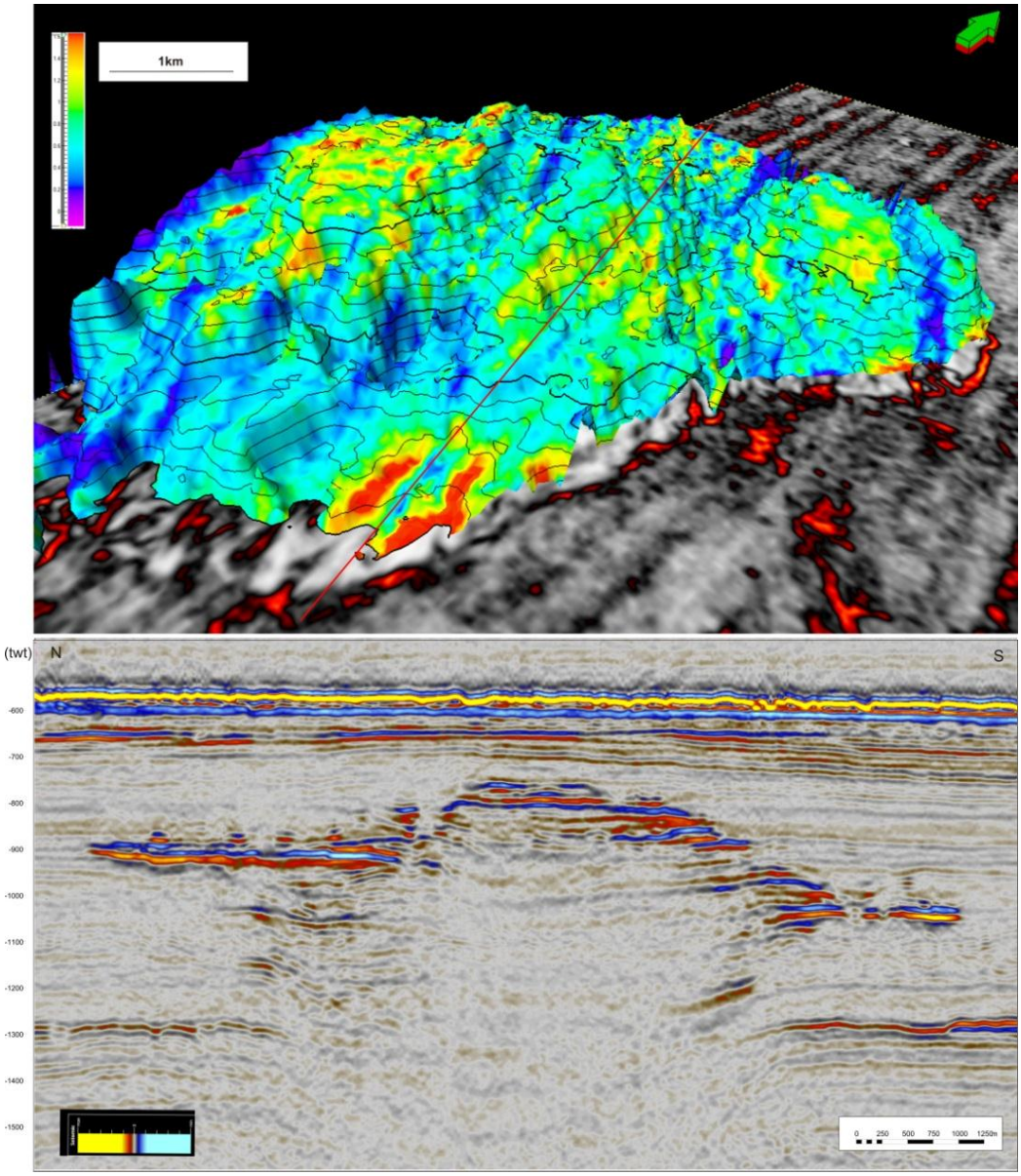

Figure 4.3.1.4: Gas chimney 1. a) 3D view displaying a RMS surface attribute following top of the gas chimney. RMS is preformed 20ms (+-10ms) of the interpreted top. Base map beneath is a time slice of a variance cube on 1000ms.Vertical exaggeration is 4x. b) Cross section of a random line through top of gas chimney 1. Position is indicated with black line on a).

Frequency analysis preformed, reveals decreased frequencies bellow the high amplitude in area and down into the chimney as seen in figure 4.3.1.5.

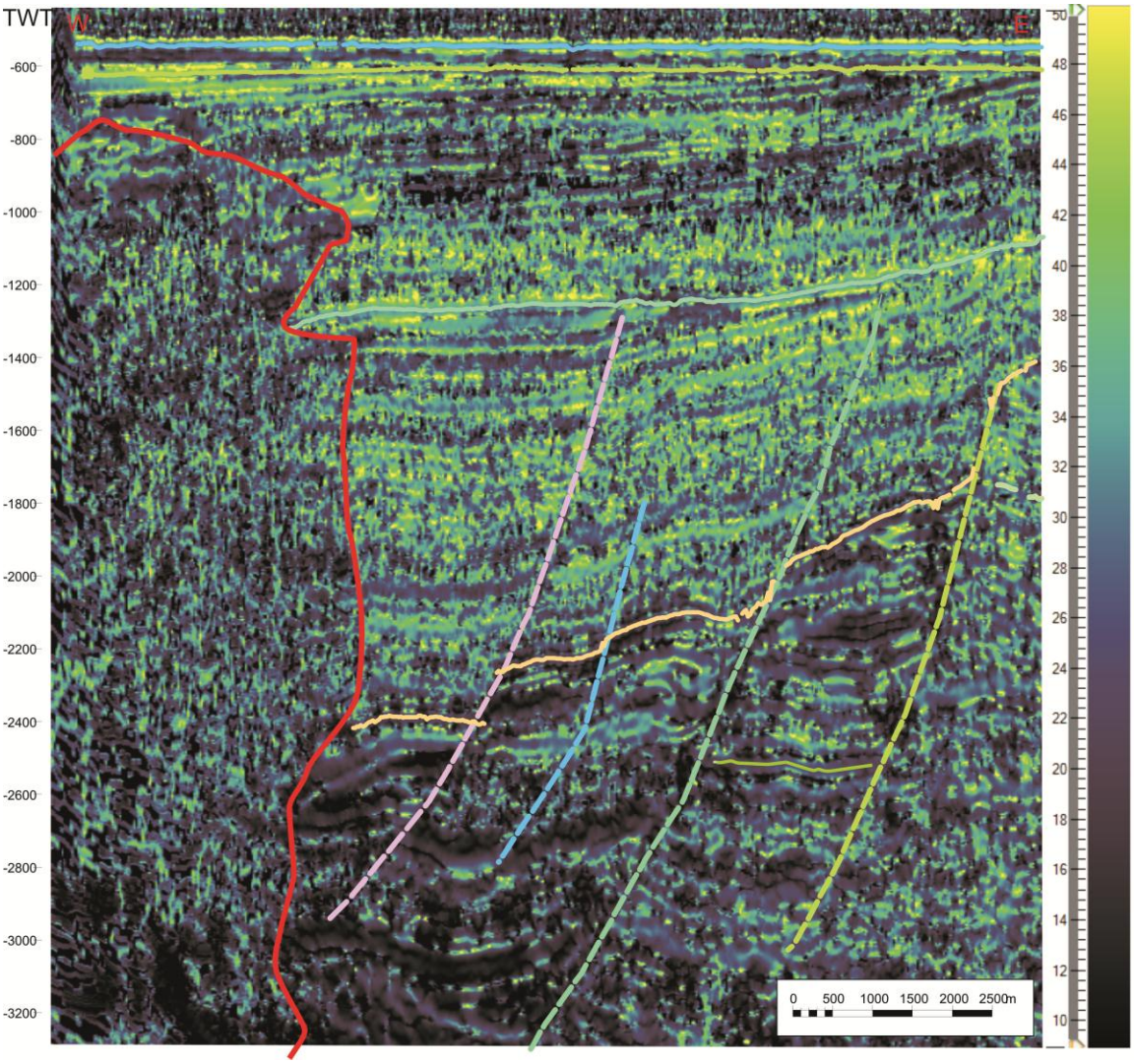

Figure 4.3.1.5 Seismic section of a dominant frequency cube indicating the decrease in frequency inside MGC1, which is indicated with a red line. Position of the seismic cross section is indicated on figure 4.3.1.2.

Gas chimney 1 is located close to several structural elements where the eastern flank of GC seems to follow fault 5. There are no clear indication of the chimney truncates a fault, still both the north and south limitations of gas chimney 1 is beyond the study area (seismic cube) and could terminate outside. Fault 17 and 18 is terminated north of chimney.

4.3.1.2 Giant Gas chimney 2:

GGC 2 is located south-east of GGC1 (Fig 4.3.1). It has a circular shape and terminates within IntraH1 at 564m to 585m below sea level. The water depth in the area is ~400m placing the anomaly ~170m beneath the seabed. The top anomalies show clearly a reflector with negative polarity (Fig. 4.3.1.6). Wipe-out zones beneath the strong corona on top and around the chimney occur in the IntraH1 sediments (Fig.4.3.1.6). The same type of frequency decrease can be seen within GGC 2 as described and visualized on figure 4.3.1.5.

The lateral extension of GGC 2 are separated and divided due to a transition a zone to GGC 3. There is a conduit transition zone between GGC2-and -3, where the anomalies truncate at a lower stratigraphic level (Fig.4.3.1.9). This transition zone will be further described in GGC2a. GGC 2 has a deeper apparent base zone than GGC1. The area of GGC 2 have been calculated by applying the formula for a circular body ($\pi * r^2$). The areal of GGC2 is 22.1 km^2 and the volume is ~73.6 km^3. The volume is based on an average p- wave velocity within the GGC 2 of 2200 m/s.

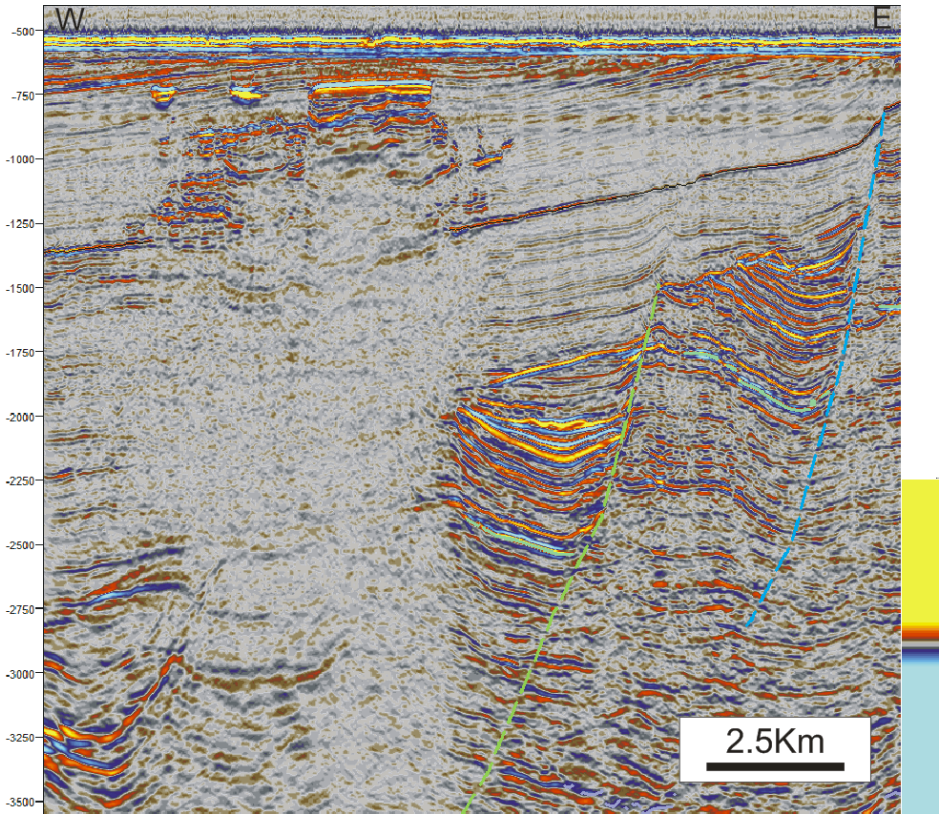

Figure 4.3.1.6: Vertical seismic section of Giant Gas Chimney 2, Structural elements indicated with dashed lines. Location is indicated with red line on overview figure on figure 4.3.1.7)

The base of GGC2 can be tracked on the variance maps down to 3800 ms (Fig.4.3.1.7) without encountering a specific stratigraphic root. There is a relative strong reflection with a long wavelength (114 ms TWT) at 3000 ms TWT (Fig.4.3.1.5).The same reflector is being dimmed in eastern part of the chimney which is similar to what has been observed in GGC 1.

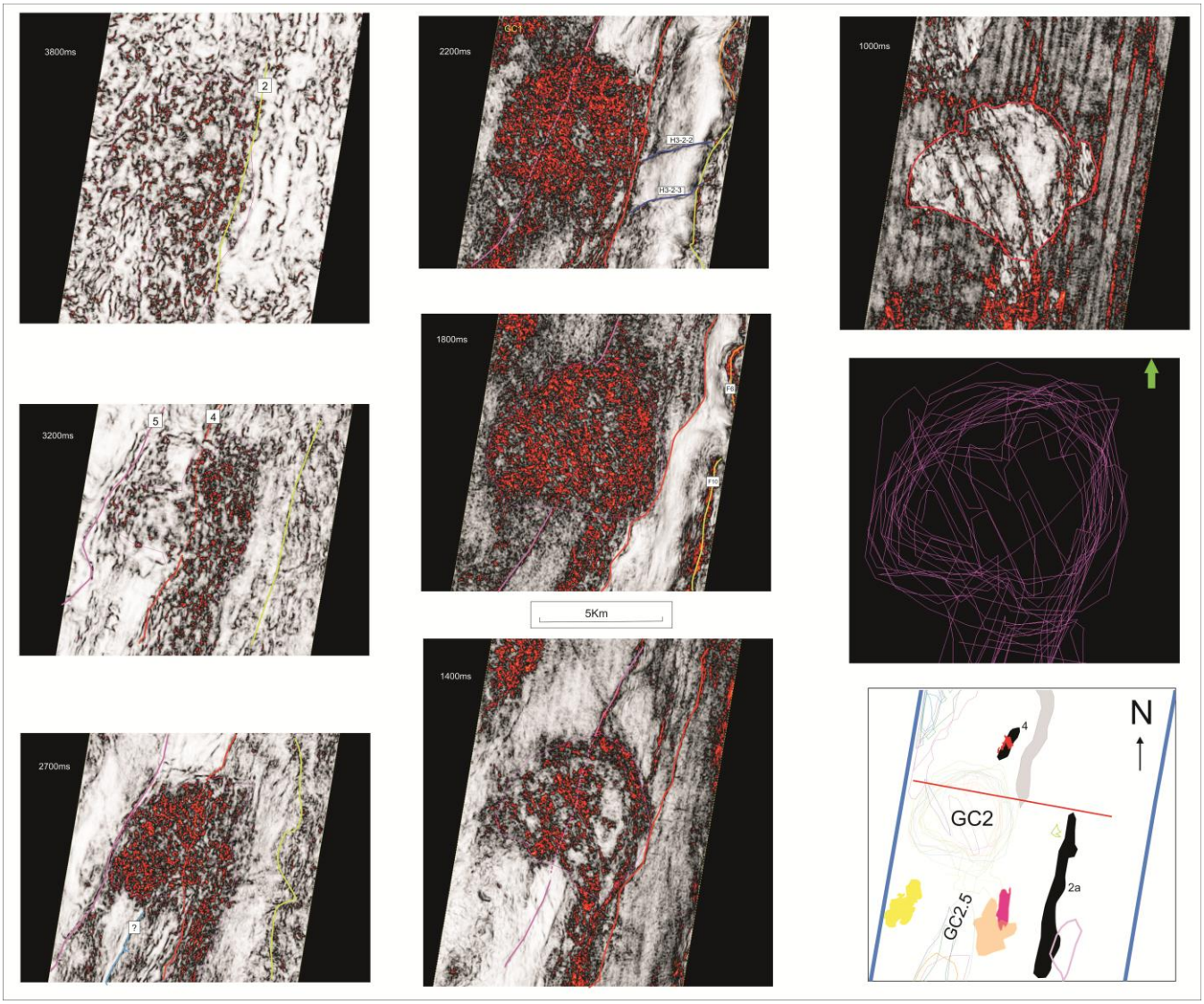

Figure 4.3.1.7: Variance maps visualizing the evolving GC2. Maps are labelled according to time in TWT. Polygon map indicates the lateral extent of GC2 and the basis for estimating volume. Faults indicated are referred to fault analysis in chapter 4.3.

The top reflector of GGC 2 has a very characteristic shape that resembles a cross cutting horizontal reflector (Fig.4.3.1.8). A zone of high reflection amplitudes are oriented in an elongated shape in a N-W trend (Fig. 4.3.1.8). They are separated from each other by zones of no reflections whit distinct boundaries similar to what's observed for GGC1 top. Figure 4.3.1.8 indicates that the top reflector dips westward, which represents the same dip direction as the main strata. The seafloor shows a slightly dip in the opposite direction of the top GGC1 anomaly (Fig. 4.3.1.8). Approximately 100 ms TWT beneath the top GGC 1 a second negative reflector are relative consistent and are dipping along the original strata (Fig.4.3.1.8).

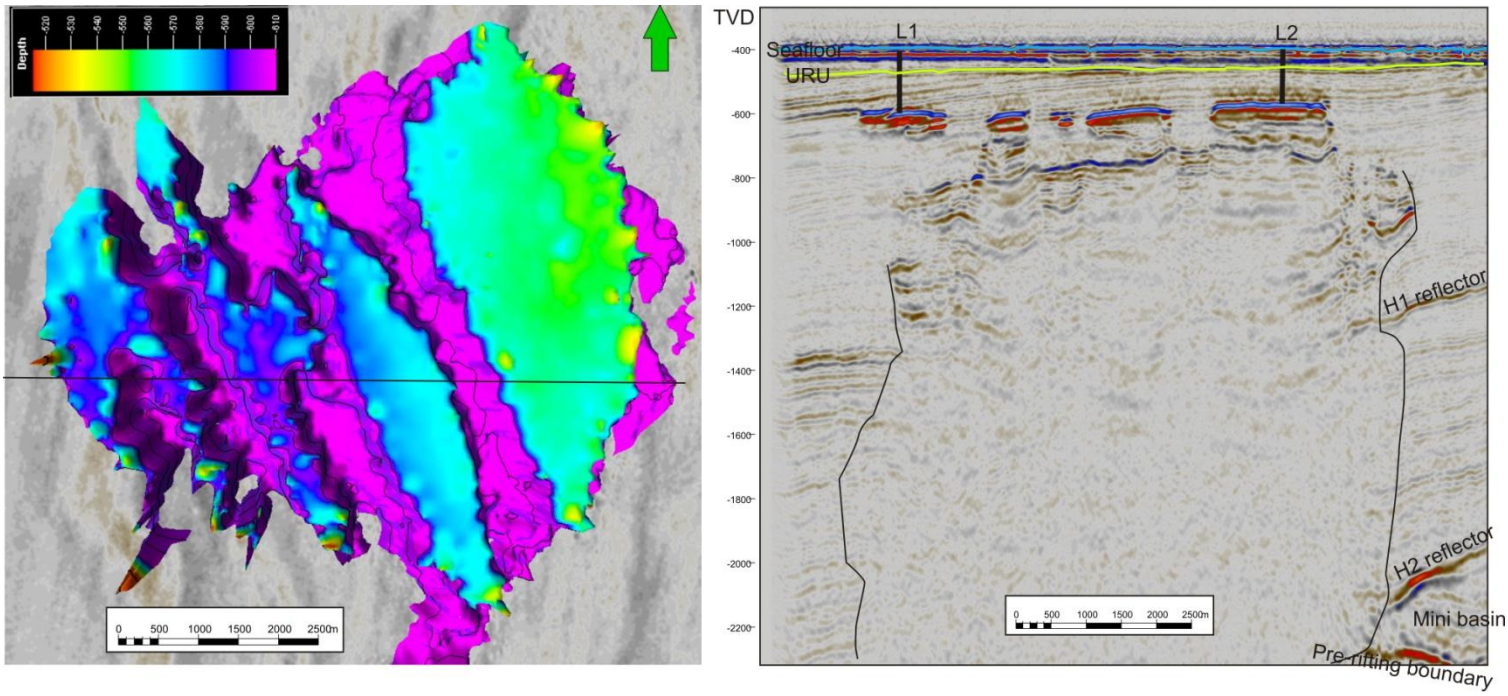

Figure 4.3.1.8: Left: Depth converted data where top of amplitude anomalies are tracked. Black line indicates location of right cross section. Right: Seismic cross section where the actual dip of the amplitude anomalies can be visualized. Also mark the reflection beneath is double dipping. The different sedimentary sequences are indicated with text.

GGC 2 is geographically located within the “Bear Island fault complex” west of Loppa High (Fig.2.3.3). Detailed structural analyses of the chimney reveals that fault 5 runs at the western flank of GGC 2 and truncates at H1 in the middle of GGC 2. Fault 9 terminates north of GGC 2, while an easterly dipping fault terminates south of the chimney. Fault 4 originate west of GCC 2 and evolves through the chimney and truncates at H1, i.e east of GCC 2. Fault 2 is limiting the eastern flank of GGC 2 and influencing the base level. GGC 2 is located in the categorized block 4 (Fig. 4.3.1).

4.3.1.3 Giant Gas Chimney 2a

GGC 2a truncates at the southern rim of GCG 2 and the northern rim of GGC 3. GGC 2a has an elongated body with a shape of a Christmas tree consistence of bright spots in the IntraH1 sediments (Fig 4.3.1.9). All reflections above H1 are of high amplitudes and truncates at top 814m TVD. There are several reflectors beneath GGC 2a that are not completely whipped out by acoustic masking. Dimmed and pushed-down reflectors are common (Fig.4.3.1.10).

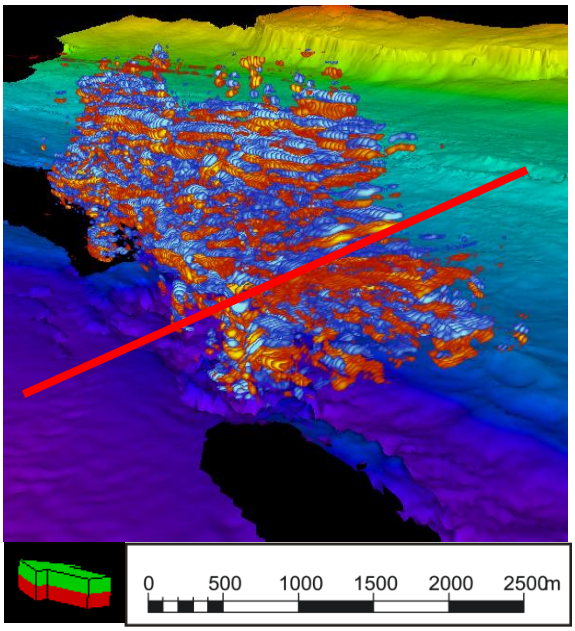

Figure 4.3.1.9 3D window of GC2.5 visualized by volume render function where only the strong reflectors are shown. Interpreted H1 is visualized and colours are based on TWT. Red line indicates roughly the location of seismic cross section in figure 4.3.1.10.

The lateral extension of chimney is 1.7 km wide and 8.4 km long which results in an area of 14.3 km^2 and volume is 47.1 km^3.

The top of GGC 2a differs from the other chimneys in the way of no clear reflector with a negative polarity is present. The base or root of the GGC 2a seems to start at the same stratigraphic level as GGC2 (Fig. 4.3.1.7). Fault 2 limits the eastern flank of GCC 2a and fault 4 limits the eastern flank from 2.2 s TWT up to H1. It is possible to study reflections beneath H1 in GGC 2a because the acoustic masking has not entirely whipped out all reflections though most of the reflections are dimmed. GGC 2a is located in the categorized block 4.

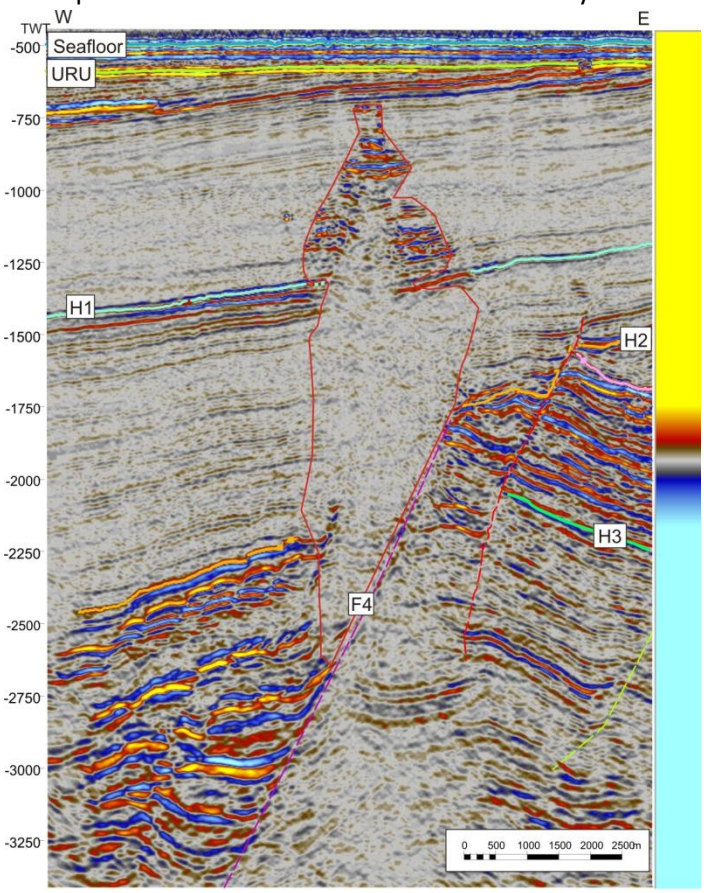

Figure 4.3.1.10 Cross section through GGC 2a which is indicated with red line, pink dashed line indicates fault 4.

4.3.1.4 Giant Gas Chimney 3:

GGC 3 is located south of GGC 2a in the "Bear Island fault complex" west of Loppa High (Fig. 4.3.1). GGC 3 consists of a top zone and a corona of high amplitudes draping the top section down to H1 (Fig.4.3.1.12). Push-down effects are identified within the chaotic zone. GGC 3 has a circular shape with a diameter of 4.5 km, which gives an area of 15.9 km^2. The height of the chimney is approx. 3454m TVD provided that the volume of GGC 3 is estimated to be 54.9 km^3.

Frequency analysis performed in the area provides the same result as seen on the previous chimneys and is visualized in figure 4.3.1.5. Detailed frequency analysis performed inside GGC 3 in the interval 1244 ms – 3280 ms TWT indicates a dominant frequency of 15-33Hz (Fig. 4.3.1.11).

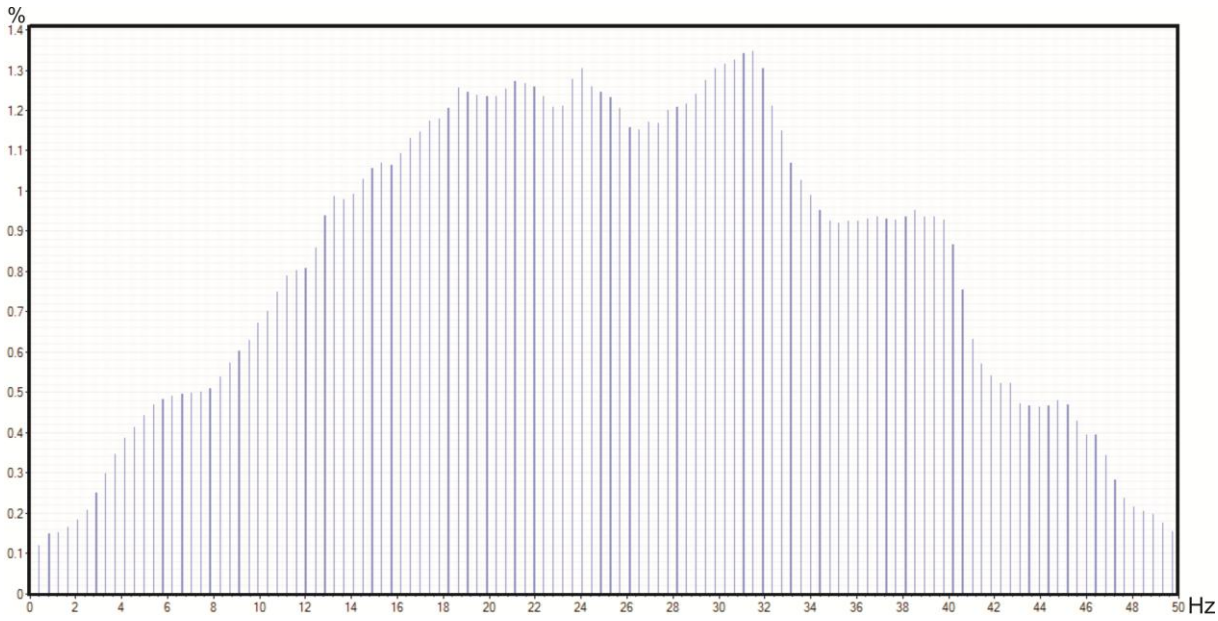

Figure 4.3.1.11 Frequency analyses done within the GGC 3 in the interval 1244-3280 ms TWT.

Geographically GGC 3 is located within the same structural elements as the already described chimneys in block 4 (Fig. 4.3.1). However, it seems that the chimney is limited by fault 4. Fault 4 turns into an E-W trend where GGC 3 terminates towards the south (Fig. 4.3.1.12).

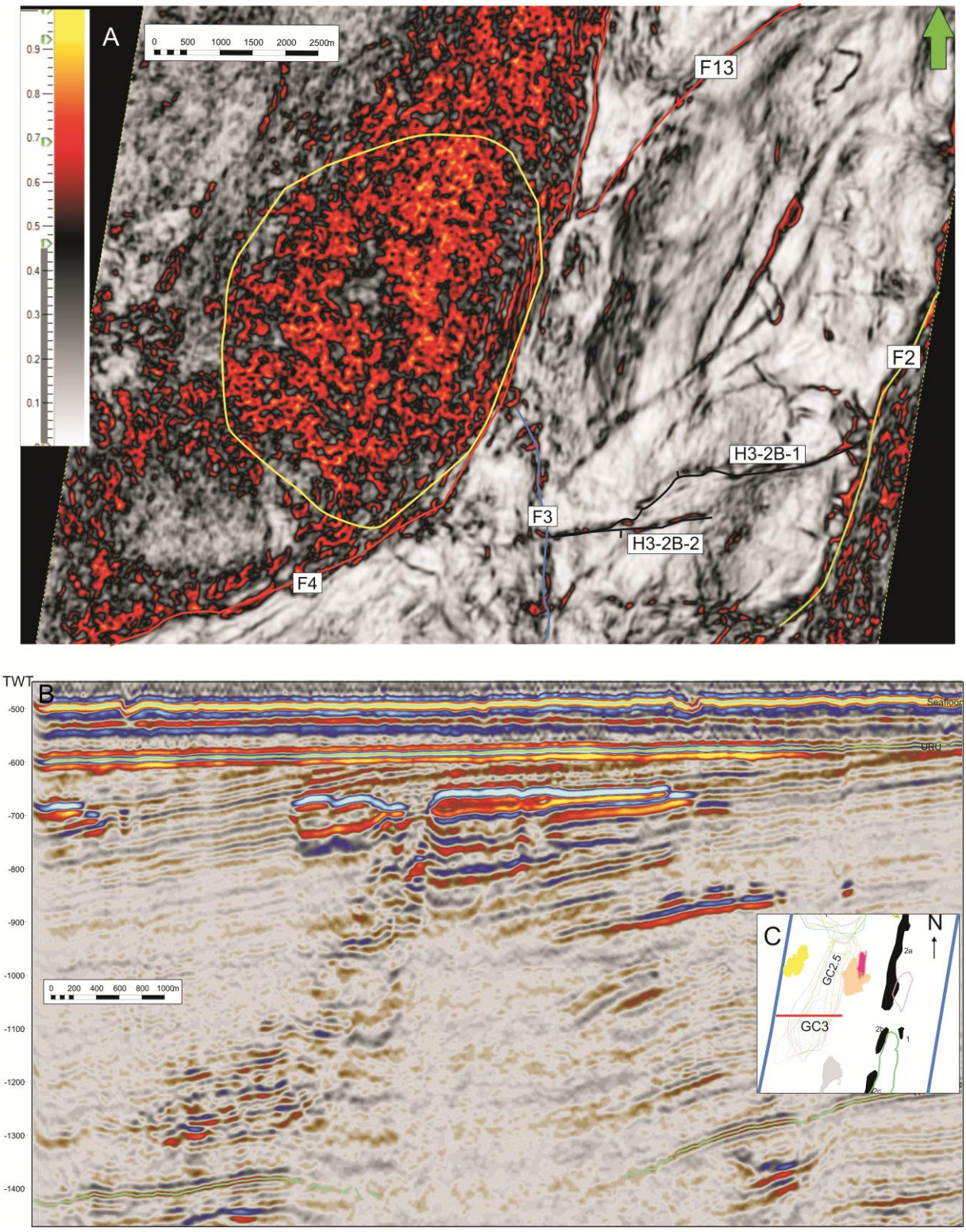

Figure 4.3.1.12: A) Variance map of gas chimney 3 at 1800ms TWT where giant gas chimney is in focus and outrimmed with yellow line. Structural features are labelled and referred to structural chapter 4.2. B) Seismic top section of mega gas chimney 3 visualize the intra H1 distribution of the seismic anomalies. C) Overview of the MGC 3 area where the seismic cross section is indicated with red line.

The top of GGC 3 consists of very strong reflections which has a negative polarity, phase reversal and cross cutting the original dipping pattern (Fig.4.3.12). This pattern forms the corona. There are a similarity between the observed amplitude tops seen in giant gas chimney 1, 2 and 3. Comparing the distance to seafloor, continuity, reflection strength and phase of signal the top GGC 3 reflector is interpret to be a bottom simulating reflector (BSR) (Chand et al., 2004; Horozal et al., 2009; Riedel et al., 2006).

4.3.1.5 Giant Gas Chimney 4

GGC 4 is located in the south-western part area of the seismic 3D cube “West Loppa 2008” and extends further south. 2D lines have been used to determine the outer rim of the chimney (Fig.4.3.1.13). The lateral extent of GGC 4 is based on variance attribute maps of different depth in time (Fig.4.3.1.14).

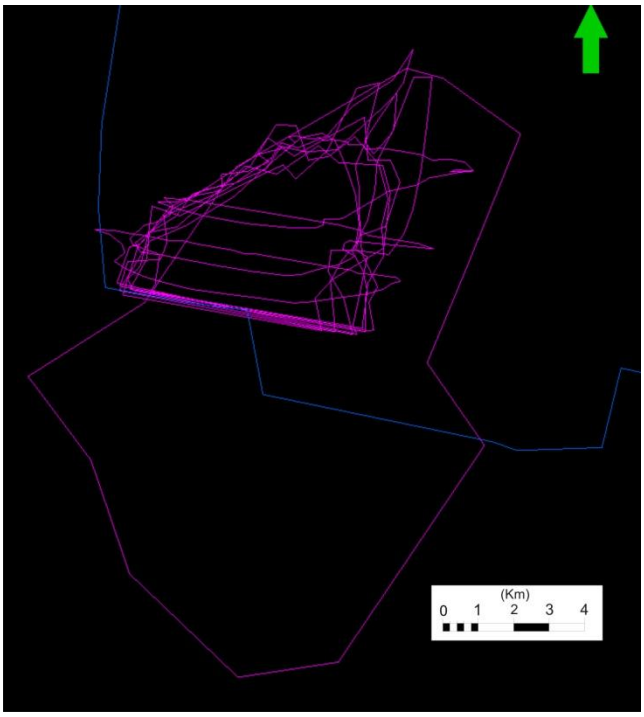

Figure 4.3.1.13: Giant Gas chimney 4 (pink lines) in map view where the lateral extension is indicated based on the 3D cube “west loppa 2008” (blue line). Single pink line indicates the low resolution of the GGC 4 of 2D lines.

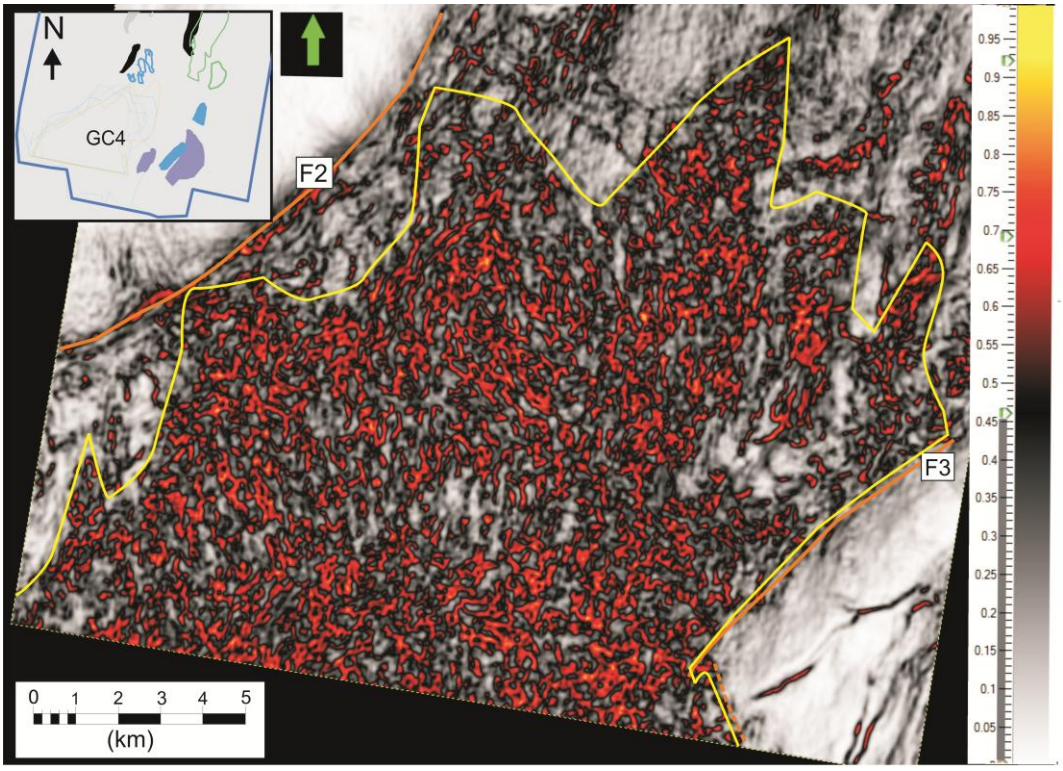

Figure 4.3.1.14 Variance attribute map at 1800ms TWT.

GGC 4 represents the largest acoustic masking zone observed in the study area. Laterally the GGC4 cover an area with a length of 17.4 km and width of 11.4 km. This provides an area of 99.2 km^2 considering a triangular shape. The base is undeterminable on the provided seismic (Fig 4.3.1.15). The outline of the chimney is still visual as low amplitudes at 4.2-4.4s TWT. The extent of GGC 4 is generally characterized by a low amplitude region (Fig. 4.3.1.16). H2 horizon is located at ~1100 ms TWT at GGC4 location. For the volume calculations a depth of 4000 ms TWT and velocity to 2400m/s (higher velocity used due to the stratigraphic depth, Tab.2.1) was used which resulted in a volume of 405.8 km^3. GGC 4 shows a top with high negative amplitude. The top has an elongated shape with narrow depressions in between (Fig 4.3.1.17 and -18). The GGC4 top is located relative flat according to seabed with a slightly down dip in the distral parts (Fig.4.3.1.17). The strata are dipping towards south-west. Large push-down effects are observed (Fig. 4.3.4.5). A strong positive reflector are dipping south-eastwards on the western flank of GGC 4 from ~700 ms to ~850 ms TWT (Fig. 4.3.1.17).

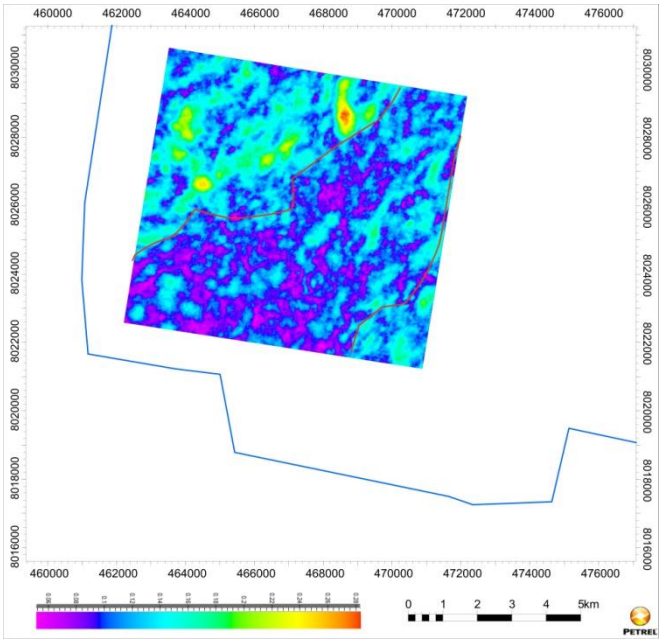

Figure 4.3.1.15: RMS attribute map of volume between 4400ms and 4200ms TWT in area of interest regarding GC4. Red line indicates the outrim of GC4.

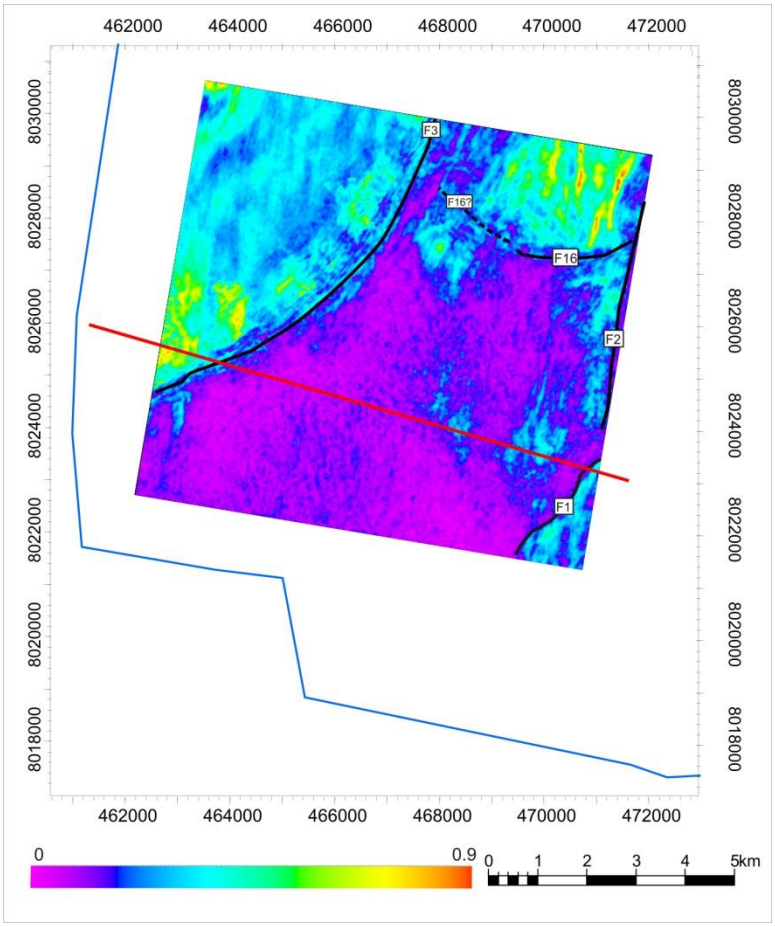

Figure 4.3.1.16: RMS attribute map of volume between 1700ms and 1500ms TWT in area of interest regarding GC4. Low amplitudes indicate the lateral extent of chimney while the black lines indicate faults which is labelled according to specific name.

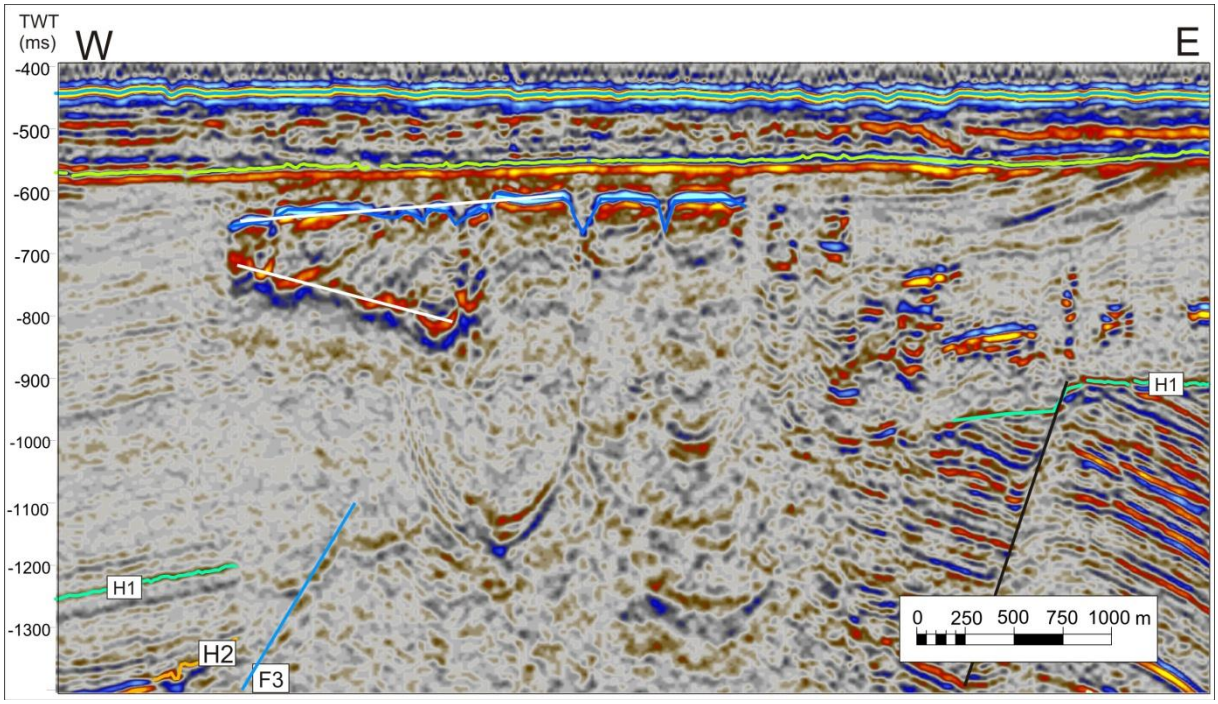

Figure 4.3.1.17 Seismic cross section through GGC 4, where location is indicated on figure 4.3.1.16, Note the dipping positive dipping reflector on the western flank of the top chimney.

The geographical location of GGC 4 is at the southern flank of "Bjørnøya trough". The water depth is about 325m, which is 75m shallower than for GGC 1. The structural setting indicates the location of GCC 4 to be located above block 2c in the Bear Island fault complex (Fig. 4.3.1). GCC 4 seems to be limited to the faultblock 2c limited by fault 3 as indicated on figure 4.3.1.16. Fault 3 seems to follow the western flank of GGC 4. Eastern flank follows fault 1- and 2 (Fig 4.3.1.16). Fault 16 can be seen just north of GC4 (Fig 4.3.1.16).

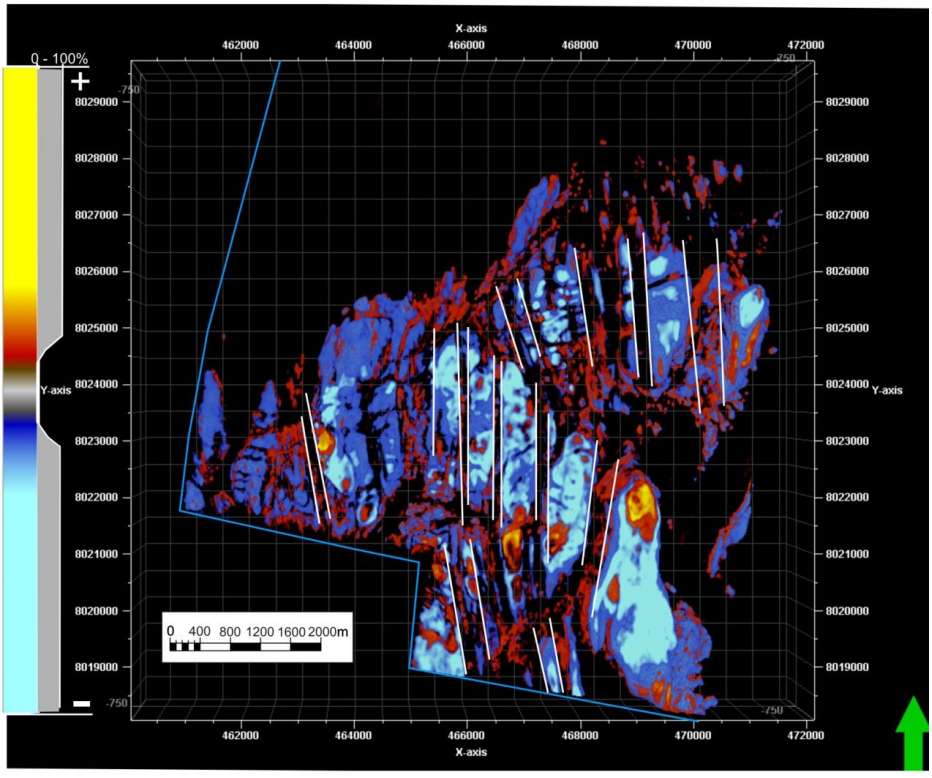

The top depressions are oriented in an N-S trend with an average width of ~300m (Fig.4.3.1.18).

Figure 4.3.1.18 Seismic cube extracted over a cropped volume of 500-700ms TWT around GGC 4 with volume render only displaying high amplitudes.

4.3.1.6 Summary GGC

								Depth converted data (m)	
h (TWT) / (m)	**l (km)**	**w (km)**	**No.**	**Shape**	**Area (km^2)/volume (km^3)**	**Top (ms TWT)**	**Base (ms TWT)**	**Top**	**sf (m)**
2625/2887.5	11,30	6,20	GGC1	Triangular	35,3 / 101	704,00	3600-3200	589	408
3080 / 3388	5,30	5,30	GGC2	Circular	22,05 / 73,61	738-709	3800	575	405
2996 / 3295	8,40	1,70	GGC2a	Elongated tube	14,28 / 47,05	804,00	3800	814	375
3140 / 3454	4,50	4,50	GGC3	Circular	15,89 / 54,9	660,00	3800	534	365
3410 / 4092	17,40	11,40	GGC4	Triangular	99,18 / 405,84	610,00	4000	491	325

Table 4-4 Summarized details for the different GGC.

4.3.2 Medium Size Gas Chimneys (MGC)

There are several medium size (~1 km^2) gas chimney structures identified in the study area (Fig.4.3.1). They are defined by their lateral (<10 km^2) and vertical extent (<1000 ms TWT).

4.3.2.1 MGC 1

MGC 1 is located south of GGC (Fig 4.3.1) and occurs within the IntraH1 sediments at 1100 ms TWT. Only a small portion of the anomaly can be followed up to 1010 ms TWT as an oblique conduit. Push-down of 7 ms is observed on the underlying H1 reflector. MGC 1 consists mainly of high amplitudes above H1. Beneath H1, one observes only dimmed and pushed down reflectors and the strata are still preserved. The dimmed and pushed down reflectors can be traced down to 1756 ms TWT (Fig.4.3.2.1). Based on depth converted data we assume an average sediment velocity of 2.47 km/s. The estimated height of the chimney is therefore 811 m.

MGC 1 is 4 km long and 1.5 km wide (Fig.4.3.2.1) and shows a rectangular shape. The total ara is 6 km^2, and the volume is calculated to be 4,87 km^3

MGC 1 is located in the Bear Island fault complex and the listric asymetrical fault 5 crosses straight beneath it. The northern part of MGC 1 is located above block 5 and the southern part are above block 4 (Fig. 4.3.1).

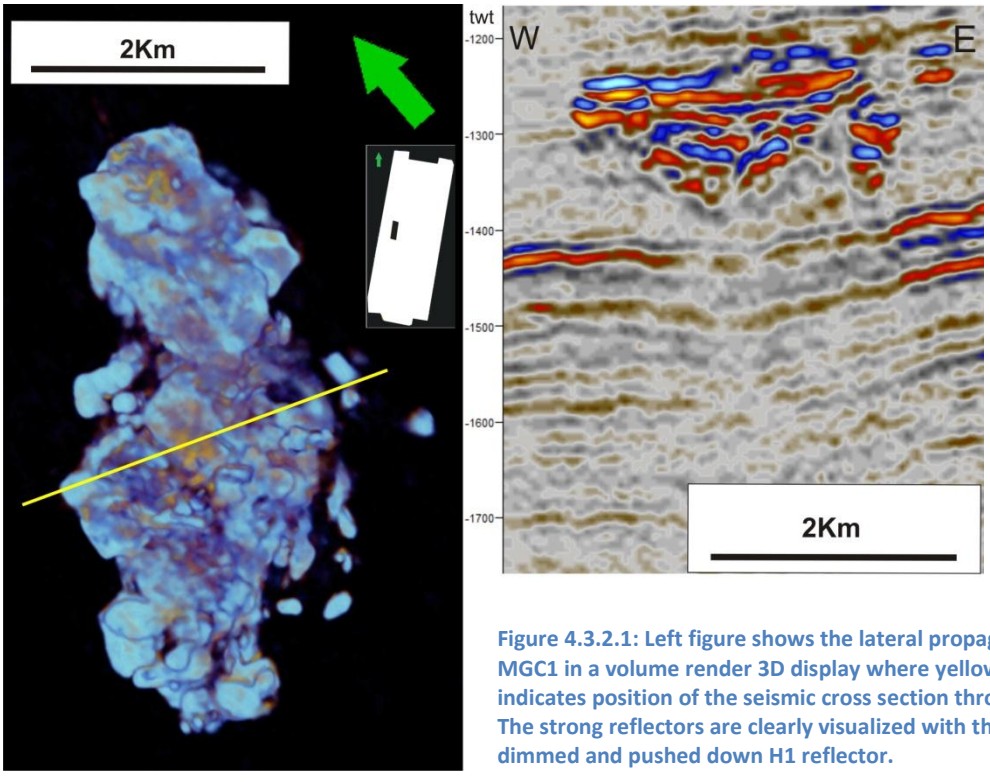

Figure 4.3.2.1: Left figure shows the lateral propagation of MGC1 in a volume render 3D display where yellow line indicates position of the seismic cross section through MGC1. The strong reflectors are clearly visualized with the underlying dimmed and pushed down H1 reflector.

4.3.2.2 MGC 2

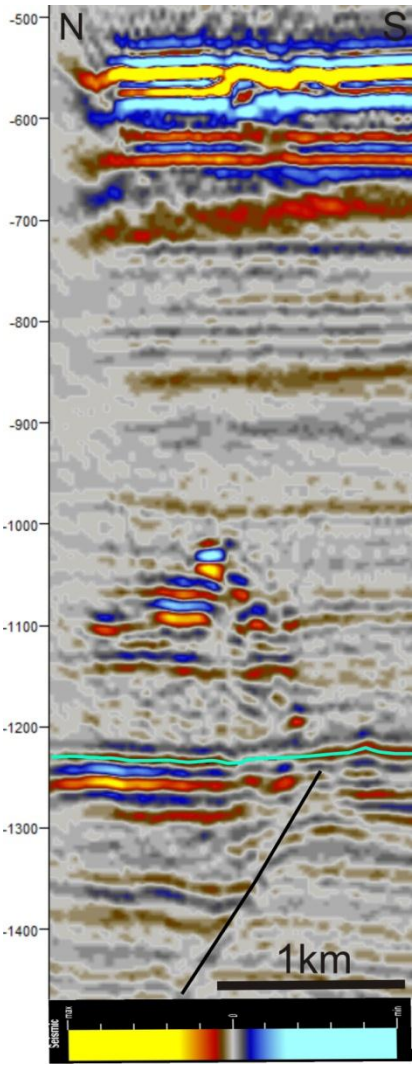

MGC 2 is located in the north western part of the 3D seismic cube "West Loppa 2008" (Fig. 4.3.1). It occurs as a cluster of bright spot with a negative polarity top reflector and disturbs the strata within the IntraH1 sediments (Fig.4.3.2.2). The top of MGC 2 is seen at 1020 ms TWT and the base at ~1230 ms TWT (Fig.4.3.2.2). The H1 reflector shows a push-down effect.

MGC 2 is located above fault block 5 and there seems to be an oblique fault truncating H1 just beneath it (Fig. 4.3.2.2), which may be fault 17.

Figure 4.3.2.2: MGC 2 on a seismic cross section from N-S.

4.3.2.3 MGC 3

MGC 3 is a small narrow chimney rising up from H1 east of the GGC 1 (Fig. 4.3.1). It occurs as a bright spots within IntraH1 sediments. Push-down effects are observed on H1. MGC 3 is 900m long and 800m wide and has a height of ~ 80m. The resulting area is 0.4 km^2 and the volume 0.04 km^3. Fault 5 is crossing H1 just beneath MGC 3 (Fig.4.3.1).

4.3.3 Potential fault related leakage zones (PLZ)

Leakage zones are separated from GGC and MGC's because of the narrow and "near vertical" continuity of the acoustic anomaly. It is observed not directly as an object, but as an array of bright- and dim spots.

4.3.3.1 PLZ 1

PLZ 1 is located in the northern part of the seismic 3D cube "West Loppa 2008" (Fig.4.3.1). It is observed within the Intra-H2 and H1 sediments and occurs as a narrow vertical conduit which can be laterally traced 7 km towards the south. The anomaly is traced on a RMS amplitude map. The amplitude strength of H1 is enhanced (Fig. 4.3.3.1) and a negative polarity reflection is observed. The anomaly seems to occur in the transition zone between fault 4 and 5, and follows fault plane 4 southwards (Fig.4.3.3.2). Figure 4.4.2 indicates a division of the anomaly. The dimmed zone can occasionally be followed to the base of the URU horizon. The potentially leakage zone 1 is situated above the structural fault blocks 2a-3 and can be related to fault 4 and 5. The anomaly occurs between 935 ms TWT and H2 (Fig.4.3.3.1).

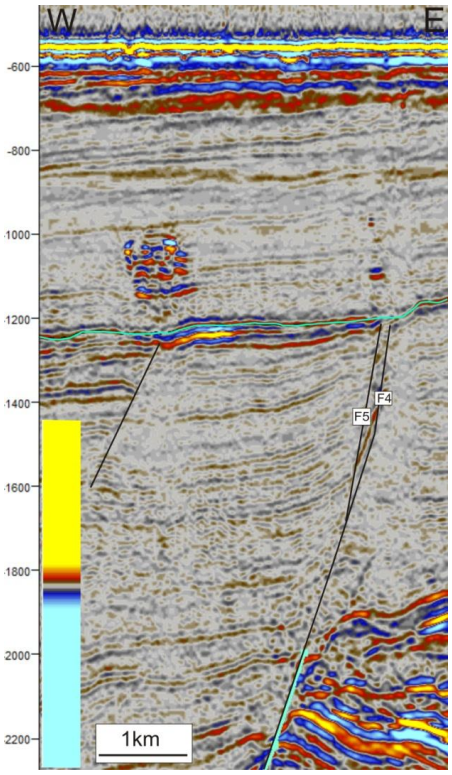

Figure 4.3.3.1: Seismic cross section of PLZ 1. Chimney in left of figure is MGC 6 which is located above F17.

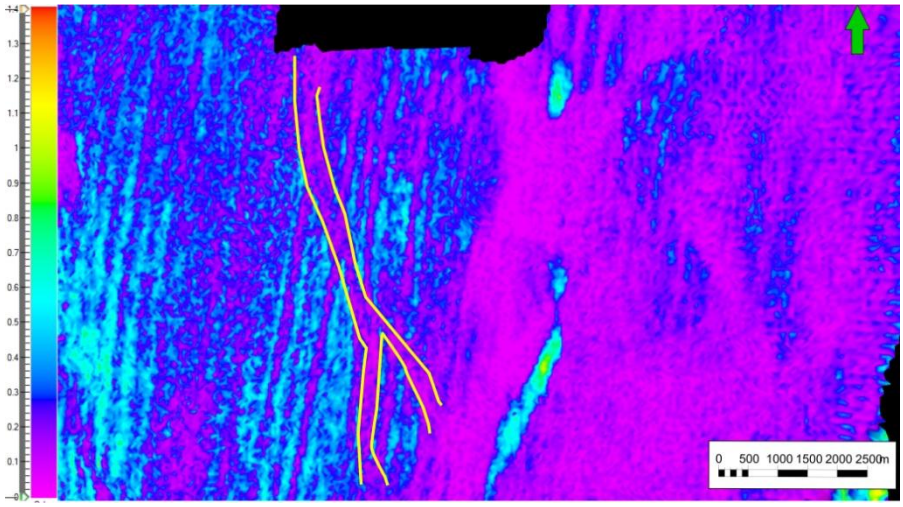

Figure 4.3.3.2 RMS amplitude map including amplitudes between 1150ms – 1250ms TWT. PLZ 1 are indicated with yellow lines.

4.3.3.2 PLZ 2:

PLZ 2 is located north of the giant gas chimney 4 (Fig. 4.3.1). It is observed within south-westerly dipping IntraH1- and H2 sediments and shows a rose shape as a cluster of bright spots. Push-down effects are observed on H1 as well as dimmed reflectors. The acoustic masking of seismic traces can be followed down the into IntraH3 sediments. PLZ 2 are laterally, at the most 1 km wide, can b traced up to 5 km in length. It terminates within GGC3 in the north and it seems to be limited by fault 14 in the south (Fig.4.3.3.3). Fault H3-2B-4 occurs where the amplitude intensity of the zone is distinctly increasing. The top seismic anomaly is located at 860 ms TWT and the base is the erosive surface H2 (Fig.4.3.3.3).

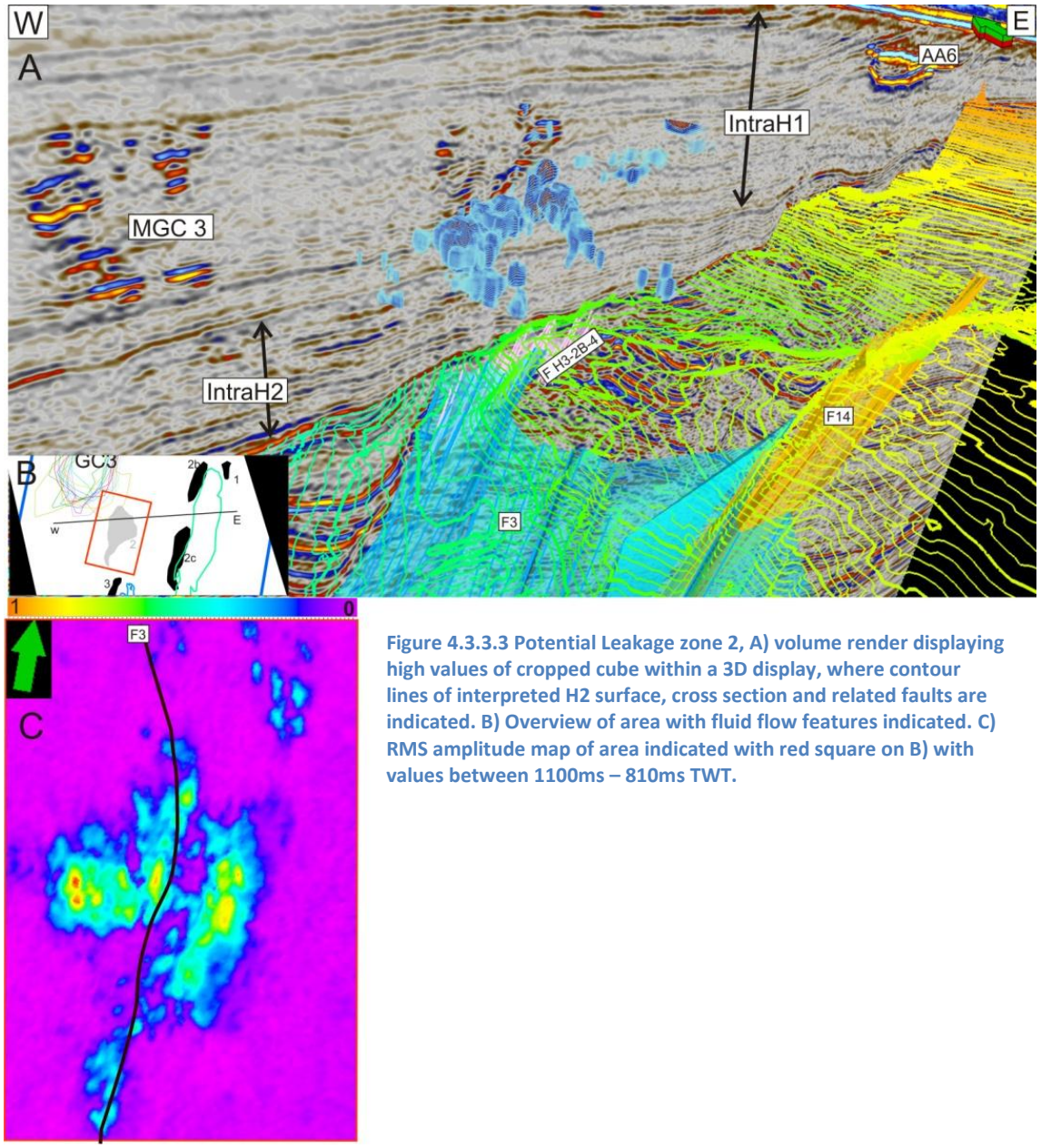

Figure 4.3.3.3 Potential Leakage zone 2, A) volume render displaying high values of cropped cube within a 3D display, where contour lines of interpreted H2 surface, cross section and related faults are indicated. B) Overview of area with fluid flow features indicated. C) RMS amplitude map of area indicated with red square on B) with values between 1100ms – 810ms TWT.

4.3.3.3 PLZ 3

PLZ 3 is located above fault 2 (Fig. 4.3.3.4) from fault 12-13 in the south and exceeds further north than provided seismic (>27 km) and has an average width of 0.82 km. The strata shows a dip towards west. PLZ 3 appears as a dim spot on the H1 reflector (Fig. 4.3.3.4).

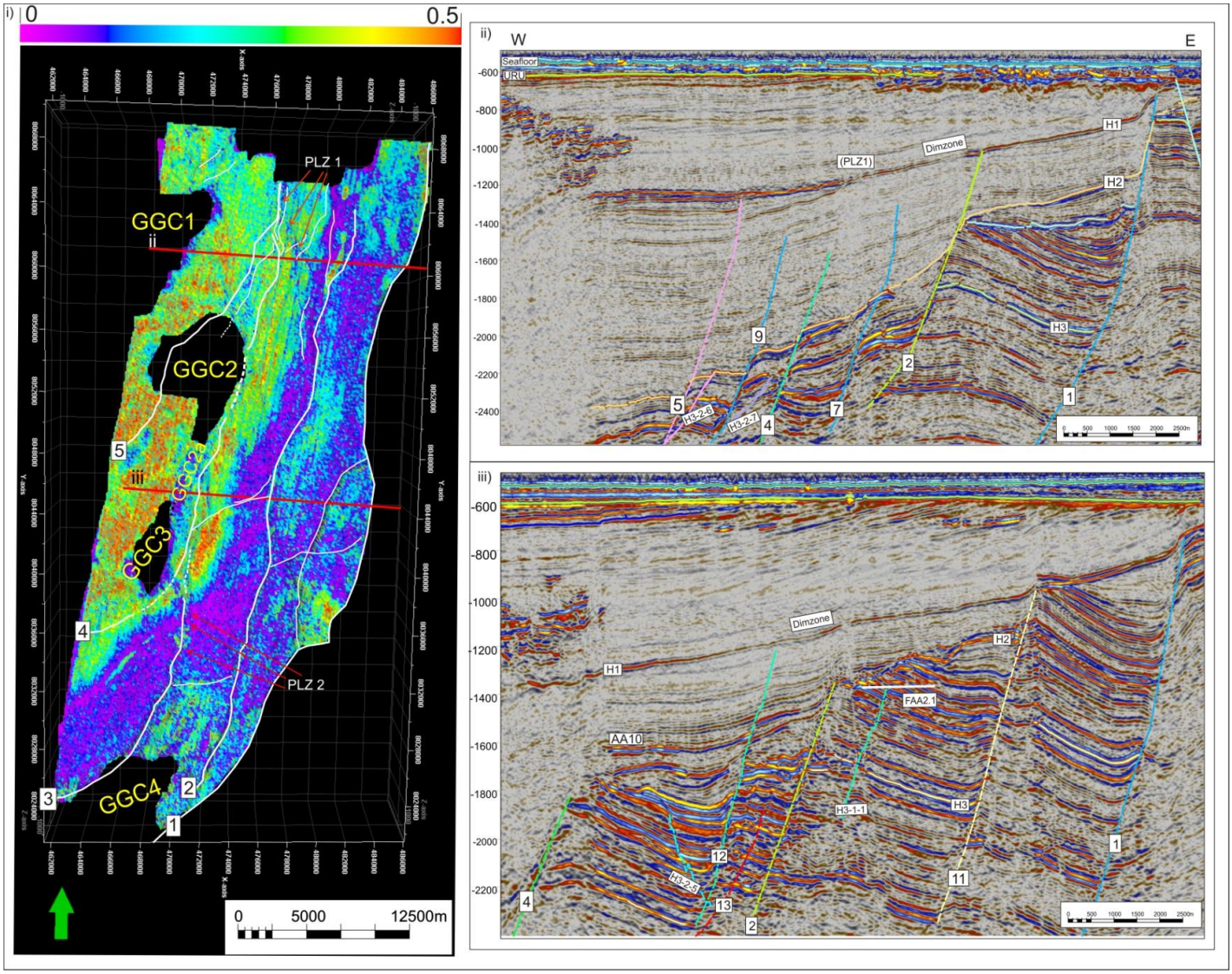

Figure 4.3.3.4 RMS amplitude map of the interpreted depositional surface H1 with an offset of +-10ms. PLZ 1 and 2 area are indicated on figure. Ii) seismic cross section, iii) seismic cross section.

								Depth converted data (m)	
h (TWT) / (m)	**l (km)**	**w (km)**	**No.**	**Shape**	**Area/volume**	**Top (TWT)**	**Base (TWT)**	**Top**	**Base**
656 / 811	4	1,5	MGC1	Rectangular	6 / 4,87	1100	1756	1089	1900
134 / 145	0,9	0,7	MGC2	Rectangular	0,63 / 0,09	1020	1230	933	1078
101 / 80	0,9	0,8	MGC3	Triangular	0,36 / 0,04	1096	1197	1047	1127
1065 / 1100	8,40	0,50	PLZ 1	Elongated tube	4,2 / 0,4,82	935	2000	1167	2314
1065 / 166	4,70	0,90	PLZ 2	Pear	4,23 / 0,702	860	1346	1147	1313
/ 505	27,00	0,82	PLZ 3	Elongated tube	22,14 / 11,18	850	1420	1025,00	1530,00

Table 4-5 Summarized details for the MGC's and PLZ's

4.3.4 Amplitude anomalies

Amplitude anomalies are sub-divided into its own group, which differ from chimneys or potential fault related leakage zone due to a single or bundle of single reflectors.

Amplitude anomaly starts at 5, due to top GGC1-4 are originally numbered as AA1-4.

4.3.4.1 Amplitude anomaly (AA) 5

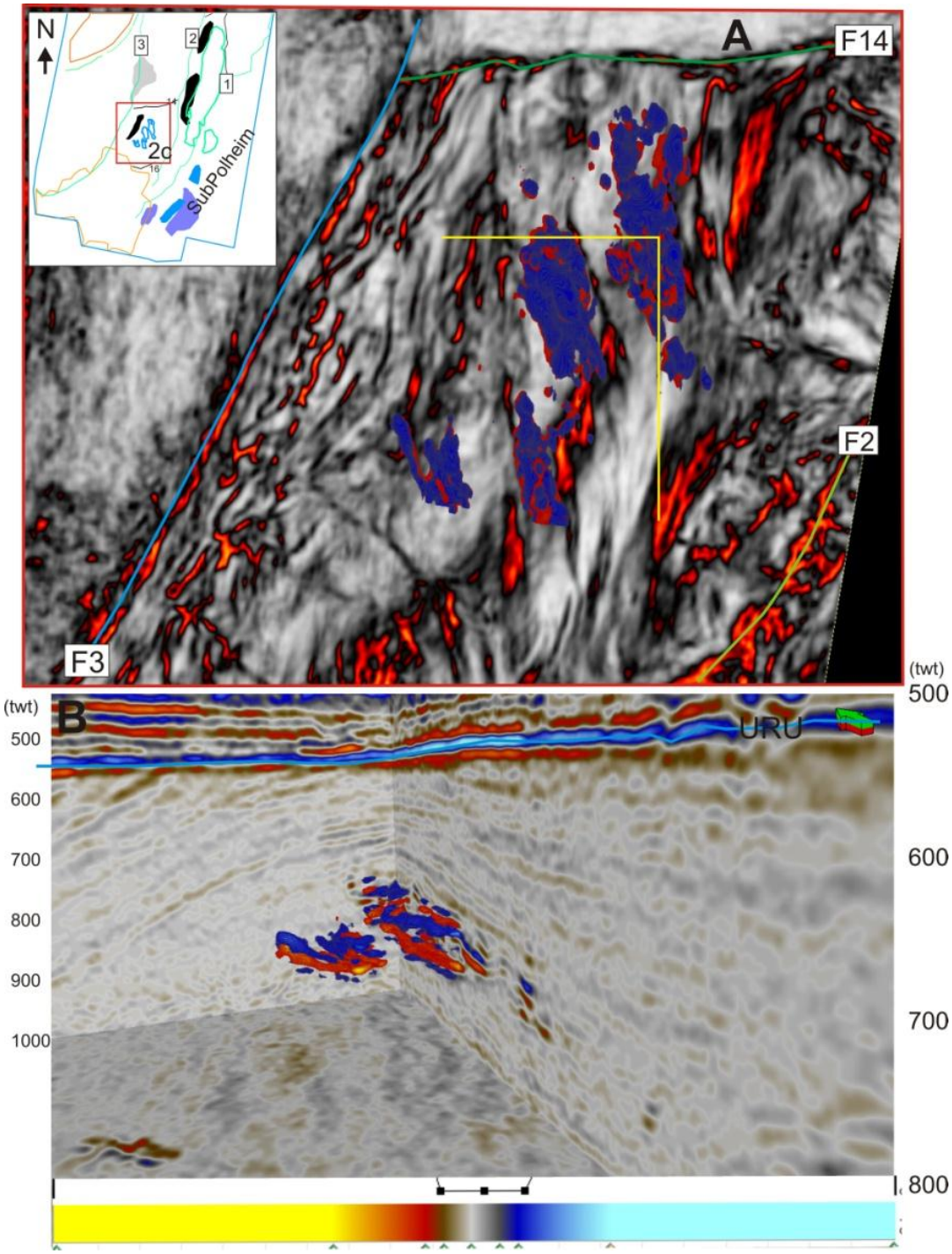

Figure 4.3.4.1 A) Variance timeslice at 1100ms TWT with volume render showing high amplitudes of AA5. Yellow line indicates seismic section visualized in B. B) Seismic cross section with volume render showing high amplitudes of AA5. Colour scale with black dots showing values excluded for volume render values.

AA 5 is located approximately 2km north of the GGC 4 (Fig.4.3.1 and Fig.4.3.4.1). It occurs within the IntraH1 sediments which are dipping in a south westerly direction showing small elongated bodies with a lateral propagation of 1 km length and 0.5m width. Each of the elongated bodies consists of stacked bright spots (Fig.4.3.4.1). Fault 3 covers the western flank and the fault 2 covers the eastern flank and provides the natural boundaries for AA5. To the north seems fault 14 seems to indicate a boundary meaning that the whole anomaly is located above the fault block 2c (Fig. 4.3.1 and Fig. 4.3.4.1).

The top of the anomaly is at 750 ms TWT and the base is traced down to 816 ms TWT. Depth converted data provide a height of 83m TVD. However, due to an estimated low velocity in gas-rich sediments, we assume a velocity of 1800m/s which results in a lower height, i.e 59,4m (TVD). The total area is estimated to be 2 km^2 and the total volume 0.12m^3.

4.3.4.2 Amplitude anomaly (AA) 6

AA 6 is located in the south-easterly part of dataset "West Loppa 2008" (Fig.4.3.1 and Fig. 4.3.4.2). Top occurs as a strong laterally continuous negative reflector in a dipping strata. A continuous positive flat reflector at 92 ms TWT beneath the top represents the base of the anomaly. The acoustic anomaly pinches out at the edges forming a tubular shape. AA 6 is oriented in a north-south direction as a long elongated body perpendicular to the dipping stratigraphic layers. The top is located at 644 ms TWT and the base at 745 ms TWT. Depth converted data suggests a height of 108m (TVD). A push-down effect is observed which indicates a lower velocity most likely due to gas. Applying a p-wave velocity of 1800m/s the total height of the anomaly is calculated to be 88.2 m TVD. The area covered by the anomaly is 20 km^2 and the volume of 1.764 km^3. The anomaly is located between fault- 2 and 1-11 but there are no clear traces of any kind of leakage features from faults (Fig. 4.3.4.3).

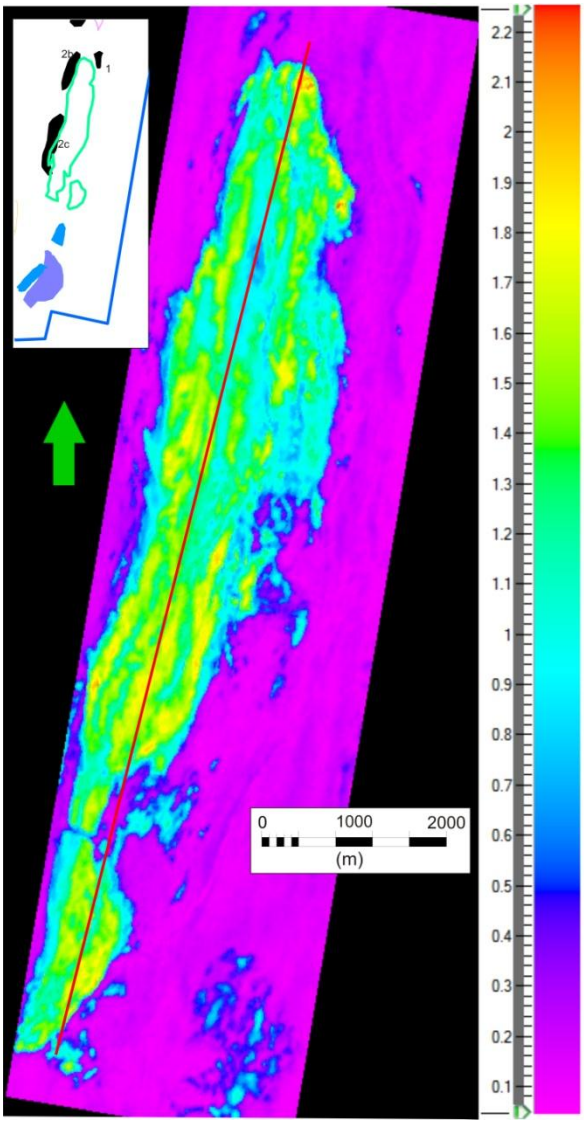

Figure 4.3.4.2 RMS map overviewing AA6, including values between 640 to 750ms TWT.

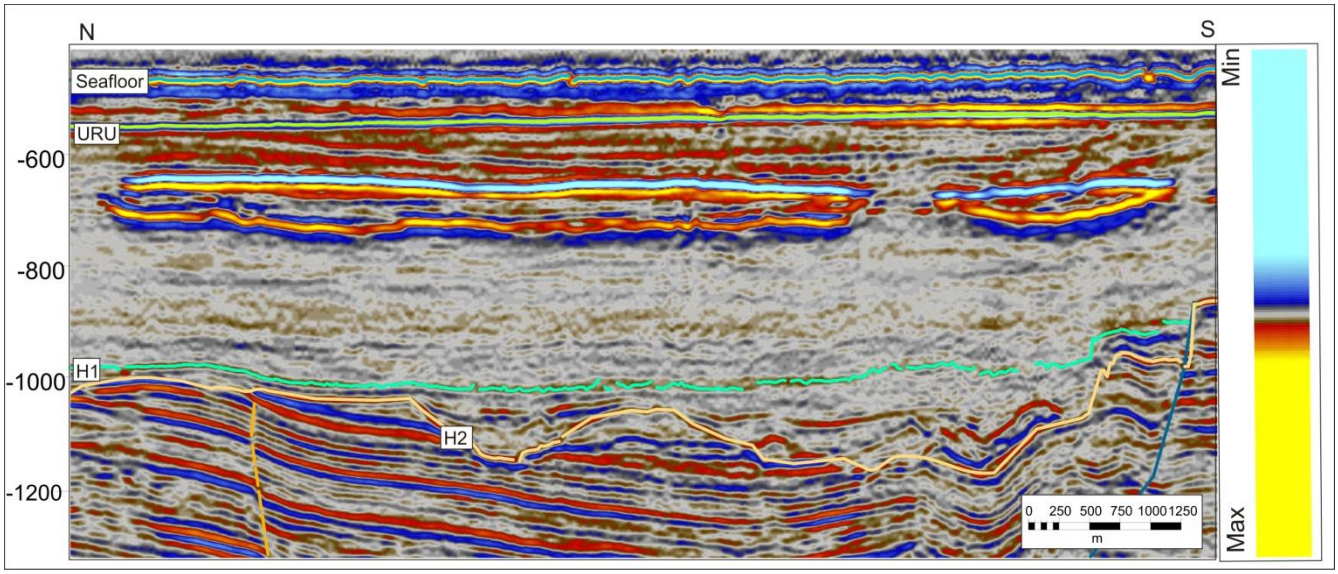

Figure 4.3.4.3 Seismic cross section of AA6. Location indicated on figure 4.3.4.2.

4.3.4.3 Amplitude anomaly (AA) 7

AA 7 is located in only 2 km east of GGC2a (Fig.4.3.4.4). The anomaly shows a phase reversal and bright spot within IntraH1 sediments (Fig. 4.3.4.4). Several weaker bright spots occur beneath AA7 in a v-shape (Fig.4.3.4.4). The whole anomaly occurs as an elongated, rectangular object oriented in a north-southward direction. It occurs perpendicular to the dipping strata (Fig. 4.3.2.4). The top is located only 92 ms TWT bellow URU and 178 ms TWT below seafloor (Fig.4.3.2.4). Depth conversion of data applying the top to be located at 550m TVD below the sea surface. The height of the object is calculated to be 117.9m (TVD) and the amplitude anomaly covers an area of 3.61 km^2 and volume of 0.415 km^3.

AA 7 is located in near vicinity to the GGC2a and is located above the fault block 2a (Fig.4.3.1).

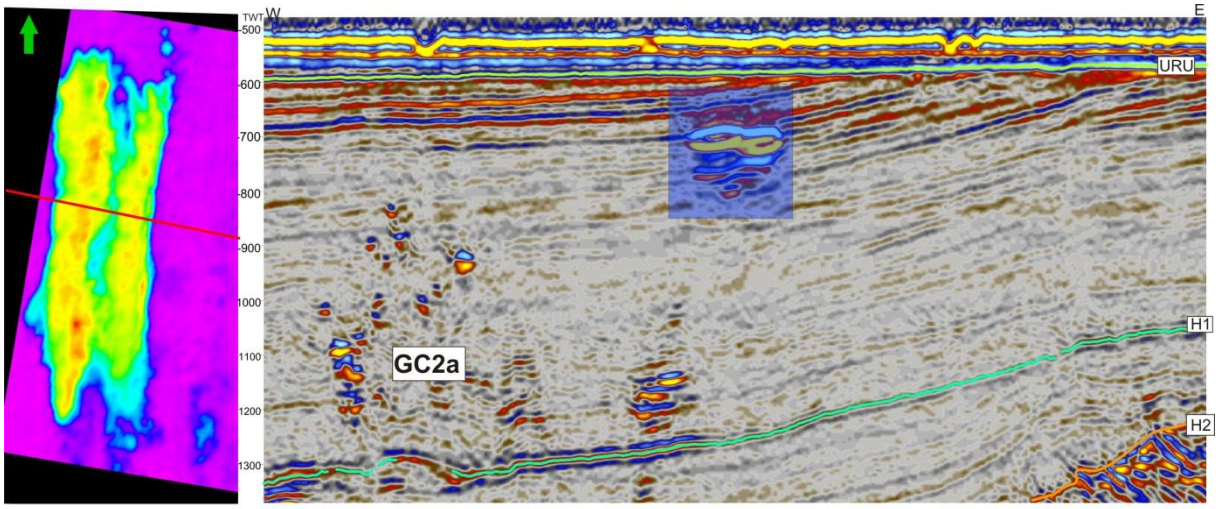

Figure 4.3.4.4 RMS amplitude map including values between 680-820ms TWT (transparent square).

4.3.4.4 Amplitude anomaly (AA) 8

AA8 is located in the southern part of the dataset "West Loppa 200" (Fig.4.3.1). The top is a negative polarity bright spot with a phase reversals that disturbs the dipping IntraH1 sediment strata (Fig.4.3.4.5). It occur as two narrow, but separated bodies located in the same layer. The distance between them is approximately 1.7 km. They show an oval shape and are oriented parallel to the dipping strata in area. There is a flat spot beneath the thickest zone of object (Fig.4.3.4.5). The total length of the objects is 2.9 km and the width are 1.7 km. The height can only be estimated on one of the objects, where it is 32 ms TWT. With an apparent velocity of 1800m/s the height of the anomaly is 28.8m. The base cannot be identified on the second object because the layer is too thin for the vertical resolution (14m). The total area of the two objects are 4.93 km^2, and the total volume is calculated to be 0,142 km^3.

AA8 is loaceted in a distance of ~1.8 km away from the GGC4 and east of fault 18 (Fig.4.3.4.5), above the sub-polheim latform where several straight faults are observed (Fig.4.3.4.5).

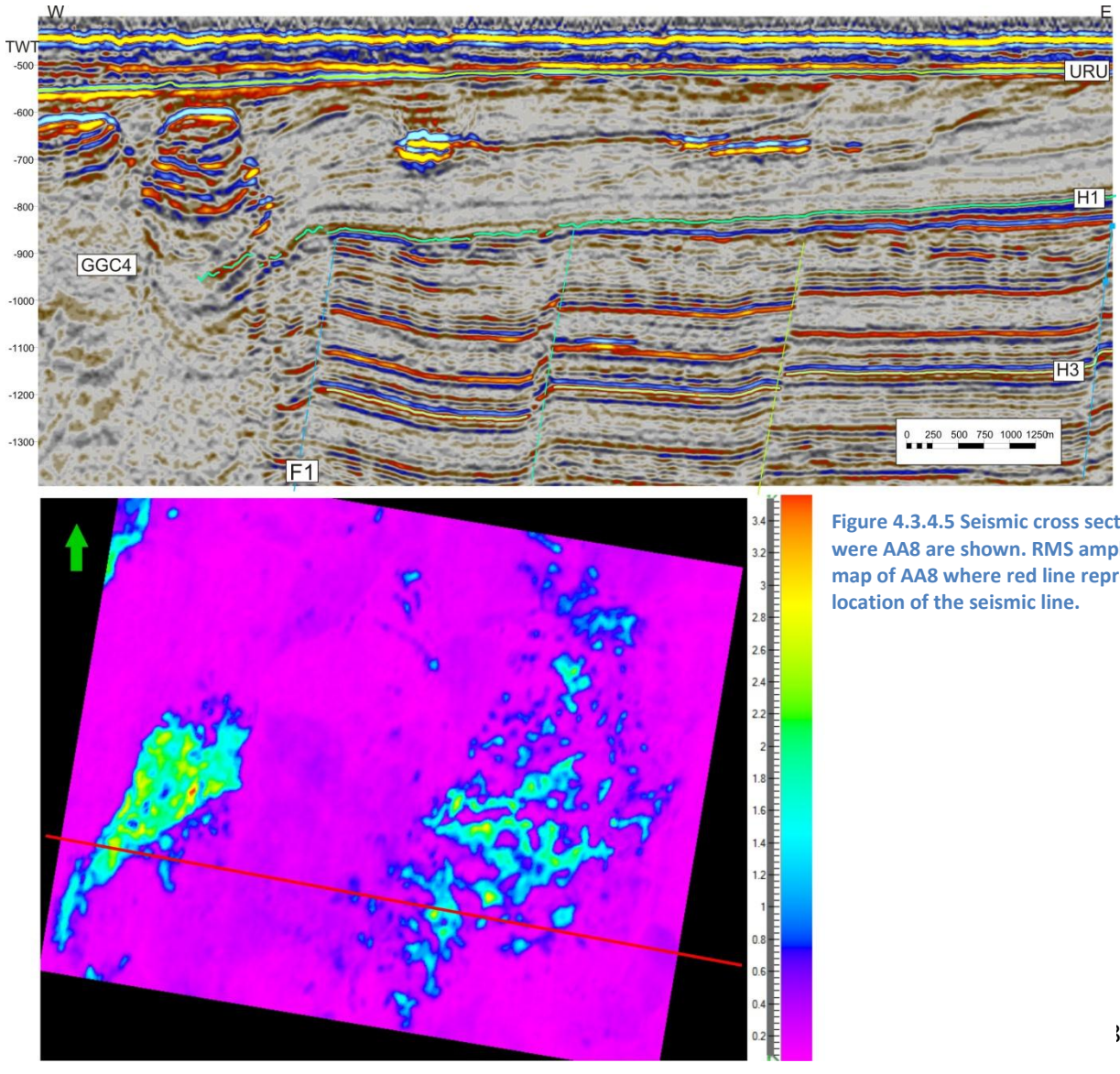

Figure 4.3.4.5 Seismic cross section were AA8 are shown. RMS amplitude map of AA8 where red line represent location of the seismic line.

4.3.4.5 Amplitude anomaly (AA) 9

AA9 is located on the Sub-Polheim platform within the IntraH3 sediment package. Occurs as negative polarity bright spot with phase reversal (Fig 4.3.4.7). AA9 can be divided into two laterally separated bright spots (Fig.4.3.4.6). The top of AA9.1 is located at 1062 ms TWT, while top AA9.2 is 1080 ms TWT. The bright spot occurs on a strong continuous reflector which is slightly southeast dipping. The reflector beneath the bright spot does not show any recognizable changes.

The top IntraH3 reflector (H3) shows also a phase reversal at 837 ms TWT straight above AA9 (Fig. 4.3.4.7). Anomaly AA9.1 is 730m wide and 2500m long, and anomaly AA9.2 is 841m wide and 1354m long. Together they cover an area of 2.96 km^2. The area consists of a fault system that seems to limit the anomaly laterally (Fig. 4.3.4.6).

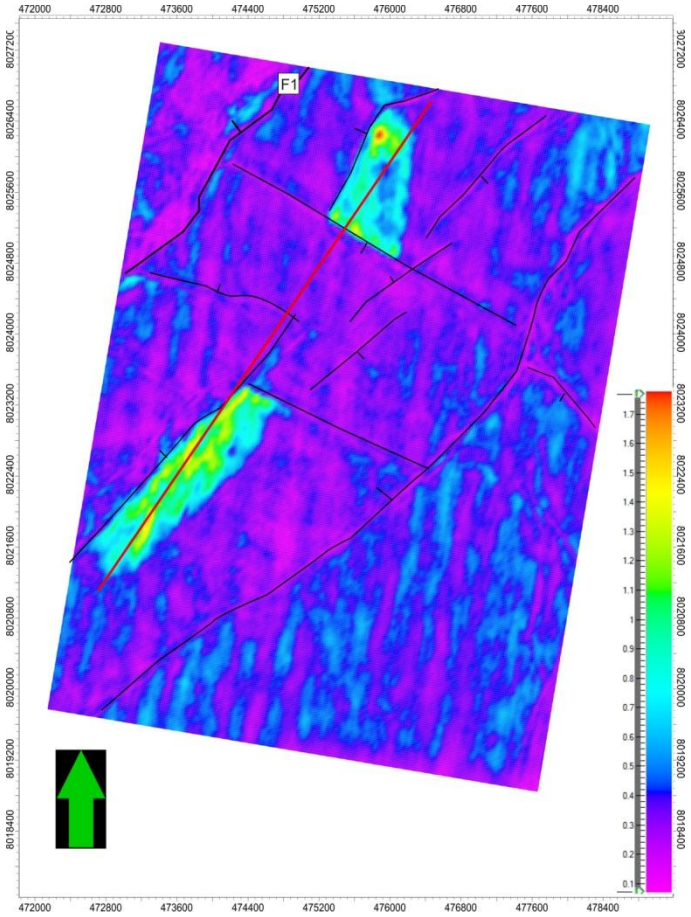

Figure 4.3.4.6 RMS amplitude map including interval 1150-1050ms TWT. Red line indicates position of random seismic line in figure 4.3.4.7.

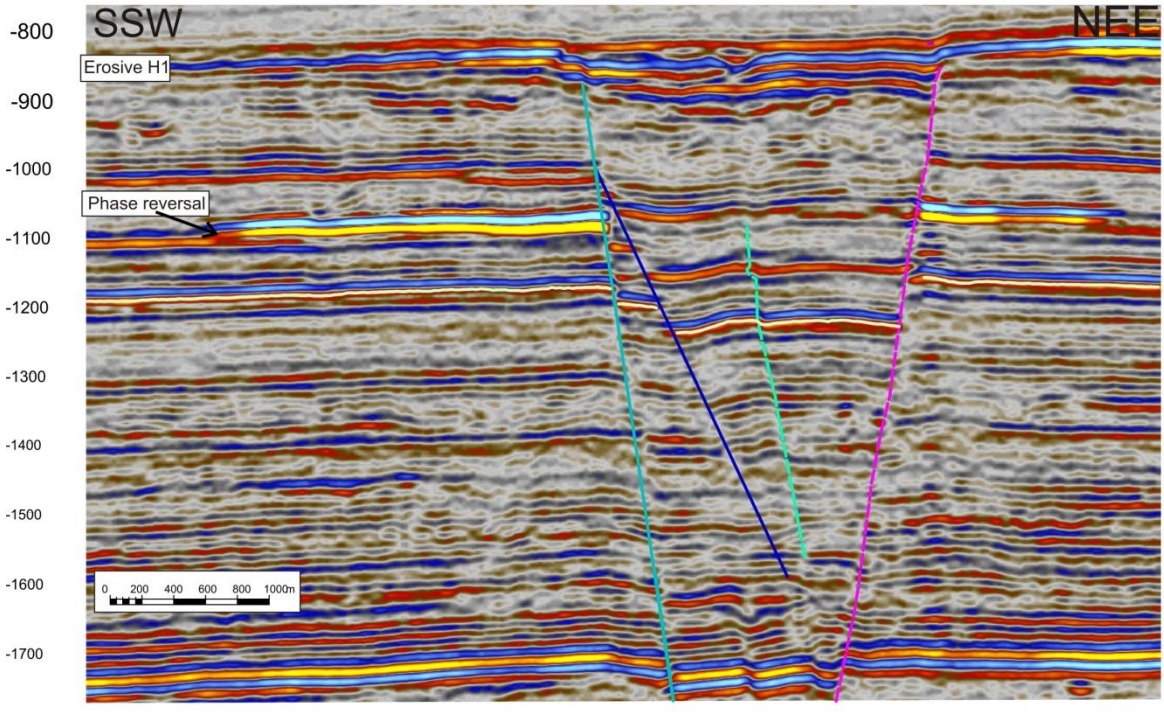

Figure 4.3.4.7 Seismic cross section through AA9. See figure 4.3.4.6 for location

4.3.4.6 Amplitude anomaly 11

An anomaly is located within the IntraH1 sediment sequence, where the depositional strata are dipping in a south-western direction. Geographical the anomaly is located in the middle of the seismic 3D cube above the fault block1. The top is occurring as a negative bright spot which is phase reversed at intersection at 639 ms TWT or 516 m TVD, the distance to seafloor is 153m TVD (Fig.4.3.4.8). The base of the layer is not distinguished on the seismic section, meaning it is lower than the vertical resolution. Assuming an apparent velocity of 2.1 km/s at the depth and dominant frequency of 40Hz the estimate maximal thickness of layer is 13m. For volume calculation, 10 m depth has been used. Laterally amplitude anomaly 11 is similar to AA6, and it is also located in the same geological setting, but AA6 is located 5 km further south. AA11 has a triangular shape where the sides are 2.7 and 3.3. Therefore the area covered by AA11 is calculated to be 4.46 km^2 and the volume of anomaly assuming a depth of 10m is calculated to be 0.0446 km^3.

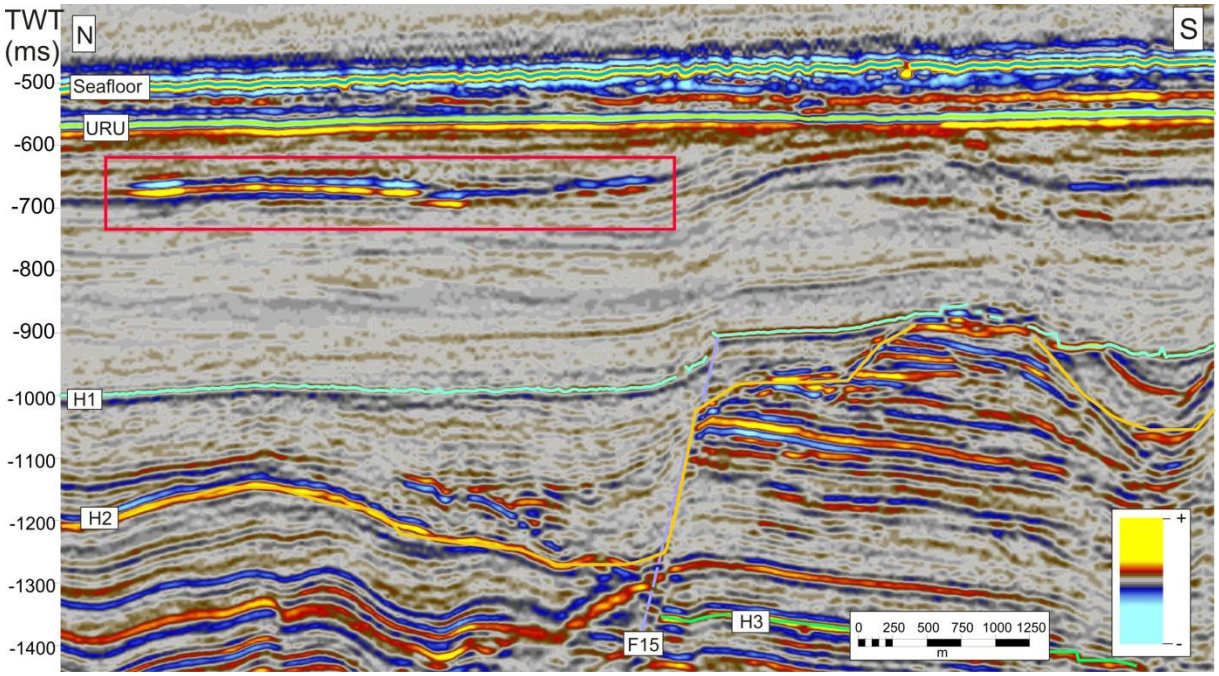

Figure 4.3.4.8 Seismic cross section through AA11. Location of AA11 is within the red square.

									Depth converted data (m)	
No	**Shape**	**Size (km)**	**Top (TWT) / (TVD)**	**Base (twt)**	**Area (km^2)**	**Volume (km^3)**	**Stratigraphic unit**	**Height (m)**	**Distance to SF (TVD)**	**SF (TVD)**
AA5	Small elongated bodies	(1x0,5)x4	750 / 640	816	2	0,120	IntraH1	59,4	313	332
AA6	Long elongated body	10x2	644 / 515	745	20	1,764	IntraH1	88,2	173	347
AA7	Elongated	3.6x1	683 / 550	814	3,61	0,415	IntraH1	117,9	160	390
AA8	Oval	2,9x1,7	659 / 532	691	4,93	0,142	IntraH1	28,8	204	328
AA9	Elongated	(0,7x2.5) x (0.8x1.4)	1062 / 1116		2,964		IntraH3		780	338
AA11	triangular	3,3x2,7	639 / 516	697	4,46	0,045	IntraH1	10	153	363

Table 4-6 Summarized details for the different AA`s.

4.3.5 Amplitude anomalies, flat spot

Flat spots are sub grouped below amplitude anomalies due to their importance for identifying areas of different fluid densities (Chap.1.5).

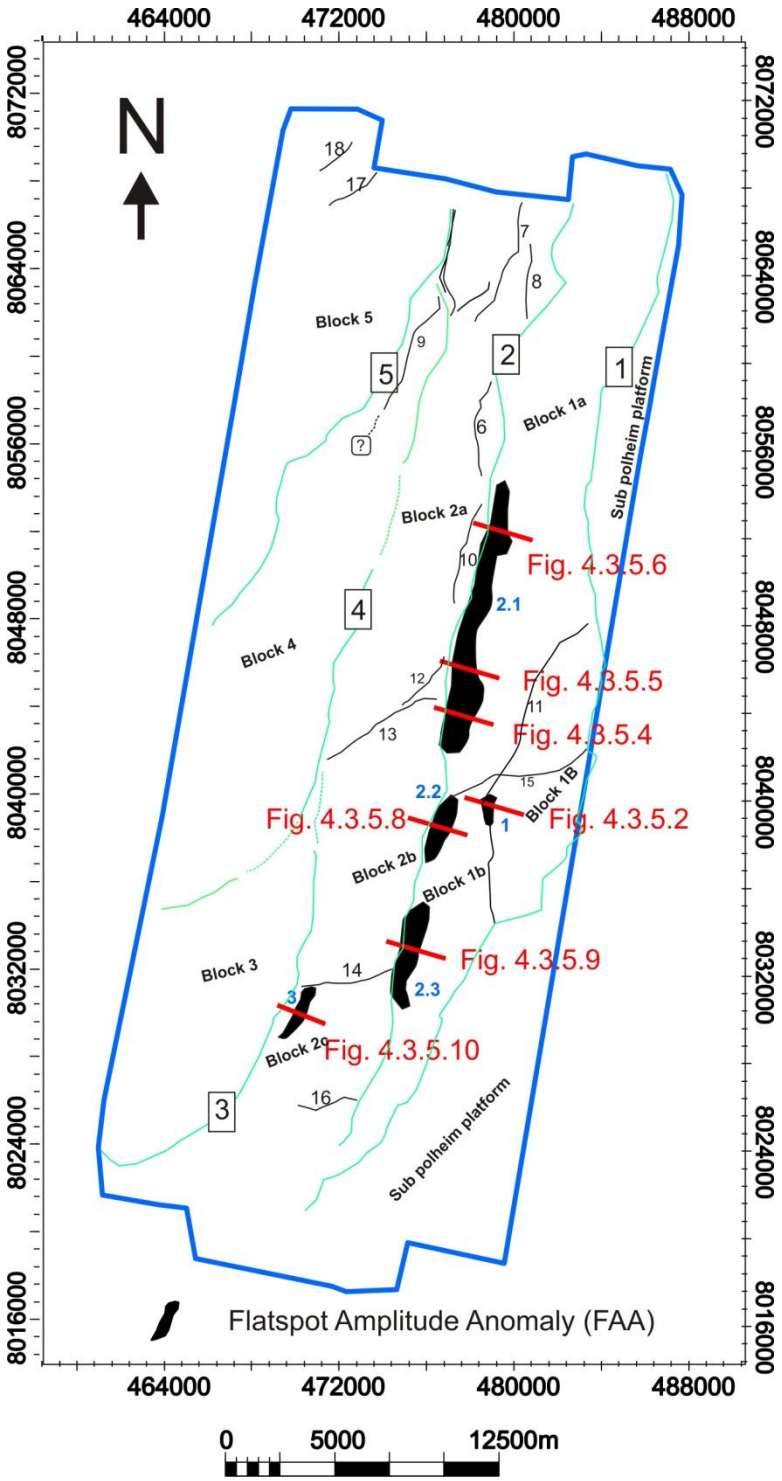

Figure 4.3.5 Overview of the Flat spot Amplitude Anomalies (FAA)

4.3.5.1 Flat spot Amplitude anomaly (FAA): 1

FAA1 is located on fault block 1b, that truncates at the base Tertiary reflector (H1), which resembles an erosive surface. FAA1 is observed in the south easterly dipping strata of IntraH3 sediments where it is limited by faults (Fig.4.3.5.2).

The whole amplitude anomaly is separated between two lateral separated negative polarity bright spots and one flat spot (Fig.4.3.5.1).

The first and southern-bright spot occurs at 811 ms with a phase reversal. The original reflector is continuous and strong with a normal polarity. It represents the unconformity from tertiary to Cretaceous. The bright spot seems to be limited by faults.

The second and more northerly located bright spot has the same characteristics as the southern bright spot but it is located slightly deeper, i.e at 851 ms TWT. While it evolves northwards, a possible flat spot is observed 38 ms TWT beneath the bright spot (856ms) (Fig.4.3.5.2). It occurs north of fault H3-1B-5 (Fig. 4.3.5.2).

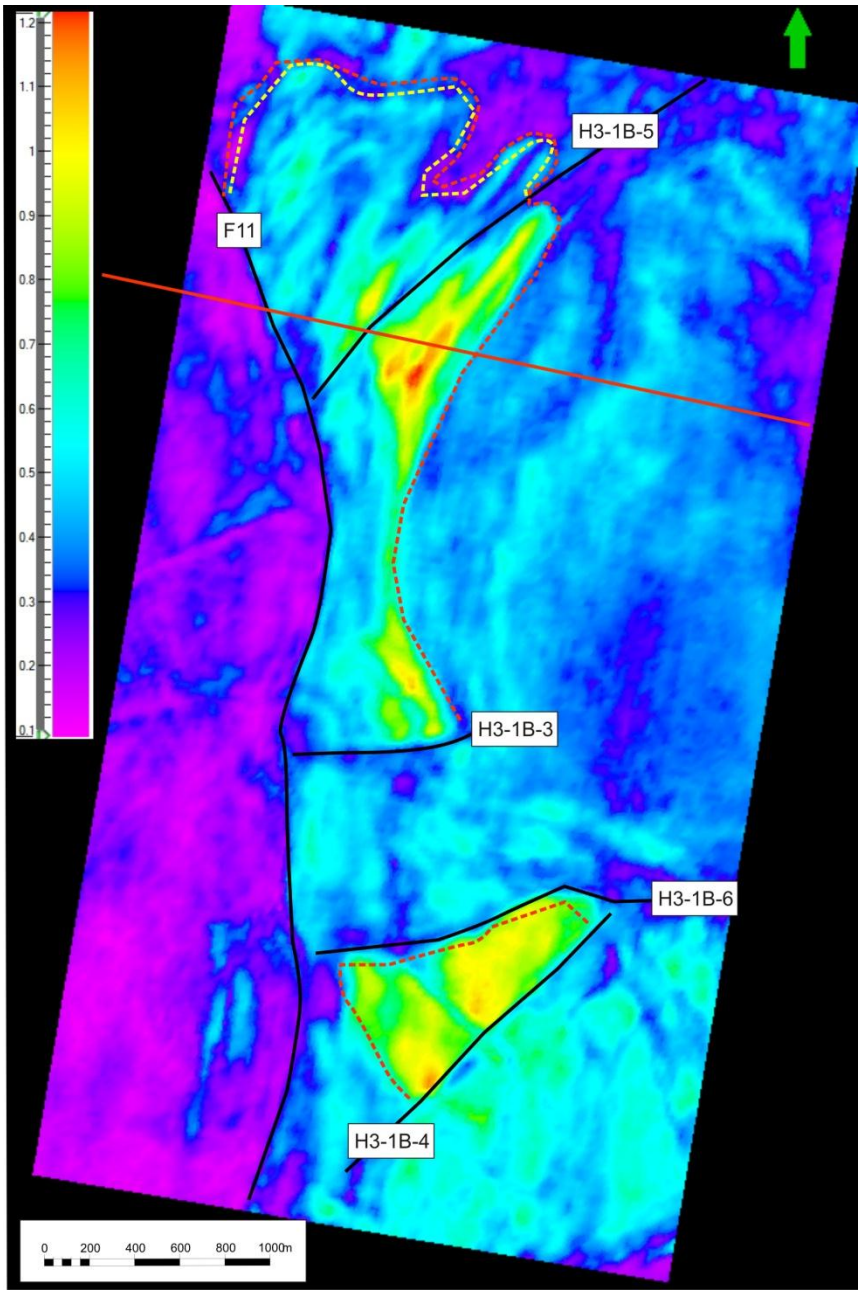

Figure 4.3.5.1: RMS amplitude map if FFA1 including volume from 780-1040ms TWT. Red dashed line indicated the lateral extent of the phase reversed bright spot while dashed yellow line indicates the lateral extension of the flat spot. Red solid line indicates position of cross section in figure 4.3.5.2.

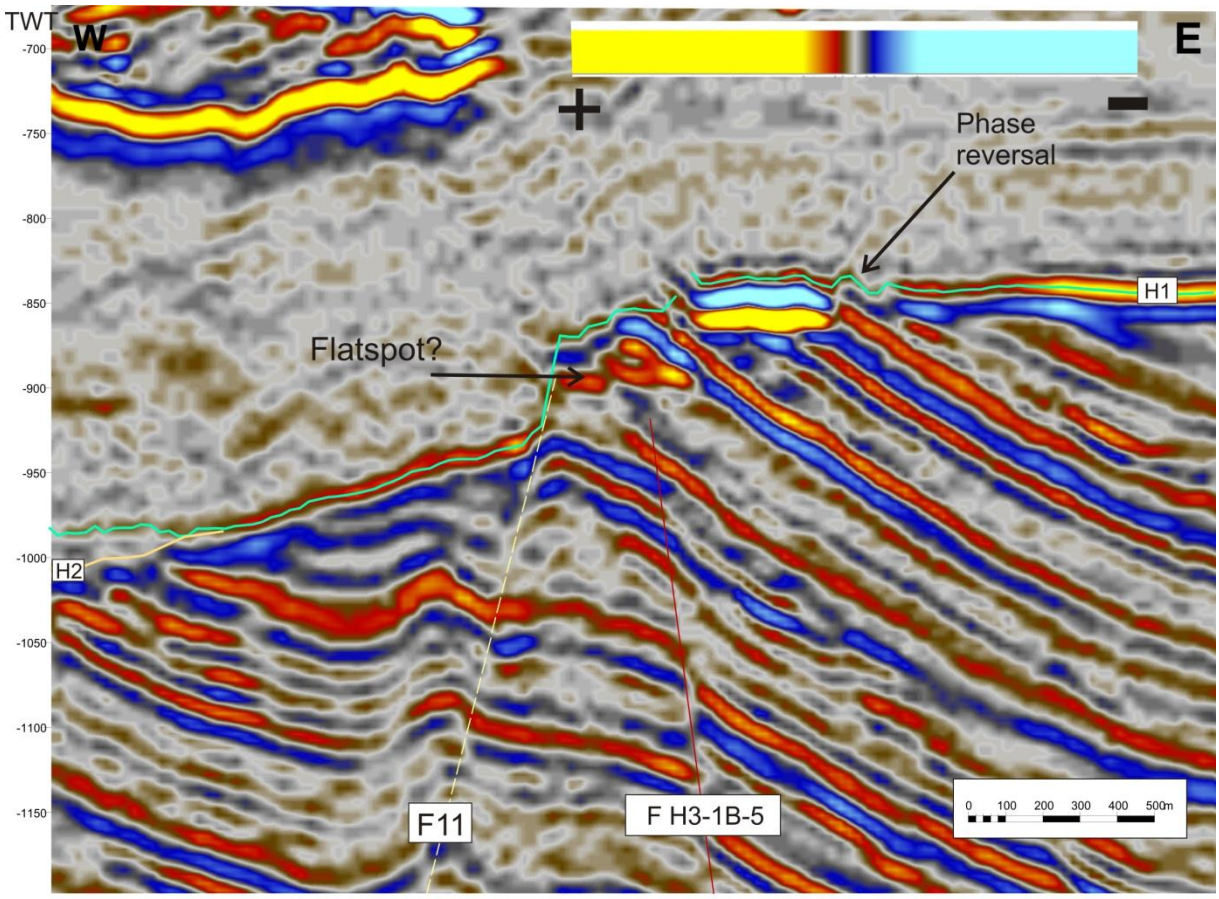

Figure 4.3.5.2 Seismic cross section showing the phase reversed bright spot with its underlying flat spot.

Northwards, the erosive surface H2 cuts into the IntraH3 sediments and both the bright spot and the flat spot is following this surface. At the northern rim the bright spot is observed at 910 ms TWT and the flat spot at 56 ms beneath it at 966 ms TWT. Fault 11 provides the western boundary of the amplitude anomaly. The observed fluid escape features are along this boundary. The total lateral extension of the bright spots excluding the area of the flat spot, is calculated to be 1,715 km^2. The lateral extent of the flat spot is calculated to be 0,84 km^2. Assuming an average velocity of 2,4 km/s the average height of anomaly is 56,4m, gives a total estimation of potentially hydrocarbon bearing sediments of 0,05 km^3.

4.3.5.2 Flat spot Ampltitude Anomaly (FAA): 2

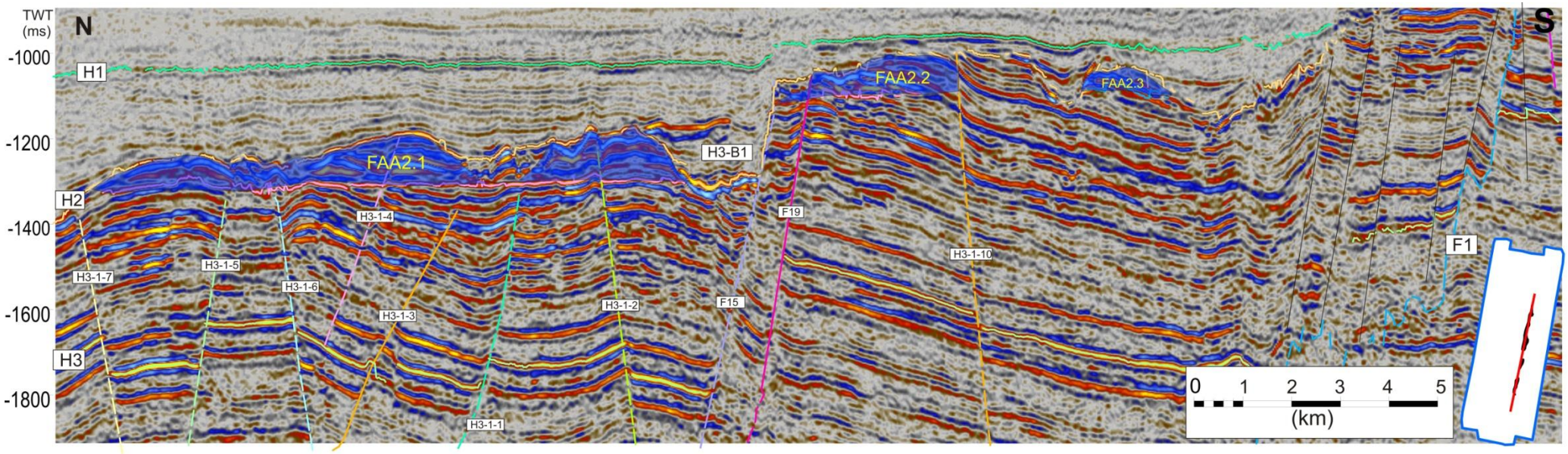

Figure 4.3.5.3 Seismic cross section through FAA2. Polarity convention is shown in figure 4.3.5.2.

FAA2 ocurs in the IntraH3 sediments on fault block 1 (Fig.4.3.1 and Fig.4.3.5.3). It propagates over a large area of almost 20 km. The depth of FAA2 varies from 1530 ms in the central parts to 1062 ms TWT in the southern part of the dataset “West Loppa 2008” (Fig.4.3.5.3). There are also observed double flat spot. FAA2 is divided into three separate flat spots due to faults causing a lateral separation of the flat spots (Fig. 4.3.5.3).

FAA 2.1 is located in fault block 1a, and encompasses the largest flat spot in the dataset (Fig.4.3.5.3). The geology in block 1a is complex due to many faults that limit and interrupts the lateral extension of the flat spot (Fig.4.3.5.3). The flat spot varies in depth due to the fact that faults form barriers. The lateral extension of FAA2.1 is limited by the erosive surface of H2 and the base of the syn-deposited small-scale basin H3-B1 that determines the southern boundary (Fig.4.3.5.3). Northwards the erosive H2 cuts less into the underlying formation and two flat spots are observed in the south easterly dipping strata. The top of the flat spot occur for the first time at 1265 ms and for the second flat spot at 1321 ms TWT (Fig.4.3.5.4).The south dipping fault H3-1-2 (Fig. 4.3.5.3), disturbs the flat spot anomaly and northwards the double flat spot disappears (Fig. 4.3.5.4).

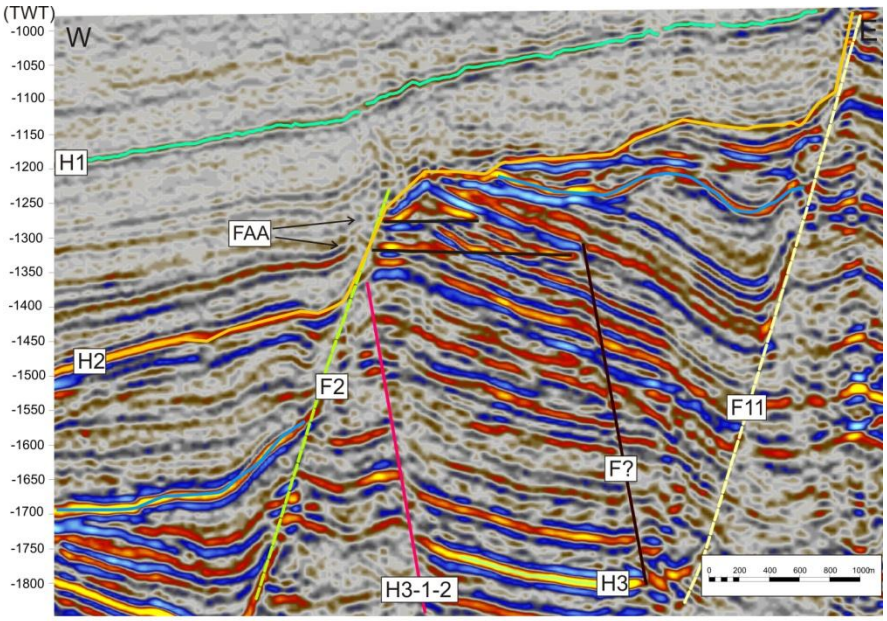

Figure 4.3.5.4 Seismic cross section through FAA2.1, location indicated as "1" on figure 4.3.5.7.

The erosive surface H2 cuts into the underlying formation and after fault H3-1-1 both the flat spots completely disappears (Fig. 4.3.5.3). North of fault H3-1-3 the double flat spot reappears but is less significant and thinner with than south of fault H3-1-1 and the first flat spot appears now at 1297- and second one at 1327 ms TWT.

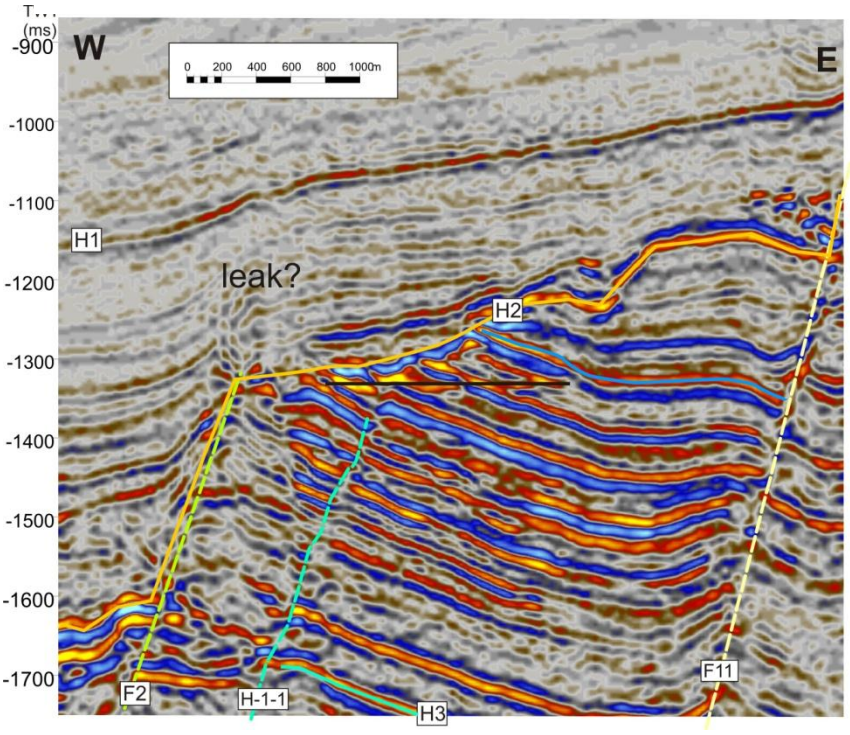

Figure 4.3.5.5 Cross section through FAA2.1, location indicated as "2" on figure 4.3.5.7.

North of fault H3-1-6 the flats pot is divided by the north – south fault H3-1-9. The western flat spot is observed at 1345 ms- and the eastern one is at 1266 ms TWT (Fig 4.3.5.6).

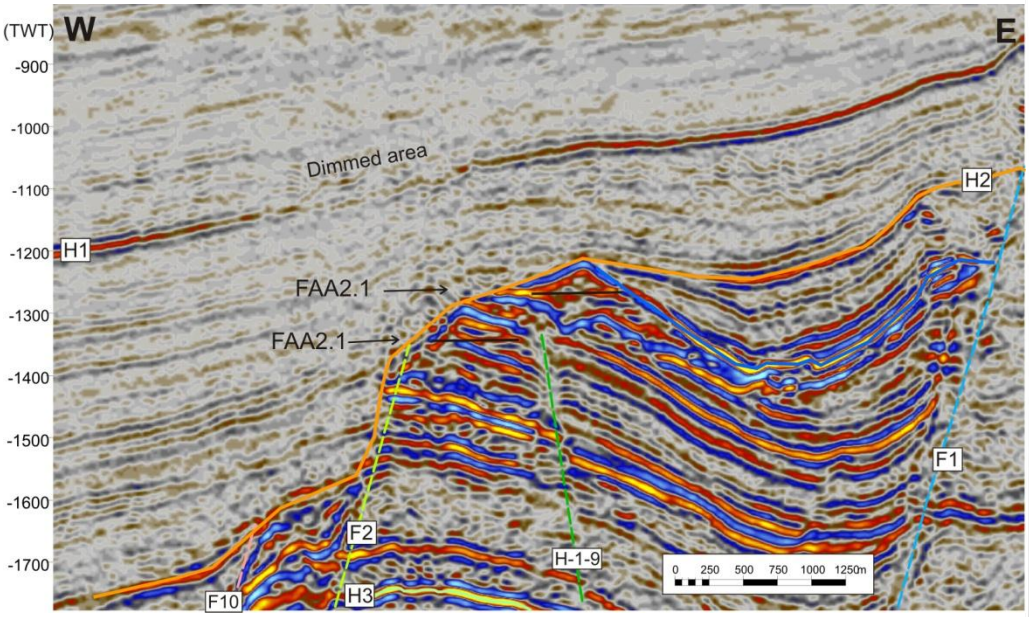

Figure 4.3.5.6 Seismic cross section of FAA2.1, location indicated as "2" on figure 4.3.5.7.

FAA2.1 is thinning while going northward toward fault H3-1-7 and the flat spot completely disappears after crossing the fault (Fig.4.3.5.3).

A continuous conduit is observed, which is rising from top anomaly that dims the H1 reflector.

The total size of FAA2.1 based on a 10.70 km long and an approximately 0.94 km wide area is calculated to be 9.47 km^2 with an estimated volume of 1.02 km^3.

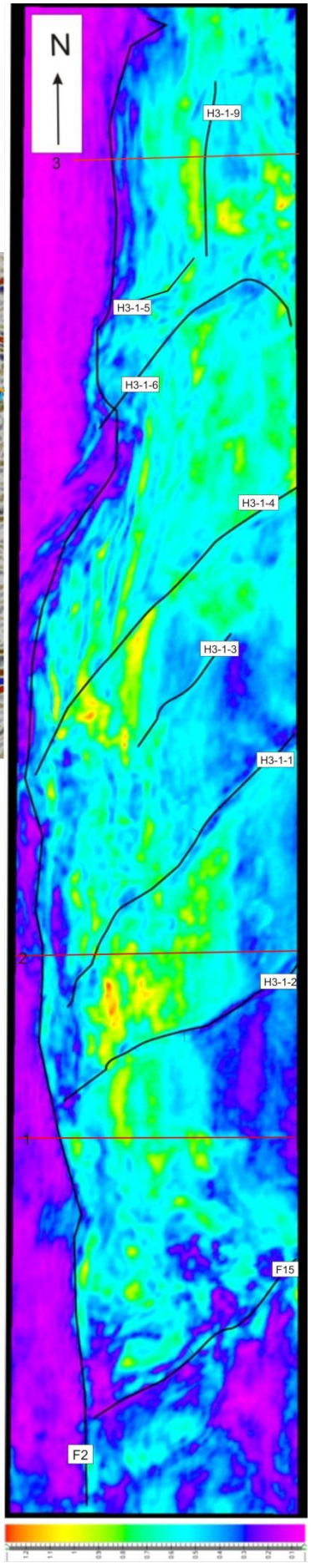

Figure 4.3.5.7 RMS amplitude map including volume between 1200 - to 1350ms TWT. Location of the seismic cross sections are indicated with 1-3.

FAA 2.2 is located on fault block 1b within the IntraH3 sediments, where strata are dipping south-eastward and the flat spot is located on the west flank of the fault block structure. Situated in the same position as FAA2.1 (Fig.4.3.5.4) regarding the western flank. Fault 15 and the erosive surface H2 are causing the north boundary for FAA2.2. The southern rim seems to be terminated by the fault H3-1-10. The erosive surface H2 is only partly sealing the bright spot and the other portion overlaying FAA2.2 is the same sequence of dipping strata IntraH3 sediments (Fig.4.3.5.8). The top of FAA2.2 is located at 1075 ms TWT and its base is continuous at 1130 ms TWT (Fig.4.3.5.8). FAA2.2 has an elongated and narrow shape with a length of 3.38 km and width of 0.569 km. The area covered is 1.92 km^2 and the volume is 0.127 km^3 assuming a height of 66m. There are no clear leakage features observed at the flat spot level.

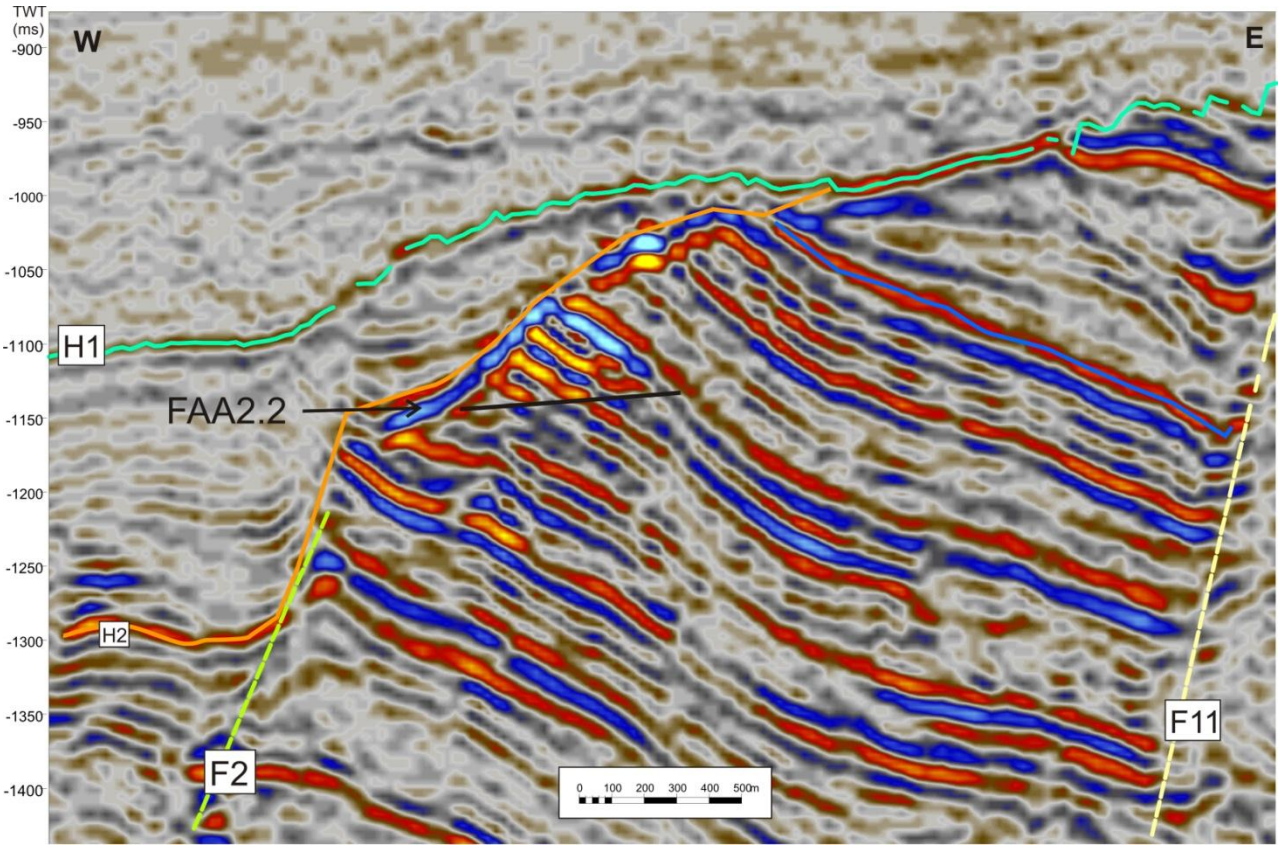

Figure 4.3.5.8 Cross section through FAA2.2

FAA 2.3 is located in the most southern block 1c and is the shallowest flat spot of the FAA2. (Fig.4.3.5.3). The top occurs at 1062 ms TWT and only a single flat spot is observed at 1120 ms TWT. The height varies from 40 ms TWT to below vertical resolution. Assuming an average velocity of 2.4 km/s (NPD and OED, 2010) within IntraH3 gas bearing sediments, the height of the anomaly is calculated to an average 36 m TVD. Sediments are dipping into a south easterly direction. The anomaly is limited on the western flank by fault 2 and the northern and in the northerly part by the erosive surface H2 (Fig.4.3.5.3). Fluid leakage features are observed at the same level as the flat spot anomaly on the western flank (Fig.4.3.5.9). The dominant frequency is reduced in the area where the flat spot occurs. The lateral extension of FAA 2.3 is 955 m long and 1025 m wide and the area is therefore calculated to be 1.02 km^2. With an estimated height of 36 m the volume is calculated to be 0.038 km^3.

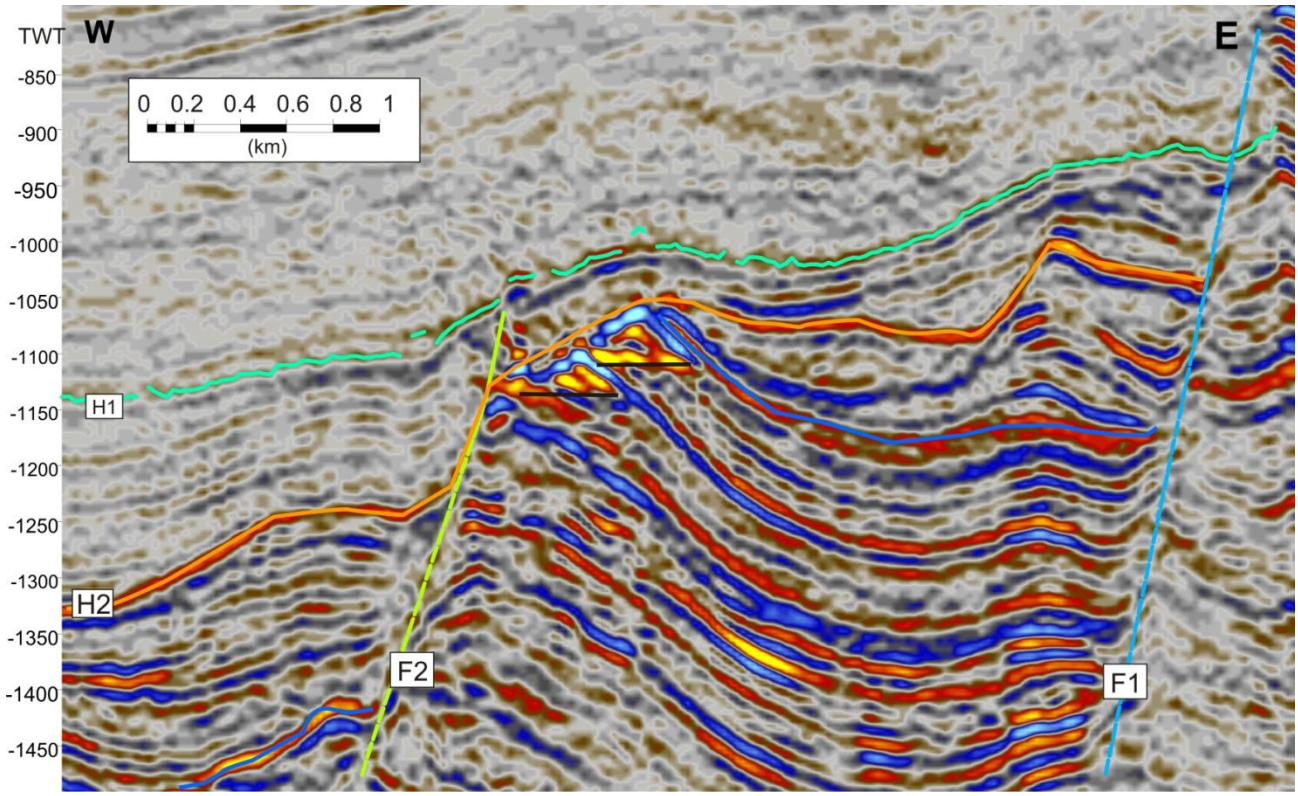

Figure 4.3.5.9 Cross section through FAA2.3

4.3.5.3 Flat spot Ampltitude Anomaly (FAA): 3

FAA 3 is located inside the structural categorized fault block 2c where the upper boundary is the erosion surface H2/H1. FAA3 is located in the north western corner of the block where the original strata are mainly dipping towards east and slightly south. The flat spot occurs in an elevated top-zone of the block. Thickness varies at the outer rims from 0 to 60 ms TWT. The western bounday are limited by fault 3. At the southern boundary several fluid leakage features are observed and giant gas chimney 4 occurs on the same fault block further south. Top anomaly is characterized with a discontinuity of reflection in area where leakage seems to occur.

Top anomaly is at 984 ms TWT which is calculated to be 918 m TVD. Possible a second flat spot is observed. The length of FAA3 is 2.6 km and the cross axis is 0.653 km. The orientation of the anomaly is northeast southwest parallel to fault 3. Area covered is 1.7 km^2 and the volume is calculated with an average velocity of 2.2 km/s. The volume is calculated to be 0,1 km^3. As mentioned above there is a possible second flat spot beneath, which is not taken into this calculation.

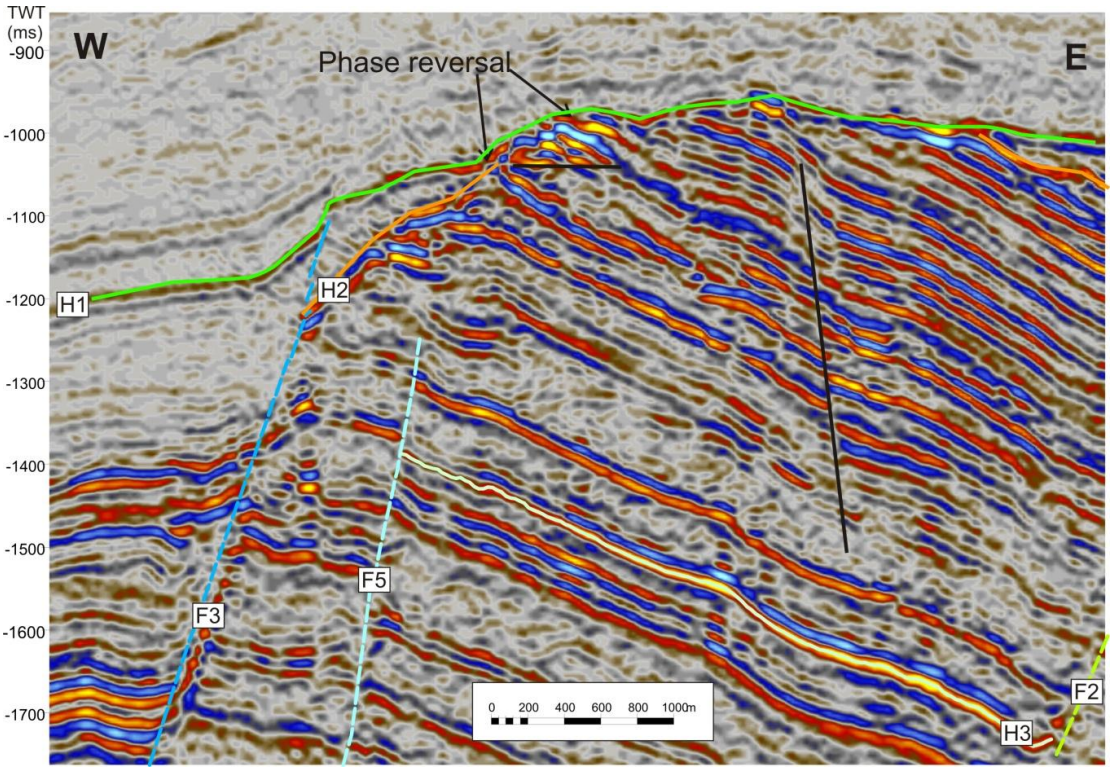

Figure 4.3.5.10 Seismic cross section through FAA 3, location indicated on figure 4.3.5.

No	Shape	Size (km)	Top (TWT)	Base (twt)	Area (km^2)	Volume (km^3)	Stratigraphic unit	Height (m)
FAA1	triangular	1,2x1,4	856	894	0,84	0,05	IntraH3	41,8
FAA2.3	rectangular	0,955x1,025	1065	1120	1,02	0,04	IntraH3	36
FAA2.2	rectangular	3,38x0,569	1075	1130	1,92	0,13	IntraH3	66
FAA2.1	rectangular	10,7x0,94	1230	1320	9,47	1,02	IntraH3	108
FAA3	Rectangular	2,6x0,65	984	1044	1,70	0,11	IntraH3	66

Table 4-7 Summarized statistics of the difference observed flat spot amplitude anomalies.

Both FAA-2.2 and 2.3 are situated directly beneath AA6.

There are observed a fluid escape features along the western boundary of flat spot. It is located at the exact same depth in time as the flat spot presented in figure (Fig.4.3.5.5, -6,-9).

4.4 GHSZ modeling

The cross cutting reflectors occurring on top of the giant gas chimneys and amplitude anomalies are suggested to represent the base of the gas hydrate stability zone (BGHSZ). Sloan (1998b) programmed the software (CSMHYD) which is based on extensive work in the laboratory measuring the stability phase of gas hydrates. One can use CSMHYD to calculate where the BGHSZ are situated in pressure based on temperature and gas composition. By applying an average bottom water temperature and geothermal gradient one can calculate where the BGHSZ are present in depth.

For calculation of the BGHSZ one have used a pressure gradient for the hydrostatic at 0.1KPa m^{-1} for the water column and additional litostatic pressure to be .101KPa m^{-1} (Weibull, 2010). The Geothermal gradient are regional suggested to be 35°C km^{-1} geothermal gradient (Chand et al., 2008), still from the reference well 7219/9-1 the gradient are measured to be 33.8°C km^{-1} (NPD, 2010). Therefore I have used 33.8°C km^{-1}. Seafloor temperature is estimated to be an average of 2.25°C but is expected to vary due to complex ocean currents and annual differences (Chand et al., 2008) There are updated temperature data at (http://www.nodc.noaa.gov/General/temperature.html).

Because of the proven rich source rock area we're in, one expect the gas of being of thermogenic orign. Measurements from well 7216/11-1 situated in the Sørvestnaget Basin confirms that (Henriksen, 2011b). Nevertheless the exact composition of the gas is not known and I have calculated with three different compositions:

TYPE 1: 90 % Methane, 6 % Ethane, 4 % Propane

TYPE 2: 96 % Methane, 3 % Ethane, 1 % Propane

TYPE 3: 99 % Methane, 1 % Ethane

The BGHSZ has been calculated for the specified water depth of the observed cross cutting reflectors (GGC tops and AA (BSR)) separately.

GGC1

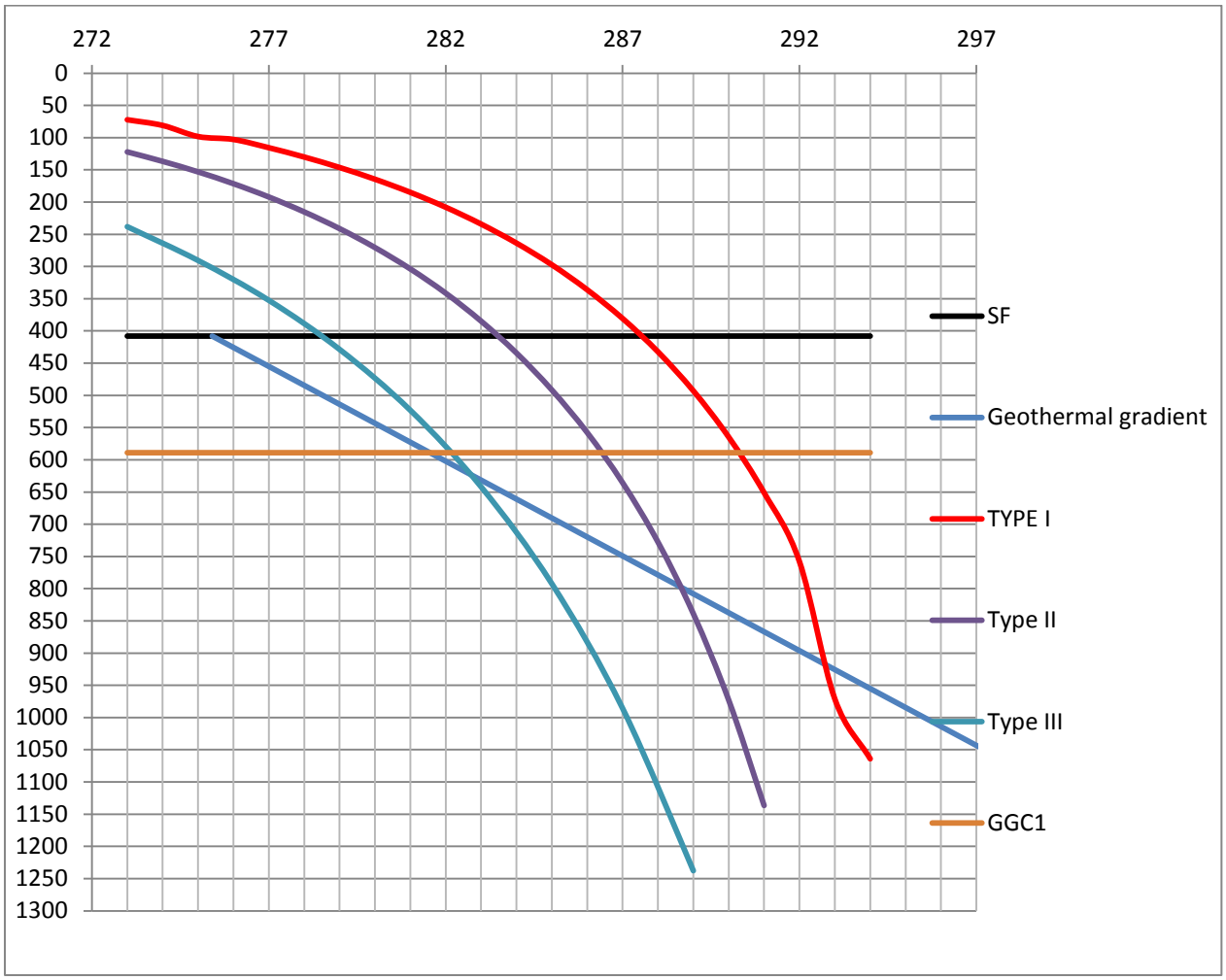

Diagram 4.1 Stability zone for gas hydrates at location of GGC1 with different gas composition calculated with the program CSMHYD (Sloan, 1998c) assuming a hydrate structure 2. The geothermal gradient used for the calculation is 33.8°C.

GGC1 is represents in the area with highest water depth (408m), which means there will be higher pressure to temperature rating than in a shallower part of the dataset due to the bottom water temperature are estimated to be the same over the entire area. Calculations of GGC1 suggest the BHSZ to be ~625m for Type II gas composition, ~800 m for Type II gas composition and ~920 m for Type I gas composition. Which means that all the different gas compositions are stable within GGC1 area. The observed GGC1 top is observed at 589m ~6% from Type III composition.

GCC2

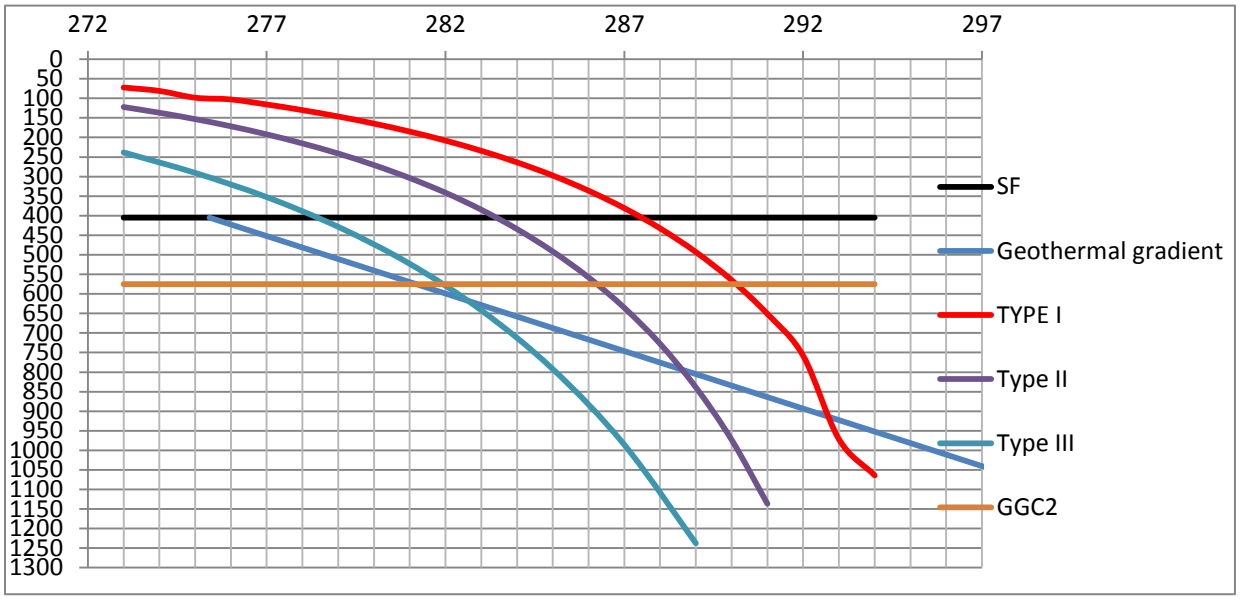

Diagram 4.2 Stability zone for gas hydrates at location of GGC2 with different gas composition calculated with the program CSMHYD (Sloan, 1998c) assuming a hydrate structure 2. The geothermal gradient used for the calculation is 33.8°C.

The GGC2 is situated in an area with an average water depth of 405m where the calculated BGHSZ is at 620 m with gas composition Type III, 790 m with gas composition Type II and 920 m with gas composition Type I. The observed top of GGC 2 is located at 575 m, ~7 % shallower than the BGHSZ of Type III.

GGC3

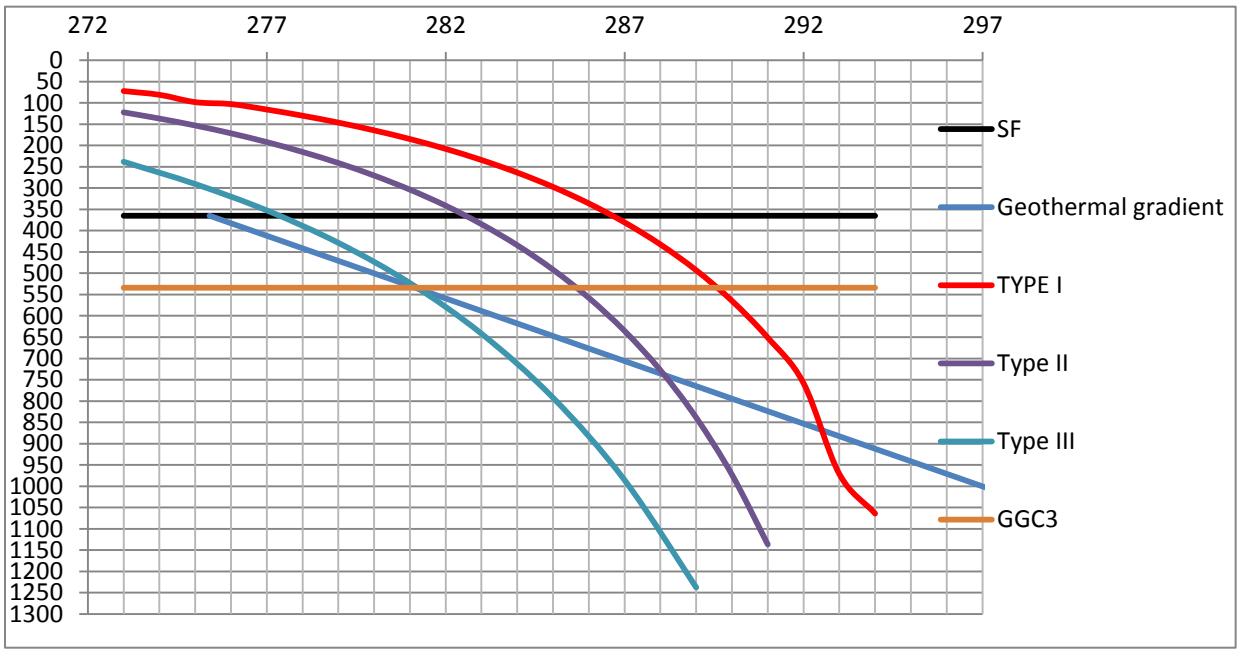

Diagram 4.3 Stability zone for gas hydrates at location of GGC3 with different gas composition calculated with the program CSMHYD (Sloan, 1998c) assuming a hydrate structure 2. The geothermal gradient used for the calculation is 33.8°C.

GGC3 is located in an area with an average water depth of 365m where the calculated BGHSZ is at 535m with gas composition Type III, 740m with gas composition Type II and 860m with gas composition Type I. The observed GGC3 top is situated at 534m, 0.2% shallower than the calculated Type III gas composition.

GGC4

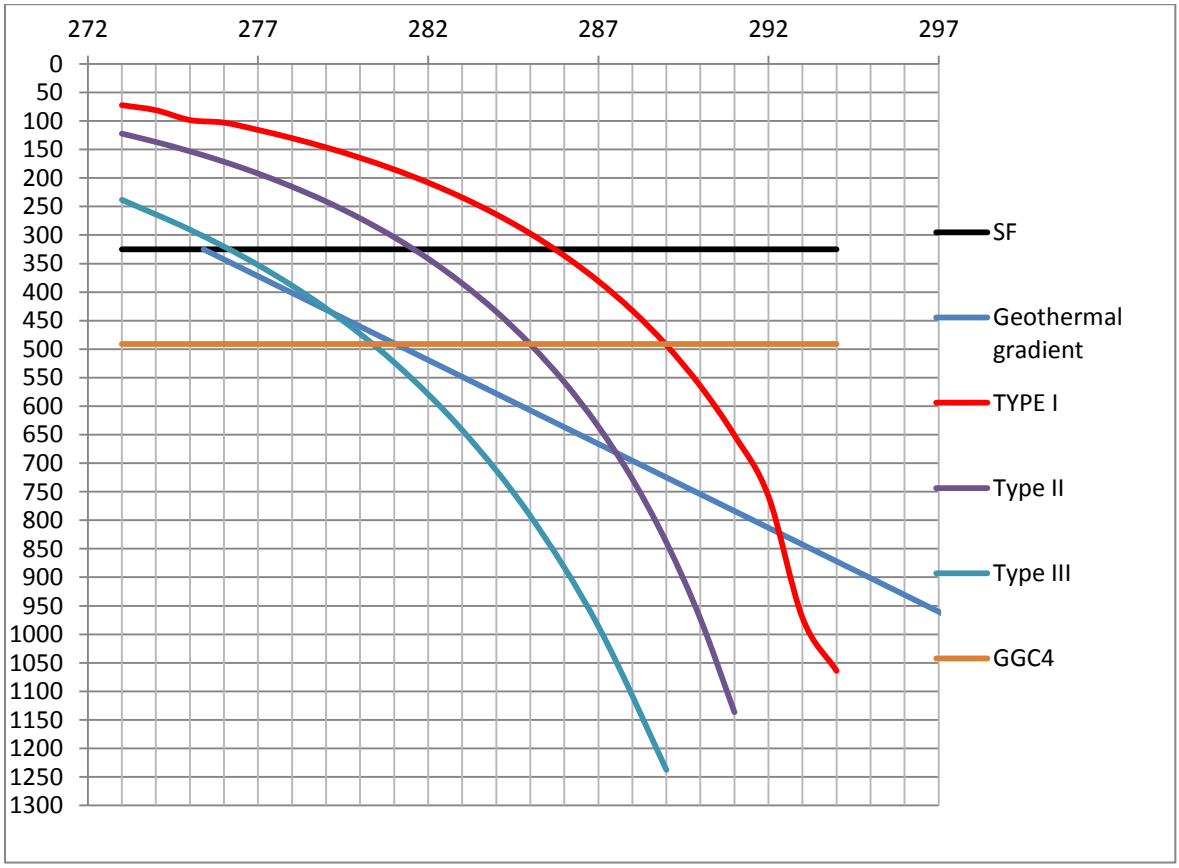

Diagram 4.4 Stability zone for gas hydrates at location of GGC4 with different gas composition calculated with the program CSMHYD (Sloan, 1998c) assuming a hydrate structure 2. The geothermal gradient used for the calculation is 33.8°C.

GGC4 is located in the shallowest water-depths of the study area (491 m) where the calculated BGHSZ are at 440 m with gas composition Type III, 680m with gas composition Type II and 825 m with gas composition Type I. The observed top of GGC 4 is situated on ~491 m, ~12 % deeper than the calculated BGHSZ for Type III gas composition.

AA6

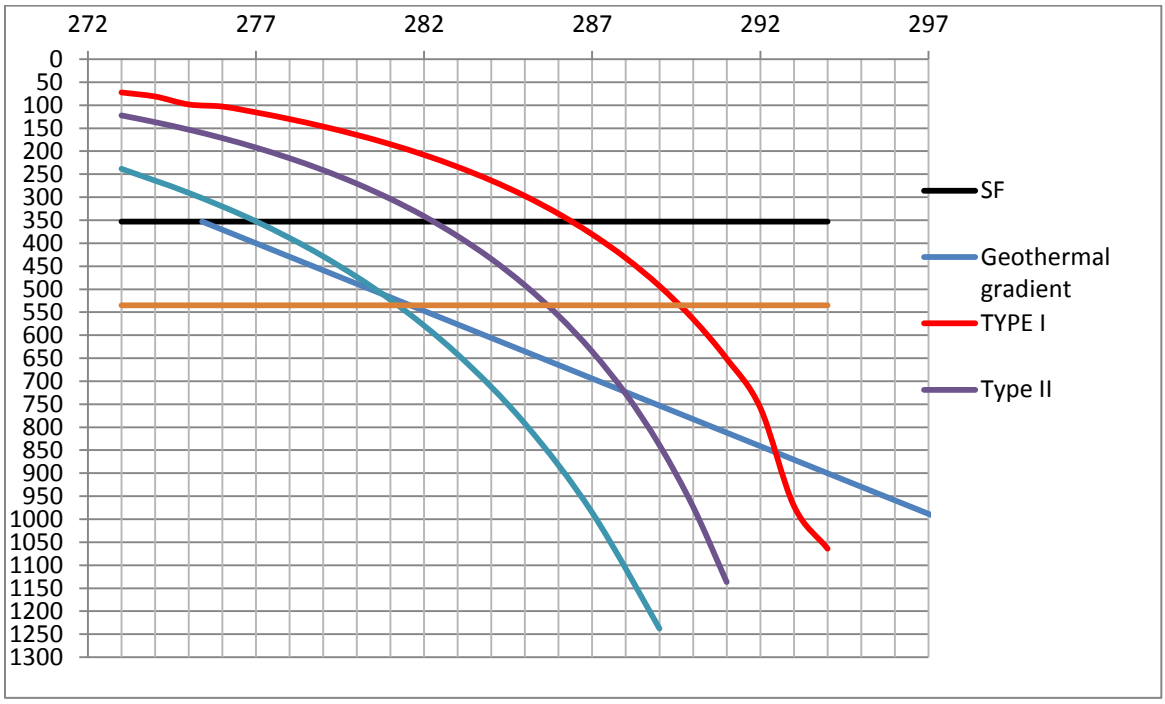

Diagram 4.5 Stability zone for gas hydrates at location of AA6 with different gas composition calculated with the program CSMHYD (Sloan, 1998c) assuming a hydrate structure 2. The geothermal gradient used for the calculation is 33.8°C.

Amplitude anomaly 6 is situated in an area with average water depth of 353m where the calculated BHGSZ are at 525m with gas composition Type III, 725m with gas composition TypeII and 855m with Type I. The top AA 6 is observed at 535m, 2% deeper than the calculated BGHSZ for Type III gas composition.

AA7

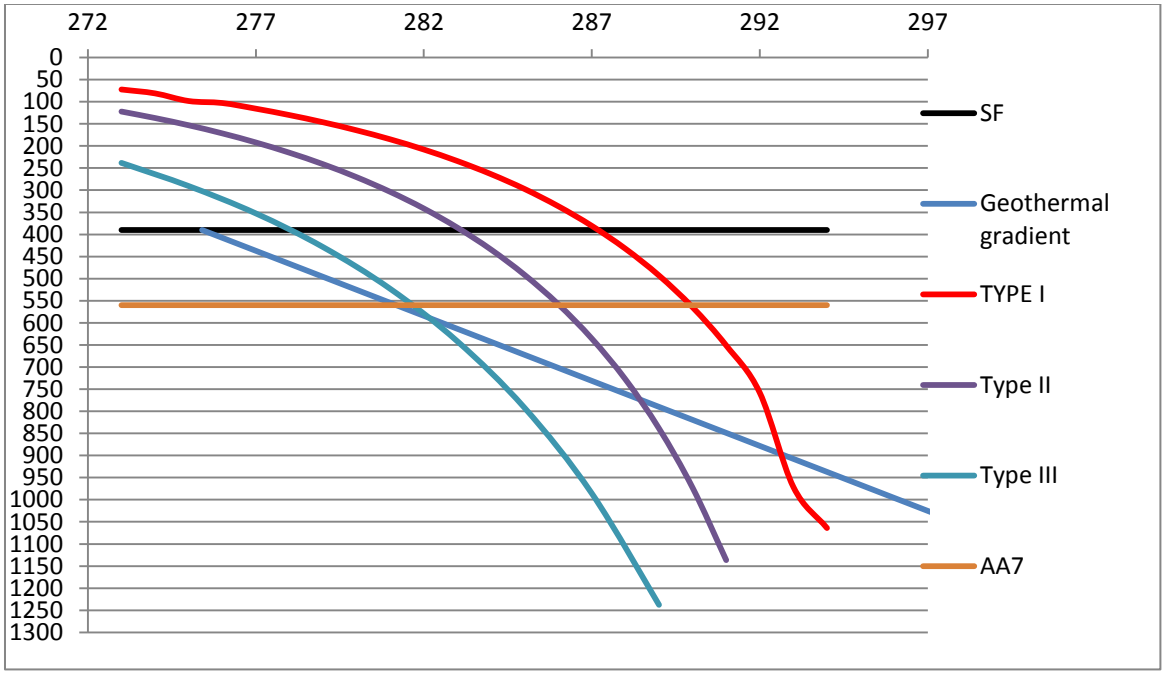

Diagram 4.6 Stability zone for gas hydrates at location of AA7 with different gas composition calculated with the program CSMHYD (Sloan, 1998c) assuming a hydrate structure 2. The geothermal gradient used for the calculation is 33.8°C.

AA 7 are located in an area with water depth of 390m where the calculated BGHSZ are at 590m with gas composition Type III, 775m with gas composition Type II and 895m with gas composition Type I. The top AA7 is observed at ~560m, 5% above the calculated BGHSZ for Type III gas composition.

AA11

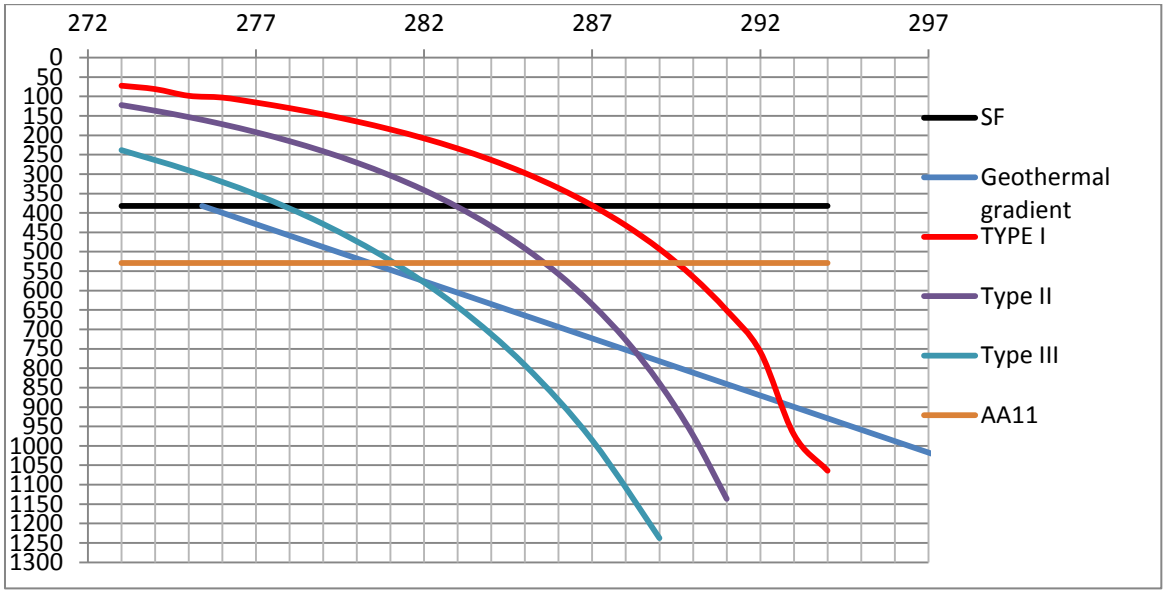

Diagram 4.7 Stability zone for gas hydrates at location of AA11 with different gas composition calculated with the program CSMHYD (Sloan, 1998c) assuming a hydrate structure 2. The geothermal gradient used for the calculation is 33.8°C.

AA 11 are located in an area with water depth of average 382m where the calculated BGHSZ are at 575m with gas composition Type III, 760m with gas composition Type II and 890m with gas composition Type I. The top AA7 is observed at ~529m, 8% above the calculated BGHSZ for Type III gas composition.

Seafloor (m)	Name	BGHSZ(m) TYPE III	BGHSZ(m) TYPE II	BGHSZ(m) TYPE I	Observed depth of Top anomaly (m)	Difference from Type III (%)
408	GGC1	625	800	920	589	6
405	GGC2	620	790	920	575	7
365	GGC3	535	740	860	534	0
325	GGC4	440	680	825	491	-12
353	AA6	525	725	855	535	-2
390	AA7	590	775	895	560	5
382	AA11	575	760	890	529	8

Tabel 4-8 Summary of BGHSZ calculation for GGC1, -2, -3. -4, AA6, -7 and -11.

5 Discussion

The discussion focuses on large scale fluid migration systems in the Bear Island fault complex and its associated geological process. The main objective of the discussion is to evaluate the different fluid flow features observed in the 3D seismic cube “West Loppa 2008” described in chapter 4. A large number of extraordinary vertical fluid-flow features and fluid accumulations have been identified in the 3D seismic data. The discussion aims at identifying common mechanisms, relationship and geological process that control fluid flow in the study area instead of explaining every fluid-flow feature in specific detail.

This chapter starts with a discussion of the geological settings and tectonic and sedimentary processes that might affect fluid flow. Thereafter, the distribution and origin of fluid-flow features are discussed. The presence of gas hydrates is assessed based on observations at the upper termination of the fluid-flow features, and an estimate is given for the total volume of sediments affected by fluid flow and its potential gas content. Finally, the discussion summarizes all observations in a conceptual model.

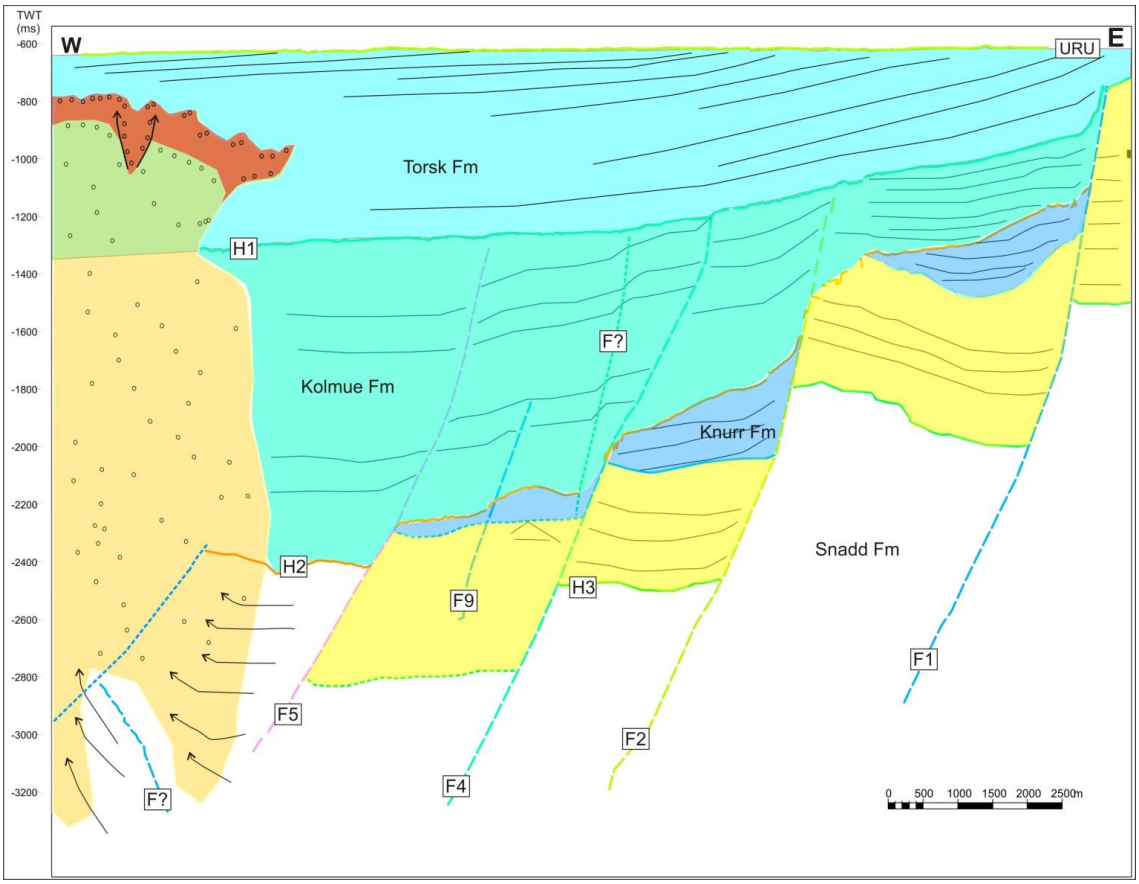

Figure 4.41 Preliminary sketch of the GGC1 area. IntraH3 sediments are labelled as yellow.

5.1 Faults and stratigraphy

The “Bear Island Fault Complex” exists of large asymmetrical listric fault blocks oriented in a NE-SW direction (Chap.4.1) and is limited in the west by the Polheim Subplatform which is a transition zone from the Mesozoic high “Loppa High” (Fig.4.2.1) and the Bear Island Fault Complex which transforms into the Bear Island – Tromsø basin in the West. The observed tectonic setting according to the faults can be divided into two different (W-E and N-S) major stress regimes.

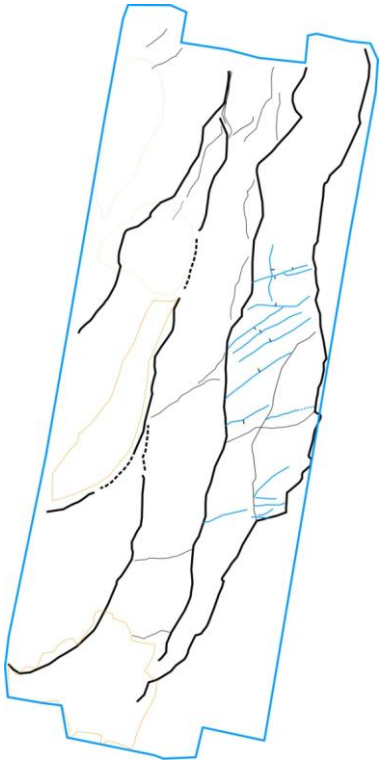

Figure 5.1.2 Fault overview, solid black are the main faults, black are small and blue are the intraH3 faults on block 1. For fault labelling see figure 4.2,1, -2 and -3.

First, the working area part of Bear Island fault complex is mainly dominated by the five large asymmetrical normal faults (Fig.4.2.1), connected with the fault blocks. These are oriented in a NNE-SSW direction (Fig.5.1.2-black) and are mostly laterally extensive throughout the whole dataset (>20 km, Tab.4-1). The upper termination of the faults is H1, which are equivalent to the base Tertiary (Torsk Fm). The faults limits the Polheim Subplatform and Loppa High and are believed to be formed during the creation of the Bear Island-Tromsø Basin and Loppa High in early Mesozoic with several reactivations throughout the Mesozoic (Gudlaugsson et al., 1998). There are several smaller faults (Chap. 4.2) limited by these major ones but are not as dominating. Nevertheless these are also believed to been active in the same period of time due to the termination within intraH2 and H1 (Fig.4.2.1 and Tab.4-2).

Second, limited by the “main” and “smaller” faults are a group of faults terminated by the erosive surface H2. These “intraH3” faults (Fig.5.1.2-blue) are oriented SWW-NEE (Table 4.3) implicating a slightly more N-S stress regime than for the N-S oriented faults. The variation in fault axis (Tab.4-3) and folding observed in the intraH3 sediment sequence (Fig 4.3.5.3) Indicates compressional forces. It is assumed that there are the same type stress regime within intraH3 in fault block 4 and 5, but due to the depth block 4 and 5 and the acoustic masking in the area the resolution of seismic is believed to be to poor for identification. These faults are believed to correlate with palaeo tension in the subsurface from the Caledonian orogonesis (Nøttvedt et al., 1992).

There are indications for the faults to be controlling and limiting the stratigraphic extension. The intraH1 (Torsk Fm) are increasing towards southwest, while the intraH2 (Kolmue Fm) are increasing

towards northwest (Fig.4.2.1) where fault 1 are located on the shallowest stratigraphic depth. The increasing depth (800 ms-1200 ms twt) into the basin and less throw for the shallower stratigraphic layers indicates the faults to been active while deposition. There are several depressions following a west-east direction on H2 (Fig.4.1.6) cutting down into intraH3 sediments with correlations to the faults (Fig.4.3.5.3-H3-B1). Such depressions may represents incised paleo valleys (Veeken, 2007), which indicates a flow regime westwards, correlated with the westwards dipping clinoforms the depositional sequence of intraH2 is most likely to originate from east (uplifted Loppa High). However IntraH3 faults shows no indications of being active while deposition.

During the tilting of the asymmetrical fault blocks in correlation with depression of the Bear Island- and Tromsø basin there are indications of locally forming basins on the eastern part of the fault block 1-5 which are represented to be Knurr-Kolje Fm (Fig.4.1.6). During deposition of theses mini basins the stratigraphic height of intraH3 sediments are believed to be eroded (Fig.5.1.3). The erosion interpretation is based on observed H2 surface and sequence stratigraphy.

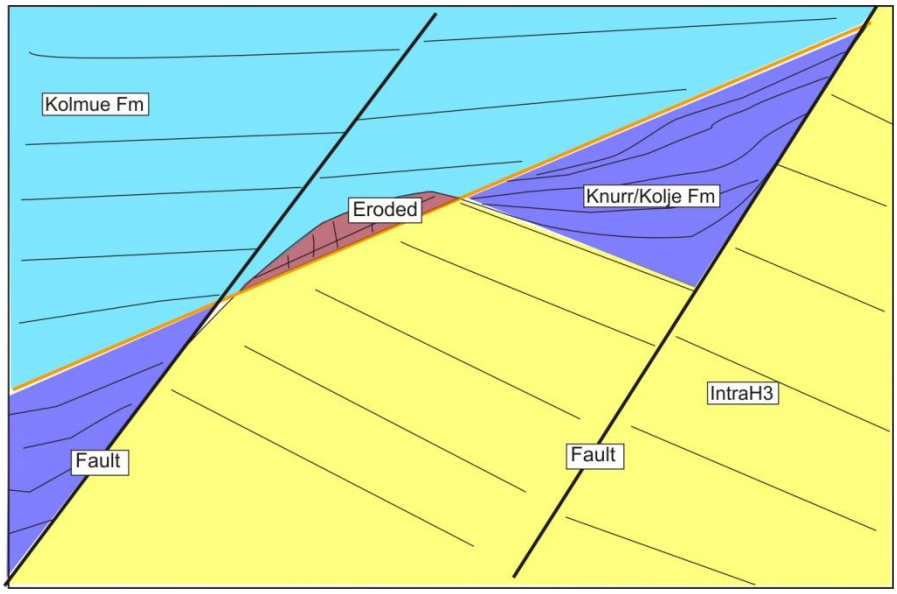

Figure 5.1.3 Interpreted sketch of the subsiding faultblocks related to deposition of Knurr/Kolje Fm and erosion. Figure is not to scale.

Faults are related to acoustic interference, as we can relate from almost all of the described fluid flow features has some contact with faults. Faults are proven to have an important role in migration acting as a seal bypass system (SBS) (Cartwright et al., 2007) and studies have shown that there is a 40% exploration success in areas with reported faults, while regions without faults the success rate is only 10% (Karlsen and Skeie, 2006). Earlier studies of the Barents Sea have shown a close relation between faults and migration (Andreassen et al., 2007a; Chand et al., 2008; Chand et al., 2009). Therefore the faults are believed to have a great importance for the features that will be discussed in the following chapters.

5.2 Fluid flow features:

An important aspect of this thesis is to discuss why and how the different fluid flow features occurs where they do.

First we need to understand where the lighter fluid (hydrocarbons) originates from. This includes knowledge of the occurrence and burial history of the source rock. Figure 2.5.1 presents the different source rocks deposited in the Barents Sea where penetrated formations in reference well 7219/9.1 are indicated. Based on the amount of source rock in area one can assume that the Barents Sea is a very promising area regarding hydrocarbon generation due to the amount of potential rich source rock represented in the area (Ohm et al., 2008). Unfortunately reality always has more than one factor which makes it more complicated. Maturity studies of the source rocks sampled in the S-W Barents sea indicates a larger depth than they are sampled at (Ohm et al., 2008). This is correlated with what we already mentioned in (Chap.2) that the Barents Sea has been under the influence of heavy uplift and major glacial erosion during late Cenozoic (Fig.5.2.1). It is believed that this huge removal of sediments has caused a great pressure and temperature decrease which has affected the fluid flow system (Vorren et al., 1991). Iver Martens (Martens, 2009) estimated an volume expansion increase between 32-42 % of gas in the "Snøhvit" field calculated with a 1000m uplift and erosion. As indicated on figure 5.2.1 the maturity for Hekkingen Fm and Triassic source rocks are mature in the exact location of the working area. Indicates primary migration as a possibility and will be further reviewed in Chapter 5.2.1.

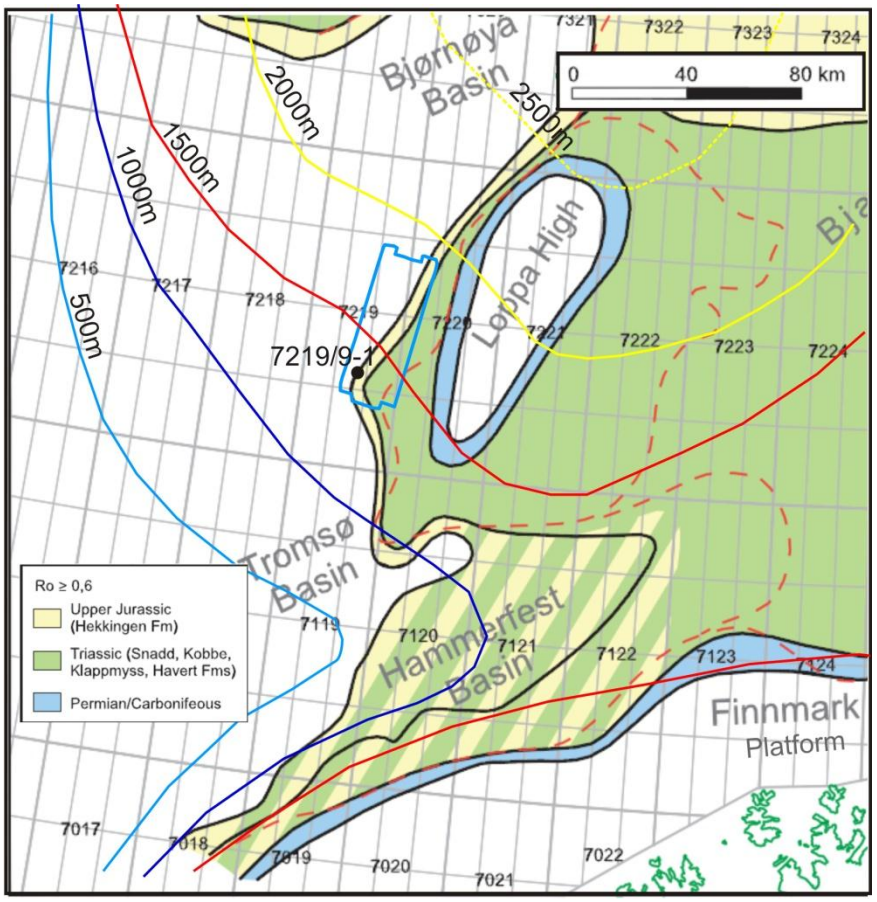

Figure 5.2.1 Geological map indicating the extension of oil mature source rock in representative stratigraphy based on maturity data from wells (R_0), semiregional trends and depth maps. Labelled lines indicate the respectively amount of sediments uplifted and eroded of the late Cenozoic major glacial events, based on vitrinite data.
(figure modified from (Ohm et al., 2008).

The main structural area in the dataset "West Loppa 2008" is the "Bear Island fault complex". The Sub Polheim platform which is east of fault 1 is not included in the fluid flow estimations. Still there can be a large flux with fluids breaching F1 and accumulates in intraH3 sediments west of F1 and vica versa. Dahl (2011) suggested a hydrocarbon input accumulating on Loppa High from Bear Island fault complex through these faults. AA9 are located within intraH3 sediments on the Sub Polheim platform (Fig.4.3.4.6) and may represent an accumulation.

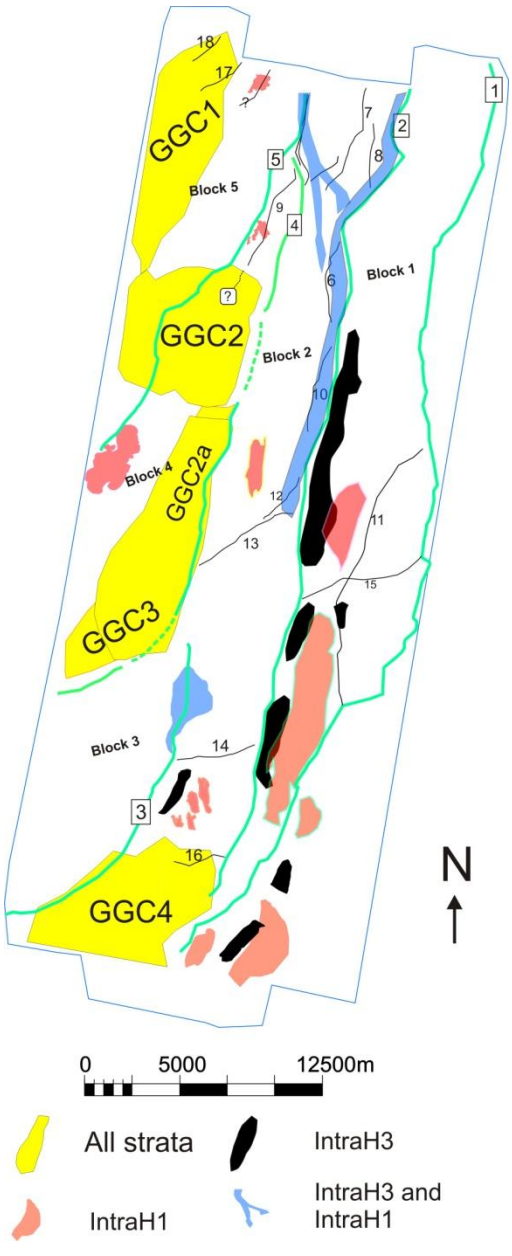

Figure 5.2.2 Over-viewing the different fluid flow features visualized based on stratigraphic depth.

In the working area west of F1 are there multiple possible fluid migration patterns and accumulations (Fig. 5.2.2) both along faults and horizontal dipping strata.

We assume that leakage have to originate from below H2, this is due to the lack of reservoir and source rock in the strata above. IntraH3 sediments are very promising both regarding source rock potential and reservoir rock (NPD, 2010) which can lead to both primary and secondary migration. Due to complex geology and different erosion levels on the H2 surface through the whole area makes it hard to determine the different stratigraphic layers within intraH3 regardless of available well data. In the reference well 7219/9-1 Knurr, Hekkingen and Fuglen was encountered before the potential reservoir rocks (Table 2.1). Stø-, Nordmela-, tubåen-, and interbedded sandstone layers in Snadd Fm are potential reservoir rocks and may be accumulated with hydrocarbons and be the source for secondary/tertiary migration. Fuglen- and Hekkingen Fm are the most promising source rocks where primary migration can occur. Also interbedded coal layers in Nordmela-, Tubåen-, Fruholmen- and Snadd can produce gas (Chap.2) which will be a source for migration fluids. Fruholmen-, Fuglen, Hekkingen-, Knurr-, Top intraH3 sediments (Fuglen and Hekking Fm) are impermeable, but due to different erosion levels the height of these are unknown. Kolmule- and Torsk Fm are partly impermeable and will act as seals where the SBS can occur (Fig.4.3.3.4c).

5.2.1 Distribution and extent of fluid migration features

The distribution of fluid flow features are of major importance to map. This is for determine the origin of the fluid flow system. Identifying the lower termination of the fluid flow features may relate to one specific stratigraphic layer and may suggest an interval were the fluid source may be.

The main fluid flow features in this thesis are the GGC's (Fig.4.3.1.1) which can be traced deep into the subsurface (<4000m TVD) (Chap.4.3.1-2-3-4-5). Were the base of the chimneys are varying from ~3200 ms to ~4000 ms TWT (Tab.4-4). This may not be entirely true because of the acoustic masking may have decrease the seismic energy (frequency and amplitude) in the current area, making the strata beneath invisible. GGC 1,-2,-2a-3,-4, are observed in contact with the intraH3 sediments which top occurs at different depths (3135m – 1098m TVD), GGC1 at the deepest in the north and GGC4 shallowest in the south (Fig.4.3.1.2, -6, -10, -17, Fig.4.2.1 and Fig. 4.3.3.4). IntraH3 sediments are as already mentioned (Chap 2.3 and Chap 5.2) possible source of hydrocarbons both as secondary migration from porous sandstones and primary migration (expulsion) from organic rich source rocks. GGC 1 occurs in contact with intraH3 sediments at the greatest depth in the dataset where we also have to assume the greatest pressure and temperatures. Assuming a geothermal gradient of 35°C (Chand et al., 2008) the estimated temperatures at top intraH3 are ~109°C meaning the source rock is within the maturity window (Chap.1.2). It must be taking into consideration that the recent uplift of ~1500m has changed the temperature significantly ~40°C in a relative short geological time frame. The orientation of the GCC 1 are the same as F5 (Fig. 4.3.1.3 and 4.3.1) indicating a leakage limited by the fault plane (Fig.5.2.3).

GGC 2, -2a and -3 are located on the structural block 4 (Fig. 4.3.1.6, -7, -10 and -12) were the H2 is shallowing southwards. Estimations indicate a top H2 temperature between ~107°C - ~70°C also within the oil generation window. Fault 4 is limiting the eastern boundary which indicates a leakage from intraH3 sediments in block 2, where temperatures would be below the estimated from top H2. The estimated thickness of IntraH3 are to be equal to reference well 7219/9-1 (Tab.2.1) the base of IntraH3, Top Snadd Fm would then be situated at ~3000-4000m TVD. The limitation of the chimney related to faults are especially well documented on the southern part of GGC 3 where F4 is bending westwards and the acoustic masking follows the structural element F4 (Fig. 4.3.1.12).

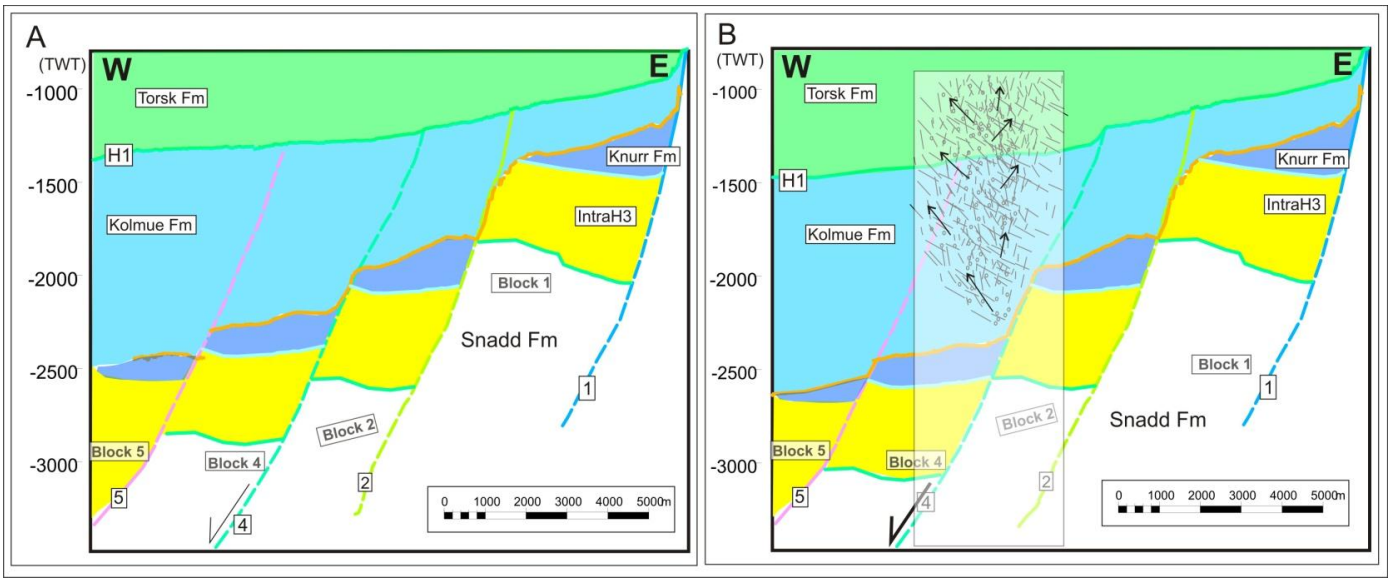

Figure 5.2.3 A) Geological situation pre gas chimney. B) Possible geological explanation of the GGC with an ongoing faulting of fault block 4, white transparent colour represents the acoustic masking area. Sketch is from the GGC2 area.

The location of GGC 4 occurs in the shallowest water depths (~325m) and H2 are only at ~1100m TVD, were the estimated temperature of top intraH3 sediments are at ~38.5°C. Applying the same thickness of intraH3 sediments as for the reference well the depth of top Snadd formation would be at ~2050m TVD where the temperature is estimated to be ~70°C. The interbedded coal layers within the Snadd Fm would be buried at even greater depths. GGC 4 is limited on the fault block 2c where fault 3 is a distinctive and abrupt separation of the GGC4 (Fig.4.3.1.14 and -16). GGC 4 may be connected with sedimentary rocks with including moveable fluids on the Polhem Subplatform where possible lateral migration can occur through fault 1 and permeable layers, however there are not seen any seismic proofs for this.

The importance of faults regarding the evolution of the GGC's has been suggested before. Kristensen (2010) and Dahl (2011) both described similar giant (horizontal extent >15 km^2) gas chimneys in the S-W Barents Sea (Loppa High) where it is concluded that acoustic masking and amplitude anomalies are related to faults. It has also been suggested that the acoustic masking creates a "shadow effect" of the underlying stratigraphic layers in areas with vertical migration (Fig.5.2.3). There are also located gas chimneys in both the North Sea at the "Tommeliten Alpha" field and the mid-Norwegian continental margin. At Tommeliten the chimney are lateral extensive of about 3 km circular wide area and vertical extensive through above 3000 ms TWT (Granli, 1999), but without a strong reflection coefficient reflector on top. On the mid-Norwegian continental margin there have been documented gas chimneys which has a vertical height from 92 to 820 ms twt and 0.1-0.7 km long axis, 0.1-0.4 short axis (Hustoft, 2010). Faulting and fractures are believed to be the essential drive mechanisms for forming the gas chimneys.

The smaller Medium sized gas chimneys (0.3-6 km^2) occurs as a cluster of high amplitude reflectors (Fig.4.3.2.1, -2) above H1 with corresponding dim spots and fault terminating beneath at H1 for MGC 1-2-3 (Fig.4.3.2.2).

Along the stratigraphic height of fault block 1 there are located flat reflectors crossing the original IntraH3 strata (Fig.4.3.5.4, -5, -6, -8 and -9). As already mentioned flat spots are a strong hydrocarbon indicator. The flat spot anomalies are limited within the intraH3 strata by erosion, Knurr/Kolje and the fault 2 (Chap.4.5). The lateral extent of FAA2.1 is ~9.5 km^2, but the height varies from < seismic resolution to 108m TVD (Fig.4.3.5.3). This seems to be controlled by IntraH3 faults and erosion of intraH3 sediments (Chap.4.3.5). In the thickest zones there are observed two flat spots separated by depth which may indicate the oil-gas contact and oil-water contact proven by the exploration well 7220/8-1 (NPD and OED, 2010). The flat spot anomaly is located within the IntraH3 sediment package which is assumed to be hydrocarbon rich. The fluid pathway is therefore estimated to originate within the same unit in the surrounding stratigraphy (Fig.5.2.4).

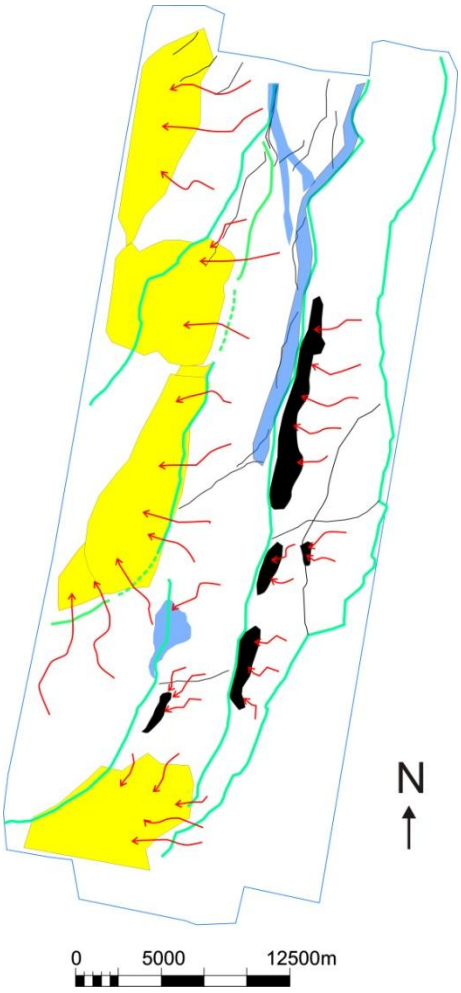

Figure 5.2.4 Potential fluid migration system from the intraH3 sequence.

Amplitude studies of the H1 indicate a zone of low amplitudes (PLZ 3) following the termination of fault 2 (Fig.4.3.3.4). The potential fault related leakage zone 3 may represent a SBS through Kolmue Fm along fault 2 where an accumulation in the hangingwall of fault block 3 represents the local zone of dimmed amplitude (Fig.4.3.5.6). Along most of fault 2 (Fig.5.2.2) there are indications of accumulation of different fluid densities, represented by the two depth separated flat cross strata cutting reflector (FAA 2.1-2-3, Chap.1.6.2 and Chap.4.3.5) as already mentioned may indicate a gas oil contact and oil water contact respectively.

The lower flat spot anomaly is terminated at the exact same depth (TWT) as the fault plane limiting the intraH3 sediments (Fig. 4.3.5.6 and Fig.5.2.5). May indicate that the fault are limiting and controls the accumulation of oil and gas and forms the spill point (Chap.1.2). Figure 5.2.5 is an interpreted geological model of the potential leakage zones 3.

One can observe the same process along fault 3 for PLZ 2 (Fig. 4.3.3.3), interesting observation here is that the PLZ first occurs north of fault 14 which throws the whole IntraH3 package down from 900

ms to 1400 ms TWT, placing the sediments at the same depth window as for PLZ1 and 3 This could relate the fluid escape of intraH3 sediments to be pressure controlled. Comparing PLZ2 with PLZ 1 and-3 indicating a more “eruptive” process and includes a cluster of high amplitude anomalies within intraH1 sediments (Fig.4.3.3.3) which can be the result of migration breaching into intraH1 (Torsk Fm). The eruptive characteristic of PLZ3 may be compared with the gas chimneys in a smaller scale or early stage of a gas chimney.

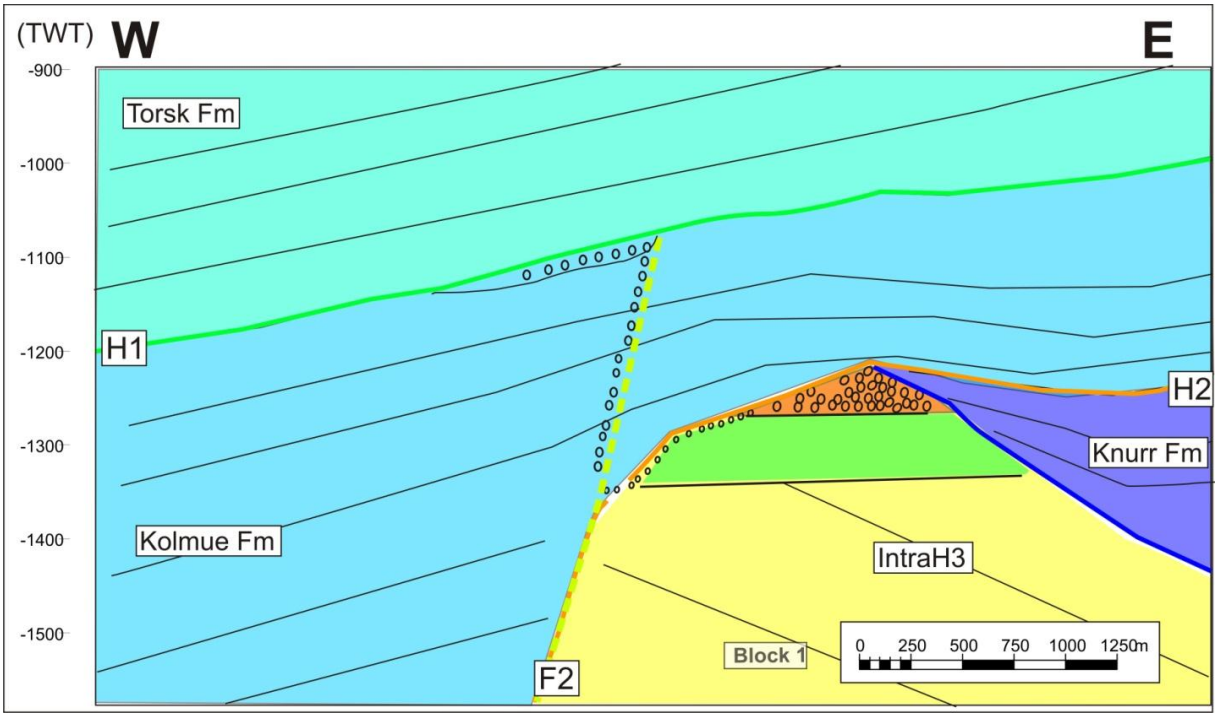

Figure 5.2.5 Potential leak zone 3 with correlation to FAA2.1 and the accumulation of hydrocarbons. Sketch is based on a seismic cross section of PLZ 3 and FAA2.1 (Chap.4.3.3 and 4.3.5).

From the cluster of bright spots within PLZ 2 there is a up dipping reflector with increased amplitude and can be followed directly up and into AA 6 (Fig. 5.2.6). This may be a possible fluid path way for the AA6. Amplitude anomaly 6 is a situated perpendicular to the interpreted dipping clinoforms of the Torsk Fm (Fig. 4.3.4.3) Situated in an elongated tube (lateral extension is 20 km^2 (Fig. 4.3.4.2) where top consist of a strong negative reflection with a strong positive flat reflector 108m TVD beneath (Fig. 4.3.4.3) which is a strong indication for shallow accumulation of gas (Chap.1.6). Acoustic masking is not observed in the area beneath, only weak push-down effect (Fig.4.3.4.3). This suggest that AA 6 may be a shallow gas accumulation. Shallow gas features are a typically observation in areas with high hydrocarbon potential due to the density differences and the high expansion factor of gas (Karlsen and Skeie, 2006).

An interesting discussion related to the distribution of gas chimneys is if there are a relation with the gas chimneys and hydrocarbon accumulation? There are proven accumulation on block 1 (Skrugard) (Fig.4.2.1) which is indicated as flat spots on the seismic (FAA2.1,-2,-3). The chimneys are absent on

block 1 and 2 excluding the GGC4 (block2c). GGC 2, -2a and -3 occur on faultblock 4 along F4 (Fig. 5.2.2, -3, -4, and -5). Block 4 is connected with block 2 in the northern part of the study area (Fig.5.2.2) and block 3 in the southern part. Reference well 7219/9-1 were drilled on block 3 showing only residual oil and gas in the same geological setting as for the Skrugard well on block 1. Together with the absence of flat spot anomalies on the fault blocks, IntraH3 sediments connected with the chimneys may be an indicator of a relation with the chimneys and accumulation of oil and gas (Fig.5.2.4). The absent of flat spot anomaly may also be because of lower resolution of the seismic data due to higher pressure and deeper in the subsurface (Chap.1.6).

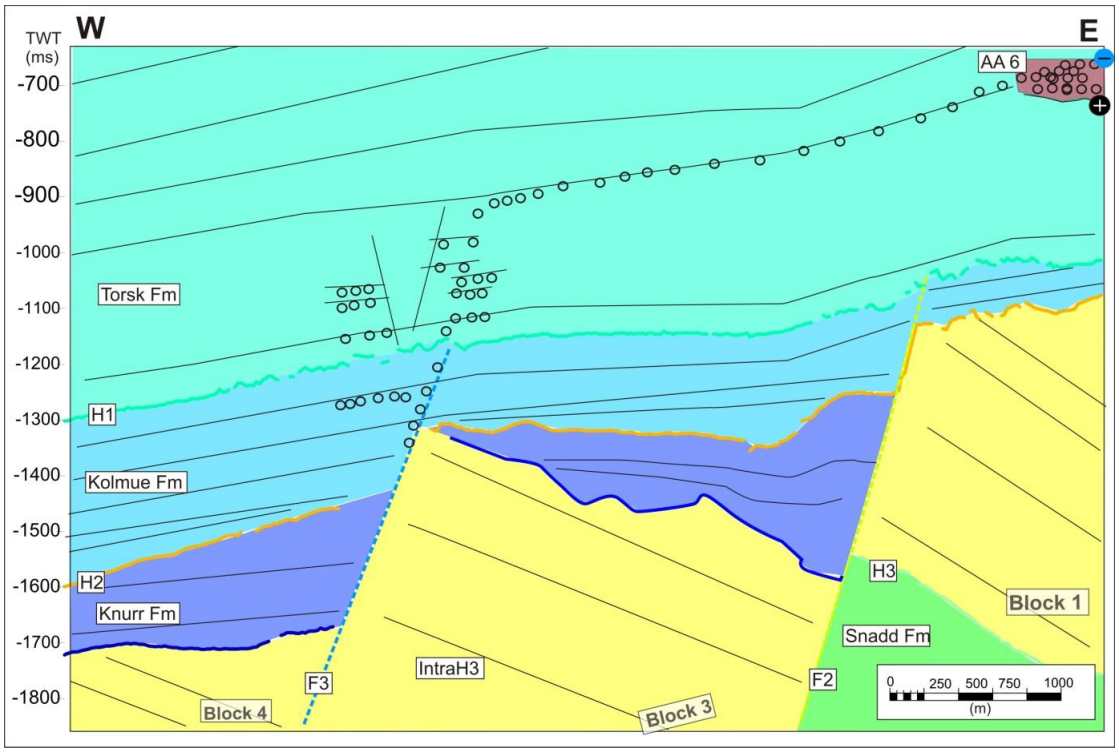

Figure 5.2.6 Schematic sketch of PLZ 2 in relation with AA6 and permeable layers.

Amplitude anomaly 5, -7, 8, -11 (Chap.4.3.4) occurs within intraH1 sediments with a lateral extension from ~2 km^2 - ~4.5 km^2. AA 11 are located in the same interval as AA6 (~5 km) and may be related to the same layer and process. AA 8 occurs in close proximity of GGC 4 (Fig.4.3.4.5) where possible flat spots are observed (Fig.4.3.5.3). Flat spots are due to density differences represented to be fluid contacts ((Andreassen et al., 2007a). AA7 is located in proximity of GGC2a and AA5 are north of GGC4. Common for all these described AA's are the occurrence along a dipping clinoform in the Torsk Fm, in proximity of one of the major GGC's and without relation with acoustic masking beneath. Kristensen (2011) suggested lateral migration of fluids will not have the same effect on the seismic signal as vertical migration and may be related to the lateral migration occurs in permeable layers. (Sylta, 2004) indicates that migration will occur confined and in conduits within an permeable layer while for low permeable layers the migration will occurs as undefined and diffuse.

5.2.2 Distribution of high amplitude anomalies within the GGC's

Due to the major events the GGC represents one need to separate the discussion of amplitudes anomalies within the giant gas chimneys to a separate chapter.

The major distribution of the GGC's are irregular, but majority of the gas chimney seems to be represented within intraH1-H2 sediments (Fig.4.3.1.6) which are equivalent to the Torsk- and Kolmue formation which is represented by silt/clay with interbedded silt/sandstones (Chap.2.4). Related with published literature gas chimneys are most likely to occur within fine grained sediments, (Karlsen and Skeie, 2006; Løseth et al., 2009) explained by diffuse migration.

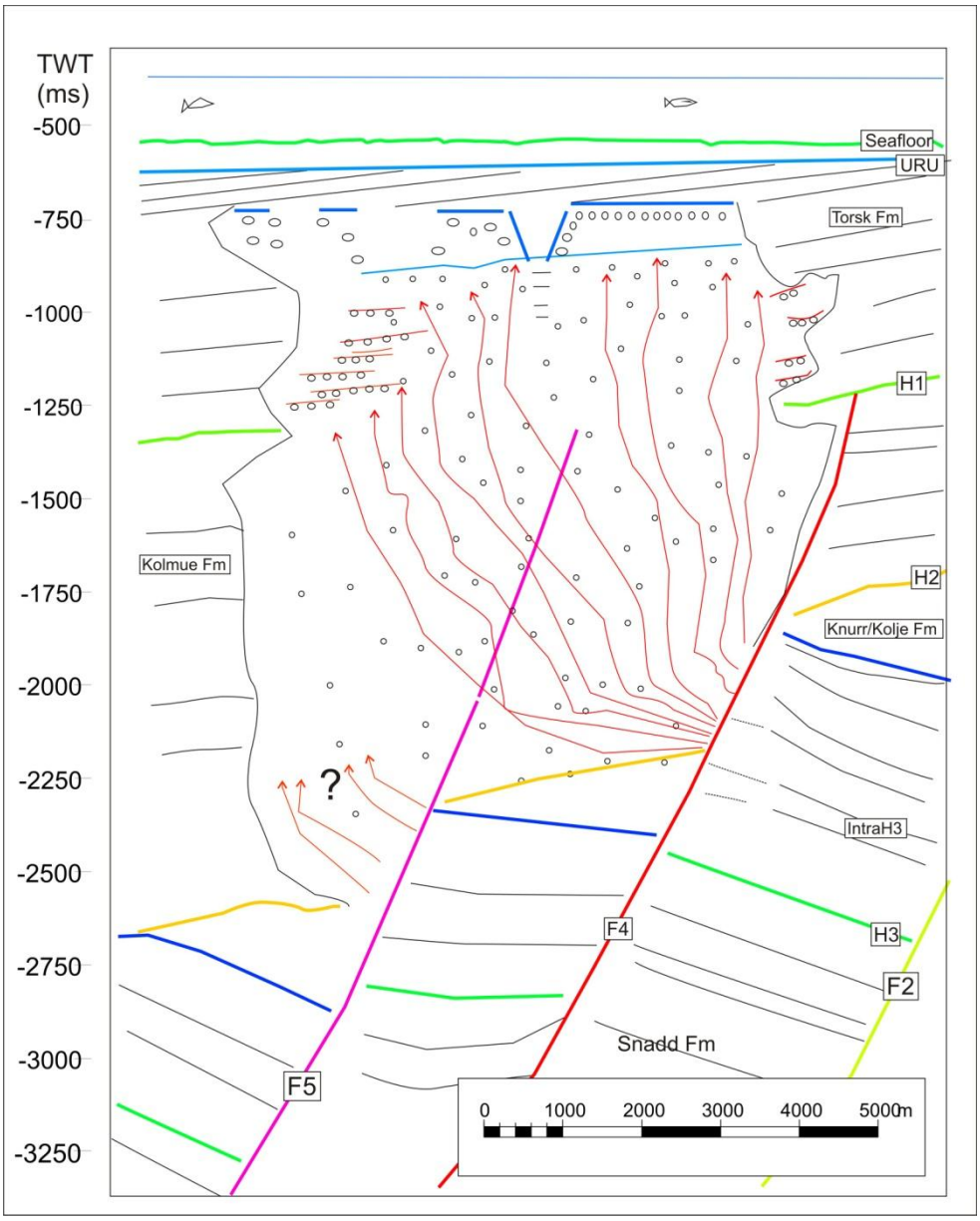

Figure 5.2.7 Sketch of GGC2 with focus on the interior distribution of reflectors and source. Note the difference in top anomaly continuity.

From studies of the GGC (Chap.4.3) there seems to be a larger portion of high amplitudes draping the chimneys (corona) in the Torsk Fm than in Kolmue Fm, such features are previous suggested to be gas carrying beds (Løseth et al., 2009). Due to anisotropy the permeability is higher horizontal than vertical in fine-grained sediments (Vasseur et al., 1995). The fact that there are more high amplitudes in Torsk Fm Indicating that there are more permeable layers (higher anisotropy) within Torks-, than Kolmue Fm (Fig.5.2.7).

Interesting observation on GGC 2 is the distribution of the corona. It seems to be more represented on the west part of chimney (Fig.4.3.1.6), which is regarding dipping strata downdip (Fig. 5.2.7). Assuming the high amplitudes (corona) represent permeable layers enriched with gas it should consider the normal laws of hydrodynamic migrates upwards / up dip (Gluyas and Swarbrick, 2004). In the Tommeliten field in the North Sea there is a gas chimney present, this gas chimney have been drilled though and implicates that the pore pressure within the GC's are significant higher (up to 100bar=10MPa) than the surroundings unaffected of the GC (Løseth et al., 2009). This indicates that permeable layers encountered regardless of dipping directions will be concentrated with gas. A possible explanation for the increased amount of high amplitudes on the western flank of GGC2 could be a litological changes, for instance a pinch out trap of a permeable layer. The Torsk Fm is known to deposit in open- to deep marine conditions (Chap.2.4) and the high amplitude area may represent a local contourite deposit. However, this is only speculations because the seismic quality is too poor for characteristics of the seismic signal in the area.

There are further implications regarding the western high amplitude area seen in GGC2. It seems to affect the interior and deeper part of the chimney ~3000 ms (Fig.4.3.1.6) which reveals a distinctive change beneath the interpreted zone of permeable layers in Torks Fm. Figure 5.2.7 shows the interpreted surfaces of the top GGC2. The eastern surface is continuous, flat and smooth, while the western surface is irregular and narrow. From the cross section profile (Fig.5.2.8) one can observe the dipping strata and the cross cutting reflector which represents the top GGC 2. Beneath the relative top GGC 2 reflector there is a negative polarity, but is dipping similar to the original strata (Fig.5.2.8). Based on the negative reflector this indicates a relative lower velocity layer. The western reflection pattern is irregular as the top and a larger push-down effect are seen relative to the eastern part of the feature (Fig.4.3.1.6). The narrow depressions are traced down to the second negative reflection (~143m TVD) and may indicate the relation of a release mechanism occurring. This top zone may indicate that the zone is filled with gas, while for the disturbed (western) area there are still a gas movement and the filling processes are currently occurring (Fig.5.2.7).

Concerning the deep strong amplitude anomaly (Fig.4.3.1.6) it may represent a lithological reflection where the limitation of it is a consequence of the movement / filling relation in the top zone or it could be an indication of source area for the chimney.

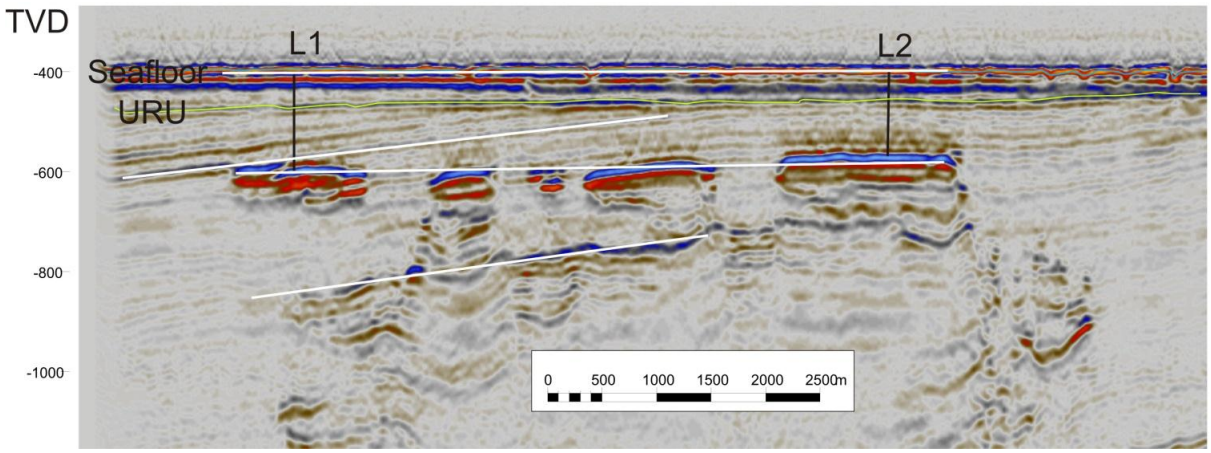

Figure 5.2.8 Seismic cross section of GGC2 top, where dips are indicated.

The filling process of GGC's may also be observed on GGC4 where there is a strong positive reflector dipping into the chimney (Fig.4.3.1.17) opposite to the original strata which may indicate a pore fluid contact (gas / water) and therefore the base of the shallow gas accumulation.

Comparing all the different top GGC reflectors one can observe the width of the narrow furrows occurring with the approximately same distance (~400-500m for GGC1,-2,-3) and are oriented NW-SE for GGC 1-2 and -3 (Fig.5.2.10). Top GGC 4 difference from the other top reflectors both regarding orientation (N-S) and width of the furrows (~300-400) which may be related to the shallow water depth of the location. The symmetry and continuity of these furrows may also be dependent on the cyclic of interbedded sand/silt stone layers where we assumed the enriched and already gas filled zones represents higher permeability layers (Fig.5.2.9). The deposition pattern of Torsk formation is not uniform and could represent the change seen for the GGC 4.

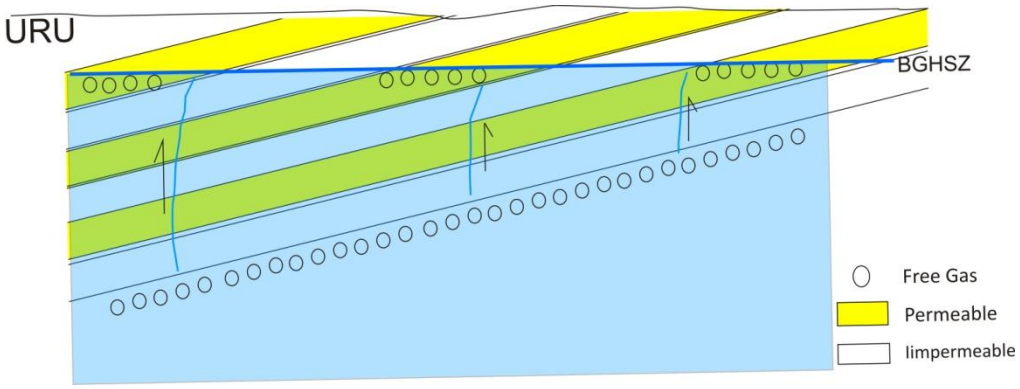

Figure 5.2.9 Sketch indicating a possible interpretation of the characteristic GGC tops.

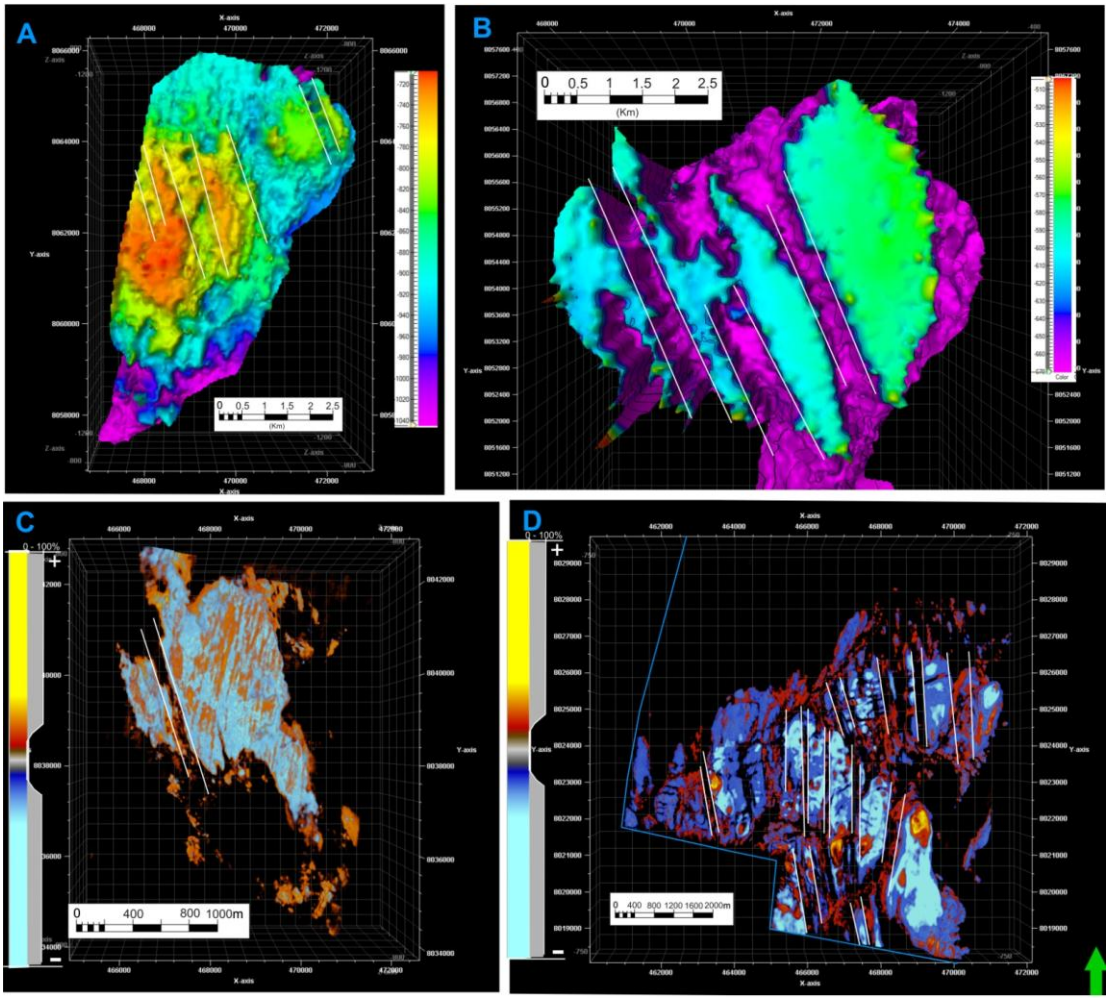

Figure 5.2.9 A) Interpreted top of GGC1 colour labelled according to scale. B) Interpreted top of GGC2 colour labelled according to scale. C) Volume render of GGC3 only showing high amplitudes as indicated at scale. D) Volume render of GGC4 only showing high amplitudes according to scale. All figures are oriented to the geographic north.

5.3 Mechanism for fluid flow

Pressure release of an accumulation is very important in an area where the overpressure has been changing (Karlsen and Skeie, 2006; Ohm et al., 2008) due to the density differences of oil and gas combined with the expansion factor of gas. Reduction in pressure of saturated oil causes liberation of gas. The amount are dependent on the type of oil and pressure release (Hamouda, 2010) which will decrease the fracture gradient of the cap-rock. Based on the major uplift from late Cenozoicum the estimated expansion of the already gas in place are as mentioned in chapter 5.1, 32-43% where the release of gases in oil are not included. This makes accumulation of oil unlikely to occur without refilling or active leaking while expansion occurring for the study area (Fig. 5.3.1). The recent discovery located within the FAA2.1 (Skrugard, (NPD and OED, 2010)) where the gas and oil column are verified as the first and second flat spot confirms oil accumulations.

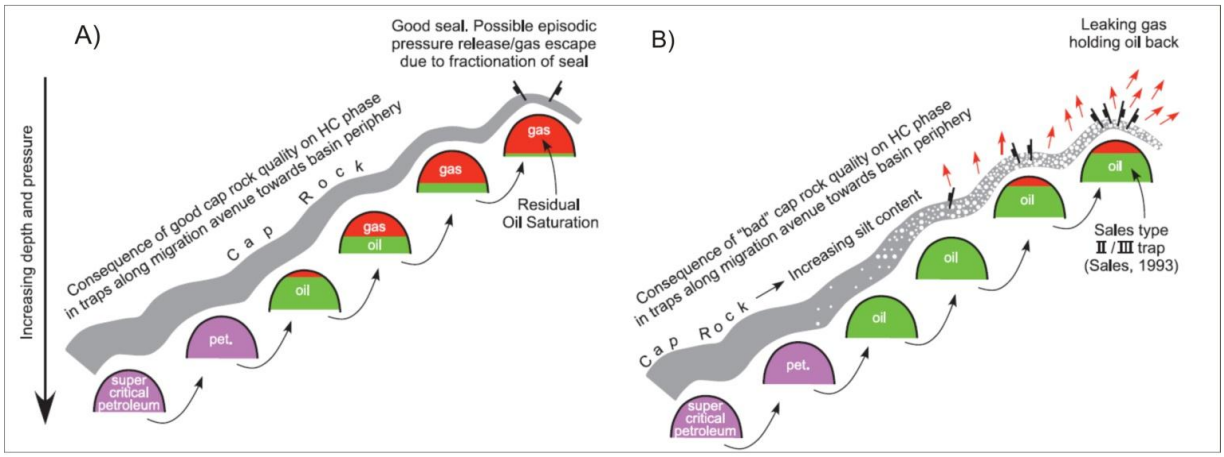

Figure 5.3.1 Schematic view of the process with a decrease of overburden. A) Shows a scenario where the trap seals of both gas and oil, while B) allows gas to migrate through low permeable siltstones and microfractures (Ohm et al., 2008).

As mentioned before the migration along faults seems to be an important fluid migration path way in the study area. Generally it is believed that faults act as both seals and pathways. There are been measured a high decease in porosity within fault zones due to grain size collapse (Knipe, 1992). However, under periods when the pore pressure exceeds a certain level due to expansion, fluid migration and removed overburden the fault zones can be highly permeable. Such zones are believed to only be “open” for a short period of geological time (Fig.5.3.2) and may act as a natural valve system for petroleum accumulation (Karlsen and Skeie, 2006; Knipe, 1992). The potential leakage zone 3 which is most likely a result of fault 2 may be a valve for the FAA2.1 system.

As suggested a leak from the traps may be a positive effect in areas with recent pressure release, due to the great expansion of gas phase compared to liquid phase providing shallow gas accumulations and deeper liquid phase accumulations. The recent major uplift in the area with subsequent erosion may have caused high enough overpressure to reactivate the faults (Fig.5.3.2) and the permeable properties.

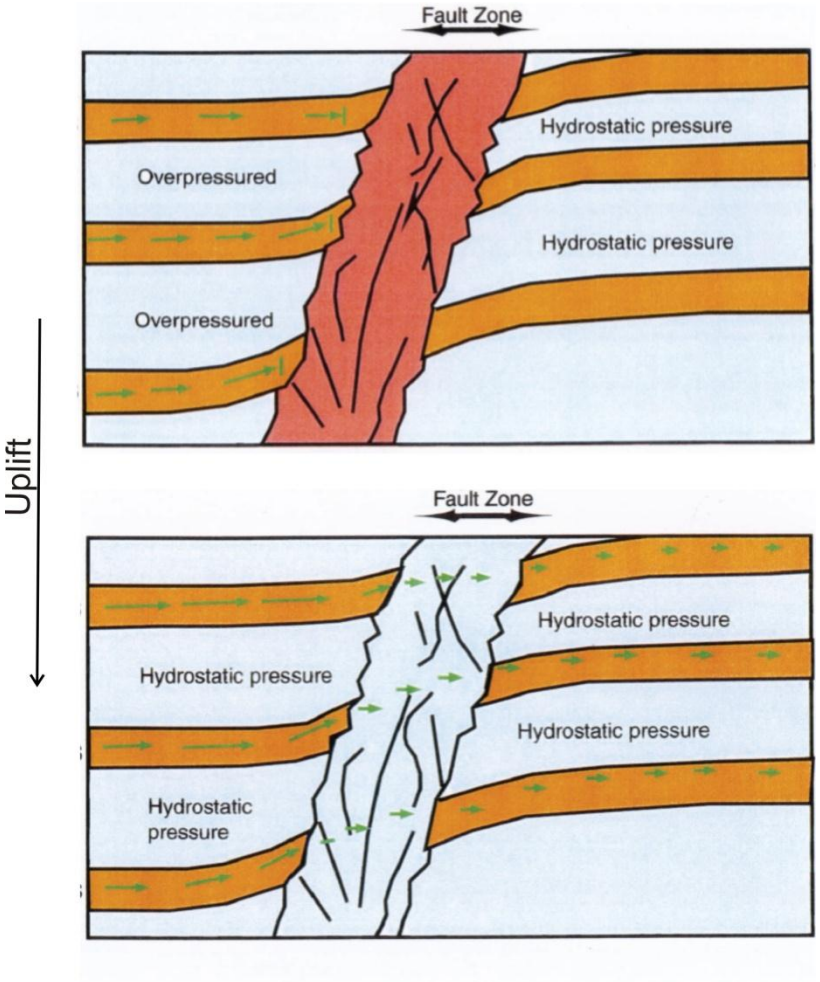

Figure 5.3.2 A) Overpressured zones before the major uplift in the Barents Sea. B) Reactivation of fault enables fluid flow between the permeable layers. Model modified from(Karlsen and Skeie, 2006).

The filling of GGC's tops are not completely understood or described in published literature. However I there are might an eruptive event related to it due to the low permeability sediments which demands pressure for migration. There might be a similar evolution as for the eruptive pockmarks in muddy sediments (Cathles et al., 2010).

5.4 Pitfalls for fluid migration

Crosscutting strata reflections are a strong fluid density variation indicator, but can be related to other geological features which have to be taken into consideration.

Piercement structures

Salt structure are a common structure present in the S-W Barents Sea (Henriksen and Vorren, 1996), and can cause a similar signature on the seismic image as for gas chimneys. Salt structures are known to increase the geothermal gradient (Laberg and Andreassen, 1996). The main observation which enables us to distinguish the chimneys with a salt structure is the negative polarity at top and the inconsistent top. Salt is knows to increase the compressional velocity therefore there would be expected a strong positive reflection at top salt.

Diagenetic effects

The diagnesis of fine grained silica rich sediments can result in a cross cutting reflector, which is caused by the transformation from Opal A to Opal CT which is controlled by temperature and pressure. Examples of cross cutting reflectors have been reported from the S-W Barents Sea (Knutsen et al., 1992; Riis, 1992). Diagnetic fronts are separated from fluid cross cutting reflectors because they are temperature controlled from 35-50°C (Berndt et al., 2004), which occurs at greater depth than for example the depth of gas hydrates. The diagnetic fronts will also cause an increase in density which in turn will cause an increase in bulk modulus and a positive reflection (relative to seafloor reflection).

Carbonate build up structures are known to cut the interior stratigraphic structure and has been related to gas emissions (Mazzini et al., 2006). Still these are local and not expected to cover a regional surface.

The observed cross cutting reflectors are observed together with phase reversal (Fig.4.3.5.2) and bright spots, therefore one can with confidence interpret the cross cutting reflections as fluid contrasts.

5.5 Gas Hydrates

The occurrence of Gas Hydrates has been proven in various locations around in the S-W Barents Sea (Andreassen et al., 1990; Chand et al., 2008; Laberg et al., 1998). As mentioned in chapter 1.7 the occurrence of gas hydrates may cause the host sediment to be impermeable and seal any upward migrating fluid (Dillon et al., 1980). Several “close to seabed cross cutting reflectors” are observed within the study area. Top GCC-1-2-3-4, AA-6-7 and -11 represents such reflectors. They occur roughly at the same sub bottom depth ~170m TVD as shown in diagram 5.1.

These are therefore interpreted to be a BSR with possible gas accumulation beneath.

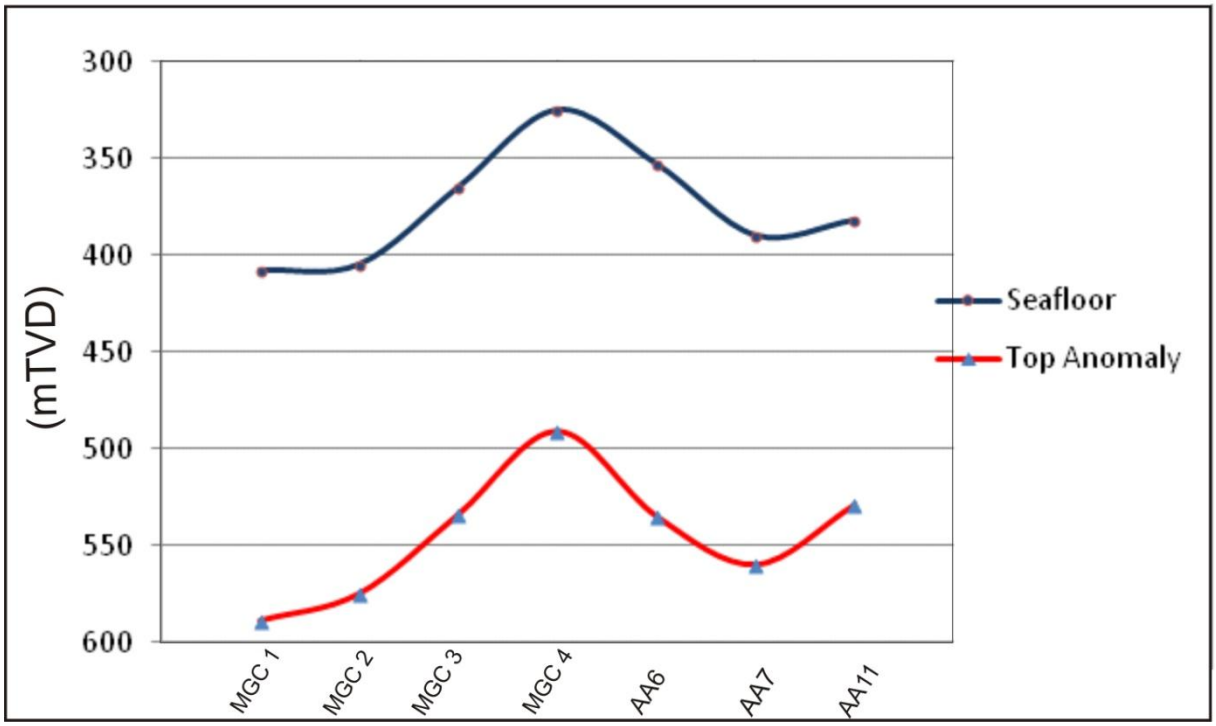

Diagram 5.1 Showing the distribution of top anomalies with relation to the seafloor.

Comparing all the stability zones (Diag.4.1,-2,-3,-4,-5,-6 and-7) suggest a gas composition of TYPE III, because all observed BSR features lie within -12% – 8% of the calculated BGHSZ with TYPE III gas composition (99 % Ethan and 1 % Propane) . There are many assumptions made for getting the calculation right (bottom water temperature, geothermal gradient, pore pressure within the sediments and gas composition) and these can easily compensate each other increasing uncertainties. However, gas compositions for Type I and Type II are reasonable and calculated to result in a BSR located at ~825-920m and ~725m-800m TVD respectively.

If the gas compositions are of Type I or Type II than there is a thermogenic source contribution. Which we must assume because of the petroleum potential in the area (Chap.5.2) However the observed BSR should be located deeper in the subsurface with such a composition according to the calculated BGHSZ (Chap.4.6). This leads us to the discussion of the geothermal gradient. If the geothermal gradient were higher the BGHSZ would be shallower due to higher temperatures at less depth / pressure. As mentioned before (Chap.1.7 and 4.6) there are several factors with uncertainties that may affect the BGHSZ. One possible explanation may be a local higher geothermal gradient within the chimneys due to an increased heat flux from the migrating fluids. Another uncertainty regarding the calculation of the BHGSZ is the bottom water temperature, which is known to be variable. A higher temperature would decrease the depth of BGHSZ.

The observed amplitude anomalies are terminating on the same relative subseabed depth as the GGC's (Tab.5.1). It indicates that they may have the same geothermal gradient as the GGC's.

Observations may also indicate a various heat flux regions that exists within the GGC's dirstral and central parts of the chimneys due to internal depth variations of the top reflector, especially on GGC4 (Fig.4.3.1.17).The top of GGC2 also shows different depth regardless of water depth (Chap.5.2.2). At this stage it is unknown whether the BSR related reflector depth variations are controlled by variations in heat flow or gas composition.

Dahl (Dahl, 2011) calculated the BGHSZ with applying the conditions that were valid under last glacial maximum, with a glacial thickness of 1250m which leads to an increase in pressure and reduction of temperature at seafloor which results in a extreme increase in thickness of BGHSZ (~1500m TVD).

The decrease in pressure and increasing temperature after the deglaciation period should have reduced significantly the BGHSZ and caused the released of large amounts of gas (Chand et al., 2008). Portions of that gas might be trapped beneath where one observes gas hydrates today.

5.6 Dimension and volume of fluid flow features

Estimating a total volume of the fluids one has to consider and determine the physical properties of the present rock. Table 2-1 provides a summary of well data from reference well 7219/9-1. Torsk and Kolmue formation consists of fine-grained sediments dominated by mudstone (Worsley et al., 1988) and have been proven to be capable as caprock (Chap.5.2). From table 2-1 and empirical mudstone porosities (Dewhurst et al., 1998) estimates the porosity to be 50 – 25 %. Data from reference well is measured with a neutron source, which calculates porosities based on the amount of hydrogen atoms detected. Neutron porosity data from 7219/9-1 present a high porosity reading in Torsk- and Kolmue Fm, which is due to the high water content in a silt/mud stone. Anyhow, the generally porosity is not connected and thus not permeable. Therefore one has to assume that in the interval where the giant gas chimneys occur, mainly Torsk- and Kolmue Fm are fractured (Chap.5.2). For the volume calculation I used an average porosity in Torsk and Kolmue Fm of 34 % (~15 % uncertainty).

We assumes intraH3 sediments as the source and origin of fluid migration and will due to several uncertainties not include these volumes in the calculations of fluid flow features, this estimate affects GGC4 the most since it is located on the shallowest fault block (Fig. 4.2.1), where also the Kolmue Fm are absent. The whole features within the IntraH2 and –H1 sequence will be used for volume calculations. As described in chapter 1.6 only small amounts of gas can already affect compressional wave velocity, (Thingnes, 2007) the estimated gas saturation is ~0.1 %. It is probably higher in accumulation intervals i.e. within interbedded layers, local traps and bellow gas hydrates. Therefore I have used 1% as the gas saturation in the MGC 2 and 3 due to their concentrated of high amplitude anomalies. Amplitude and flat spots anomalies have not been included into this calculation due to fact that they probably represent an already accumulation of fluid than fluid migration.

$$V_g = \frac{\phi \, x \, S}{100 x V} \qquad \text{Equation 15}$$

Equation for volume of gas, Φ = porosity and S= gas saturation

The different features have earlier been described and basic trigonometric equations are used to calculate area and volume.

Top (strata)	BSR	BSR	Torsk Fm	BSR	BSR	H1	H1	H1	Torsk Fm	Torsk Fm	Torsk Fm	
	GGC 1	GGC2	GGC2a	GGC3	GGC4	PLZ#1	PLZ#2	PLZ#3	MGC1	MGC2	MGC3	
Top (m)	589	575,0	814,0	534,0	491,0	1167,0	1147,0	1025,0	1100,0	933,0	1047,0	
Base (m)	3135	3080,0	1944,0	2041,0	1098,0	2315,0	1313,0	1530,0	1756,0	1078,0	1127,0	
												SUM
Area (km^2)	35,3	22,1	14,3	15,9	99,2	4,2	4,2	22,1	6,0	0,6	0,4	224
Height (km)	2,5	2,5	1,1	1,5	0,6	1,1	0,2	0,5	0,7	0,1	0,1	
Volume (km^3)	89,87	55,24	16,14	23,95	60,20	4,82	0,7022	11,1807	3,9360	0,09	0,03	266
Vg (km^3)	0,031	0,019	0,006	0,008	0,021	0,002	0,000	0,004	0,001	0,000	0,000	0,09
											Gas amount (km^3):	0,067

Table 5-1 Calculated volumes of the different GGC's. PLZ's and MGC's.

The uncertainty of the volume calculations are rather large (total 75 %). For the total gas amount the calculated volume is 6.7 x 10^7 +- 5 x 10^7 kg gas assuming STP[11] and 100% methane concentration of the gas with density of 0.72 kg/m^3 (Nordling and Österman, 2006), which provides additional uncertainty.

Uncertainty volume calculation	
Parameter	**Uncertainty (%)**
Porosity	15
Gas Saturation	50
Volume	10

[11] Standar Temperature, 293°K and Pressure, 0.1 MPa.

5.7 Conceptual Model

Leakage features are not unusual in the south-western Barents Sea and have been described and interpreted in several master thesis and articles before (Dahl, 2011; Kristensen, 2010; Lammers et al., 1995; Martens, 2009; Solheim and Elverhøi, 1985; Thingnes, 2007). The Cenozoic uplift and erosion caused by the opening of the Greenland – Norwegian Sea and the late Cenozoic deglaciation period (Faleide et al., 1984; Vorren et al., 1991) are related with gas expansion and the main drive mechanism for remobilization of different fluids (Laberg and Andreassen, 1996) (Fig.5.7.1).

The gas expansion and the overall uplift have increased the probability of fracturing the sealing rocks (Doré and Jensen, 1996). The migrating fluids are assumed to originate from both already accumulated reservoirs (secondary migration) and generated from source rock in an active kitchen (primary migration) within the IntraH3 sediments and interbedded coal layers within the Snadd formation (Chap.5.2.1; Fig.5.7.1). Recent published literature suggests an even more rapid deglaciation of the Barents Sea ice sheet than prior assumed (Laberg et al 2011 and Knis et al 2010). The rapid deglaciation would lead to a sudden pressure decrease, which enforces the theory for sudden gas expansion, causing fracturing and migration.

Based on the observed BSR features, the migration of free gas is believed to be sealed by gas hydrates (Fig.5.7.1) and by the irregular surface of the top chimneys together with interior reflectors the migration is believed to still be ongoing.

There is a difference between the seismic response of fluid accumulation and fluid flow in a horizontal and vertical plane. This may very well be dependent on the lithological changes. In figure 5.7.1 the area shaded with grey indicates the chimneys and the area affected by acoustic masking of the seismic signal.

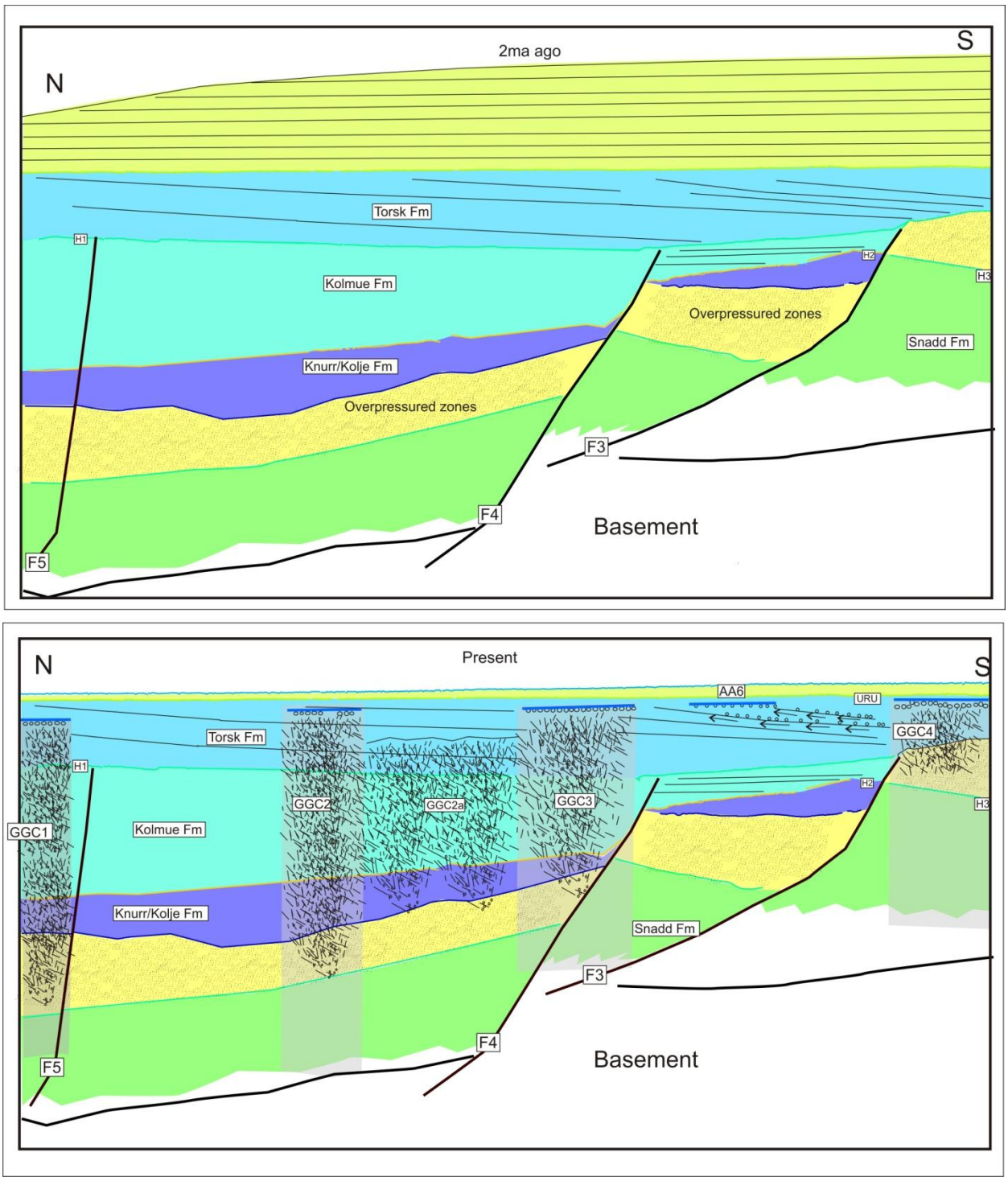

Figure 5.7.1 Interpreted sketch of the study area seen from west were horizontal migration towards AA6 are projected. Gray shading indicates area affected by acoustic masking. Figure is not to scale.

6 Conclusion:

The three-dimensional seismic survey “West Loppa 2008” allowed seismic interpretation and visualization of exceptionally large fluid-flow features along the Bear Island Complex in SW-Barents Sea.

The following fluid-flow related features were identified in the 3D seismic data in the study area:

- 5 giant gas chimneys (GGC) with a height of ~4000 ms to ~600 ms TWT, covering a total area of ~187 km^2.
- 3 medium size gas chimneys (MGC) with a height between ~1750 ms to ~1020 ms TWT, covering in total an area of 7 km^2.
- 3 potential leakage zones (PLZ) crossing strata between ~2000 ms to ~1350 ms TWT, over a total area of ~30 km^2.
- 6 amplitude anomalies (AA) occurring between ~640 ms to ~1060 ms TWT, covering in total an area of ~37 km^2.
- 3 flat spot amplitude anomalies (FAA) which rather represents an accumulation of different fluid densities than migration, occuring in strata between ~850 ms to 1320 ms TWT, covering in total an area of ~15 km^2.

The Giant Gas Chimneys are a result of vertical migration of gas through micro-fractures which causes an irregular compressional velocity response which leads to scattering and attenuation of the reflected seismic wave causing that large area are acoustically masked.

Horizontal migration along permeable layers and accumulation of hydrocarbons do not cause acoustic masking.

Most of the gas chimneys shows a BSR at its upper termination indicating the presence of gas hydrates within the sediments. The BSR coincides with the BGHSZ located at approximately 179 m TVD below seafloor. Gas hydrate stability modelling showed that a gas composition of 99 % methane and 1 % ethane corresponds to the observed BSR depth. Also, some of the amplitude anomalies (AA6, 7 and 11) coincide with the BSR depth and might represent shallow gas accumulations below a BSR.

High amplitude anomalies draping (corona) the GGC’s within the Torsk formation represent interbedded permeable layers enriched with gas.

Regional faults are the main contributor for the distribution and limitation of the giant gas chimneys. GGC2,-2a and 3 are limited along the western boundary of fault 4, while GGC4 are limited by fault 3.

The fluid flow features are calculated to contain 6.7×10^7 ($+- 5 \times 10^7$) kg gas in the study area.

The migrating fluids are believed to originate from already accumulated reservoir rocks within the IntraH3 sequence and generated from expulsion of organic rich source rock and interbedded coal layers within the IntraH3 sequence.

7 Reference

Andreassen, K., 2009, Marine Geophysics. Lecture notes for GEO-3123. University of Tromsø., p. 106.

Andreassen, K., Hogstad, K., and Berteussen, K. A., 1990, Gas hydrate in the southern Barents Sea, indicated by a shallow seismic anomaly: First Break, v. 8, no. 6, p. 235-245.

Andreassen, K., Nilssen, E., and Ødegaard, C., 2007a, Analysis of shallow gas and fluid migration within the Plio-Pleistocene sedimentary succession of the SW Barents Sea continental margin using 3D seismic data: Geo-Marine Letters, v. 27, no. 2, p. 155-171.

Andreassen, K., Ødegaard, C. M., and Rafaelsen, B., 2007b, Imprints of former ice streams, imaged and interpreted using industry 3D seismic data from the south-western Barents Sea: Application to Hydrocarbon Exploration and Production. Special Publication, v. 277, no. Geological Society, London, p. 151-169.

Archer, D., Eby, M., Brovkin, V., Ridgwell, A., Cao, L., Mikolajewicz, U., Caldeira, K., Matsumoto, K., Munhoven, G., Montenegro, A., and Tokos, K., 2009, Atmospheric Lifetime of Fossil Fuel Carbon Dioxide: Annual Review of Earth and Planetary Sciences v. 37, p. 17.

Arntsen, B., Wensaas, L., Loseth, H., and Hermanrud, C., 2007, Seismic modeling of gas chimneys: Geophysics, v. 72, no. 5, p. SM251-SM259.

Badley, M. E., 1985, Practical Seismic Interpretation, International Human Resources Development Corporation: Boston.

Berndt, C., Buenz, S., Clayton, T., Mienert, J., and Saunders, M., 2004, Seismic character of bottom simulating reflectors; examples from the mid-Norwegian margin: Marine and petroleum geology, v. 21, no. 6, p. 723-733.

Bjørlykke, K., 2001, Sedimentologi og petroleumsgeologi, p. 233-322.

Breivik, A. J., Faleide, J. I., and Gudlaugsson, S. T., 1998, Southwestern Barents Sea margin: late Mesozoic sedimentary basins and crustal extension: Tectonophysics, v. 293, p. 21-44.

Brown, A. R., 1999, Interpretation of three-dimensional seismic data.

Bulat, J., 2005, Some considerations on the interpretation of seabed images based on commercial 3D seismic in the Faroe-Shetland Channel: Basin Research, v. 17, no. 17, p. 21.

Bünz, S., and Mienert, J., 2004, Acoustic imaging of gas hydrate and free gas at the Storegga Slide: J. Geophys. Res., v. 109.

Bünz, S., Mienert, J., and Berndt, C., 2003, Geological controls on the Storegga gas-hydrate system of the mid-Norwegian continental margin: Earth and Planetary Science Letters, v. 209, no. 3-4, p. 291-307.

Cartwright, J., Huuse, M., and Aplin, A., 2007, Seal bypass systems: AAPG Bulletin, v. 91, no. 8, p. 1141-1166.

Cathles, L. M., Su, Z., and Chen, D., 2010, The physics of gas chimney and pockmark formation, with implications for assessment of seafloor hazards and gas sequestration: Marine and Petroleum Geology, v. 27, no. 1, p. 82-91.

Chand, S., Mienert, J., Andreassen, K., Knies, J., Plassen, L., and Fotland, B., 2008, Gas hydrate stability zone modelling in areas of salt tectonics and pockmarks of the Barents Sea suggests an active hydrocarbon venting system: Marine and Petroleum Geology, v. 25, no. 7, p. 625-636.

Chand, S., and Minshull, T. A., 2003, Seismic constraints on the effect of gas hydrate on sediment physical properties and fluid flow: a review: Geofluids, v. 3, no. 4, p. 275-289.

Chand, S., Minshull, T. A., Gei, D., and Carcione, J. M., 2004, Elastic velocity models for gas-hydrate-bearing sediments;A comparison: Geophysical Journal International, v. 159, no. 2, p. 573-590.

Chand, S., Rise, L., Ottesen, D., Dolan, M. F. J., Bellec, V., and Bøe, R., 2009, Pockmark-like depressions near the Goliat hydrocarbon field, Barents Sea: Morphology and genesis: Marine and Petroleum Geology, v. 26, p. 1035-1042.

Chopra, S., Marfurt. K.J., 2005, Seismic attributes - A historic perspective: Geophysics, v. 70, no. 5, p. 3SO-28SO.
CorelDraw, 2007, Coreldraw Help.
Dahl, P., 2011, Fluidmigrasjon og akkumulasjon på Loppahøyden i sørvestlige deler av Barentshavet: Unpublished cand. scient. thesis, v. University of Tromsø, p. 99.
Dewhurst, D. N., Aplin, A. C., Sarda, J. P., and Yang, Y., 1998, Compaction-driven evolution of porosity and permeability in natural mudstones; an experimental study: Journal of Geophysical Research, B, Solid Earth and Planets, v. 103, no. 1, p. 651-661.
Dillon, W. P., Grow, J. A., and Paull, C. K., 1980, Unconventional gas hydrate may trap gas off southeast USA: Oil & Gas Journal, v. 78, p. 124-130.
Dore, A. G., 1995, Barents Sea Geology, Petroleum Resources and Commercial Potential: Arctic, v. 48, no. 3, p. 207-221.
Doré, A. G., and Jensen, L. N., 1996, The impact of late Cenozoic uplift and erosion on hydrocarbon exploration: offshore Norway and some other uplifted basins: Global and Planetary Change, v. 12, no. 1-4, p. 415-436.
Faleide, J. I., and Gudlaugsson, S. T., 1984, Evolution of the western Barents Sea: Marine and Petroleum Geology, v. 1, no. 2, p. 123-128.
Faleide, J. I., Gudlaugsson, S. T., and Jacquart, G., 1984, Evolution of the western Barents Sea: Marine and Petroleum Geology, v. 1, no. 2, p. 123-128.
Faleide, J. I., Vagnes, E., and Gudlaugsson, S. T., 1993, Late Mesozoic-Cenozoic evolution of the south-western Barents Sea in a regional rift-shear tectonic setting: Marine and Petroleum Geology, v. 10, no. 3, p. 186-214.
Gassman, F., 1951, Elasticity of porous media: Ubre die elastizitat poroser medien: Vierteljahrsschrift der Naturforschenden Gesselschaft, v. 96, p. 1-12.
Gerhardt Einsele, G., J. M. Gieskes, J. Curray, and D. M. Moore,, 1980, Intrusion of basaltic sills into highly porous sediments and resulting hydrothermal activity: Nature, v. 283, p. 4.
Ginsburg, G. D., and Soloviev, V. A., 1997, Methane migration within the submarine gas-hydrate stability zone under deep-water conditions: Marine Geology, v. 137, no. 1-2, p. 49-57.
Gluyas, J., and Swarbrick, R., 2004, Petroleum Geoscience, p. 147-148.
Granli, J. R., Arntsen. Børge., Sollid. Anders., Hilde. Eilert., 1999, Imagin through gas-filled sediments using marine shear-wave data: Geophysics, v. 64, no. 3, p. 9.
Gudlaugsson, S. T., Faleide, J. I., Johansen, S. E., and Breivik, A. J., 1998, Late Palaeozoic structural development of the South-western Barents Sea: Marine and Petroleum Geology, v. 15, no. 1, p. 73-102.
Hamouda, A. A., 2010, Gas-Liquid Equilibria: Unpublished lecture notes, p. 15.
Henriet, J. P., and Mienert, J., 1998, Gas hydrates; relevance to world margin stability and climate change, Geological Society special publication.
Henriksen, E., Ryseth, A.E., Larsen, C.B., Heide, T., Rønning, K., Sollid, K., 2011b, Tectonostratigraphy of the greater Barents Sea. Implications for petroleum systems: In press.
Henriksen, S., and Vorren, T. O., 1996, Late Cenozoic sedimentation and uplift history on the mid-Norwegian continental shelf: Global and Planetary Change, v. 12, no. 1-4, p. 171-199.
Horozal, S., Lee, G. H., Yi, B. Y., Yoo, D. G., Park, K. P., Lee, H. Y., Kim, W., Kim, H. J., and Lee, K., 2009, Seismic indicators of gas hydrate and associated gas in the Ulleung Basin, East Sea (Japan Sea) and implications of heat flows derived from depths of the bottom-simulating reflector: Marine Geology, v. 258, no. 1-4, p. 126-138.
Hovland, M., Gardner, J. V., and Judd, A. G., 2002, The significance of pockmarks to understanding fluid flow processes and geohazards: Geofluids, v. 2, no. 2, p. 127-136.
Hovland, M., and Judd, A., 1988a, Seabed pockmarks and seepages : impact on geology, biology and the marine environment
Hovland, M., and Judd, A. G., 1988b, Seabed pockmarks and seepages: Impact on geology, biology and the marine environment, London, Graham & Trotman, 293 p.:

Hubbert, M. K., and Willis, D. G. W., 1957, Mechanics of hydraulic fracturing: Trans. Am. Inst. Min. Eng., v. 210, p. 153-168.
Hunt, J. M., 1996, Petroleum geochemistry and geology.
Hustoft, S., Bünz. S., Mienert. J., 2010, Three-dimensional seismic analysis of the morphology and spatial distribution of chimneys beneath the Nyegga pockmark field, offshore mid-Norway: Basin Research, v. 22, no. 2010, p. 15.
J.E.Skeie, D. A. K. a., 2006, Petroleum migration, faults and overpressure, part I: Jornal of petroleum geology, v. 29, p. 39.
Karlsen, D. A., and Skeie, J. E., 2006, Petroleum migration, faults and overpressure, Part 1: Calibrating basin modelling using petroleum in traps - A review: Journal of Petroleum Geology, v. 29, no. 3, p. 29.
Knipe, R. J., 1992, Faulting processes and fault seal, *in* Larsen, R. M., Brekke, H., Larsen, B. T., and Talleraas, E., eds., Structural and Tectonic modelling and its application to Petroleum Geology Volume 1, NPF, p. 325-342.
Knutsen, S. M., Skjold, L. J., and Skott, P. H., 1992, Palaeocene and Eocene development of the Trosmø Basin - sedimentary response to rifting and early sea-floor spreading in the Barents Sea area: Norsk Geologisk Tidsskrift, v. 72, p. 191-207.
Kristensen, L., 2010, Fluid migration and shallow gas accumulation on the south-western flank of Loppa High, SW Barents Sea: Unpublished cand. scient. thesis, v. University of Tromsø, p. 119.
Laberg, J. S., and Andreassen, K., 1996, Gas hydrate and free gas indications within the Cenozoic succession of the Bjørnøya Basin, western Barents Sea: Marine and Petroleum Geology, v. 13, no. 8, p. 921-940.
Laberg, J. S., Andreassen, K., and Knutsen, S. M., 1998, Inferred gas hydrate on the Barents Sea shelf — a model for its formation and a volume estimate: Geo-Marine Letters, v. 18, no. 1, p. 26-33.
Lammers, S., Suess, E., and Hovland, M., 1995, A large methane plume east of Bear Island (Barents Sea): implications for the marine methane cycle: International Journal of Earth Sciences, v. V84, no. 1, p. 59-66.
Løseth, H., Gading, M., and Wensaas, L., 2009, Hydrocarbon leakage interpreted on seismic data: Marine and Petroleum Geology, v. 26, no. 7, p. 1304-1319.
Løseth, H., Wensaas, L., Arntsen, B., Hanken, N., Basire, C., and Graue, K., 2001, 1000 m long gas blow-out pipes, 63rd EAGE Conference & Technical Exibition, 11-15 June, Extended Abstract: Amsterdam, Netherlands, EAGE, p. 524.
Magoon, E. A. B. a. L. B., 2003, Petroleum systems Exploring for oil and gas traps, v. Chapter 3.
Manne, A. S., and Richels, R. G., 2001, An alternative approach to establish trade-offs among greenhouse gasses: Nature v. 410, p. 3.
Marfurt, S. C. a. K. J., 2005, Seismic attributes - A historical prespective society of Exploration geopysicists, v. 70, no. 5, p. 3SO-28SO.
Martens, I., 2009, Fluidmigrasjon i Snøhvitområdet - drivmekanismer og strømningsprosesser: Unpublished cand. scient. thesis, University of Tromsø, p. 200.
Maslin, M. O. M., Betts, R., Day, S., Jones, T.D., Ridgwell, A., 2010, Gas hydrates: past and future geohazards: The royal society v. 368.
Mazzini, A., Svensen, H., Hovland, M., and Planke, S., 2006, Comparison and implications from strikingly different authigenic carbonates in a Nyegga complex pockmark, G11, Norwegian Sea: Marine Geology, v. 231, no. 1-4, p. 89-102.
McIver, R. D., 1982, Role of naturally occurring gas hydrates in sediment transport: American Association of Petroleum Geologists Bulletin, v. 66, no. 6, p. 789-792.
Mienert, J., Vanneste, M., Bünz, S., Andreassen, K., Haflidason, H., and Sejrup, H. P., 2005, Ocean warming and gas hydrate stability on the mid-Norwegian margin at the Storegga Slide: Marine and Petroleum Geology, v. 22, p. 233-244.

Morten Smelror, O. V. P., Geir Birger Larssen and Stephanie C. Werner, 2009, Geological History of the Barents Sea.

Nordling, C., and Österman, J., 2006, Physics Handbook for Science and Engineering, Lund, Sweden, Studentlitteratur, 475 p.:

NPD, 2007, The NPD's Fact Pages.

-, 2010, Norwegian Petroleum Directorate Fact pages. .

NPD, and OED, 2010, Fakta, Norsk Petroleumsverksemd.

Nøttvedt, A., Cecchi, M., Gjelberg, J., Kristensen, S. E., Lønøy, A., Rasmussen, A., Rasmussen, E., Skott, P. H., and Veen, V., P.M., 1992, Svalbard - Barents sea correlation, a short review, *in* Vorren, T. O., Bergsager, E., Dahl-Stamnes, O. A., Holter, E., Johansen, B., Lie, E., and Lund, T. B., eds., Arctic geology and pet. pot., Elsevier, p. 363-375.

Ohm, S. E., Karlsen, D. A., and Austin, T. J. F., 2008, Geochemically driven exploration models in uplifted areas: Examples from the Norwegian Barents Sea: AAPG Bulletin, v. 92, no. 9, p. 1191-1223.

Riedel, M., Novosel, I., Spence, G. D., Hyndman, R. D., Chapman, R. N., Solem, R. C., and Lewis, T., 2006, Geophysical and geochemical signatures associated with gas hydrate-related venting in the northern Cascadia margin: Geol Soc Am Bull, v. 118, no. 1-2, p. 23-38.

Riis, F., 1992, Dating and measuring of erosion, uplift and subsidence in Norway and the Norwegian shelf in glacial periods: Norsk Geologisk Tidsskrift, v. 72, p. 325-331.

Ristinen, R. A., and Kraushaar, J. J., 2006, Energy and the environment, Boulder Colorado.

Ryseth, A., Augustson, J. H., Charnock, M., Haugerud, O., Knutsen, S.-M., Midbøe, P. S., Opsal, J. G., and Sundbø, G., 2003, Cenozoic stratigraphy and evolution of the Sørvestnaget Basin, Barents Sea: Norwegian Journal of Geology, v. 83, no. 257-281.

Schlumberger, 2009, Seismic interpretation and visualization, Petrel 2009.

Selley, R. C., 1998, Elements of Petroleum Geology (2.ed.), no. 2. ed.

Sheriff, R., and Robert, E., 1995, Exploration seismology.

Sheriff, R. E., 2006, Encyclopedic Dictionary of Applied Geophysics, Society of Exploration Geophysicists, 429 p.:

Shipley, T. H., Houston, M. K., Buffler, R. T., Shaub, F. J., McMillan, K. J., Ladd, J. W., and Worzel, J. L., 1979, Seismic reflection evidence for the widespread occurrence of possible gas hydrate horizons on continental slopes and rises: American Association of Petroleum Geologists, Bulletin, v. 63, p. 2201-2213.

Sloan, E. D. J., 1998a, Clathrate Hydrates of Natural Gases, New York & Basel, Marcel Dekker Inc., 705 p.:

-, 1998b, Gas Hydrates: Review of Physical/Chemical Properties: Energy Fuels, v. 12, no. 2, p. 191-196.

-, 1998c, Physical/chemical properties of gas hydrates and application to world margin stability and climatic change, *in* Henriet, J.-P., and Mienert, J., eds., Gas Hydrates, Relevance to world margin stability and climatic change: London, The Geological Society, p. 31-50.

Solheim, A., and Elverhøi, A., 1985, A pockmark field in the central Barents Sea; gas from a petrogenic source?: Polar research, v. 3, no. 1, p. 11-19.

Sylta, Ø., 2004, Hydrocarbon migration modelling and exploration risk.

Taner, M. T., 2001, Seismic attributes: CSEG Recorder, v. 26, no. 7, p. 48-56.

Thingnes, V., 2007, Fluid migration pathways in the Snøhvit area, SW-Barents Sea: Master's thesis in geology, v. In press.

Tissot, B. P., and Welte, D. H., 1984, Petroleum Formation and Occurrence, Springer Verlag.

Torsvik, T. H., and Cocks, R. M., 2005, Norway in space and time: A Centennial cavalcade: Norwegian Journal of Geology, v. 85, no. 1-2, p. 73-86.

Vasseur, G., Djeran-Maigre, I., Grunberger, D., Rousset, G., Tessier, D., and Velde, B., 1995, Evolution of structural and physical parameters of clays during experimental compaction: Marine and petroleum geology, v. 12, no. 8, p. 941-954.

Veeken, P., 2007, Seismic Stratigraphy, basin analysis and reservoir characterisation.: Handbook in Seismic Exploration v. 37, p. 1-58.

Vorren, T. O., Laberg, J. S., Blaume, F., Dowdeswell, J. A., Kenyon, N. H., Mienert, J., Rumohr, J., and Werner, F., 1998, The Norwegian-Greenland Sea continental margins: morphology and Late Quaternary sedimentary processes and environment: Quaternary Science Reviews, v. 17, no. 1-3, p. 273-302.

Vorren, T. O., Lebesby, E., Andreassen, K., and Larsen, K. B., 1989, Glacigenic sediments on passive continental margin as exemplified by the Barents Sea: Marine Geology, v. 85, p. 251-271.

Vorren, T. O., Richardsen, G., Knutsen, S.-M., and Henriksen, E., 1991, Cenozoic erosion and sedimentation in the western Barents Sea: Marine and Petroleum Geology, v. 8, no. 3, p. 317-340.

Weibull, W., Mienert, J., Buenz, S., Hustoft. S, 2010, Fluid migration directions inferred from gradietn of time surfaces of the sub seabed: Marine and Petroleum Geology, v. 27, no. 9, p. 1898-1909.

Wikipedia, 2011, www.wikipedia.org.

Worsley, R. J., Edrich, S. P., and Hutchison, I., 1988, The Mesozoic and Cenozoic succession of Tromsøflaket In: A Lithostratigraphic Scheme for the Mesozoic and Cenozoic Succession Offshore Mid- and Northern Norway (Eds A. Dalland, D. Worsley and k. Ofstad): Norwegian Petroleum Directorate Bulletin, v. No. 4, p. 42-65.

Yilmaz, O., 2001, Seismic data analysis: Processing, inversion and interpretation of seismic data. Investigations in Geophysics, v.2.

8 Figure reference: